Universitat Politècnica de València
I.U.I. CMT - Clean Mobility & Thermofluids

UNIVERSITAT
POLITÈCNICA
DE VALÈNCIA

Doctoral Thesis

Evaluation by detailed CFD modelling of the effect of renewable fuels on the flame structure under compression ignition engine conditions

Presented by:
Daiana De León Ceriani

Supervised by:
Dr. José María García Oliver

in fulfillment of the requirements for the degree of
Doctor of Philosophy

Valencia, May 2024

Ph.D. Thesis

Evaluation by detailed CFD modelling of the effect of renewable fuels on the flame structure under compression ignition engine conditions

Presented by: Daiana De León Ceriani
Supervised by: Dr. José María García Oliver

Examination committee:

Chairman: Dr. José Vicente Pastor Soriano
Secretary: Dra. María Arántzazu Gómez Esteban
Member: Dr. Fabien Tagliante Saracino

Reviewing board:

Dr. Michele Bardi
Dr. Adrian Pandal Blanco
Dr. Fabien Tagliante Saracino

Valencia, May 2024

Abstract

The significant impact of the transportation sector on global CO_2 emissions and its effect on climate change has led to a shift towards more efficient and environmentally sustainable technologies. However, the pace of this transformation is slow relative to what is needed to mitigate existing global warming. In this regard, pathways toward transformation have diversified recently, with the concept of defossilization emerging as an alternative to decarbonization. Defossilization emphasizes the possibility of incorporating a greater variety of synthetic and renewable fuels, which can yield equally effective results. Among these alternatives, Polyoxymethylene dimethyl ether ($OMEn$) fuels stand out due to their oxygenated character and absence of carbon-carbon bonds, making them promising in reducing soot formation. Furthermore, their similarities and compatibilities with conventional diesel enable the utilization of the existing global fleet of internal combustion engine vehicles, thus potentially accelerating the transition on a global scale.

This thesis aims to conduct a fundamental study on the combustion process and flame structure of Diesel-like sprays when $OMEn$-type fuels are utilized. To achieve this objective, the proposed methodology is eminently computational, addressing significant gaps in the existing literature. A study of chemical kinetics and diffusion effects in the fuels under investigation uses canonical configurations such as homogeneous reactors and counterflow flamelets. Subsequently, the combustion process and flame structure are examined in detail through extensive Computational fluid dynamics (CFD) simulations, employing RANS and LES turbulence models in conjunction with an advanced combustion model based on the flamelet concept, UFPV.

All studied cases are defined according to the Engine Combustion Network (ECN) guidelines, representing sprays injected into quiescent environments with single-hole nozzles. Specifically, Spray A and D are evaluated, along with the impact of varying ambient temperatures.

In conclusion, it can be affirmed that the CFD models accurately predict combustion development under the analysed conditions, and these fuels can develop different flame structures highly dependent on the imposed boundary conditions.

Resumen

El alto impacto del sector transporte respecto a las emisiones globales de CO_2 y su efecto en el cambio climático ha llevado a que éste transite hacia tecnologías más eficientes y medioambientalmente sostenibles. Sin embargo, el ritmo de transformación es lento en relación a lo que se necesita para frenar el calentamiento global existente. En este sentido, en los últimos tiempos los caminos hacia la transformación se han diversificado; el concepto de "defossilization" ha surgido como alternativa a la descarbonización, ya que destaca la posibilidad de incluir una mayor cantidad de combustibles sintéticos y renovables, con los cuales se pueden obtener resultados igualmente efectivos. Dentro de estos, destacan los combustibles Polioximetileno dimetil éter ($OMEn$), su carácter oxigenado y no poseer enlaces carbono-carbono, los hace prometedores respecto a la formación de hollín. Además, presentan grandes similitudes y compatibilidades con el diésel convencional, lo cual posibilita el uso de la flota de vehículos con motores de combustión interna existente a nivel mundial, acelerando así la transición y siendo una alternativa con alcance global.

La presente tesis tiene como objetivo llevar a cabo un estudio fundamental sobre el proceso de combustión y la estructura de la llama de chorros tipo Diésel cuando se utilizan combustibles tipo $OMEn$. Para la consecución de dicho objetivo, la metodología planteada es eminentemente computacional, encontrando aquí las mayores brechas en la literatura. Se lleva a cabo un estudio de la cinética química y el efecto de la difusión en los combustibles estudiados mediante configuraciones canónicas, como reactores homogéneos y *flamelets* de contraflujo. Posteriormente, se estudia detalladamente el proceso de combustión y la estructura de la llama mediante el uso extensivo de Dinámica de fluidos computacional (CFD, en inglés), con modelos de turbulencia RANS y LES, en conjunto con un modelo de combustión avanzado basado en el concepto de *flamelets*, denominado UFPV.

Todos los casos estudiados están definidos siguiendo las directrices de la Engine Combustion Network (ECN), los cuales representan chorros inyectados en ambientes quiescentes con toberas monoorificio. Particularmente, se evalúan los Sprays A y D, y el impacto de variar la temperatura ambiente.

Como conclusión general, se puede afirmar que estos modelos CFD predicen correctamente el desarrollo de la combustión bajo las condiciones analizadas, y que estos combustibles son capaces de desarrollar diferentes estructuras de llama altamente dependientes de las condiciones de contorno impuestas.

Resum

L'alt impacte del sector del transport respecte a les emissions globals de CO_2 i el seu efecte en el canvi climàtic ha portat a que aquest transite cap a tecnologies més eficients i mediambientalment sostenibles. No obstant això, el ritme de transformació és lent en relació amb el que es necessita per frenar l'escalfament global existent. En aquest sentit, en els últims temps els camins cap a la transformació s'han diversificat; el concepte de "defossilització" ha sorgit com a alternativa a la descarbonització, ja que destaca la possibilitat d'incloure una major quantitat de combustibles sintètics i renovables, amb els quals es poden obtenir resultats igualment efectius. Dins d'aquests, destaquen els combustibles tipus polioximetilen dimetil èters ($OMEn$), el seu caràcter oxigenat i al no posseir enllaços carbó-carbó, els fa prometedors respecte a la formació de sutge. A més, presenten grans semblances i compatibilitats amb el dièsel convencional, la qual cosa possibilita l'ús de la flota de vehicles amb motors de combustió interna existent a nivell mundial, accelerant així la transició i essent una alternativa amb abast global.

La present tesi té com a objectiu dur a terme un estudi basic sobre el procés de combustió i l'estructura de la flama de dolls tipus Dièsel quan s'utilitzen combustibles tipus $OMEn$. Per a la consecució d'aquest objectiu, la metodologia plantejada és eminentment computacional, trobant ací les majors mancances en la literatura. Es realitza un estudi de la cinètica química i l'efecte de la difusió en els combustibles estudiats mitjançant configuracions canòniques, com ara reactors homogenis i *flamelets* de contraflux. Posteriorment, s'estudia detalladament el procés de combustió i l'estructura de la flama mitjançant l'ús extensiu de dinàmica de fluids computacional (CFD, en anglés), amb models de turbulència RANS i LES, conjuntament amb un model de combustió avançat basat en el concepte de *flamelets*, anomenat UFPV.

Tots els casos estudiats estan definits seguint les directrius de l'Engine Combustion Network (ECN, en anglés), els quals representen dolls injectats en ambients quiescents amb toveres mono-orifici. Particularment, s'avaluen els Sprays A i D, i l'impacte de variar la temperatura ambient.

Com a conclusió general, es pot afirmar que aquests models CFD prediuen correctament el desenvolupament de la combustió sota les condicions analitzades, i que aquests combustibles són capaços de desenvolupar diferents estructures de flama altament dependents de les condicions de contorn imposades.

A los que buscan
aunque no encuentren

a los que avanzan
aunque se pierdan

a los que viven
aunque se mueran.

– Mario Benedetti.

A mi familia.
En especial a ti, Abuela.

Acknowledgements

Quisiera en estas líneas expresar mi agradecimiento a todos los que han contribuido en el desarrollo de este trabajo, de infinitas maneras. Este largo camino me ha permitido conocer nuevas personas que han dejado su huella, y a su vez, reafirmar vínculos y valorarlos aún más, desde la distancia.

En lo más directo al desarrollo de esta tesis, quiero agradecer a mi tutor, Xemary. El comienzo de doctorado con el covid llegando para cambiárnoslo todo, ha influido y de qué manera en el camino imaginado... Aun así, recuerdo ese tiempo difícil para todos a nivel personal, y en mi caso, más que desafiante a nivel profesional, no haberme sentido sola ni perdida gracias a ti. También quiero agradecer lo que más valoro de todo lo compartido durante estos más de cuatro años, el procurar siempre, y enseñarnos de muchas formas, pero principalmente con el ejemplo, a trabajar en la calidad y el detalle del trabajo por sobre todo lo demás. Además de agradecer todo lo que he aprendido en este tiempo sobre sprays y su combustión, que era un mundo desconocido para mí. En este contexto, me gustaría extender el agradecimiento a José Manuel, quien también ha influido y de gran forma en la consecución de esta tesis, gracias por siempre tener consejos para dar, y por ser una referencia en CFD.

Así mismo, agradecer también al instituto CMT-Clean Mobility and Thermofluids por darme la oportunidad de llevar a cabo mis estudios de doctorado en esta institución. Y dedicarle un especial agradecimiento a Amparo, tu labor es invaluable para los que transitamos el doctorado aquí, no hay palabras para describir y agradecer tu ayuda diaria durante todo este tiempo, mil gracias.

I would also like to thank the team at STFS-Simulation of reactive Thermo-Fluid Systems, and especially to Christian Hasse who gave me the opportunity to be part of this amazing research group. Philip, it has been a real pleasure to work with you. Thank you for all the time we have shared and also for your recommendations about places to visit in Hessen; also thanks to Sandra H., for your dedicated time to share and teach me. Big thanks to everyone on the team for making me feel like part of the group every day. A special shout-out to Sandra R., Andrea, and Paul for all the fun social stuff we do together. You guys rock!

Como institución, también quiero agradecer al IIMPI-Instituto de Ingeniería Mecánica y Producción Industrial. Gracias por haber despertado en mí el interés por la investigación y la educación. Porque muchas veces, ha sido la memoria de lo ahí transitado, un motor invisible que ayudaba a continuar cuando la pendiente era grande. Porque no puedo dar nombres, ya que son numerosas las personas que me han inspirado con su ejemplo y su calidez humana. Por

ello, quiero reconocer y agradecer especialmente a todo el grupo que conforma el instituto. Gracias por ser ese lugar donde poder realizarse profesionalmente, priorizando el vínculo y respeto entre las personas, lo que resulta en siempre querer volver. Mirando hoy a distancia, puedo decir: qué privilegio ser parte, gracias por permitírmelo.

Quiero continuar agradeciendo a las personas que más he podido conocer en este tiempo, Els Xiquets: Ale, Rodri, Frank, Brayan, Arturo, Oscar y Javi (nuestro último gran fichaje). Qué regalo haber transitado este camino con ustedes al costado, la diversidad de esta pequeña família es maravillosa y seguramente lo que hace a este camino compartido más bonito y enriquecedor, porque cada uno, con sus formas, costumbres, modos, han acompañado cada paso, individual y colectivo. Sens dubte que m'hagin permès compartir un trosset dels seus camins, ha estat, és i serà un dels premis més grans del doctorat. Moltes gràcies.

A los compañeros de despacho, especialmente a Felipe, Alba, Leo, Usama y Jiawei, que han hecho el día a día más divertido y cómo no, más fácil y más humano. Vivir cotidianamente sus logros y dificultades, así como ustedes los míos, han hecho que me sienta muchas veces comprendida, y otras, no tan perdida. Aquí, me gustaría además, Leo, agradecerte a ti, que has logrado que mi camino estuviera guiado y especialmente, tanto menos duro. Gracias por el pasaje de la posta, lo has hecho genial, por compartir conmigo todo tu conocimiento sobre sprays y CFD; y por invitarme a pasar mi primera Navidad lejos de casa, contigo y los tuyos. También querría extender este agradecimiento a un grupo más amplio de amigos que fui recogiendo en este andar, y que también han dejado su huella en mí, tanto profesional como personalmente: Cassio, Rami, Maggie, Victor, Andrés y Weiwei.

A mis compis, Mariu et Emma, solo puedo decir ¡lo han bordado! Qué acierto haber creado y compartido hogar con ustedes. Gracias, porque la armonía en la convivencia entre tres personas tan diferentes no es casualidad, por las cenas compartidas, las charlas y los infaltables detalles. Todo ha sido más fácil con sus presencias en mi vida, por siempre agradecida: Amigas. Gràcies et Merci.

Amigos de Uruguay, porque luego de más de cuatro años siguen tan presentes en mi día a día como cuando estábamos al lado, son muchos a los que agradecer y no podría poner todos los nombres aquí. Gracias por mantener este vínculo intacto, por estar pendientes, por las siempre difíciles de coordinar videollamadas con las cinco horas de diferencia; por conocer cada paso que he dado, cada dificultad a la que me he enfrentado y haber sido un apoyo fundamental e incomparable estando a diez mil kilómetros de distancia. También

mil gracias a los que están de este lado del charco, que han sido un inmenso refugio en el cual sentirme segura y han representado, con su ser, mi hogar.

A vos, Bastien, por las infinitas montañas reales y simbólicas que hemos subido y coronado juntos. Gracias por siempre encontrar motivos para abrir un nuevo vino y celebrar, cuando la semana venía difícil y parecía no poder seguir. También agradecer a tu familia que ha sido la mía durante todo este tiempo. Gracias nuevamente, por el camino recorrido y los sueños compartidos. Santé et merci infiniment à toi.

El último, y también, el más importante Gracias es a mi familia, no tengo palabras suficientes para expresarles lo que siento hacia ustedes. Gracias por ser esa roca fuerte desde donde afrontar la vida, sin importar la distancia ni las circunstancias. A vos mamá, por ser incondicional, por ser ejemplo de perseverancia, por nutrirme de valores y transmitirme siempre tu cariño inconmensurable. Abuela, a ti, sé que estarás feliz donde estés. Gracias por enseñarme el amor auténtico, sin límites ni condiciones; por tu sabiduría, por la forma en que me transmitiste el amor por el estudio y la lectura, que es hoy gran responsable del camino recorrido. Familia toda, a ustedes, muchas gracias, muchas veces.

"Al final del camino me preguntarán: ¿Has vivido?, ¿Has amado? Y yo, sin decir nada, abriré el corazón lleno de nombres" A todos estos nombres, infinitas gracias, esto también les pertenece.

Funding acknowledgements

The respondent wishes to acknowledge the financial support received through a grant from Vicerrectorado de Investigación of Universitat Politècnica de València with reference FPI UPV SUBP2 (PAID-01-20).

Technical acknowledgements

The author also would like to special thank to "Rigel" from Universitat Politècnica de València, and the HPC Cluster from CMT-Clean Mobility & Thermofluids for allowing their cluster to perform the simulations carried out in this work, and the technical support received.

Thanks to Dr. Bertrand Naud from CIEMAT for the support in the use and application of the flamelet solver used in this work.

Last but not least, thanks to Convergent Science for allowing the author to use their software to carry out this thesis.

Contents

List of Figures

List of Tables

Nomenclature

Acronyms

AMR	Adaptive Mesh Refinement.
BEV	Battery Electric Vehicles.
C12	n-Dodecane.
CAD	Crank Angle Degree.
CFD	Computational Fluid Dynamics.
CI	Compression Ignition.
CMT	Clean Mobility and Thermofluids - Research Institute.
CN	Cetane Number.
CO2	Carbon Dioxide.
CO	Carbon Monoxide.
DBI	Diffused Back-Illumination.
DDM	Discrete-Droplet Method.
DME	Dimethyl Ether.
DNS	Direct Numerical Simulations.
ECN	Engine Combustion Network.
EGR	Exhaust Gas Cecirculation.
EoS	Equation of State.
EU	European Union.
EV	Electric Vehicle.
FGM	Flamelet-Generated Manifolds.
FT	Fischer-Tropsch.
GHG	Greenhouse Gases.
HC	Hydrocarbons
HRR	Heat Release Rate.
HTC	High-Temperature Ignition.

HVO	Hydrotreated Vegetable Oil.
ICE	Internal Combustion Engines.
ID	Ignition Delay.
IEA	International Energy Agency.
IMEP	Indicated Mean Effective Pressure.
KH	Kelvin-Helmholtz.
LCA	Life Cycle Analysis.
LCF	Low Carbon Fuel.
LES	Large-Eddy Simulations.
LHV	Lower Heating Value.
LIF	Laser-Induced Fluorescence.
LL	Liquid Length.
LOL	Lift-Off Length.
LTI	Low-Temperature Ignition.
MR	Most Reactive.
MW	Molecular Weight.
NL	Natural Luminosity.
NOx	Nitrogen Oxides.
NTC	Depending on the context, Negative Temperature Coefficient or No Time Counter.
NZE	Net Zero Emissions.
ODE	Ordinary Differential Equation.
OESI	Oxygen Extended Sooting Index.
OMEn	poly-Oxymethylene Dimethyl Ethers (Generic).
OMEx	Specific composition of $OMEn$ used in this thesis.
PAH	Polycyclic Aromatic Hydrocarbons.
PDF	Probability Density Function.
PIV	Particle Image Velocimetry.
PLIF	Planar Laser-Induced Fluorescence.
PNSD	Particle Number Size Distribution.
PN	Depending on the context, Particle Number or Normalized Profile.
RANS	Reynolds-Averaged Navier-Stokes.
RT	Rayleigh-Taylor.
SA	Spray A.
SCH	Schlieren.

SD	Spray D.
SOI	Start of injection.
SP	Smoke Point.
SR	Strain Rate.
S	Spray vapour/tip penetration.
TCI	Turbulence-Chemistry Interaction.
TSI	Threshold Sooting Index.
TTW	Tank-To-Wheel.
UFPV	Unsteady Flamelet Progress Variable.
WTT	Well-To-Tank.
WTW	Well-To-Wheel.

Greek symbols

α_ν	Constant used to determine IQ_ν in LES.
$\beta-$	Beta function.
χ	Scalar dissipation rate.
χ_{st}	Scalar dissipation rate for stoichiometric conditions.
ΔP_{inj}	Injection pressure.
Δ	Cell size.
δ_{ij}	Kronecker delta function.
$\dot{\omega_k}$	Chemical cource term per unit volume.
λ	Wavelenght.
λ_k	Kolmogorov scale.
μ	Dynamic viscosity.
ν	Kinematic viscosity.
ν', ν''	Stoichiometric coefficients for the reactants and products species.
ν_{num}	Numerical viscosity in LES.
ν_{sgs}	Subgrid scale viscosity in LES.
ω	Acentric factor.
ω_k	Rate of reaction.
ϕ	Equivalence ratio.
ψ	Reactive scalar.
ρ	Density.
ρ_{amb}	Ambient density.
τ_{chem}	Characteristic chemical time.

τ_{ij}	*(i,j)* component of the Reynolds stress tensor.
τ_{physic}	Characteristic physical time.
ε	Turbulent kinetic energy dissipation.
ϑ	Molar volume.

Latin symbols

$\dot{M}$	Momentum flux.
$\dot{m}$	Mass flow rate.
$\dot{Y}_c$	Progress variable source term.
ℓ	Turbulent lenght scale.
a, b	Constants used in the Peng-Robinson equation of state.
a_f	Fuel age.
a_M	Eulerian fluid residence time or fluid age.
A_r	Pre-exponential constant in the Arrhenius equation.
a_{mw-f}	Mass-weighted stream age.
b_r	Temperature exponent in the Arrhenius equation.
C	Normalized progress variable.
c	Speed of light.
C_A	Area coefficient.
c_k	Molar species concentration.
c_p	Specific heat.
C_v	Velocity coefficient.
C_χ	Constant of proportionallity for the mean scalar dissipation rate model.
C_μ	Turbulent viscosity constant in k-ε model.
$C_{\varepsilon i}$	Constants in ε transport equation in the k-ε model.
D	Mass diffusivity.
d_o	Nozzle effective diameter.
d_{eq}	Equivalent nozzle diameter.
Da	Damköhler number.
E_a	Activation energy.
h	Depending on the context, Total enthalpy or Planck's constant.
h_f	Enthalpy of formation.
K	Conductivity.
k	Turbulent kinetic energy.
$k_{b,j}$	Rate coefficient of the backward reactions.

$k_{f,j}$	Rate coefficient of the forward reactions.
N_A	Avogadro's number.
N_c	Total number of species in the system.
N_r	Total number of elementary reaction.
$O_2\%$	Oxygen concentration.
P	Pressure.
P_{cr}	Critical pressure.
Pr	Prandtl number.
R_u	Universal gas constant.
S	Depending on the context, source term or segregation factor.
s	Total entropy.
S_{ij}	Mean strain rate tensor.
Sc	Schmidt number.
T	Temperature.
t	Time.
T_{amb}	Ambient temperature.
T_{cr}	Critical temperature.
u	Velocity.
u_o	Velocity at the nozzle.
x	Coordinate.
x^*	Normalized axial coordinate.
Y_c	Progress variable.
Y_k	Mass fraction of species k.
Y_{RC}	Carbon reconstructed species mass fraction.
$\tilde{Z}''^2$	Mean Mixture Fraction variance.
$\tilde{Z}$	Mean Mixture Fraction.
C	Carbon.
H	Hydrogen.
IQ_ν	Viscosity Index of Quality.
O	Oxygen.
Z_{rms}	Mixture Fraction root mean square.
Z_{st}	Stoichiometric Mixture Fraction.
Z_{var}	Mixture Fraction variance.
Z	Mixture Fraction.

Chapter 1

Introduction

Contents

1.1 Motivation

In recent decades, climate change has caused impacts on natural and human systems across all continents and oceans, indicating the sensitivity of these systems to climate variations. Some of these changes have been associated with human influences, such as the decrease in extreme cold temperatures, the increase in extreme warm temperatures, the rise in maximum sea levels, and the more significant number of intense precipitation events in various regions, among others [1].

In a 2016 report, the World Meteorological Organization indicated that 79 extreme weather events had been studied, and it was concluded that climate change had influenced more than half of them [2]. Furthermore, several sources [1, 3–6] indicate that contributions to climate change are unequal, and the most affected regions, with risks even to life, are predominantly those that contribute the least to global warming, associated with lower economic and/or industrial development. Therefore, existing and future treaties and commitments, like the Paris Agreement [7] or, more recently, the one achieved in COP28 [8], are vital for mitigating climate change and improving actual and future trends.

Climate change mitigation entails endeavours aimed at curtailing the release of greenhouse gases (GHGs) into the atmosphere and/or diminishing their concentrations therein. Mitigation strategies encompass initiatives to reduce GHGs emissions from energy generation and consumption, such as reducing fossil fuel utilization and land-use practices. Additionally, mitigation efforts include deploying methods to counteract warming effects, such as carbon sinks, which sequester emissions from the atmosphere via land-use practices or other means, including artificial mechanisms [4].

If current global carbon dioxide (CO_2) emissions persist, it is anticipated that the remaining carbon allowance for restricting warming to 1.5°C will likely be depleted prior to 2030. Between 1850 and 2019, the cumulative CO_2 emissions stemming from the fossil fuel industry and agriculture, forestry, and other land use amounted to 2400±240 $GtCO_2$. Of this total, approximately 410 ± 30 $GtCO_2$ were emitted since 2010. This quantity aligns closely with the remaining carbon allowance for constraining global warming to 1.5°C and represents between one-third and one-half of the 1150 ± 220 $GtCO_2$ allowance for limiting global warming below 2°C with a 67% probability [9].

In 2020, the International Energy Agency (IEA) published the distribution of global energy-related CO_2 emissions by sector [10], indicating that industry, transportation, and power (including oil, gas and coal) are the sectors contributing the most, with a 23 %, 23 % and 40 % respectively (Figure 1.1).

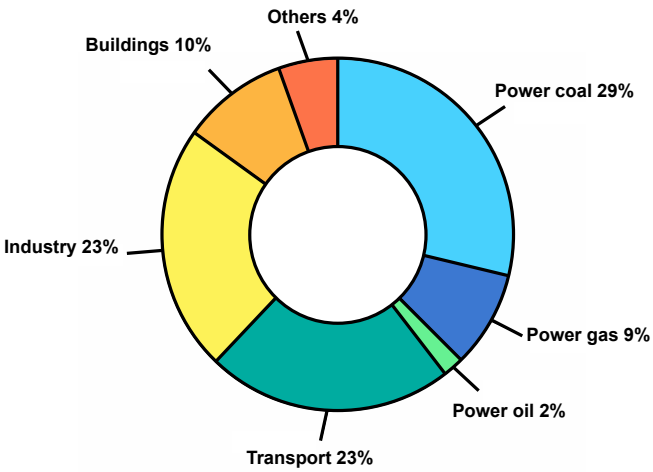

Figure 1.1: Distribution of global energy-related CO_2 emissions by sector [10].

Then, in another IEA report issued in 2022 [11], CO_2 emissions from energy combustion and industrial processes were shown to grow by 0.9% or 321 Mt reaching a new all-time high of 36.8 Gt. Figure 1.2 illustrates the changes in CO_2 emissions during the 2021-2022 period by region (left) and sector (right). While positive developments can be gleaned from it, such as reductions in emissions from both Europe and China, the net change remains unfavourable and far from the considered global objectives towards Net Zero Emissions (NZE).

In terms of sectors, transportation, and power led the emissions in this period. Global CO_2 emissions from power and transport (including international bunkers) increased by 261 Mt and 254 Mt, respectively, surpassing reductions from industry and buildings, sectors that have reduced their emissions. As a conclusion, the pace of change is still too slow, and more robust measures and behavioural changes will be needed to get on track with the NZE scenario.

Figure 1.2 encourages sustained efforts towards improving sector emissions while also emphasizing reflection. It underscores the United Nations' recognition of the unequal contributions to and simultaneous impacts from climate change, thus highlighting the complexity and injustice inherent in the issue.

From this standpoint, consideration must be given to the renowned *energy transition*, emphasizing that this transition should encompass possibilities for diverse economies, societies, natural resources, and infrastructures, among other factors. The fight against climate change is a global challenge and requires global solutions.

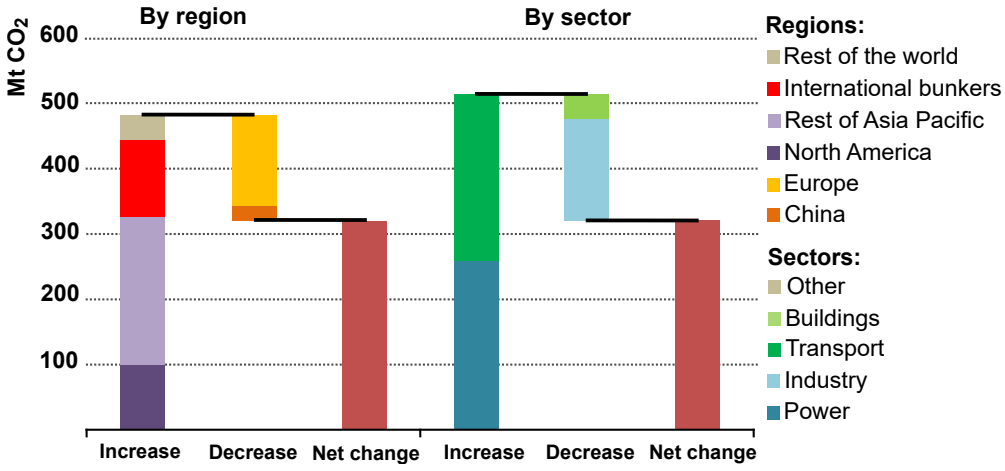

Figure 1.2: Change in CO_2 emissions by region and by sector, 2021-2022. Taken from IEA "CO_2 emission in 2022" report [11].

Regarding the transportation sector, one of the two main CO_2 emitters today, and the focus of this thesis, novel technologies are crucial for reducing CO_2 emissions. While Battery Electric Vehicles (BEVs) powered by renewable electricity can potentially decrease CO_2 emissions in the passenger transport sector [12], electrification of marine, aviation, or heavy-duty applications poses important challenges. However, electrification is one of many paths, and there are alternatives to complement it in the energy transition of the transportation sector.

Within this context, electrofuels (e-fuels) also referred to as power-to-liquid or power-to-gas fuels. Which are electricity-based liquid or gaseous fuels produced from hydrogen and CO_2 are all environmentally and climate-friendly. The e-fuel alliance highlights some of its advantages: it allows the global potential of solar and wind power to be unleashed around the world, are produced by using renewable electricity as well as atmospheric CO_2 from the air and hydrogen from water, resulting in a climate-neutral solution; most of them do not produce additional greenhouse gases while they are in use, and can be used in today's transport and heating systems allowing the sustainable use of existing infrastructure in the transport and heating sectors, among others benefits [13].

Within the broad range of the existing e-fuels, a large quantity are liquids. Many of these alternative fuels have the potential to power internal combustion engines (ICEs) [14–18], the sector is particularly immersed in an unstoppable and promising transition towards electric mobility, but in any case, the autonomy needs of the vehicle make electrification difficult for high power and long-range applications. Typically, the term *decarbonizing* the transport sector is discussed, but the term decarbonizing translates to removing carbon from the conversion process, leaving only a tiny group of e-fuels, such as Hydrogen and Ammonia inside, and naturally, electrification. However, if *defossilization* is considered, it offers a broader and equally specific approach to the objective of reducing CO_2 emissions and, therefore, working towards mitigating climate change, considering that the quicker way to abate GHGs emissions from road transport is to replace fossil-based fuel as fast as possible. Furthermore, these renewable and synthetic fuels provide value for different countries in different ways: as powerfuels suppliers, technology providers, demand countries, and some countries that combine several such motives [19].

In 2022, nearly one in five cars sold were electric in Europe, an increase of roughly 35% from the year before. If the pace of growth in electric vehicles (EVs) sales over the past two years is sustained through 2030, CO_2 emissions from cars can be put on a path in line with the NZE Scenario [20]. However,

widespread deployment of electric vehicles is still not a global phenomenon. Outside of China, sales in developing and emerging economies have been slow to pick up due to the relatively high purchase price of an EV and lack of charging infrastructure [13].

The path laid out and imposed by the European Commission last year, which solely focused on the electrification of transportation by eliminating ICEs, has been reconsidered. This reconsideration comes in light of opposition to this drastic decision from certain countries, which is perceived as hasty and incorrect. This is especially so considering the stance of the e-fuel alliance [13], which indicates that there are currently over 300 million vehicles in the EU (with approximately 270 million being passenger cars) and over 1.3 billion vehicles worldwide, the majority of which are powered by ICEs. Even with a significant adoption of battery electric vehicles in the coming years, the existing fleet will remain the backbone of mobility for decades. Millions of ICE-powered cars will still be on Europe's roads until 2030 and beyond. Furthermore, the limited range associated with the battery capacity and the scarcity of raw materials for manufacturing presents a tremendous opportunity to harness, in conjunction with compatible liquid e-fuels, the enormous climate protection potential and easy integration that ICE represents.

At this point, it is imperative to ascertain the contribution of this technology to climate protection. Ideally, a vehicle carbon footprint should be evaluated based on its entire life cycle. Several authors have conducted many life cycle assessments (LCA) to evaluate a vehicle environmental impact across its entire lifespan. The cradle-to-grave analysis encompasses all stages of the vehicle's life cycle, from the initial processing of raw materials (cradle) to its final disposal (grave). This comprehensive approach includes assembly, maintenance, refuelling, disassembling, and recycling of components.

Within the cradle-to-grave framework, various phases are considered, including cradle-to-gate, well-to-tank (WTT), tank-to-wheel (TTW), and end-of-life stages, each focusing on different aspects of the vehicle lifecycle. The WTT phase concentrates on the energy source used to fill the vehicle tank. At the same time, TTW focuses on the energy carrier from the tank to the vehicle propulsion system during operation. The combination of WTT and TTW is known as well-to-wheel (WTW), which is commonly employed to analyse energy conversion efficiency, total energy consumption, carbon footprint, and emission impacts of vehicles [21].

Among these two approaches, TTW has been the first to be used to justify electrification, given that these vehicles eradicate tailpipe emissions when they are entirely electric, as they do not have an exhaust pipe, thereby enabling the

eradication of local emissions. However, in recent years, there has been progress in considering the issue more comprehensively, which has been achieved through the WTW perspective. It is from this approach that several authors [22–26] emphasize the advantages that e-fuels can offer, even surpassing electrification in certain scenarios.

In particular, and as an example of the TTW versus WTW analysis and even compared with the complete LCA, Garcia et al. [24] have investigated the potential for emission reduction through the LCA of CO_2 emissions from electrified vehicles compared to ICE vehicles powered by e-fuel, using poly-Oxymethylene Dimethyl Ethers ($OMEn$, n stands for the chain length) as the e-fuel. The main conclusions of this study indicate that CO_2 emissions are similarly reduced both through the use of e-fuels and EVs. However, when conducting a complete LCA, which includes not only emissions during operation and production (WTW) but also usage, maintenance, assembly, disposal, and recycling, it was found that e-fuels have lower emission values than EVs, mainly due to the high emissions stemming from manufacturing associated to EVs. Based upon such kind of results, some countries in the UE opposed the European Commission preliminary regulation considering only electrified vehicles. Thus, e-fuels and particularly $OMEn$-type fuels, present themselves as a feasible choice for generating carbon-neutral fuels, providing an additional technology alongside vehicle electrification. Importantly, they can be quickly deployed, playing a crucial role in meeting the targets established for 2050 while tackling the present limitations of electrification.

1.2 Context

Liquid spray combustion, such as that occurring within a compression ignition (CI) engine, is a very complex process. A large quantity of subprocesses, such as liquid atomization, evaporation, mixing and eventually chemical reaction within a highly turbulent flow are present, which makes it very difficult to isolate and adequately quantify in real engine conditions. In that context, the role played by fundamental studies, or the reason for their importance in combustion processes, is primarily found in their ability to evaluate fuel performance by being isolated from other effects, such as wall conditions and interaction with other jets, and also in the fact that they allow models to be validated for later use in the development of safe and efficient engines. Thus, fundamental studies are generally well-defined within an experimental environment where fuels can be characterized through optical techniques, generating a vast database. By making use of this database to validate Computational Fluid

Dynamics CFD) calculations, insights into fundamental processes can be gained. Therefore, knowledge and understanding can be obtained by combining these three elements, highly-controlled experimental environment, optical techniques, and CFD. This ideal trinomial currently exists in the context of ICEs and is motivated and coordinated by the Engine Combustion Network (ECN) [27]. ECN comprises a consortium of renowned research institutions investigating reference injectors within highly controlled combustion chambers, serving as representative models for Diesel engine combustion, among other configurations. Standardized boundary conditions are established and made publicly accessible. This collaborative endeavour has compiled a vast experimental and numerical reference database, offering a comprehensive understanding of Diesel combustion. Notably, ECN Spray A (SA) and ECN Spray D (SD) represent automotive and heavy-duty diesel injectors that have been studied at various boundary conditions and by many institutions. Historically, investigations have made use of n-Dodecane as Diesel fuel surrogate. However, recent workshops organized by the ECN have shifted focus towards renewable Diesel fuels.

In this context, the research institute CMT, in which the present thesis is conducted, was involved in carrying out the experimental campaign of the ENERXICO Project [28]. Within this project, research has been conducted on using renewable fuels in future sustainable transportation systems. This encompasses both biofuels and power-to-liquid fuels. A thorough understanding of their combustion characteristics is imperative before their application in combustion systems with optimal efficiency and minimal pollutant emissions. The investigations were carried out through highly controlled experiments. These experiments emulate the operating conditions that such advanced fuels would encounter within the combustion chamber of an engine, using an optically accessible vessel based on the aforementioned ECN configurations. The highly controlled conditions of the ECN experiments enable the utilization of advanced optical diagnostic tools to quantify parameters that would otherwise be inaccessible during regular engine operation. From this campaign, two experimental PhD theses were involved within the CMT institute; one was presented by Garcia in 2021 [29] and the second one by Tejada [30] in 2023. In these studies, the global combustion parameter and flame structure of two oxygenated e-fuels, $OMEn$, OME_1, as well as Hydrotreated Vegetable Oil (HVO) and reference hydrocarbons like n-Dodecane and diesel, have been characterized using advanced optical techniques. Through the characterization, authors found that HVO presents a similar behaviour to n-Dodecane. At the same time, oxygenated fuels represent the most interesting cases regarding their particular flame structure and potential to reduce soot emissions highly. These PhD theses represent the experimental side of the trinomial mentioned above,

whereas the present thesis represents the CFD side, and both are articulated within the ECN.

Additionally, to completely define the context of this thesis, it is necessary to mention the numerical background of the CMT research group. The application of advanced flamelets models for diesel-like spray combustion modelling originated within the research group through the thesis conducted by Winklinger [31] in 2014. The initial implementation of the model was carried out in *OpenFOAM* [32], employing a RANS approach. This work was then extended in 2019 by Perez-Sanchez [33], who extensively used the model for liquid sprays defined under ECN conditions, also presenting the initial LES results by this author. Lastly, the preceding step to the current thesis was taken by Pachano [34] in 2020, who implemented the model in *CONVERGE* CFD [35]. He incorporated a two-equation model for soot prediction and applied it to n-Dodecane sprays under a RANS approach.

The proposal of this thesis is derived from the recently described context. The new fuels to be studied are defined through the experimental database of the ENERXICO project. These fuels will be the oxygenated ones, $OMEn$ and OME_1, selected due to their novelty and potential found with experiments. Additionally, the previous numerical theses allow for a step towards extensive utilization of advanced modelling tools for high-fidelity combustion simulations.

1.3 Thesis Objective

The motivation and context set forth above have determined the objectives of this thesis. Considering liquid e-fuels integration, road transport with combustion engines could continue to operate in a climate-neutral manner and thus contribute directly to the defossilization of the existing fleet. For the correct integration of these fuels, a characterization of them is necessary, both at a practical and fundamental level. It is on this last point where the literature exhibits important gaps, mainly in terms of detailed CFD studies, which will be made explicit in the following chapter. And taking into account the experimental results of previous theses, the family of the so-called $OMEn$-type have turned out to be very promising candidates.

In that context, the general objective of the thesis it is a *detailed CFD evaluation of the changes in quantitative combustion parameters (Ignition delay, lift-off length, tip vapour penetration, etc) and in the topology of the flame with OMEn-type fuels.*

The specific objectives defined to achieve the general objective are as follow:

- Evaluation of chemical mechanisms available for the fuels to be studied and search for physical properties necessary for modelling.
- Evaluation of combustion evolution under canonical configuration that make it possible to isolate chemical kinetics and diffusion effects, in particular homogeneous reactors and flamelets.
- Modelling of ECN single-hole nozzle experiments with a RANS approach, as a first approximation to the characterization of the flame and combustion parameters of n-Dodecane, OME_1 and $OMEn$.
- Modelling of ECN single-hole nozzle experiments with a Large Eddy Simulation approach and detailed analysis of the spray combustion evolution.

1.4 Thesis outline

The thesis is organized in seven chapters, starting with this brief introduction (**Chapter 1**), that presented the motivation and context of the present thesis, and finally the objectives of the work.

Chapter 2 The chapter is initiated with a comprehensive description of the combustion process in a Diesel spray, covering from liquid atomization to the establishment of the characteristic diffusion flame, and also taking into consideration the coexistence of different flame regimes within a diesel-like spray combustion. Subsequently, the current understanding of $OMEn$-type fuel is presented, encompassing characterization, significant differences and similarities to reference hydrocarbons, as well as their applicability and performance in internal combustion engines.

Chapter 3: This chapter describes the numerical models, including, chemical kinetics, spray model, turbulence and turbulence-chemistry interaction approach, the developed tools within this thesis, as well as the computational methodology employed in conducting the research.

Chapter 4: In this chapter, combustion canonical configurations such as homogeneous reactors and laminar diffusion flamelets have been employed to investigate the chemical kinetics of the fuels addressed in this thesis. The effect of diffusion in a non-premixed combustion process has been clarified, and a comparison between the available chemical mechanisms has been performed.

Chapter 5: This chapter is focused on discussing the results from RANS framework and a flamelet-based combustion model, UFPV. The combustion

process and flame structure of single-hole liquid sprays for the two oxygenated and renewable target fuels, namely $OMEn$ and OME_1, operating under ECN SA conditions is computationally examined. Three different levels of ambient temperature have been evaluated, comparing the results with experimental data.

Chapter 6: In this chapter, ECN SA and SD has been modelled in the frame of LES simulations and the UFPV combustion model. The two temperature levels selected for both sprays are 800 K and 900 K. In that context, the effect of two different boundary conditions has been analysed. Through this work, information is provided on the autoignition process and the structure of the flame, with a more in-depth analysis than that of the Chapter 5, thanks to high-fidelity simulation.

Chapter 7: This chapter compiles the principal conclusions derived from the research, alongside suggestions for future endeavours aimed at expanding knowledge beyond the limits of this thesis.

References

[1] Pachauri, R.K and Reisinger, A. (eds.) *Climate Change 2007: Synthesis Report. Contribution of Working Groups I, II and III to the Fourth Assessment Report of the Intergovernmental Panel on Climate Change*. Tech. rep. IPCC, Geneva, Switzerland, 2007.

[2] Organización Meteorológica Mundial. "Estado del clima mundial en 2011–2015". In: (2016).

[3] Lee, H. and (eds.), J. Romero. *IPCC, 2023: Climate Change 2023: Synthesis Report. Contribution of Working Groups I, II and III to the Sixth Assessment Report of the Intergovernmental Panel on Climate Change*. Tech. rep. IPCC, Geneva, Switzerland, 2023. DOI: 10.59327/IPCC/AR6-9789291691647.

[4] Shukla, P.R and J. Skea, (eds.) *Climate Change 2022: Mitigation of Climate Change. Contribution of Working Group III to the Sixth Assessment Report of the Intergovernmental Panel on Climate Change*. Tech. rep. Cambridge University Press, 2022.

[5] *Emissions Gap Report 2023: Broken Record – Temperatures hit new highs, yet world fails to cut emissions (again)*. Tech. rep. United Nations Environment Programme, Nairobi, 2023.

[6] Pajares, Miguel. *Refugiados climáticos: Un gran reto del siglo XXI*. Rayo Verde, 2020.

[7] *United Nations climate change: the Paris Agreement*. Tech. rep. United Nations, 2020.

[8] *United Nations Climate Change Conference COP28*. Tech. rep. United Nations, 2023.

[9] Canadell, Josep G and Jackson, Robert B. *Ecosystem collapse and climate change*. Springer, 2021.

[10] *Global energy-related CO2 emissions by sector*. Tech. rep. IEA, Paris, 2020.

[11] *CO2 Emissions in 2022, IEA, Paris https://www.iea.org/reports/co2-emissions-in-2022*. Tech. rep. IEA, Paris, 2023.

[12] Brennan, John W. and Barder, Timothy E. *Battery Electric Vehicles vs Internal Combustion Engine Vehicles : A United States-Based Comprehensive Assessment*. Tech. rep. 2016.

[13] eFuel Alliance. *https://www.efuel-alliance.eu/*. 2023.

[14] Pastor, José V., García, Antonio, Micó, Carlos, and Lewiski, Felipe. "An optical investigation of Fischer-Tropsch diesel and Oxymethylene dimethyl ether impact on combustion process for CI engines". In: *Applied Energy* 260 (2020). DOI: 10.1016/j.apenergy.2019.114238.

[15] García, Antonio, Gil, Antonio, Monsalve-Serrano, Javier, and Sari, Rafael Lago. "OMEx-diesel blends as high reactivity fuel for ultra-low NOx and soot emissions in the dual-mode dual-fuel combustion strategy". In: *Fuel* 275 (2020). DOI: 10.1016/j.fuel.2020.117898.

[16] Barro, Christophe, Parravicini, Matteo, and Boulouchos, Konstantinos. "Neat polyoxymethylene dimethyl ether in a diesel engine; part 1: Detailed combustion analysis". In: *Fuel* 256 (2019), p. 115892. DOI: 10.1016/j.fuel.2019.115892.

[17] Barro, Christophe, Parravicini, Matteo, Boulouchos, Konstantinos, and Liati, Anthi. "Neat polyoxymethylene dimethyl ether in a diesel engine; part 2: Exhaust emission analysis". In: *Fuel* 234 (2018), pp. 1414–1421. DOI: 10.1016/j.fuel.2018.07.108.

[18] Härtl, Martin, Seidenspinner, Philipp, Jacob, Eberhard, and Wachtmeister, Georg. "Oxygenate screening on a heavy-duty diesel engine and emission characteristics of highly oxygenated oxymethylene ether fuel OME1". In: *Fuel* 153 (2015), pp. 328–335. DOI: 10.1016/j.fuel.2015.03.012.

[19] Global Alliance Powerfuels. "Powerfuels: Missing link to a successful energy transition". In: *Global Alliance Powerfuels: Berlin, Germany* (2019).

[20] *The Role of E-fuels in Decarbonising Transport*. Tech. rep. IEA, Paris, 2024.

[21] *The overall CO2 impact for drive technologies in individual transport today and in the future*. Tech. rep. Frontier economics, 2019.

[22] Hank, Christoph et al. "Comparative well-to-wheel life cycle assessment of OME 3–5 synfuel production via the power-to-liquid pathway". In: *Sustainable Energy & Fuels* 3.11 (2019), pp. 3219–3233. DOI: 10.1039/C9SE00658C.

[23] Garcia, Antonio, Monsalve-Serrano, Javier, Villalta, David, and Mendoza, María Guzmán. *OMEx Fuel and RCCI Combustion to Reach Engine-Out Emissions Beyond the Current EURO VI Legislation*. Tech. rep. SAE Technical Paper, 2021.

[24] Garcia, Antonio, Monsalve-Serrano, Javier, Villalta, David, and Tripathi, Shashwat. *Electric vehicles vs e-fuelled ICE vehicles: comparison of potentials for life cycle CO2 emission reduction*. Tech. rep. SAE Technical Paper, 2022.

[25] Guzmán, María Gabriela. "Impact of different e-fuels type on light-duty compression ignition engine performance, emissions and CO2 Life cycle analysis". PhD thesis. Universitat Politecnica de Valencia, 2023.

[26] Tripathi, Shashwat. "Life Cycle Analysis of Different Powertrain Technologies for Decarbonising Road Transportation". PhD thesis. Universitat Politecnica de Valencia, 2023.

[27] Engine combustion network. *https://ecn.sandia.gov/*.

[28] ENERXICO Project. *https://enerxico-project.eu/*. 2022.

[29] Garcia-Carrero, Alba. "Experimental study of the fuel effect on diffusion combustion and soot formation under diesel engine-like conditions". PhD thesis. Universitat Politecnica de Valencia, 2021.

[30] Tejada, Francisco Jose. "Analysis of fuel effects on the diffusive flame structure using advanced optical techniques in a single cylinder optical engine". PhD thesis. Universitat Politecnica de Valencia, 2023.

[31] Winklinger, Johannes Franz. "Implementation of a Combustion Model based on the Flamelet Concept and its Application to turbulent reactive Sprays". PhD thesis. Universitat Politecnica de Valencia, 2014.

[32] OpenFOAM. *https://www.openfoam.com/*. The Open Source CFD Toolbox. User Gide Version 1.6, 2009.

[33] Pérez-Sánchez, E.J. "Application of a flamelet-based combustion model to diesel-like reacting sprays". PhD thesis. Universitat Politecnica de Valencia, 2019.

[34] Pachano, Leonardo. "CFD Modeling of combustion and soot production in diesel spray". PhD thesis. Universitat Politecnica de Valencia, 2020.

[35] CONVERGE CFD Software. *https://convergecfd.com*.

Chapter 2

Fundamentals and literature review

Contents

2.1 Introduction

Global energy transitions are inherently gradual processes spanning several decades, as evidenced by historical shifts. For instance, the transition from renewable biomass like wood to the coal-driven era took over a century, followed by another transition to oil and gas over approximately 90 years. Similarly, shifts such as moving from oil-based electricity to nuclear power also took decades to materialize. The ongoing global shift towards renewable energy sources is anticipated to follow a similar protracted timeline. However, specific

sectors, such as light-duty vehicles, may undergo faster transitions, mainly if catalysed by government interventions or technological breakthroughs. But this is not a global trend because, though efficient, direct electrification from renewable sources may not be feasible for several applications.

Given the imminent threat of global climate change, as outlined in Chapter 1, e-fuels generated from electricity hold promise for defossilization or even decarbonization of hard-to-abate sectors. In the case of CI engines, focusing on this thesis, leveraging existing infrastructure designed for conventional fuels is advantageous, as developing new infrastructure for renewable alternatives such as hydrogen would likely be more expensive and, therefore, unattainable for many economies. Likewise, the advances in knowledge of the combustion process in CI engines and the characterization of the flame structure that exists today are an excellent starting point for evaluating the potential of these new fuels.

Thus, this chapter initiates by examining the consolidated literature concerning the evolution of diesel flame structure and its combustion characteristics. The comprehension of the diesel combustion process has advanced, and the characterization of the flame structure has been enhanced due to the progression of numerous diagnostic techniques, encompassing experimental, numerical, and analytical methods. A brief description of the cause-effect chain during the diesel-like spray combustion will be presented.

The subsequent section introduces the $OMEn$ family of e-fuels. These liquid e-fuels exhibit significant promise for utilization in internal combustion engines, showcasing commendable efficacy in mitigating pollutants. Consequently, a thorough, deep characterization of these fuels will be provided, alongside findings derived from diverse studies documented in the literature, covering the use of $OMEn$ in CI engines and fundamental $OMEn$ spray combustion.

2.2 Diesel-like spray combustion

In the modern world, liquid fuel combustion is one of the primary sources of energy production. High specific energy on a volumetric basis and relative ease of storage are two benefits of liquid fuel. In the realm of energy systems, liquid fuels are commonly introduced into devices via the injection process, which is usually characterized by a significant degree of turbulence, leading to the formation of sprays. The efficiency of gas turbines, rocket combustors and internal combustion engines is significantly influenced by spray characteristics, which go through intricate processes which are complexly linked to one another and are difficult to separate from the individuals.

Fuel injection, atomization, droplet dispersion, evaporation, fuel-air mixing, combustion, and pollutant emissions are the main sub-processes that compose and characterize spray combustion. Figure 2.1 shows a schematic representation of these processes. Before being atomized into a huge amount of tiny droplets, liquid fuel is first injected into the combustion chamber through the nozzle in bulk liquid. Primary and secondary atomization are two more divisions of the atomization process. The process from bulk liquid to filaments and droplets is known as primary atomization, and the process from filaments and droplets to much smaller droplets is known as secondary atomization. Droplets evaporate, and the system is powered by autoignition and combustion that follows.

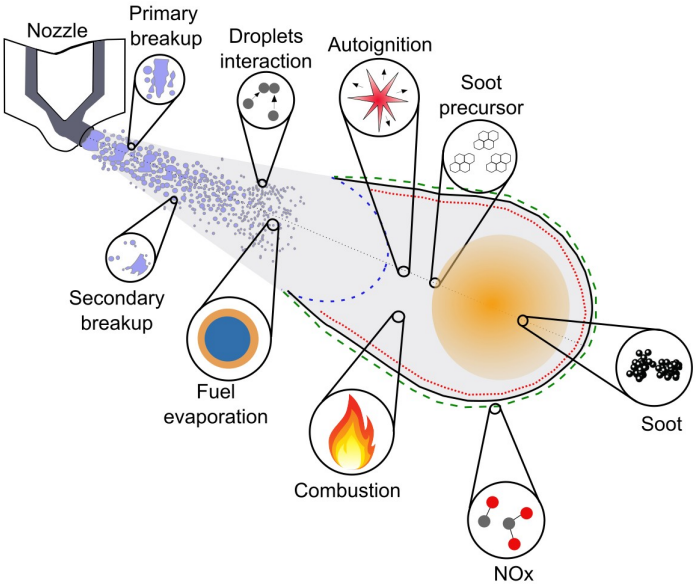

Figure 2.1: Cause-effect chain of Diesel-like spray combustion. Adapted from [1].

The following sections will review the main chain events on the reacting Diesel-like spray combustion, the study subject of this work, and the working principle for CI engines. In order to clarify, each event will be described individually, unifying the whole conceptual model proposed in the literature at the end.

2.2.1 Atomization

The initial process that occurs when liquid fuel enters the combustion chamber and interacts with the high-density, high-temperature air environment is

known as atomization in the context of the Diesel-like sprays. The liquid fuel injected through the nozzle at high velocity begins to disintegrate into droplets, expanding the surface area that comes into contact with the surrounding gas phase. Mass, momentum, and energy transfer are all improved by this increased phase interaction, and these phenomena are all important for the following stages of the combustion process.

As illustrated in Figure 2.2, it is common to divide the initial millilitres of the spray into two zones. The term "near field" refers to the area nearest the nozzle origin. It consists of the unbroken liquid core, whose length is known as the breakup length, and primary atomization is the most common event in this area. The subsequent region is known as the "far field". It stretches beyond the final location of liquid fuel, also known as the liquid length, and is distinguished in terms of atomization by secondary atomization of droplets interacting with the gas phase.

The disintegration of the liquid core in the near field results from primary breakup, a mechanism accountable for the emergence of the initial droplets in the spray. Complex phenomena such as cavitation, turbulence, and inertial instabilities govern the mechanism.

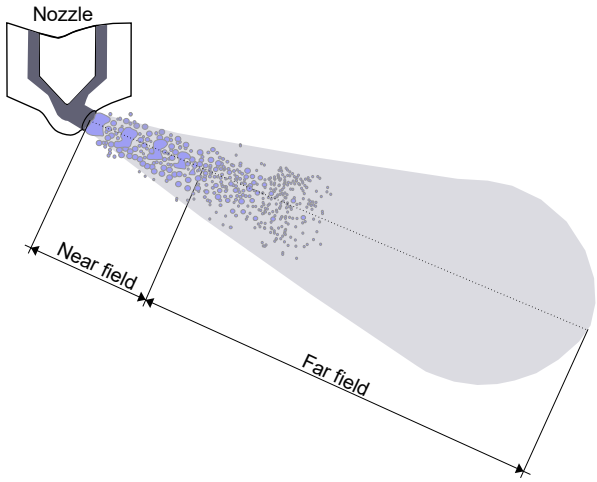

Figure 2.2: Scheme of spray regions.

Different breakup regimes can be defined depending on the liquid and gas phase properties and nozzle exit velocity. Reitz and Bracco [2] suggested a classification inlcuding four regimes:

- Rayleigh regime: This regime is observed in sprays with very low injection velocity and Reynolds number. In this case, the rupture of the liquid vein occurs due to the growth of instabilities initially generated on the spray surface by the effect of surface tension. The droplets generated in this manner are of uniform size and larger than the diameter of the nozzle orifice outlet.

- First regime induced by aerodynamic interaction: As a consequence of the increased velocity, the effect of the forces originated by the relative velocity between the liquid and the gas in the discharge chamber becomes increasingly important, even leading to oscillations of the spray concerning its helical symmetry axis. In this case, the effects of surface tension and aerodynamic friction have a similar influence on the breakup of the spray. Thus, the initial unstable oscillations generated are amplified and lead to the disintegration of the spray into droplets. In this regime, similar to the previous case, atomization occurs far from the orifice, while the generated droplets have a diameter similar to that of the outlet orifice.

- Second regime induced by aerodynamic interaction: A significantly more efficient atomization process is achieved by further increasing the spray's velocity. The initial oscillations grow due to aerodynamic forces, and breakup occurs closer to the orifice. The droplets have a much smaller average diameter than that of the orifice.

- Atomization regime: The spray completely disintegrates in the vicinity of the orifice (the closer, the higher the injection velocity). In this case, there are two possibilities, depending on whether or not the intact core of the spray exists. This distinguishes between the regimes of incomplete or complete atomization, respectively. The generated droplets have a much smaller diameter than that of the orifice. Here, the Reynolds number is high; the atomization regime is characterized by a breakup length that tends to zero.

In modern Diesel engines working conditions, experimental investigations indicate the prevalence of solely the atomization regime within the spray [3], wherein the break-up length remains unaffected by the exit velocity and is approximately equivalent to the diameter of the nozzle. The atomization regime is distinguished by a densely compact liquid core and droplets significantly smaller than the nozzle diameter, thereby substantially enhancing the level of complexity for both experimental and modelling endeavours [4].

Beyond the breakup length downstream, relatively large droplets resulting from primary atomization are subjected to aerodynamic forces. Should these forces exceed the surface tension inherent to a droplet, secondary breakup occurs, yielding smaller droplets. Various outcomes stemming from secondary breakup are conceivable [5], with several of the prevailing regimes depicted in Figure 2.3. The transition from one regime to another can be elucidated through consideration of the droplet Weber number, which correlates aerodynamic forces with the droplet surface tension. Consequently, vibrational breakup manifests at low Weber numbers, contrasting with catastrophic breakup. All regimes hold significance in the context of the Diesel spray; however, catastrophic breakup predominates owing to the high Weber number near the nozzle, where atomization phenomena are more pronounced [4]. Additionally, it is noteworthy that as secondary breakup occurs, interactions between droplets intensify, leading to the emergence of the coalescence phenomenon, which has been identified as one of the primary contributors to the substantial temporal and spatial variability observed in droplet sizes [6].

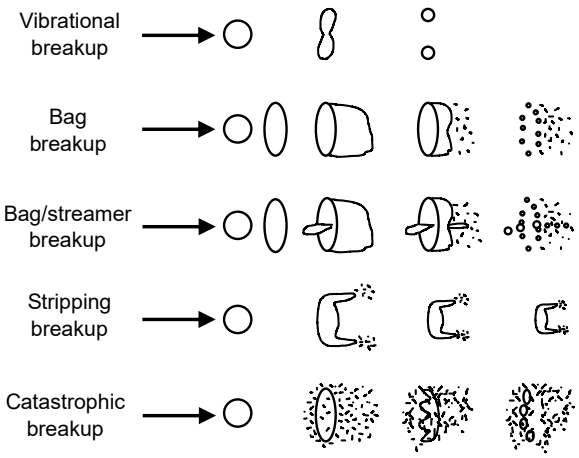

Figure 2.3: Secondary atomization regimes diagram [5].

At this point, the ultimate result of the various phenomena associated with fuel injection into the high-density, high-temperature air environment is the rapid and complete atomization of the liquid phase within the vicinity of the nozzle orifice. Consequently, the liquid and gas phases swiftly attain dynamic equilibrium, enabling the air-fuel mixture to exhibit a singular velocity, local composition, and thermodynamic state [7].

2.2.2 Evaporation and fuel-air mixing

Proceeding from the nozzle orifice, droplets progress downstream and initiate interactions with the surrounding gas phase, thereby facilitating air entrainment, a phenomenon intricately linked with the momentum induced by fuel injection. The entrainment heats the droplets, which causes the fuel vapour pressure at the droplet surface to rise, consequently inducing evaporation. This process is characterized by three distinct events: the deceleration of droplets attributable to aerodynamic drag, heat exchange from the air to the droplets, and the transfer of fuel vapour mass to the surrounding air.

Figure 2.4 depicts a schematic illustration of the phenomena associated with air entrainment and evaporation at the fuel-air interface. Due to evaporation, the liquid is present only from the nozzle exit up to a specific axial distance, referred to as the liquid length. This parameter has been extensively studied to characterize the evaporation process within the spray.

The liquid length significantly depends on boundary conditions, such as nozzle diameter, thermodynamic conditions and fuel properties. However, other important parameters, such as injection pressure and heat released during combustion, have been demonstrated not to influence the liquid length so much [8–12]. Espey and Dec [10] observed that the primary mechanism of heat transfer to the droplets stemmed from the surrounding gas atmosphere, as evidenced by the stabilization of the liquid length prior to the onset of combustion. Fuel temperature affects the spray breakup behaviour by dominantly causing cavitation [13]. Increasing fuel temperatures cause more cavitation, which helps spray breakup, faster liquid atomization and increased air entrainment.

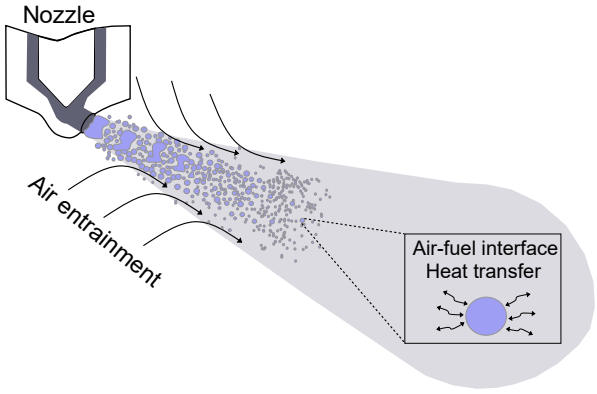

Figure 2.4: Fuel evaporation and air entrainment diagram.

Regarding injection pressure, Siebers [14] noted that the fuel-air mixing process regulates the liquid length. With higher injection pressures, smaller droplets are created, and liquid momentum is increased. This enables the liquid droplets to interact intensely with the ambient air, resulting in a liquid length that does not change. This interaction occurs throughout the lateral and front periphery of the spray plume which increases the air entrainment. This observation reinforces the hypothesis of thermal equilibrium at any given point under evaporative conditions in Diesel-like sprays.

The spray penetrates the gas phases downstream of the liquid length, and evaporated fuel blends with the surrounding air. Air entrainment and spray penetration are fundamental to ensure the efficient use of air in the combustion chamber. Due to its importance, fuel-air mixing has been extensively characterized. One approach is to split the phenomenon into macroscopic and microscopic spray metrics.

The spray penetration and cone angle usually describe the macroscopic scale [15–18]. On the one hand, spray penetration, indicated in Figure 2.4 as the farthest axial distance reached by the spray tip, has been identified as the principal measure for air entrainment in the distant region of the spray [15]. On the other hand, the cone angle is typically defined by the furthest cone angle observed in experiments, as suggested by Naber et al. [19]. These two macroscopic parameters facilitate the delineation of two distinct regions within the spray. Firstly, a steady region characterized by a conical shape, and secondly, a transient region proximate to the spray tip penetration.

At the microscopic level, the condition of fuel-air mixing is determined by the concept of mixture fraction (Z). The mixture fraction is a parameter of great importance in the characterization of a non-premixed flame. It is commonly defined based to the conservation of elements (the mass of elements is conserved during the reaction). However, under inert conditions where there are no chemical reactions, the mixture fraction simply corresponds to the fuel mass fraction. Anticipating the following section (Section 2.2.3), where the phenomenon of autoignition is introduced, a general definition of mixture fraction is presented independently of whether the conditions are for an inert or reacting mixture.

Bilger [20] introduced a mixture fraction definition to characterize mixing between a fuel and oxidizer stream in a two-feed system. Given a global reaction written on the element level, considering Carbon (C), Hydrogen (H) and Oxygen (O) the reaction can be represented as Equation 2.1,

$$\nu_c C + \nu_H H + \nu_O O \rightarrow P \tag{2.1}$$

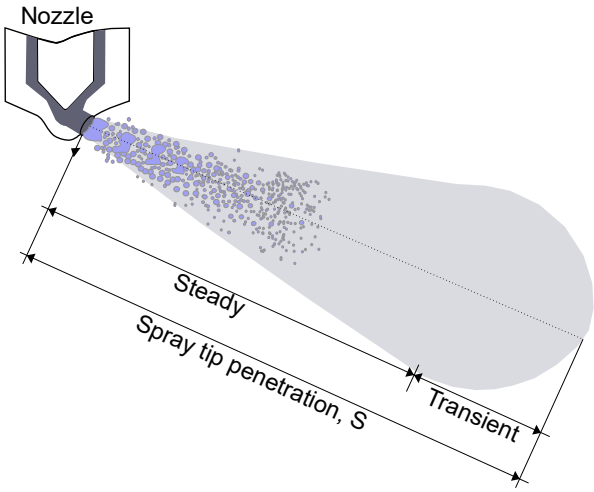

Figure 2.5: Macroscopic fuel-air mixing spray metrics.

A mixture fraction based on the atomic element mass fraction Z_j can be defined for an arbitrary composition in a reactive multi-species system, as in Equation 2.2,

$$Z_j = \sum_{i=1}^{N} \frac{a_{ij} MW_j}{MW_i} Y_i \tag{2.2}$$

here, a_{ij} is the number of elements j in species i, Y_i stands for the mass fraction of the species i, while MW_i the molecular weight of the specie i and MW_j the atomic weight of the element j.

Mixture fraction is usually defined in terms of a so-called "coupling function" β, which is a composition of variables (conservative or not) that results into a conservative one (Equation 2.3).

$$\beta = 2\frac{Z_C}{MW_C} + 0.5\frac{Z_H}{MW_H} - \frac{Z_O}{MW_O} \tag{2.3}$$

where MW stands for the atomic weight of C, H and O. Bilger mixture fraction definition (Z_B) ends up being normalized by comparing with fuel stream and oxidizer stream, Equation 2.4:

$$Z_B = \frac{\beta - \beta_{ox}}{\beta_f - \beta_{ox}} = \frac{2\frac{Z_C - Z_{C,ox}}{MW_C} + 0.5\frac{Z_H - Z_{H,ox}}{MW_H} + \frac{Z_O - Z_{O,ox}}{MW_O}}{2\frac{Z_{C,f} - Z_{C,ox}}{MW_C} + 0.5\frac{Z_{H,f} - Z_{H,ox}}{MW_H} + \frac{Z_{O,f} - Z_{O,ox}}{MW_O}} \tag{2.4}$$

Therefore, the mass originating from the fuel for any mixture is measured by Z. Furthermore, this Bilger definition offers the advantage of being independent of the fuel molecule itself, as it relies on atoms. It is applicable regardless of whether the fuel is a typical hydrocarbon (C_nH_m) or an oxygenated fuel ($C_nH_mO_p$) (an important aspect within this thesis), and whether exhaust gas recirculation (EGR) is present in the air or not. It is also commonly used in experiments, based on measurement of major species mass fractions.

2.2.3 Autoignition

Autoignition is the spontaneous ignition (no external sources) and burning of a fuel for given thermodynamic conditions. During autoignition, molecular bonds are broken releasing an amount of energy that increases the mean kinetic energy of the molecules and, hence, the system temperature. During this process, hundreds of species are produced and thousands of reactions occur, taking place with very different time scales.

Once fuel has vaporized and mixed with air, the spray may burn if there is high pressure and temperature in the environment. The fuel evaporation introduces an additional timescale to the problem, and the droplet size and spacing introduce additional length-scales. These parameters influence autoignition in a complicated manner, also manifested in the simplest problem of a single droplet suddenly immersed in a hot environment. In this situation, which has been examined extensively experimentally [21, 22], analytically [23] and numerically [24–28], the autoignition time increases with increasing droplet diameter and decreases with increasing fuel volatility. The time elapsed from the start of injection (SOI) until the mixture ignites is known as the ignition delay (ID), and it is composed of characteristic physical and chemical times related by the Damköler number (Da). Tanabe et al. [29], and Moriue et al. [30] have experimentally investigated the autoignition process of isolated fuel droplets of n-Heptane, n-Decane, and n-Dodecane in air, under several operating conditions. The same conditions have been further investigated by Cuoci et al. [31] numerically. The authors found from both fronts, that the types of ignition process were specified as no-ignition, cool flame ignition, single-stage, and two-stage ignition.

Single-stage autoignition has been extensively examined both numerically and experimentally, with Mastorakos providing a comprehensive review of

this topic [32]. Earlier studies by Mastorakos et al. [33] revealed that high-temperature autoignition initiates within what are termed as the most reactive (MR) pockets of fluid, typically comprising lean mixtures experiencing low scalar dissipation rates. This conceptualization has been corroborated by subsequent experimental inquiries [34–36] and numerical simulations [37, 38] which have delineated the formation of autoignition kernels serving as precursors for the ignition of the main flame and consequent heat release. Furthermore, the MR mixture fraction concept is also useful for the first stage of the two-stage autoignition.

Two-stage autoignition, is common in hydrocarbon fuels such as long-chain alkanes and in dimethyl ethers, which are extensively studied under Diesel-like spray combustion. In general, the transition from low-temperature ignition (LTI) to high-temperature combustion (HTC) occurs, through a negative temperature coefficient (NTC) region. Within this region, the autoignition delay paradoxically increases with rising temperature. During the low-temperature stage, oxygen addition and isomerization instigate chain branching reactions, leading to the generation and subsequent oxidation of oxygenated intermediates, such as ketohydroperoxides. However, it is important to note that these reactions yield minimal heat release. At a certain critical temperature threshold, the direction of oxygen addition reverses, transitioning to HTC. During HTC, hydrogen peroxide (H_2O_2) undergoes decomposition, and carbon monoxide oxidation reactions ensue, precipitating thermal runaway [39–43].

Figure 2.6 presents a conceptual model for non-premixed ignition under NTC conditions, which illustrates the complexity of the transition from low to high-temperature autoignition and is consistent with the recent studies [44–47]. In this model, low-temperature combustion (LTC) evolves as a primary autoignition event occurring at the leanest Z values where the temperature is sufficiently low to sustain LTC. The initiation of LTC ignition typically aligns with a time comparable to the minimum homogeneous ignition delay time, τ_1, and shows little sensitivity to turbulence [48]. Subsequently, LTC progresses towards richer mixtures, following the direction of the gradient of the first-stage ignition delay times. Nevertheless, studies have indicated that LTC propagation can resemble that of a cool flame rather than a spontaneous ignition front [49]. As a result, LTC is triggered earlier in rich mixtures compared to the timing of LTC ignition in a homogeneous mixture at the same local Z. This premature onset of LTC impacts the second stage of autoignition, such that the HTC ignition kernels form earlier and in richer mixtures than expected. The rich HTC kernels expand towards both lean and rich mixtures and may propagate either as a premixed flame [50] or as a spontaneous ignition front [51]. The HTC kernels converge with the cool flame in the direction of increasing Z. Conversely,

in the direction of decreasing Z, the expanding HTC kernels encompass and ignite the stoichiometric mixture fraction (Zst) iso-surface. [50, 51]. Hinging on the configuration, the ignition of the Zst iso-surface may induce the generation of edge flames, which then propagate into the partially reacted mixture [50–52]. In this model, the overall ignition process comprises the following stages: an initial phase of mixing with minimal chemical involvement, succeeded by the formation and propagation of cool flames, followed a subsequent rich premixed ignition and ultimately, non-premixed burning.

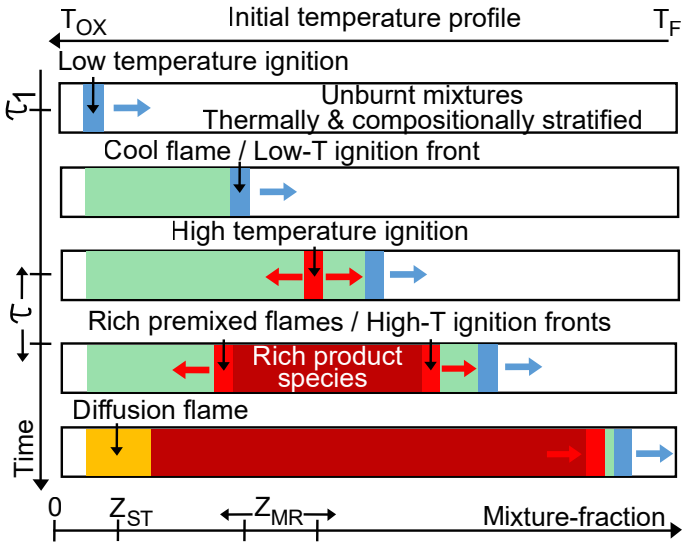

Figure 2.6: Model of non-premixed ignition under NTC conditions. Adapted from [48]

2.2.4 Mixing-controlled combustion

In the final stage of the Diesel spray combustion process, as it was recently explained, the premixed combustion instigated by autoignition evolves into a diffusion flame. The sustained flame front is maintained by the continuous provision of fuel and oxygen, with the rate being contingent upon the momentum supplied by fuel injection. Consequently, the combustion process during this phase is governed by mixing dynamics. A schematic representation of the flame structure proposed by Dec [53] is depicted in Figure 2.7. Dec's conceptual model stands as one of the widely accepted perspectives on the structure of reacting Diesel spray, offering a comprehensive overview of the intricate phenomena involved. Notably, in Figure 2.7, a significant observation is that the flame front (illustrated by the solid line) does not extend to the nozzle outlet. The distance from the nozzle outlet to the furthest upstream

position of the flame is referred to as the lift-off length (LOL). Along the LOL, a rich mixture is present, which undergoes combustion within the partially premixed zone. Progressing downstream, the flame front encompasses the spray core composed of intermediate combustion products and soot, which are oxidized in proximity to the flame front. Finally, nitrogen oxides (NOx) are generated in the outer region of the spray, facilitated by lean mixtures and elevated temperatures.

Continuous advancements in optical diagnostics have paved the way for a comprehensive characterization of the structure of Diesel-like reacting sprays. Maes [54] has presented findings on the structure at quasi-steady state from experiments conducted at various research institutions worldwide within the context of the ECN. Results include measurements of low- and high-temperature combustion species, specifically formaldehyde (CH_2O) and hydroxyl radicals (OH), as well as measurements of polycyclic aromatic hydrocarbons (PAHs) and soot. Maes observed the presence of CH_2O in fuel-rich mixtures downstream of the liquid length and upstream of the lift-off length (LOL). Combined measurements of OH and CH_2O indicate that the latter species is consumed in the vicinity of the high-temperature reaction zone. PAHs were detected around the centre of the spray, followed by the appearance of soot, which undergoes oxidation ultimately within the flame front.

The integration of optical diagnostics with numerical simulations has enabled a better understanding of relevant characteristics, such as the lift-off length. Comprehending the mechanisms behind flame stabilization at the LOL is integral to advancing towards cleaner combustion. It has been reported that flame stabilization is influenced by both autoignition and the downstream topology of the flame, contributing to advancements in this direction.

The intimate correlation between lift-off length and soot generation has been firmly established within the academic discourse. Nevertheless, a spectrum of stabilization mechanisms has been postulated and remains subject to ongoing scholarly deliberation. In this context, Tagliante et al. [55] conducted a study based on experimental observations and a dedicated DNS approach. The authors systematically categorizes and examines the occurrences facilitating flame stabilization at a specific LOL relative to the fuel injector based on the DNS findings. Both DNS simulations and experimental data collectively indicate that this stabilization process is characterized by intermittent behaviour: sections of the flame undergo autoignition initially, followed by downstream convection until another abrupt autoignition event occurs in closer proximity to fuel injector. The outcomes elucidate that the primary mechanism facilitating flame stabilization is autoignition. Nevertheless, the presence of multiple

configurations of reaction zones, in particular triple flames, is also observed at the margins of the spray. These configurations aid in flame stabilization by occupying regions of high-temperature burnt gases concentrated at the periphery, thereby instigating subsequent autoignition events.

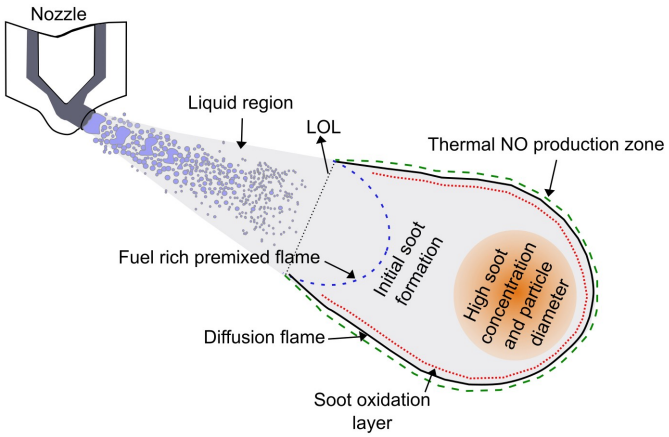

Figure 2.7: Scheme illustrating the reacting Diesel spray according to Dec's conceptual model.

Based on these observations and significant advancements in the framework of Diesel-like sprays, decades of study have led to the formulation of various combustion models aiming to minimize soot and NOx production. However, the focus has shifted from new technologies to investigating novel fuels in recent years. These fuels not only have the potential to achieve minimal emission levels but also contribute to reducing dependence on fossil fuels. Given the complexity of combustion in Diesel engines, as previously characterized, comprehensive studies of potential new fuels are necessary to determine the feasibility of this transition. These studies should encompass all phases involved, including these fuels production, utilization, and fundamental behavioural aspects. This goal may be attainable through collaboration across various research domains. While the primary aim of this thesis is to investigate the combustion process and flame structure of novel fuels under Diesel-like spray conditions, understanding the characterization of the target fuels and their potential is of paramount importance and has been essential to defining specific objectives for this work. For this reason, the following section provides a literature review on these topics.

2.3 OMEn-type fuels

Drawing upon the benefits outlined in Chapter 1 regarding e-fuels, these could serve as the pivotal element in achieving climate objectives. E-fuels all originate from hydrogen, generated through water electrolysis using renewable electricity. The utilization of hydrogen varies depending on its intended application. Figure 2.8 illustrates various pathways for transforming hydrogen and CO_2 into different types of e-fuels.

As depicted in the central pathway of Figure 2.8, hydrogen can undergo conversion with CO_2 to produce methane or syngas. CO_2 may be obtained from combustion products, biogenic sources, or directly extracted from the atmosphere [56]. Syngas can then be transformed into liquid fuels such as gasoline, Diesel, or kerosene through Fischer-Tropsch synthesis [57] or methanol via catalytic synthesis [58]. Further dehydrogenation of methanol yields dimethyl ether (DME). Methanol or DME can be subsequently refined to generate oxymethylene ethers, denoted as $OMEn$ (also known as polyoxymethylene dimethyl ethers). $OMEn$ have been the focus of study for years within the transport sector, particularly for CI engines, given their particular characteristics and compatibility with typical hydrocarbons. Characterized by the general structure CH3-O-(CH2-O)n-CH3 [59], where the (-CH2-O-) functional group forms multiple bonds with oxygen atoms for $n > 1$. When renewable electricity is utilized, and CO_2 is directly extracted from the atmosphere, a closed CO_2 cycle throughout the process is possible and electrofuels are nearly carbon-neutral.

In 2020, Awad et al. [61] conducted a systematic review of the application of oxygenated methyl esters ($OMEn$). Their research methodology employed primary sources, primarily scientific data from ScienceDirect, SAE International, and the Web of Science. They selected works covering at least one of the following topics: 1) effects of $OMEn$ as additive fuels on fuel properties, 2) $OMEn$ as additive fuels for Diesel engines, 3) $OMEn$ as additive fuels for gasoline compression ignition and homogeneous charge compression ignition engines, 4) $OMEn$ as alternative pilot fuels for dual-fuel engines, and 5) potential of $OMEn$ as future additive fuels for DISI engines. Additionally, they considered several specific keywords (for further details, please refer to the original paper [61]). Figure 2.9 presents the results of this comprehensive review, revealing numerous scientific contributions regarding the applications as mentioned above, with a growing number of papers since 2013, which has been sustained over time, indicating the potential of these fuels and mainly given its status as an eco-friendly. It is important to note that the decline in 2019 is since the work was conducted during that year.

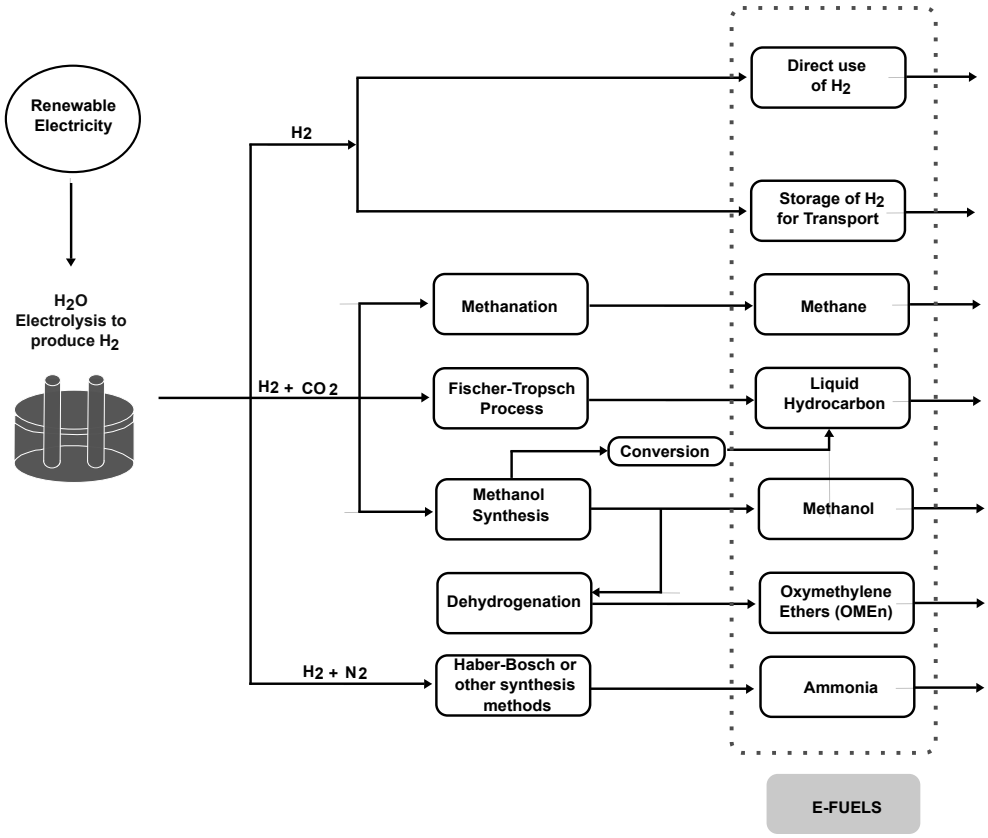

Figure 2.8: The pathways for various electrofuels begin with the electrolysis of water to produce hydrogen, utilizing renewable electricity. Subsequently, the middle pathway demonstrates the generation of diverse oxygenates and hydrocarbons, akin to conventional fuels [60].

$OMEn$ are synthesized using feedstocks with end-group (CH_3O-) providers, and chain groups ($-CH_2O-$) providers. From these possibilities, the conventional way to produce $OMEn$ nowadays proceeds by reacting methanol (as Figure 2.8 shows), which is a basic feedstock for the chemical industry, with one of the formaldehyde sources for chain elongation. According to the chemical equilibrium, a substantial chain growth necessitates a significant surplus of formaldehyde units, while any water present in the system compromises chain elongation. Instead, dimethoxymethane (OME_1) can serve as a feedstock to be combined with a formaldehyde source to produce $OMEn$, with n $>$ 1, in an anhydrous approach [62].

Therefore, from a production point of view, OME_1 as it is an intermediate

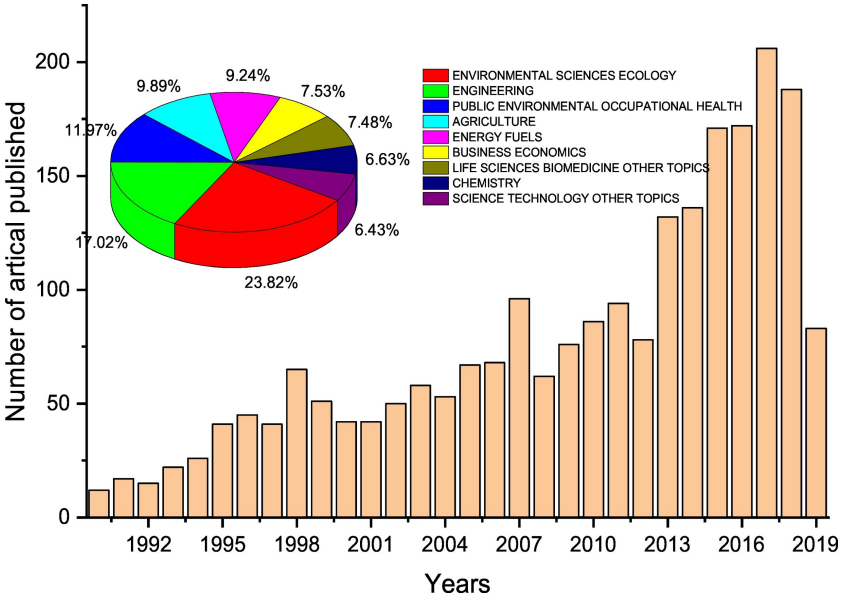

Figure 2.9: Web of Science data, covering the period since 1990, includes publications on polyoxymethylene dimethyl ether (POMDMEn) fuels, with PODEn and OMEn fuels serving as primary indices. Additionally, data since 1990 encompasses publications on POMDMEn fuels, with PODEn, OMEn, POMDMEn, and OMDMEn fuels serving as primary indices [61].

step in the production of $OMEn$, stands out as the most appealing $OMEn$ due to its higher exergetic efficiency in synthesis compared to $OMEn$ (with n > 1) variants with longer chain lengths. The exergetic efficiency of OME_1 production, at 85% [63], is only marginally lower than that of dimethyl ether (DME or OME_0) at 89% [64]. However, OME_1 exhibits significant differences in liquid fuel properties compared to conventional Diesel fuel [65]. On the combustion front, the derived cetane number of OME_1, at 28 [65], falls well below the minimum cetane number of 51 specified in EN 590 for Diesel fuel. Nevertheless, OME_1 boasts a higher lower heating value (LHV) than any $OMEn$ variant with n > 1. So, this fuel presents both advantages and disadvantages compared to $OMEn$ (n > 1), making it a subject of current research focus as well.

2.3.1 Characterization

Fuel properties are crucial engine efficiency indicators and must adhere to country-specific regulations and specifications. For instance, European countries follow EN 590 (already mentioned above), EN 228, and EN 589 standards

for Diesel fuel, gasoline, and automotive LPG, respectively, to ensure automotive fuel quality. $OMEn$ has advantageous features, including high oxygen content, high cetane number, and absence of aromatic hydrocarbons and sulphur, enhancing combustion performance and significantly reducing soot emissions in Diesel engines. However, challenges arise from its low flash point and heating value, impacting transportation, storage safety, and fuel economy. Additionally, further verification of the intersolubility of Diesel and $OMEn$ blends at low temperatures is needed. Table 2.1 summarizes the physicochemical characteristics of $OMEn$ with polymerization degree from n= 1 to n= 6, Diesel and n-Dodecane (C12, typically used to model Diesel).

Properties	$CH_3O(CH_2O)_nCH_3$							**Diesel**	**C12**
	n = 0	n=1	n=2	n=3	n=4	n=5	n=6		
Chemical formula	C_2H_6O	$C_3H_8O_2$	$C_4H_{10}O_3$	$C_5H_{12}O_4$	$C_6H_{14}O_5$	$C_7H_{16}O_6$	$C_8H_{18}O_7$	n.a.	$C_{12}H_{26}$
Molecular weight (g/mol)	46.07	76	106	136	166	196	226	n.a.	170
Cetane number	60	29	63	78	90	100	104	51.5	74
Flash point (ºC)	-42	<0	16	20	77	103	169	66	83
Density at 20 ºC (kg/m3)	670	860	960	1024	1067	1100	1130	822	751.2
Oxygen content (% m/m)	35	42.1	45.3	47.1	48.2	49	49.6	0	0
Boiling point (ºC)	-25	42	105	156	202	242	280	310	215
Lower heating value (MJ/kg)	28.4	22.44	20.32	19.14	18.38	17.86	17.47	42.6	44.2
Viscosity at 25 ºC (mm^2/s)	<1	0.36	0.79	1.08	1.72	2.63	n.a.	1.74	1.8
Lubricity at 60 ºC (μ m)	n.a	759	n.a.	534	465	437	n.a.	233	n.a

Table 2.1: Properties of pure OME_0 (or DME) to OME_6, Diesel and n-Dodecane [66–69].

Based on the characteristics listed in the table, some general advantages and disadvantages of $OMEn$ and their utilization in CI engines can be established. These characteristics will be further detailed in the next section through dedicated studies involving the use of $OMEn$ in ICEs.

The cetane number is a critical metric for assessing the ignition characteristics of Diesel and other fuels under compression ignition within the engine [70]. As the cetane number rises, the fuel autoignition capability improves, resulting in a shorter ID period and facilitating smoother cold starts. However, excessively high cetane numbers can cause uneven combustion and increased soot emissions. In compression ignition engines, Diesel fuel typically possesses a cetane number of at least 49. However, the cetane number of OME_1 is merely 29, falling short of the requirements for Diesel engine application. As the degree of polymerization of $OMEn$ exceeds 2, its cetane number significantly increases, surpassing that of Euro V Diesel fuel. This suggests that blending $OMEn$, with n $>$ 2, into Diesel can elevate the cetane numbers of the fuel. Nevertheless, the energy content of $OMEn$ decreases as n increases, implying that blends of Diesel-OME_1 also remain effective and sometimes favoured.

The inherent oxygen transport mechanism in oxygenated fuels during combustion offers a promising avenue for addressing the soot production issue [71]. In recent years, numerous studies have investigated the efficacy of oxygenated fuels such as DME [72], biodiesel [73], ethanol [74], and $OMEn$ in mitigating particulate matter (PM) emissions from Diesel engines. According to soot formation models, polycyclic aromatic hydrocarbons (PAHs) are primary precursors [75]. Concerning molecular structure of $OMEn$, the primary chain consists of alternating carbon and oxygen atoms without C–C bonds, resulting in a higher oxygen content than other oxygenated alternative fuels. $OMEn$ typically exhibits oxygen content between 42.1% to 50% (Table 2.1), with specific values dependent on the mass proportion of $OMEn$ with varying polymerization degrees. Notably, methanol, among alcohol fuels, possesses the highest oxygen content at approximately 49.93%. As molecular weight increases, oxygen content in alcohol fuels sharply decreases, with pentanol registering only 18.15%, but in $OMEn$, the trend is the opposite. Consequently, $OMEn$ demonstrates an a priori ability to significantly reduce soot emissions whether blended with Diesel fuel or used independently.

Figure 2.10 obtained from a characterization of various fuels [76], illustrates the combined results of oxygen content and CN of different fuels, including alcohols, biodiesel, and ethers (among which $OMEn$ is situated), demonstrating that $OMEn$, with $n > 1$, exhibits significantly higher CNs and oxygen content compared to alcohols and Diesel, which, according to the same study, exhibit a cetane number of 56.6. Moreover, an exceptionally high oxygen content ranges from 42.1% to 49.6% by mass, depending on the number of CH_2O groups present.

The presence of oxygen content combined with the absence of C–C bonds in $OMEn$ molecules is crucial, as it was already mentioned, in determining the sooting capacity of a fuel. Furthermore, in the early combustion phases, the CH2-O- functional group aids in producing hydroperoxides. These hydroperoxides subsequently break down into OH radicals during oxidation, promoting the further oxidation of soot precursors [59].

Therefore, more than one factor can contribute to achieving cleaner combustion with $OMEn$. In a kinetic study, Sun et al. [77] concluded that the soot-reduction potential was due to the absence of C–C bonds in $OMEn$. However, the influence of the individual polyether compounds present in $OMEn$ on its sooting propensity and the effect of chain length is still unknown. Meanwhile, Tan et al. [78] investigated the sooting characteristics of polyoxymethylene dimethyl ether blended with Diesel in a diffusion flame. They based their analysis on measuring the smoke point (SP) of the fuel blends. The SP of

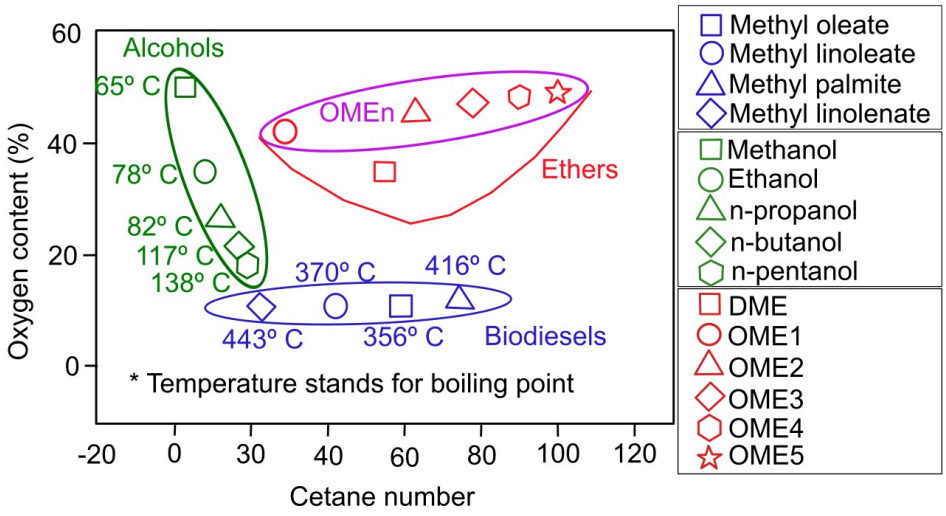

Figure 2.10: Characteristics of some oxygenated fuels. Adapted from [76].

a fuel is defined as the maximum flame height (in mm) produced in the SP lamp without smoke leaving the flame. The higher the SP, the lower the sooting tendency of the fuel tested. Usually, an empirical correlation known as the Threshold Sooting Index (TSI) is used to evaluate the SP in conjunction with the molecular weight. In this work, the molecular weight was included to account for the higher oxygen requirement for stoichiometric combustion as the molecular weight in the fuel increases. However, this approximation is unsuitable for oxygenated fuels because it fails to account for the oxygen provided by the fuel [79]. Barrientos et al. [80] proposed modifying the TSI, known as the Oxygen Extended Sooting Index (OESI) which accounts for oxygen in the fuel. The OESI is proportional to the sooting propensity. A decrease in the OESI corresponds to a decreased sooting tendency of the fuels. With this approach, Tan et al. have conducted a series of $OMEn$ studies, as it permits a systematic increase in the oxygen content within the molecule without adding C–C bonds.

The OESI of the $OMEn$ blends is plotted against the volume fraction (as fuels are commonly blended by volume per cent in engine applications) of the fuel in Figure 2.11. All the $OMEn$ decrease the sooting tendency of the fuel mixture by increasing its volume fraction. Figure 2.11 indicates that an increase in oxygen content in the fuel additive, via chain length increase, has a negligible effect on the sooting propensity of the fuel mixtures. However,

the oxygen content in the fuel blend is different for each at the same volume fraction added to Diesel. Therefore, the OESI was plotted over the oxygen content in the fuel blend in the right panel of Figure 2.11. Interestingly, at a given oxygen content in the blend, the OESI seems to decrease with decreasing chain length. This becomes especially evident in the region of 10–20wt.% oxygen fraction, while the OESI converges towards similar values at higher oxygen concentrations. Thus, the oxygen content in the oxygenated additives is not the sole factor in defining the sooting reduction; the decomposition pathways and the identification of 'active' oxygenated soot-reducing moieties play a more crucial role.

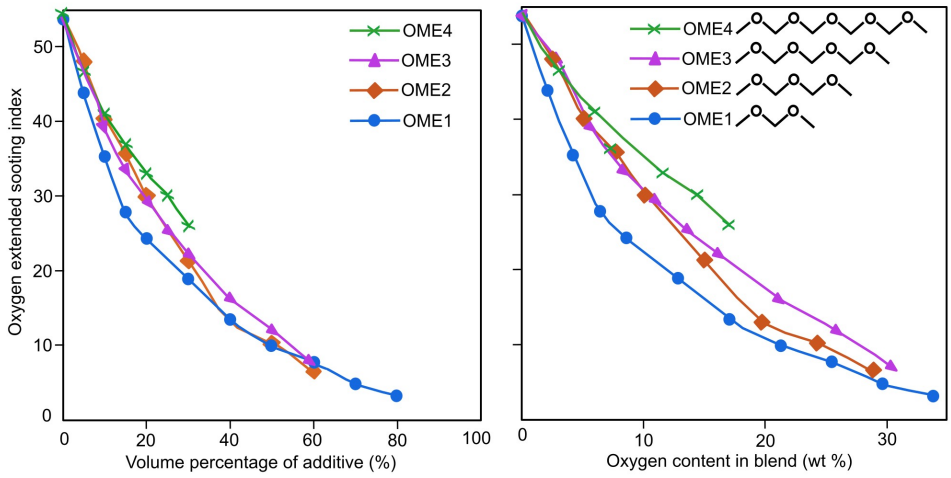

Figure 2.11: OESI versus the volume percentage of OMEn additive in Diesel, on the left, and OESI versus the oxygen content in the right. Adapted from [78].

With its low boiling point, $OMEn$ offers a notable advantage over Diesel fuel, facilitating rapid evaporation upon injection into the combustion chamber. This feature promotes homogeneous charge formation and combustion promotion, whether $OMEn$ is blended with Diesel or used directly in CI engines. Furthermore, experimental results demonstrate the excellent inter-solubility of $OMEn$ with Diesel fuel, particularly at low ambient temperatures. This quality enhances the physicochemical properties of Diesel fuel when blended with $OMEn$. Even at temperatures exceeding 20°C, $OMEn$ and Diesel fuel exhibit miscibility in any proportion without density stratification. Moreover, including butanol as a co-solvent further enhances the solubility of $OMEn$ and Diesel fuel. Moreover, $OMEn$'s lower flash point than Diesel mitigates ignition

issues, especially during engine startup in cold weather. Additionally, blending $OMEn$ with Diesel reduces the fuel's ignition temperature and activation energy, improving engine performance during cold starts.

Despite their numerous advantages and compatibility, these fuels drawbacks must be considered. To this end, extensive research has been carried out to characterize them correctly and subsequently address these challenges when using them in engines.

One significant disadvantage is the low energy density of $OMEn$ regardless of the polymerization degree, amounting to only 50 % of Diesel fuel in the best case (OME_1). This necessitates increased injection pressure and prolonged injection duration for $OMEn$ to achieve equivalent power output, potentially elongating combustion duration and lacking heat release concentration.

Furthermore, $OMEn$ lower viscosity than Diesel fuel poses concerns regarding lubrication performance, potentially leading to intensified surface wear on moving parts within the fuel supply system. Moreover, $OMEn$ notably tends to cause rubber swelling, particularly when blended with Diesel fuel. This can result in fuel leakage due to swelling in rubber tubes and gaskets within the engine fuel circuit, alongside potential injection nozzle blockage from impurities and colloids adhering to oil pipe walls. Additionally, the water solubility and biodegradability of $OMEn$ pose environmental concerns. While water solubility decreases with larger end-group sizes, biodegradability evaluations are crucial for assessing environmental persistence. The release of $OMEn$ into the environment during fuel transportation and usage, especially given its high solubility and poor biodegradability, may lead to water contamination [66].

Given the plethora of advantages and compatibilities of these fuels, which make them energy careers, along with the imperative to address their drawbacks, a significant amount of research has been conducted regarding their utilization in engines. The principal findings will be outlined below.

2.3.2 Use of OMEn-type fuels in ICEs.

In the past decades, several authors have investigated the performance of light and heavy-duty engines fuelled by Diesel-$OMEn$ blends or even 100% of $OMEn$-type fuels. Most of the results, indicate that these fuels can be an excellent alternative to fossil fuels, highlighting that the increase of the $OMEn$ content in blends of Diesel and gasoline, as expected based on the characterization recently presented, was shown to reduce soot and NOx. Selected work will be exposed in the following, starting with results obtained through studies on metallic engines, both light-duty and heavy-duty, general

considerations regarding engine performance, emissions, fuel consumption, etc., can be obtained. Subsequently, results from studies on optical engines will be presented, which allow for a deeper understanding by visualizing the flame structure within the combustion chamber, as well as the formation and oxidation of soot in the cylinder.

Pellegrini et al. [81] propose a study where the test engine was removed from an in-use light-duty vehicle. The objective of this study was to compare the regulated and non-regulated emissions, particularly PAHs and particle number size distribution (PNSD), from an ageing Euro-3 Diesel engine fuelled with a 7.5% blend of $OMEn$. The findings, focused on emissions, reveal a noteworthy decrease in soot and particulate matter (PM) emissions. Under low-speed and low-load operating conditions, there is a slight increase in the number of particles smaller than 30 nm, whereas at high speed, the number concentration of particles larger than 30 nm is reduced. However, PAHs emissions were observed to be higher for the oxygenated fuel blend compared to the base fuel. This outcome aligns with exhaust gas temperature profiles during PAHs sampling, suggesting that the oxidation catalyst may exhibit slightly lower catalytic activity when utilizing this oxygenated fuel.

On the heavy-duty front, Pelerin et al. [82] conducted in 2020, a characterization study comparing the combustion of OME_1 and OME_{3-6} with paraffinic Diesel fuel at various load points, focusing on combustion behaviour, emission characteristics and indicated efficiency. The objective of the work was to determine the operational boundaries focusing on ignitability for OME_1 due to its low CN and explore options to speed up the injection strategy for OME_{3-6} due to their favourable ignitability. They demonstrate that particle emissions from $OMEn$ combustion are equivalent to urban emission levels, irrespective of significantly increased EGR rates or very low injection pressures. However, methane emissions increase sharply under stoichiometric conditions, regardless of the molecular chain length of the utilized $OMEn$ fuel. Furthermore, it was shown that a simplified injection strategy employing only a main injection may be feasible when the engine operates with long-chained $OMEn$ fuels. Also, Hartl et al. [83] conducted a similar study on a heavy-duty engine, comparing the engine performance fuelled with OME_1 and OME_{3-5}, highlighting that $OMEn$ with n = 3, 4, 5 have boiling points more similar to Diesel fuel, then are more suitable for application in a Diesel engine as neat substance [84]. Compared with OME_1, this $OMEn$ have a higher O/H ratio [85], so it could further reduce soot and methane emissions.

Recently, Benajes et al. [86] presented an interesting review of several studies that yielded similar results regarding using $OMEn$. They compared

and analysed all the findings concerning soot, NOx, CO, and HC emissions from various sources and different engines sizes.

One of the studies considered in the review is that of García et al. [87], wherein the authors conducted a combustion study of $OMEn$ under stoichiometric conditions in a medium-duty engine. They found that equivalent fuel consumption (which accounts for the total indicated specific fuel consumption scaled by the energy density ratio of $OMEn$ and Diesel) increased by 14% to 39% compared to baseline lean Diesel combustion. In direct comparison, $OMEn$ exhibited up to a 207% increase in fuel consumption compared to Diesel. However, the authors emphasize that the primary advantage of $OMEn$ as an ICE fuel is its ability to significantly diminish soot emissions to nearly undetectable levels.

These results had allowed for calibrating CI engines to implement NOx reduction strategies without increasing soot levels, as depicted in Figure 2.12, illustrating the NOx-soot trade-off for different $OMEn$ proportions. Garcia et al. [87] demonstrated the most significant reductions in NOx and soot emissions through stoichiometric combustion of pure $OMEn$. The almost complete reduction in NOx is attributed to reduced peak combustion temperatures and the utilisation of considerable amounts of EGR as heat sinks.

Other studies [88, 89] identified that under certain conditions, $OMEn$ blends can produce higher NOx emissions than Diesel, but mostly, emissions remained below Diesel thresholds. The decrease in NOx emissions primarily stems from decreased HRR and premixed combustion. Although soot emissions are typically reported to be extremely low with $OMEn$. Dworschank et al. [90] observed a correlation associated with the molecular chain length. $OMEn$ molecules with higher n values appear to increase the particle number of size 10 nm. However, the authors indicate that particles of 23 nm remain almost constant regardless of the $OMEn$ length. They suggest that one potential explanation could be the reduced combustion temperature, potentially resulting from shortened combustion duration.

Zacherl et al. [91] observed for heavy-duty engine lower volatile organic compounds and CO emissions with $OMEn$ compared to Diesel, primarily attributed to $OMEn$ oxygen content and improved mixture formation. However, emissions increased during later combustion cycles due to lower combustion temperatures, leading to incomplete oxidation. Factors such as lower turbulence in the cylinder and spray deterioration, resulting from low back pressure and temperatures, also contribute to this effect.

Similarly, Liu et al. [88] found that with $OMEn$ blends up to 80% also in a heavy-duty engine, CO emissions were similar to those of Diesel engines under

lighter loads, as Diesel contains sufficient oxygen for complete oxidation to CO_2. However, at higher loads, the use of $OMEn$ demonstrated an advantage.

In another study by Omari et al., [89], which evaluated four OME_1-Diesel blends and Diesel as a reference in a light-duty vehicle, it was observed that increasing the proportion of OME_1 relative to Diesel reduced both CO and HC emissions at higher loads while maintaining the same level of NOx. Conversely, higher percentages of OME_1 at lighter loads led to increased CO emissions. The authors argued that at extremely light loads, the low CN of the fuel becomes critical, leading to increased premixed combustion and consequently, elevated levels of CO emissions.

Regarding this topic, the study by Garcia et al. [87] documented the most notable rise in CO and HC emissions, as depicted in the bottom panel of Figure 2.12. They reported a staggering 68-fold increase in HC emissions and an astonishing 602-fold increase in CO emissions compared to Diesel. It is crucial to note that in their research, the combustion process was stoichiometric, involving high levels of EGR, resulting in a mixture lacking sufficient oxygen for complete combustion despite the fuel 47.1% oxygen content by mass. Additionally, the combustion temperature decreased, diminishing the reactivity of these emissions. However, when the authors experimented with leaner fuel mixtures containing abundant oxygen, they achieved engine emissions meeting or exceeding Euro VI requirements for vehicles of that class without the need for aftertreatment.

Regardless of engine size, the challenges, and incompatibilities encountered with vehicle components that compromise the mechanical performance of the engine when fuelled with $OMEn$ are numerous, and the main ones found in the literature are listed below.

$OMEn$ fuels with longer chain lengths exhibit higher CN, but excessively long chains may adversely impact fuel viscosity, potentially leading to pumping issues [92]. Moreover, larger $OMEn$ molecules may lead to larger droplet diameters during atomization, which can influence mixture quality and combustion efficiency.

In that context, Pelerin et al. [82], which were already cited, addressed the issue of material compatibility, prompted by earlier studies indicating poor compatibility of $OMEn$ fuels with conventional elastomer sealing materials [93]. Since Diesel fuel hydrocarbon components are non-polar, oxygen in $OMEn$ molecules results in a notable dipole moment, rendering $OMEn$ a strongly polar fuel [94]. Consequently, non-polar elastomer materials resistant to polar substances are necessary.

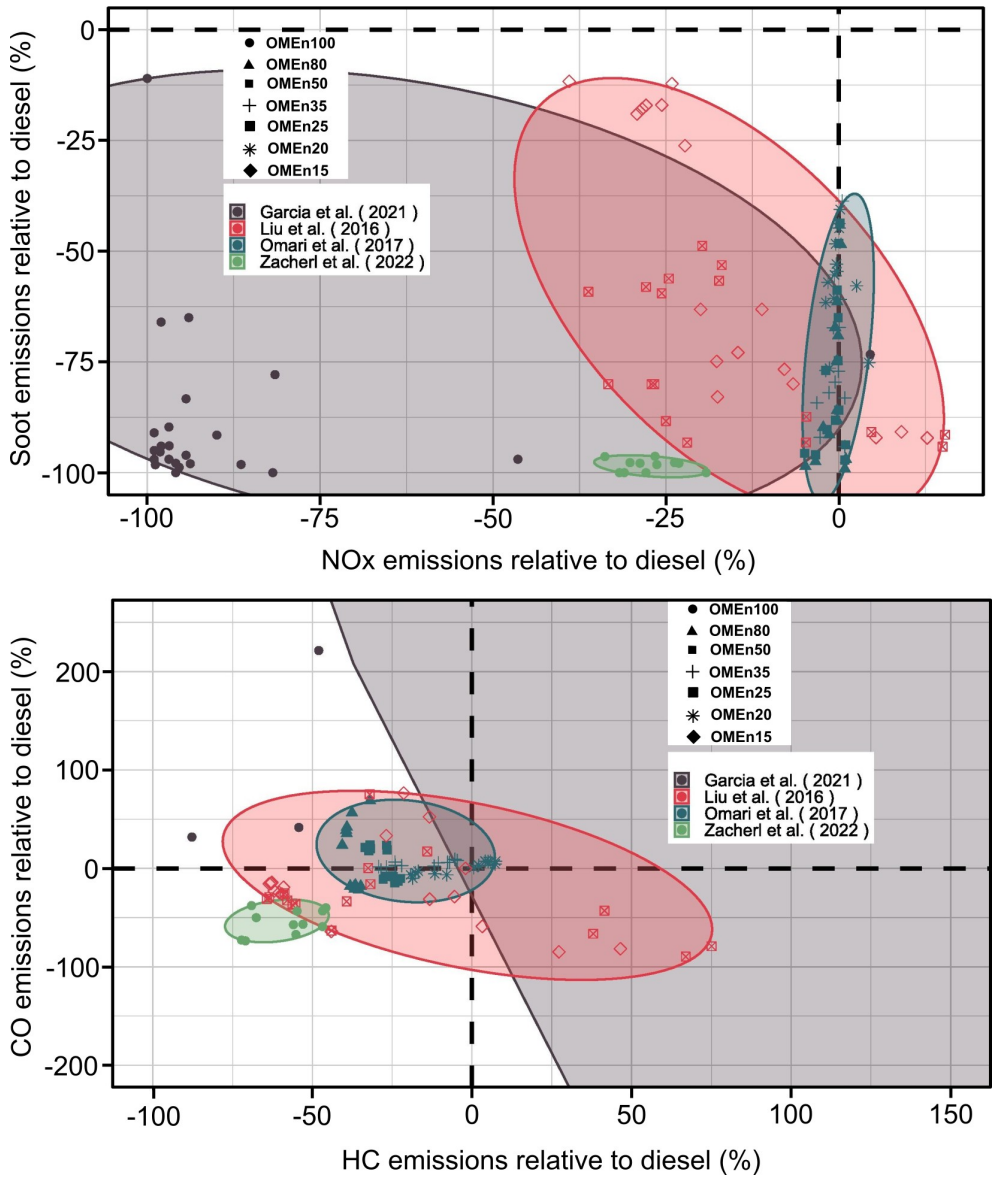

Figure 2.12: NOx-Soot and HC-CO tradeoff compared to Diesel across different studies with OMEn. Adapted from [86]

Furthermore, Kass et al. [95] suggest that adjustments to the rubber components within the engine are necessary to withstand blends of OME_{3-5} or a lower proportion of OME_{3-5} should be considered for blending. Additionally, in research conducted by Pastor et al., [96] involving $OMEn$ as a fuel, a fuel pump replacement was implemented, substituting a regular fuel pump with a diaphragm pump that uses polymerizing tetrafluoroethylene, which is better suited for low-lubricant hydrocarbons. This latter effort underscores the necessity of potentially redesigning the fuel injection system to effectively incorporate $OMEn$ into vehicles.

In her thesis, Guzmán [97] delves into evaluating the potential of various fuels within the Low Carbon Fuels (LCFs) category when applied to a conventional light-duty engine. She finds that all tested LCFs can operate within a similar range to Diesel under drop-in operation, with some exhibiting greater efficiency in fuel consumption and engine-out emission control. However, adverse effects were observed during testing, particularly concerning the fuel injection system. Oxygenated fuels, specifically $OMEn$, diminished the durability of common-rail injectors and fuel pumps. The study underscores the necessity for thorough durability and wear testing, suggesting that fuel additives or hardware design improvements may be necessary to address the identified corrosion and oxidation issues.

The aforementioned demonstrates the potential of $OMEn$ fuels, given the performance of both light-duty and heavy-duty engines when fuelled with these fuels. However, additional characterization of this fuel is required, which includes a more comprehensive database on combustion process characteristics under real operating conditions. These can be studied using optical techniques in optical engines.

In this regard, Pastor et al. [98] conducted a study using a single-cylinder optical CI engine with a commercial piston geometry fuelled by two e-fuels, Fischer-Tropsch (FT) Diesel and $OMEn$. Employing three optical techniques (Natural Luminosity–NL, OH^* chemiluminescence, and 2-color pyrometry-2C), they analysed the combustion evolution and quantified soot formation at different loads (1.5, 4.5, and 7.5 bar IMEP). Their findings revealed that $OMEn$ exhibited the longest injection duration due to its LHV. With NL analysis, $OMEn$ demonstrated the lowest light intensity across the three loads tested, indicating minimal soot production. Despite the low NL intensity, $OMEn$ displayed the highest OH^* chemiluminescence signal, suggesting a greater presence of near-stoichiometric zones due to the high oxygen content. In another study by the same authors [99], and for light-duty CI as well, they evaluate the soot formation when using different substitution rates of Diesel

in $OMEn$, focusing on the increase in soot formation as the Diesel content increased in the blend. They reported that a 10% Diesel blend (90 % $OMEn$) was sufficient to increase the natural light intensity emitted by the flame by one order of magnitude. With up to 30% Diesel blend, the light intensity increased proportionally with the Diesel mass quantity. However, beyond 50% Diesel mass, the increment in light intensity was significantly reduced. Spectroscopy measurements confirmed the absence of soot during pure $OMEn$ combustion. As Diesel mass increased in the blend, radiation for higher wavelengths (related to soot thermal radiation) also increased. Through the chemiluminescence technique, they observed significant OH^* emission for blends with up to 30% Diesel mass, which could be linked to a high concentration of this radical aiding in the oxidation of soot and its precursors before 40 crank angle degree (CAD). Finally, 2-color pyrometry revealed that soot formation could be kept very low up to a 20% Diesel mass substitution rate. Even at 50% Diesel content, soot reduction remained remarkable. However, the longer injection duration compared to pure Diesel extended the late soot oxidation.

Furthermore, Pellegrini et al. [84] use a transparent single-cylinder research engine with optical access for combustion visualization with spatially-resolved measurements of flame temperature and soot concentration. Their focus was investigating the combustion behaviour of neat and blended $OMEn$ in Diesel fuel. The study reveals that the presence of $OMEn$ in the fuel essentially affects the stage of soot oxidation. The most evident effect is a marked increase in the soot oxidation rate in the final phase of combustion, which resulted from the availability of in-situ intramolecular oxygen as the oxidation agent.

A similar study was reported, focusing on medium-duty optical engines [100]. The author compared different blends of $OMEn$ with Diesel and neat HVO. High-speed imaging of OH^* chemiluminescence and NL of the flame was simultaneously recorded to comprehend the combustion process and distinguish the differences between fuels. The conclusion drawn was that increasing the proportion of $OMEn$ in the blend under the same engine settings resulted in a noticeable decrease in heat release, which needed to be compensated for by increasing injection pressure or adjusting injection timings. Additionally, in the late stages of combustion, where soot radiation was weak or absent, UV radiation corresponding to OH^* chemiluminescence revealed the progress of combustion. Therefore, the results indicated that the proportion of $OMEn$ in the blend affected combustion velocity, with a faster reaction as the $OMEn$ proportion increased.

In the realm of heavy-duty engines, optical analyses have also been conducted. On the one hand, Hartl et al. [101] have examined the injection

process of $OMEn$ to provide a comprehensive analysis of the spray behaviour of $OMEn$ with n 3, 4, 5 and 6, under realistic conditions in an optically accessible engine. The study of spray behaviour elucidates the impact of various injectors and different engine parameters such as rail pressure, engine load, pre-injection, or combustion chamber pressure on liquid penetration length and injection behaviour. The findings indicate that the in-cylinder pressure mainly influences the liquid length penetration, whereas the rail pressure affects the opening and closing dynamics of the injector without impacting the liquid length penetration. The authors suggest that these findings are applicable for optimizing the injection system or other components, such as piston geometry, to utilize $OMEn$. On the other hand, another work focusing on the use of $OMEn$ in heavy-duty has been carried out [102], using optical techniques to evaluate the performance and exhaust emissions when the engines are fuelled with different $OMEn$-Diesel blends. Similar results as in light-duty have been found from the comparison between $OMEn$-Diesel blends and pure Diesel, a significant reduction in soot emissions, close to 35%, and no significant increase in NOx emissions.

As a complement to the experimental findings, studies employing numerical simulations can be found in the literature aimed at delving deeper into understanding how the properties and stoichiometry of $OMEn$ affect the combustion process and pollutant formation in $OMEn$-fossil fuel blends in real CI engines conditions. On the one hand, García-Oliver et al. [103] conducted CFD simulations with operating conditions representative of a medium load point of a light-duty engine. From the analysis of the results, the authors highlighted remarkable differences between Diesel and $OMEn$. $OMEn$ fuel was found to provide lower equivalence ratio fields, promoting oxidation reactions in wider areas within the combustion chamber, thereby leading to a faster combustion process. Moreover, soot formation was drastically decreased compared to the other fuel, with the CFD results agreeing with the experimental findings. On the other hand, the same author [104] extended a similar analysis to a medium-duty CI engine, along with an evaluation of the chemical mechanism. Both simulations have been done in $CONVERGE$ CFD [105], Cai [106] chemical mechanism was used to model chemical kinetics, and combustion has been simulated using the well-mixed SAGE detailed chemical kinetics solver. From these two related works, it can be concluded that in general terms, similar to the experimental observations, despite the increase in engine size and the associated complexities, these fuels remained effective and promising in reducing the well-known soot-NO trade-off in compression ignition engines.

A step forward in this regard has been taken by Novella et al. [107], who, based on the literature findings regarding the need for longer injections due

to the low LHV of $OMEn$ or reduction in the HRR, among other factors, proposed the integration of optimization algorithms and CFD codes to assess the behaviour of an engine fuelled with the low-sooting fuel $OMEn$. The CFD calculation has been carried out in OpenFOAM [108], and again, the Cai mechanism has been used. The objective was to develop a dedicated combustion system for an engine fuelled with this alternative fuel to improve efficiency and reduce NOx emissions. Their results revealed an optimized combustion system with an efficiency increase of approximately 2.2% and a 35.7% reduction in NOx compared to the baseline engine fuelled with conventional fuel. Additionally, a neural network was trained in the same work to examine the influence of each parameter on emissions and efficiency. From this analysis, they concluded that the EGR rate and injection pressure significantly affect NOx emissions, with a variability range of 63% and 38%, respectively.

2.3.3 Reference spray flames of OMEn-type fuels

Based on the results of studies on the use of $OMEn$ in engines, both experimental and numerical, have illustrated the advantages of these fuels and why they represent a potential solution in the defossilization journey of the transportation sector, as well as the challenges that may be encountered. It is evident that, fundamental knowledge of the flame structure is needed, as well as a detailed study of the chemical kinetics of $OMEn$ under CI conditions. Therefore, experimental and numerical studies have moved towards more fundamental works.

From a more fundamental perspective, the oxygenated character of these fuels could result in a different flame topology compared to regular hydrocarbons. Using the ECN single-orifice SA or SD nozzle configurations, the combustion process of different fuels can be characterized and analysed. Most of these works are carried out in a constant-volume combustion chamber, where it is possible to achieve a quasi-steady environment to simulate top-dead centre conditions of a CI engine, but, independently of conditions imposed by an engine, such as sprays interaction, wall boundaries, intermittency, etc.

Research into $OMEn$ sprays has uncovered significant changes in the mixture formation process through experimental studies. In Dageförde et al. [109], $OMEn$ performance in the SA injector has been examined, revealing through Phase-Doppler-Anemometry comparisons with n-Dodecane, that $OMEn$ exhibited reduced spray velocities and lower levels of air entrainment. Furthermore, the investigation conducted by Strauß et al. [110] elucidated notable distinctions between n-Dodecane and $OMEn$ within the Spray A3 (a new version of ECN Spray A) configuration. Despite $OMEn$ higher volatility,

it was observed that the liquid penetration of $OMEn$ surpassed that of the comparatively less volatile n-Dodecane. Moreover, investigations involving neat OME_3 and neat OME_4 in a heavy-duty injector indicate disparities in the mixture formation [111]. Simulations of inner-nozzle flow indicate the potential occurrence of cavitation [111]. This propensity for cavitation in $OMEn$ has been validated in the ECN Spray C by Singh et al. [112]. Regarding flame structure, first works reveals that $OMEn$ exhibits a reduced formation of the excited OH radical, as reported by Ma et al. [113].

Iannuzzi et al. [114] utilized OH^* chemiluminescence and two-dimensional 2C techniques to investigate the processes of soot formation and oxidation after the combustion of OME_1, OME_2, $OMEn$ (predominantly n = 2, 3, 4), Diesel, and OME_2-Diesel blends within a cylindrical constant volume chamber. Their findings indicated the absence of detectable soot during the combustion of pure OME_2 fuel, suggesting minimal soot production from pure fuel combustion. Additionally, the results underscored nearly smokeless combustion for pure oxygenated fuels and a non-linear reduction in soot emission with increasing O_2 content in the blend.

Furthermore, research by Ma et al. [115] revealed that both flame luminance and flame area decreased with an increase in the blending ratio of $OMEn$. However, they noted that the low volume fraction of $OMEn$ blends had negligible effects on liquid penetration. In this sense, they suggest that there is no need to modify fuel injection strategies when blending low fractions of $OMEn$.

Sun et al. [116] present a fundamental study investigating the combustion and soot characteristics of $OMEn$ Diesel blends with varying ratios. The research delves into experiments examining ID, HRR, and natural luminosity under diverse ambient conditions. Additionally, the study analyses the influence of oxygen concentration and $OMEn$ content on ID. The findings underscore a decrease in ID with an increase in $OMEn$ percentage within blends, with ambient temperature noted as a crucial factor affecting this parameter. Notably, the ID of $OMEn$ exhibits minimal sensitivity to a reduction in ambient O_2 concentration.

The spray flame structure of $OMEn$ has been experimentally studied in SA and SD by García [117]. A key observation is the absence of soot production in $OMEn$ within both injectors, as in light- and heavy-duty real ICEs conditions. Moreover, the ID for this fuel proves to be considerably shorter than n-Dodecane, despite $OMEn$ lower CN. Although the ID time increases with nozzle size, $OMEn$ displays less sensitivity to this parameter than n-Dodecane. Additionally, the spray flame structure for $OMEn$ appears

marginally narrower than that observed with n-Dodecane. Chemiluminescence imaging reveals that the distribution of OH^* formation is closer to the spray centreline for $OMEn$, and not completely on the sides, as in hydrocarbons. Deluding that, possibly the distribution of a stoichiometric mixture in this was different. Furthermore, the authors have investigated OME_1, revealing notable distinctions compared to $OMEn$, despite their common oxygenated character. The differing momentum flux between both sprays, in general, results in SD demonstrating faster vapour penetration (S) and longer liquid length (LL) than SA. It was observed that the ignition delay for OME_1 and SD was 9% lower than for SA, contrasting with the behaviour observed for other fuels, including hydrocarbons and $OMEn$, where a higher ignition delay was noted for SD. Regarding the lift-off length, the trend mirrors that of ignition delay, except for OME_1, where the LOL of SD surpasses that of SA, changing the trend.

Tejada [118] presents a characterization of the flame structure under constant-pressure combustion vessel of two types of oxymethylene ethers ($OMEn$ and OME_1) using high-speed chemiluminescence imaging and Planar Laser-Induced Fluorescence (PLIF) applied on CH_2O molecules and OH radical, in order to characterize the low and high-temperature zones within the spray, with the ECN nominal operating conditions and for ECN SA and SD. From this work, the author concludes that the combustion of OME_1 with SA is characterized by a flame structure very different to that of a diffusion flame. It has a large cool flame region and a short high-temperature zone. Furthermore, the combustion of $OMEn$ with both nozzles and OME_1 with Spray D show more similarities with a diffusion flame structure. The author suppose that the stoichiometry of the fuel and the equivalence ratio fields influenced by the fuel molecular composition strongly affect the structure and later evolution of the flames.

Also in 2024, Xuan et al. [119] propose a conceptual model for n-Dodecane and OME_3 for two levels of ambient temperature, 800 and 900 K. This comprehensive study combines results from several optical techniques employed in a high-temperature high-pressure combustion vessel, which covers CH_2O PLIF, OH^* Chemiluminescence and soot distribution. Also, they present an analysis based on chemical kinetics and 1D spray model [120–122]. Results reveal that OME_3 flame structure differs significantly from typical diffusion flames, which is extreme when ambient temperature decreases; the authors relate this behaviour to the chemical kinetics of CH_2O and CO.

One of the first simulations of OME_1 has been presented by Goeb et al. [123]. The spray and ignition properties of neat OME_1 and n-Dodecane as

reference fuel, and a blend of these two fuels with 35 vol% OME_1, based on Omari et al. [89] experimental results are shown. Goeb et al. performed experiments and numerical simulations under ECN SA conditions in a high-pressure, high-temperature combustion vessel. From the numerical front, the ignition behaviour of OME_1 and an n-Dodecane blend is investigated using one-dimensional unsteady flamelet and LES simulations. The OME_1 chemical mechanism is extracted from Jacobs et al. [124] and incorporated into the reduced n-Dodecane mechanism [125]. Furthermore, Blanquart et al. [126] chemical mechanism is added to consider PAHs chemistry. Based on flamelet calculations, it was deduced that the slow ignition behaviour of OME_1 stemmed from stoichiometry effects rather than its chemical reactivity. Additionally, an inquiry into the ignition behaviour of OME_1 and n-Dodecane blends revealed that the ignition of the blend is primarily influenced by the n-Dodecane fraction for blending ratios below 60 vol%. Consequently, the late ignition characteristics of OME_1 are unlikely to impede its suitability in fuel blends containing higher CN fuels.

Wiesmann et al. [127] in 2022, perform RANS simulation under inert and reacting ECN configuration using Niu et al. chemical mechanism [128] for the reacting ones. Calculations have been carried out using AVL FIRE software [129]. The turbulence chemistry interaction (TCI) has been modelled via a presumed (Gaussian) probability density function (pPDF). This work confirms differences in the mixture formation of $OMEn$ in the SA3 injector. However, the ID for $OMEn$ is consistently underestimated for different boundary conditions. The authors observed that the good agreement of inert results with experimental data implies that the deviations between measurements and simulation observed for the combustion process are mainly driven by the reaction kinetics, at least downstream of the liquid length. In 2024, Wiesmann presented a new work [130], which seeks to underscore advancements achieved by improving an adapted oxidation mechanism tailored for $OMEn$. This improved mechanism is subsequently incorporated into a validated CFD model for spray combustion involving $OMEn$. The simulations encompass variations in ambient temperatures and oxygen content. Substantial enhancements in predicting the ID are in the new work achieved, maintaining excellent agreement for the flame LOL. The adaptation of reaction kinetics notably influenced spatial zones of high-temperature reaction activity, displaying an increased propensity for OH^* radical formation within the spray centre, aligning well with experimental observations.

The study of Haspel et al. [131] investigate neat OME_3 and neat OME_4 in a close-to-series heavy-duty injector with an LES framework, using the Cai mechanism to model the chemical kinetics [106]. Combustion is described with

tabulated chemistry, using the unsteady flamelet progress variable (UFPV) approach [132]. Noticeable distinctions in the mixture formation process among the fuels were noted. While the flame structure analysis in the flamelet simulation indicated an earlier ignition for neat OME_3, the spray flame of OME_4 ignited prior to OME_3, which can be attributed to a distinct mixture formation process in the spray. The research conducted by Haspel et al. [131] unveiled that the mixture formation process plays a crucial role in the ignition process and the flame structure of $OMEn$.

2.4 Summary

Based on the preceding discourse, it becomes apparent that combustion is an integral part of the solution, rather than being viewed as the problem itself. Combustion experts worldwide are actively collaborating with other disciplines, especially within the domain of renewable energy, and this collective knowledge base is poised to propel the advancement of cleaner power conversion technologies. This holds true regardless of the predominant e-fuels during the gradual transition away from traditional fuels. The progress in developing accurate and robust predictive capabilities for turbulent mixed-mode combustion, encompassing autoignition, premixed and non-premixed flames, is of utmost importance.

These circumstances underscore the significance of research in turbulent combustion, chemical kinetics, and modelling as fundamental pillars for propelling future engines towards achieving zero-emission levels, fuel flexibility, and enhanced efficiencies. Attaining fuel flexibility requires a comprehensive understanding of chemical kinetics and its interplay with turbulence to facilitate the control of critical processes such as auto-ignition, combustion rates, and the formation and emission of soot particles.

E-fuels like oxymethylene ethers ($OMEn$) (CH3 –O-(CH2 –O)n -CH3) also present intricate autoignition and combustion chemistry, so, from a fundamental research point of view, they attract considerable attention. Pure $OMEn$ compounds with n $>$ 1, exhibit characteristics of low-temperature chemistry during autoignition, albeit without clear evidence of negative temperature coefficient (NTC) behaviour [77, 106, 124, 133–135]. While the underlying mechanisms for this phenomenon are still evolving, they appear to be associated with the presence of the methylenedioxy group. Therefore, reliable high-fidelity simulations are crucial to ensure that turbulent combustion remains a vibrant field of research during this transitional phase and continues to play a pivotal

role in the design and development of next-generation engines that will drive transportation and industry for decades.

Identifying the significance of fundamental studies and their potential contributions, in conjunction with the extensive literature review presented in this chapter, it can be stated that concerning engine innovation, over the last decade there has been extensive research on the use of $OMEn$ in CI engines. This research has been deepened through studying combustion in optical engines and progressed towards more fundamental studies framed within the ECN configurations. In this context, the number of identified works is limited, with the thesis by Garcia-Carrero [117] standing out on the experimental front. This thesis extensively characterizes these fuels (OME_1 and $OMEn$), presenting the effect of various boundary conditions on autoignition and combustion. It covers two nozzle sizes, ECN SA and SD, three temperature levels (800, 900, and 1000 K), three levels of injection pressure (500, 1000 and 1500 bar) and two different ambient compositions, 15% and 21% of O_2. On the other hand, Tejada [118] has characterized the flame of these two fuels using more advanced optical techniques such as PLIF, identifying zones of low and high temperature. This work also encompasses both nozzle orifice sizes; however, it does not study the effect of temperature or pressure on the flame. From these works, the authors found that oxygenated fuels can develop a very different flame structure and flame stabilization, depending on the nozzle diameter or ambient temperature. However, understanding why some phenomena happen is still pending, and CFD simulation has great potential to improve this knowledge.

Transitioning to computational studies, there has been a noticeable increase in publications in the field over the last five years. However, significant gaps have been identified. Only Wiesmann et al. [127, 130] have studied the effect of temperature on the autoignition and combustion of $OMEn$, and these studies have been conducted with an RANS approach. Therefore, a study in this regard using LES could complement and delve deeper into the effect of this boundary condition.

From the review, it is evident that a study of SA has been primarily conducted, but not as much for SD, with only the work of Haspel et al. [131] reported in this regard. Given the aforementioned difficulties about electrification of heavy-duty vehicles, conducting more fundamental studies on the mixing and ignition process of a larger injector like the SD could cover a significant gap in the literature.

Additionally, the validation of these numerical models has mainly been performed through the mixing process under inert conditions and with global combustion parameters, such as ID, LOL, and S, under reactive conditions.

Therefore, developing techniques to validate the spatial and temporal flame structure would be highly beneficial, considering the current contribution of numerical simulations in the field of turbulent combustion. Moreover, continuing to assess the performance of advanced combustion models, such as those based on flamelets, mainly when the spray exhibits vastly different flame structures depending on boundary conditions, is considered a significant contribution to the literature.

Finally, based on the extensive review, it can be considered that implementing complex soot prediction models [136–138] is not paramount given the unanimity regarding this point from experimental results.

References

[1] Gierth, Sandro. "Advanced flamelet tabulation strategies for Large Eddy Simulations of single- and multi-phase turbulent jet flames". en. PhD thesis. Darmstadt: Technische Universität, 2022. DOI: 10.26083/tuprints-00021122.

[2] Reitz, R. and Bracco, F. "Mechanisms of Breakup ofRound Liquid Jets, The Encyclopedia of Fluid Mechanics". In: *The Encyclopedia of Fluid Mechanics* Vol. 3 (1986), pp. 223–249.

[3] F. Payri, J. M. Desantes and Arrègle, J. "Characterization of D.I. Diesel Sprays in High Density Conditions". In: *Journal of Engines, SAE International* (1996).

[4] Baumgarten, C. *Mixture Formation in Internal Combustion Engines*. Heat and Mass Transfer. Berlin; New York: Springer, 2006.

[5] Wierzba, A. "Deformation and breakup of liquid drops in a gas stream at nearly critical Weber numbers". In: (2006). DOI: 10.1007/BF00575336.

[6] Mico, C. "Development of measurement and visualization techniques for characterization of mixing and combustion processes with surrogate fuels." PhD thesis. niversitat Politècnica de València, 2015. DOI: 10.4995/Thesis/10251/58991.

[7] García-Oliver, J.M. "Aportaciones al Estudio Del Proceso de Combustión Turbulenta de Chorros En Motores Diesel Del Inyección Directa". PhD thesis. Universitat Politècnica de València, 2005.

[8] Higgins, Brian S., Mueller, Charles J., and Siebers, Dennis L. "Measurements of Fuel Effects on Liquid-Phase Penetration in Dl Sprays". In: *SAE Transactions* 108 (1999), pp. 630–643.

[9] Pastor, J. V., Garcia-Oliver, J. M., Bermudez, V., and Micó., C. "Spray Characterization for Pure Fuel and Binary Blends under Non-Reacting Conditions". In: *SAE International* (2014). DOI: 10.4271/2014-01-1407.

[10] Espey, C. and Dec, J.E. "The Effect of TDC Temperature and Density on the Liquid-Phase Fuel Penetration in a D. I. Diesel Engine". In: *SAE International* (1995).

[11] Payri, R., Gimeno, J., Bardi, M., and Plazas., A. H. "Study Liquid Length Penetration Results Obtained with a Direct Acting Piezo Electric Injector". In: *Applied Energy* (2013). DOI: 10.1016/j.apenergy.2013.01.027.

[12] Payri, R., Gimeno, J., Bracho, G., and Vaquerizo, D. "Study of Liquid and Vapor Phase Behavior on Diesel Sprays for Heavy Duty Engine Nozzles". In: *Applied Energy* (2016). DOI: 10.1016/j.applthermaleng.2016.06.159.

[13] Zeng, Wei, Xu, Min, Zhang, Gaoming, Zhang, Yuyin, and Cleary, David J. "Atomization and vaporization for flash-boiling multi-hole sprays with alcohol fuels". In: *Fuel* 95 (2012), pp. 287–297. DOI: 10.1016/j.fuel.2011.08.048.

[14] Siebers and L., Dennis. "Liquid-Phase Fuel Penetration in Diesel Sprays". In: *International Congress & Exposition*. SAE International, 1998.

[15] Pickett, Lyle M. et al. "Relationship Between Diesel Fuel Spray Vapor Penetration/Dispersion and Local Fuel Mixture Fraction". In: *SAE Int. J. Engines* (2011).

[16] Pastor, Jose V, Payri, Raul, Garcia-Oliver, Jose M, and Nerva, Jean-Guillaume. "Schlieren Measurements of the ECN-Spray A Penetration under Inert and Reacting Conditions". In: *SAE 2012 World Congress & Exhibition*. SAE International, 2012.

[17] Bruneaux, Gilles. "Liquid and vapor spray structure in high-pressure common rail diesel injection". In: *Atomization and Sprays* 11 (2001), p. 24. DOI: 10.1615/AtomizSpr.v11.i5.40.

[18] Pastor, J., Payri, Raul, Garcia-Oliver, Jose, and Briceno, Francisco. "Analysis of transient liquid and vapor phase penetration for diesel sprays under variable injection conditions". In: *Atomization and Sprays* 21 (2011), pp. 503–520. DOI: 10.1615/AtomizSpr.2011003721.

[19] Naber, J. and Siebers, D. "Effects of Gas Density and Vaporization on Penetration and Dispersion of Diesel Sprays". In: *SAE International* (1996).

[20] Bilger, R. W. "The Structure of Diffusion Flames". In: *Combustion Science and Technology* 13.1-6 (1976), pp. 155–170. DOI: 10.1080/00102207608946733.

[21] Ching-Hua Wang, Kung-Hui Shy and Lieu, Liang-Chi. "An Experimental Investigation on the Ignition Delay of Fuel Droplets". In: *Combustion Science and Technology* 118.1-3 (1996), pp. 63–78. DOI: 10.1080/00102209608951972.

[22] Khan, Q, Baek, Seung, and Ghassemi, Hojat. "On the autoignition and combustion characteristics of kerosene droplets at elevated pressure and temperature". In: *Combustion Science and Technology - Combustion Sci Technol* 179 (2007), pp. 2437–2451. DOI: 10.1080/00102200701484605.

[23] Law, C. K. and Chung, S. H. "An Ignition Criterion for Droplets in Sprays". In: *Combustion Science and Technology* 22.1-2 (1980), pp. 17–26. DOI: 10.1080/00102208008952370.

[24] Stauch, Rainer and Maas, U. "The ignition of methanol droplets in a laminar convective environment". In: *Combustion and Flame* 153 (2008), pp. 45–57. DOI: 10.1016/j.combustflame.2007.12.001.

[25] Cuoci, Alberto et al. "Autoignition and burning rates of fuel droplets under microgravity". In: *Combustion and Flame* 143 (2005), pp. 211–226. DOI: 10.1016/j.combustflame.2005.06.003.

[26] Stauch, Rainer and Maas, U. "The ignition of single n-heptane/iso-octane droplets". In: *International Journal of Heat and Mass Transfer* 50 (2007), pp. 3047–3053. DOI: 10.1016/j.ijheatmasstransfer.2006.12.005.

[27] Stauch, Rainer, Lipp, S., and Maas, U. "Detailed numerical simulation of the autoignition of single n-heptane droplets in air". In: *Combustion and Flame* 145 (2006), pp. 533–542. DOI: 10.1016/j.combustflame.2005.12.013.

[28] Moriue, Osamu, Mikami, Masato, Kojima, Naoya, and Eigenbrod, C. "Numerical simulations of the ignition of n-heptane droplets in the transition diameter range from heterogeneous to homogeneous ignition". In: *Proceedings of the Combustion Institute* 30 (2005), pp. 1973–1980. DOI: 10.1016/j.proci.2004.08.248.

[29] Tanabe, M et al. "Spontaneous ignition of liquid droplets from a view of non-homogeneous mixture formation and transient chemical reactions". In: *Symposium (International) on Combustion*. Vol. 26. 1. Elsevier. 1996, pp. 1637–1643.

[30] Moriue, O. et al. “Effects of dilution by aromatic hydrocarbons on staged ignition behavior of n-decane droplets”. In: 28.1 (2000), pp. 969–975. DOI: 10.1016/S0082-0784(00)80303-3.

[31] Cuoci, Alberto, Frassoldati, Alessio, Faravelli, Tiziano, and Ranzi, Eliseo. “Numerical modeling of auto-ignition of isolated fuel droplets in microgravity”. In: *Proceedings of the Combustion Institute* 35.2 (2015), pp. 1621–1627. DOI: 10.1016/j.proci.2014.06.035.

[32] Mastorakos, Epaminondas. “Ignition of turbulent non-premixed flames”. In: *Progress in Energy and Combustion Science* 35.1 (2009), pp. 57–97. DOI: 10.1016/j.pecs.2008.07.002.

[33] Mastorakos, E., Baritaud, T.A., and Poinsot, T.J. “Numerical simulations of autoignition in turbulent mixing flows”. In: *Combustion and Flame* 109.1 (1997), pp. 198–223. DOI: 10.1016/S0010-2180(96)00149-6.

[34] Cabra, R et al. “Simultaneous laser Raman-Rayleigh-LIF measurements and numerical modeling results of a lifted turbulent H2/N2 jet flame in a vitiated coflow”. In: *Proceedings of the Combustion Institute* 29.2 (2002), pp. 1881–1888. DOI: 10.1016/S1540-7489(02)80228-0.

[35] Gordon, Robert L., Masri, Assaad R., and Mastorakos, Epaminondas. “Heat release rate as represented by [OH] × [CH2O] and its role in autoignition”. In: *Combustion Theory and Modelling* 13.4 (2009), pp. 645–670. DOI: 10.1080/13647830902957200.

[36] Yi, T et al. “Autoignition-controlled flame initiation and flame stabilization in a reacting jet in crossflow”. In: *Proceedings of the Combustion Institute* 37.2 (2019), pp. 2109–2116. DOI: 10.1016/j.proci.2018.06.057.

[37] Schroll, Peter, Wandel, Andrew P, Cant, R Stewart, and Mastorakos, E. “Direct numerical simulations of autoignition in turbulent two-phase flows”. In: *Proceedings of the Combustion Institute* 32.2 (2009), pp. 2275–2282. DOI: 10.1016/j.proci.2008.06.057.

[38] Stanković, I and Merci, Bart. “Analysis of auto-ignition of heated hydrogen–air mixtures with different detailed reaction mechanisms”. In: *Combustion Theory and Modelling* 15.3 (2011), pp. 409–436. DOI: 10.1080/13647830.2010.542830.

[39] Westbrook, Charles K. “Chemical kinetics of hydrocarbon ignition in practical combustion systems”. In: *Proceedings of the combustion institute* 28.2 (2000), pp. 1563–1577. DOI: 10.1016/S0082-0784(00)80554-8.

[40] Battin-Leclerc, Frédérique. "Detailed chemical kinetic models for the low-temperature combustion of hydrocarbons with application to gasoline and diesel fuel surrogates". In: *Progress in Energy and Combustion Science* 34.4 (2008), pp. 440–498. DOI: 10.1016/j.pecs.2007.10.002.

[41] Zádor, Judit, Taatjes, Craig A, and Fernandes, Ravi X. "Kinetics of elementary reactions in low-temperature autoignition chemistry". In: *Progress in energy and combustion science* 37.4 (2011), pp. 371–421. DOI: 10.1016/j.pecs.2010.06.006.

[42] Goldsborough, S Scott et al. "Advances in rapid compression machine studies of low-and intermediate-temperature autoignition phenomena". In: *Progress in Energy and Combustion Science* 63 (2017), pp. 1–78. DOI: 10.1016/j.pecs.2017.05.002.

[43] Sarathy, S Mani et al. "Three-stage heat release in n-heptane autoignition". In: *Proceedings of the Combustion Institute* 37.1 (2019), pp. 485–492. DOI: 10.1016/j.proci.2018.07.075.

[44] S., Deng, P., Zhao, M., Mueller, and C., Law. "Stabilization of laminar nonpremixed DME/air coflow flames at elevated temperatures and pressures". In: *Combustion and Flame* 162.12 (2015), pp. 4471–4478. DOI: 10.1016/j.combustflame.2015.08.019.

[45] Sreedhara, S. and Lakshmisha, K.N. "Autoignition in a non-premixed medium: DNS studies on the effects of three-dimensional turbulence". In: *Proceedings of the Combustion Institute* 29.2 (2002), pp. 2051–2059. DOI: 10.1016/S1540-7489(02)80250-4.

[46] Borghesi, Giulio, Mastorakos, Epaminondas, and Cant, R. Stewart. "Complex chemistry DNS of n-heptane spray autoignition at high pressure and intermediate temperature conditions". In: *Combustion and Flame* 160.7 (2013), pp. 1254–1275. DOI: 10.1016/j.combustflame.2013.02.009.

[47] Mukhopadhyay, Saumyadip and Abraham, John. "Influence of compositional stratification on autoignition in n-heptane/air mixtures". In: *Combustion and Flame* 158.6 (2011), pp. 1064–1075. DOI: 10.1016/j.combustflame.2010.10.007.

[48] A., Krisman, E., Hawkes, and J., Chen. "A parametric study of ignition dynamics at ECN Spray A thermochemical conditions using 2D DNS". In: *Proceedings of the Combustion Institute* 37.4 (2019), pp. 4787–4795. DOI: 10.1016/j.proci.2018.08.026.

[49] Dahms, Rainer N., Paczko, Günter A., Skeen, Scott A., and Pickett, Lyle M. "Understanding the ignition mechanism of high-pressure spray flames". In: (2017). DOI: 10.1016/j.proci.2016.08.023.

[50] Krisman, Alex, Hawkes, Evatt R., Talei, Mohsen, Bhagatwala, Ankit, and Chen, Jacqueline H. "Characterisation of two-stage ignition in diesel engine-relevant thermochemical conditions using direct numerical simulation". In: 172 (2016), pp. 326–341. DOI: 10.1016/j.combustflame.2016.06.010.

[51] Borghesi, Giulio, Krisman, Alexander, Lu, Tianfeng, and Chen, Jacqueline H. "Direct numerical simulation of a temporally evolving air/n-dodecane jet at low-temperature diesel-relevant conditions". In: *Combustion and Flame* 195 (2018), pp. 183–202. DOI: 10.1016/j.combustflame.2018.02.020.

[52] Minamoto, Yuki and Chen, Jacqueline H. "DNS of a turbulent lifted DME jet flame". In: *Combustion and flame* (2016). DOI: 10.1016/j.combustflame.2016.04.007.

[53] Dec, J. "A Conceptual Model of DI Diesel Combustion Based on Laser-Sheet Imaging". In: *SAE International* (1997).

[54] N., Maes. "The Life of a Spray". PhD thesis. Technische Universiteit Eindhoven, 2019.

[55] Tagliante, Fabien et al. "A conceptual model of the flame stabilization mechanisms for a lifted Diesel-type flame based on direct numerical simulation and experiments". In: *Combustion and Flame* 201 (2019), pp. 65–77. DOI: 10.1016/j.combustflame.2018.12.007.

[56] Assen, Niklas von der, Müller, Leonard J, Steingrube, Annette, Voll, Philip, and Bardow, André. "Selecting CO2 sources for CO2 utilization by environmental-merit-order curves". In: *Environmental science & technology* 50.3 (2016), pp. 1093–1101. DOI: 10.1021/acs.est.5b03474.

[57] Giesen, Coen van der, Kleijn, René, and Kramer, Gert Jan. "Energy and climate impacts of producing synthetic hydrocarbon fuels from CO2". In: *Environmental science & technology* 48.12 (2014), pp. 7111–7121. DOI: 10.1021/es500191g.

[58] Matzen, Michael and Demirel, Yaşar. "Methanol and dimethyl ether from renewable hydrogen and carbon dioxide: Alternative fuels production and life-cycle assessment". In: *Journal of cleaner production* 139 (2016), pp. 1068–1077. DOI: 10.1016/j.jclepro.2016.08.163.

[59] Burger, Jakob, Siegert, Markus, Ströfer, Eckhard, and Hasse, Hans. "Poly(oxymethylene) dimethyl ethers as components of tailored diesel fuel: Properties, synthesis and purification concepts". In: *Fuel* 89.11 (2010), pp. 3315–3319. DOI: 10.1016/j.fuel.2010.05.014.

[60] Masri, A.R. "Challenges for turbulent combustion". In: *Proceedings of the Combustion Institute* 38.1 (2021), pp. 121–155. DOI: 10.1016/j.proci.2020.07.144.

[61] Awad, Omar I. et al. "Overview of polyoxymethylene dimethyl ether additive as an eco-friendly fuel for an internal combustion engine: Current application and environmental impacts". In: *Science of the Total Environment* 715 (2020). DOI: 10.1016/j.scitotenv.2020.136849.

[62] Gierlich, Christian Henning, Beydoun, Kassem, Klankermayer, Jürgen, and Palkovits, Regina. "Challenges and Opportunities in the Production of Oxymethylene Dimethylether". In: *Chemie Ingenieur Technik* 92.1-2 (2020), pp. 116–124. DOI: 10.1002/cite.201900187.

[63] Deutz, Sarah et al. "Cleaner production of cleaner fuels: wind-to-wheel–environmental assessment of CO 2-based oxymethylene ether as a drop-in fuel". In: *Energy & Environmental Science* 11.2 (2018), pp. 331–343. DOI: 10.1039/C7EE01657C.

[64] Bongartz, Dominik et al. "Comparison of light-duty transportation fuels produced from renewable hydrogen and green carbon dioxide". In: *Applied energy* 231 (2018), pp. 757–767. DOI: 10.1016/j.apenergy.2018.09.106.

[65] Lautenschütz, Ludger et al. "Physico-chemical properties and fuel characteristics of oxymethylene dialkyl ethers". In: *Fuel* 173 (2016), pp. 129–137. DOI: 10.1016/j.fuel.2016.01.060.

[66] Liu, Junheng et al. "An overview of polyoxymethylene dimethyl ethers as alternative fuel for compression ignition engines". In: *Fuel* 318 (2022), p. 123582. DOI: 10.1016/j.fuel.2022.123582.

[67] Pastor, José V., García-Oliver, José M., Micó, Carlos, García-Carrero, Alba A., and Gómez, Arantzazu. "Experimental Study of the Effect of Hydrotreated Vegetable Oil and Oxymethylene Ethers on Main Spray and Combustion Characteristics under Engine Combustion Network Spray A Conditions". In: *Applied Sciences* 10.16 (2020), p. 5460. DOI: 10.3390/app10165460.

[68] Pandal, Adrian et al. "Computational and Experimental Investigation of Interfacial Area in Near-Field Diesel Spray Simulation". In: *SAE International Journal of Fuels and Lubricants* 10 (2017). DOI: 10.4271/2017-01-0859.

[69] Larson, Eric D and Yang, Huiyan. "Dimethyl ether (DME) from coal as a household cooking fuel in China". In: *Energy for sustainable development* 8.3 (2004), pp. 115–126. DOI: 0.1016/S0973-0826(08)60473-1.

[70] Bamgboye, A.I. and Hansen, A.C. "Prediction of cetane number of biodiesel fuel from the fatty acid methyl ester (FAME) composition". In: *International Agrophysics* 22.1 (2008), pp. 21–29.

[71] Wei, Jiangjun et al. "Morphology analysis of soot particles from a modern diesel engine fueled with different types of oxygenated fuels". In: *Fuel* 267 (2020), p. 117248. DOI: 10.1016/j.fuel.2020.117248.

[72] Theinnoi, Kampanart, Suksompong, Porjade, and Temwutthikun, Wari-rat. "Engine performance of dual fuel operation with in-cylinder injected diesel fuels and in-port injected DME". In: *Energy Procedia* 142 (2017), pp. 461–467. DOI: 10.1016/j.egypro.2017.12.072.

[73] Zheng, Zunqing et al. "Experimental study on the combustion and emissions fueling biodiesel/n-butanol, biodiesel/ethanol and biodiesel/2, 5-dimethylfuran on a diesel engine". In: *Energy* 115 (2016), pp. 539–549. DOI: 10.1016/j.energy.2016.09.054.

[74] Nour, Mohamed, Attia, Ali MA, and Nada, Sameh A. "Improvement of CI engine combustion and performance running on ternary blends of higher alcohol (Pentanol and Octanol)/hydrous ethanol/diesel". In: *Fuel* 251 (2019), pp. 10–22. DOI: 10.1016/j.fuel.2019.04.026.

[75] Matsukawa, Yoshiya et al. "Reaction pathway for nascent soot in ethylene pyrolysis". In: *Combustion and Flame* 167 (2016), pp. 248–258. DOI: 10.1016/j.combustflame.2016.02.008.

[76] Li, Bowen et al. "Combustion and emission characteristics of diesel engine fueled with biodiesel/PODE blends". In: *Applied Energy* 206 (2017), pp. 425–431. DOI: 10.1016/j.apenergy.2017.08.206.

[77] Sun, Wenyu et al. "Speciation and the laminar burning velocities of poly (oxymethylene) dimethyl ether 3 (POMDME3) flames: An experimental and modeling study". In: *Proceedings of the Combustion Institute* 36.1 (2017), pp. 1269–1278. DOI: 10.1016/j.proci.2016.05.058.

[78] Tan, Yong Ren et al. "Sooting characteristics of polyoxymethylene dimethyl ether blends with diesel in a diffusion flame". In: *Fuel* 224 (2018), pp. 499–506. DOI: 10.1016/j.fuel.2018.03.051.

[79] Calcote, HF and Manos, DM. "Effect of molecular structure on incipient soot formation". In: *Combustion and Flame* 49.1-3 (1983), pp. 289–304. DOI: 10.1016/0010-2180(83)90172-4.

[80] Barrientos, Eduardo J, Lapuerta, Magín, and Boehman, André L. "Group additivity in soot formation for the example of C-5 oxygenated hydrocarbon fuels". In: *Combustion and Flame* 160.8 (2013), pp. 1484–1498. DOI: 10.1016/j.combustflame.2013.02.024.

[81] Pellegrini, Leonardo, Patrini, Renata, and Marchionna, Mario. "Effect of POMDME Blend on PAH Emissions and Particulate Size Distribution from an In-Use Light-Duty Diesel Engine". In: *SAE 2014 World Congress and Exhibition*. SAE International, 2014. DOI: 10.4271/2014-01-1951.

[82] Pélerin, Dominik, Gaukel, Kai, Härtl, Martin, Jacob, Eberhard, and Wachtmeister, Georg. "Potentials to simplify the engine system using the alternative diesel fuels oxymethylene ether OME1 and OME36 on a heavy-duty engine". In: *Fuel* 259 (2020), p. 116231. DOI: 10.1016/j.fuel.2019.116231.

[83] Härtl, Martin, Seidenspinner, Philipp, Jacob, Eberhard, and Wachtmeister, Georg. "Oxygenate screening on a heavy-duty diesel engine and emission characteristics of highly oxygenated oxymethylene ether fuel OME1". In: *Fuel* 153 (2015), pp. 328–335. DOI: 10.1016/j.fuel.2015.03.012.

[84] Pellegrini, Leonardo et al. *Combustion behaviour and emission performance of neat and blended polyoxymethylene dimethyl ethers in a light-duty diesel engine*. Tech. rep. SAE Technical Paper, 2012.

[85] Maus, Dipl-Ing Wolfgang and Jacob, E. "Synthetische Kraftstoffe-OME1: Ein potenziell nachhaltig hergestellter Dieselkraftstoff Synthetic Fuels-OME1: A Potentially Sustainable Diesel Fuel". In: *https://www.emitec. com/* 12.21 (2014), p. 2018.

[86] Benajes, Jesús, García, Antonio, Monsalve-Serrano, Javier, and Guzmán-Mendoza, María. "A review on low carbon fuels for road vehicles: The good, the bad and the energy potential for the transport sector". In: *Fuel* 361 (2024), p. 130647. DOI: 10.1016/j.fuel.2023.130647.

[87] Garcia, Antonio, Monsalve-Serrano, Javier, Villalta, David, and Fogue-Robles, Alvaro. "Evaluating OMEx combustion towards stoichiometric conditions in a compression ignition engine". In: *Fuel* 303 (2021), p. 121273. DOI: 10.1016/j.fuel.2021.121273.

[88] Liu, Jialin et al. "Effects of diesel/PODE (polyoxymethylene dimethyl ethers) blends on combustion and emission characteristics in a heavy duty diesel engine". In: 177 (2016), pp. 206–216. DOI: 10.1016/j.fuel.2016.03.019.

[89] Omari, Ahmad, Heuser, Benedikt, and Pischinger, Stefan. "Potential of oxymethylenether-diesel blends for ultra-low emission engines". In: *Fuel* 209.July (2017), pp. 232–237. DOI: 10.1016/j.fuel.2017.07.107.

[90] Dworschak, Patrick, Berger, Vinicius, Härtl, Martin, and Wachtmeister, Georg. *Neat oxymethylene ethers: combustion performance and emissions of OME 2, OME 3, OME 4 and OME 5 in a single-cylinder diesel engine*. Tech. rep. SAE Technical Paper, 2020.

[91] Zacherl, Florian, Wopper, Christoph, Schwanzer, Peter, and Rabl, Hans-Peter. "Potential of the Synthetic Fuel Oxymethylene Ether (OME) for the Usage in a Single-Cylinder Non-Road Diesel Engine: Thermodynamics and Emissions". In: *Energies* 15.21 (2022), p. 7932. DOI: 10.3390/en15217932.

[92] Schemme, Steffen, Samsun, Remzi Can, Peters, Ralf, and Stolten, Detlef. "Power-to-fuel as a key to sustainable transport systems – An analysis of diesel fuels produced from CO2 and renewable electricity". In: *Fuel* 205 (2017), pp. 198–221. DOI: 10.1016/j.fuel.2017.05.061.

[93] Härtl, M., Gaukel, Kai, Pélerin, Dominik, and Wachtmeister, Georg. "Oxymethylene Ether as Potentially CO2-neutral Fuel for Clean Diesel Engines Part 1: Engine Testing". In: *MTZ worldwide* 78 (2017), pp. 52–59. DOI: 10.1007/s38313-016-0163-6.

[94] Uchida, Tadashi, Kurita, Yukio, and Kubo, Masaji. "The dipole moments and the structure of polyoxymethylene dimethyl ethers". In: *Journal of Polymer Science* 19.92 (1956), pp. 365–372. DOI: 10.1002/pol.1956.120199215.

[95] Kass, Michael, Wissink, Martin, Janke, Chris, Connatser, Raynella, and Curran, Scott. "Compatibility of Elastomers with Polyoxymethylene Dimethyl Ethers and Blends with Diesel". In: *SAE International Journal of Advances and Current Practices in Mobility-V129-99EJ* (2020).

[96] Pastor, Jose V., García-Oliver, Jose M., Micó, Carlos, and Tejada, Francisco J. "Characterization of the oxymethylene ether fuels flame structure for ECN Spray A and Spray D nozzles". In: *Applied Energy* 332 (2023). DOI: 10.1016/j.apenergy.2022.120475.

[97] Guzmán, María Gabriela. "Impact of different e-fuels type on light-duty compression ignition engine performance, emissions and CO2 Life cycle analysis". PhD thesis. Universitat Politecnica de Valencia, 2023.

[98] Pastor, José, Antonio, Garcia, Micó, Carlos, and Lewiski, Felipe. "An optical investigation of Fischer-Tropsch diesel and Oxymethylene dimethyl ether impact on combustion process for CI engines". In: *Applied Energy* 260 (2020), p. 114238. DOI: 10.1016/j.apenergy.2019.114238.

[99] Pastor, José V., García, Antonio, Micó, Carlos, and Lewiski, Felipe. "Simultaneous high-speed spectroscopy and 2-color pyrometry analysis in an optical compression ignition engine fueled with OMEX-diesel blends". In: *Combustion and Flame* 230 (2021), p. 111437. DOI: 10.1016/j.combustflame.2021.111437.

[100] Pastor, Jose V., Garcia-Oliver, Jose M, Micó, Carlos, and Tejada, Francisco J. "Combustion Behaviour of Blends of Synthetic Fuels in an Optical Single Cylinder Engine". In: *15th International Conference on Engines and Vehicles*. SAE International, 2021. DOI: 10.4271/2021-24-0038.

[101] Pöllmann, Simon, Härtl, Martin, and Wachtmeister, Georg. "Injection Process of the Synthetic Fuel Oxymethylene Ether: Optical Analysis in a Heavy-Duty Engine". In: *SAE Powertrains, Fuels & Lubricants Meeting*. SAE International, 2020.

[102] Iannuzzi, Stefano Emanuele, Barro, Christophe, Boulouchos, Konstantinos, and Burger, Jakob. "POMDME-diesel blends: Evaluation of performance and exhaust emissions in a single cylinder heavy-duty diesel engine". In: *Fuel* 203 (2017), pp. 57–67. DOI: 10.1016/j.fuel.2017.04.089.

[103] García-Oliver, José M, Novella, Ricardo, Micó, Carlos, and Leon-Ceriani, Daiana De. "Numerical analysis of the combustion process of oxymethylene ethers as low-carbon fuels for compression ignition engines". In: *International Journal of Engine Research* 24.5 (2023), pp. 2175–2186. DOI: 10.1177/14680874221113749.

[104] García-Oliver, José M., Novella, Ricardo, Micó, Carlos, and Bin-Khalid, Usama. "A numerical investigation of the performance of oxymethylene ethers blended with fossil diesel to reduce soot emissions in compression ignition engines". In: *Fuel* 324 (2022), p. 124768. DOI: 10.1016/j.fuel.2022.124768.

[105] CONVERGE CFD Software. *https://convergecfd.com*.

[106] Cai, Liming et al. “Auto-ignition of oxymethylene ethers (OMEn, n = 2–4) as promising synthetic e-fuels from renewable electricity: shock tube experiments and automatic mechanism generation”. In: *Fuel* 264 (2020), p. 116711. DOI: 10.1016/j.fuel.2019.116711.

[107] Novella, Ricardo, Bracho, Gabriela, Gomez-Soriano, Josep, Fernandes, Cássio S., and Lucchini, Tommaso. “Combustion system optimization for the integration of e-fuels (Oxymethylene Ether) in compression ignition engines”. In: *Fuel* 305 (2021), p. 121580. DOI: 10.1016/j.fuel.2021.121580.

[108] OpenFOAM. *https://www.openfoam.com/*. The Open Source CFD Toolbox. User Gide Version 1.6, 2009.

[109] Dageförde, Toni, Gröger, Karsten, Kawaharada, Noritsune, and Dinkelacker, Friedrich. “Velocity Field Measurements with High Speed Structural Image Velocimetry in the Primary Atomization Region of Future Diesel Fuels”. In: *SAE International Journal of Advances and Current Practices in Mobility* 3 (2020). DOI: 10.4271/2020-01-2112.

[110] Strauß, Lukas, Rieß, Sebastian, and Wensing, Michael. “Mixture formation of OME35 and 1-Octanol in comparison with diesel-like Dodecane under ECN Spray A conditions”. In: *Frontiers in Mechanical Engineering* 9 (2023). DOI: 10.3389/fmech.2023.1083658.

[111] Peter, Andreas et al. “Mixture formation analysis of polyoxymethylenether injection”. In: *Atomization and Sprays* 30.11 (2020), pp. 843–859. DOI: 10.1615/AtomizSpr.2020035250.

[112] Singh, Srijna, Ailaboina, Akhil, Battistoni, Michele, Danish, Mohammad, and Saha, Kaushik. “Numerical Investigation of Cavitation Behavior for Dodecane and OME3 Fuel in ECN Spray C Injector Nozzle”. In: *Proceedings of the 1st International Conference on Fluid, Thermal and Energy Systems*. Ed. by Sudev Das, Narasimha Mangadoddy, and Jaap Hoffmann. Singapore: Springer Nature Singapore, 2024, pp. 59–69.

[113] Ma, Yue, Cui, Longxi, Ma, Xiao, and Wang, Jianxin. “Optical study on spray combustion characteristics of PODE/diesel blends in different ambient conditions”. In: *Fuel* 272 (2020), p. 117691. DOI: 10.1016/j.fuel.2020.117691.

[114] Iannuzzi, Stefano Emanuele, Barro, Christophe, Boulouchos, Konstantinos, and Burger, Jakob. “Combustion behavior and soot formation/oxidation of oxygenated fuels in a cylindrical constant volume chamber”. In: *Fuel* 167 (2016), pp. 49–59. DOI: 10.1016/j.fuel.2015.11.060.

[115] Ma, Xiao et al. "PLII-LEM and OH* Chemiluminescence Study on Soot Formation in Spray Combustion of PODEn-Diesel Blend Fuels in a Constant Volume Vessel". In: *International Powertrains, Fuels and Lubricants Meeting*. SAE International, 2017. DOI: 10.4271/2017-01-2329.

[116] Sun, Zhongcheng et al. "Combustion characteristics of oxymethylene dimethyl ether-diesel blends: An experimental investigation using a constant-volume combustion chamber". In: *Fuel* 360 (2024), p. 130587. DOI: 10.1016/j.fuel.2023.130587.

[117] Garcia-Carrero, Alba. "Experimental study of the fuel effect on diffusion combustion and soot formation under diesel engine-like conditions". PhD thesis. Universitat Politecnica de Valencia, 2021.

[118] Tejada, Francisco Jose. "Analysis of fuel effects on the diffusive flame structure using advanced optical techniques in a single cylinder optical engine". PhD thesis. Universitat Politecnica de Valencia, 2023.

[119] Xuan, Tiemin et al. "A conceptual model of polyoxymethylene dimethyl ether 3 (PODE3) spray combustion under compression ignition engine-like conditions". In: *Combustion and Flame* 261 (2024), p. 113296. DOI: 10.1016/j.combustflame.2024.113296.

[120] Desantes, JM, Pastor, JV, García-Oliver, JM, and Pastor, JM. "A 1D model for the description of mixing-controlled reacting diesel sprays". In: *Combustion and Flame* 156.1 (2009), pp. 234–249. DOI: 10.1016/j.combustflame.2008.10.008.

[121] Pastor, José V, López, J Javier, García, José M, and Pastor, José M. "A 1D model for the description of mixing-controlled inert diesel sprays". In: *Fuel* 87.13-14 (2008), pp. 2871–2885. DOI: doi.org/10.1016/j.fuel.2008.04.017.

[122] Desantes, José M, García-Oliver, José M, Xuan, Tiemin, and Vera-Tudela, Walter. "A study on tip penetration velocity and radial expansion of reacting diesel sprays with different fuels". In: *Fuel* 207 (2017), pp. 323–335. DOI: 10.1016/j.fuel.2017.06.108.

[123] Goeb, Dominik et al. "Oxymethylene ether n-dodecane blend spray combustion: Experimental study and large-eddy simulations". In: *Proceedings of the Combustion Institute* 000 (2020). DOI: 10.1016/j.proci.2020.08.017.

[124] Jacobs, Sascha et al. “Detailed kinetic modeling of dimethoxymethane. Part II: Experimental and theoretical study of the kinetics and reaction mechanism”. In: *Combustion and Flame* 205 (2019), pp. 522–533. DOI: 10.1016/J.COMBUSTFLAME.2018.12.026.

[125] Cai, Liming et al. “Optimized reaction mechanism rate rules for ignition of normal alkanes”. In: *Combustion and Flame* 173 (2016), pp. 468–482. DOI: 10.1016/j.combustflame.2016.04.022.

[126] Blanquart, G, Pepiot-Desjardins, P, and Pitsch, H. “Chemical mechanism for high temperature combustion of engine relevant fuels with emphasis on soot precursors”. In: *Combustion and Flame* 156.3 (2009), pp. 588–607. DOI: 10.1016/j.combustflame.2008.12.007.

[127] Wiesmann, Frederik et al. “Numerical and Experimental Investigations on the Ignition Behavior of OME”. In: *Energies* 15.18 (2022). DOI: 10.3390/en15186855.

[128] Niu, Bo et al. “Construction of reduced oxidation mechanisms of polyoxymethylene dimethyl ethers (PODE1–6) with consistent structure using decoupling methodology and reaction rate rule”. In: *Combustion and Flame* 232 (2021), p. 111534. DOI: 10.1016/j.combustflame.2021.111534.

[129] GmbH, AVL List. *AVL List GmbH. FIRE General Gas Phase Reactions Module v2018; Manual; AVL List GmbH: Graz, Austria, 2018.* 2018.

[130] Wiesmann, Frederik et al. “Numerical study of novel OME16 combustion mechanism and spray combustion at changed ambient environments”. In: *Frontiers in Energy* (2024). DOI: 10.1007/s11708-024-0926-8.

[131] Haspel, Philip et al. “Large eddy simulation of OME3 and OME4 spray combustion under heavy-duty conditions”. In: *Fuel* 353 (2023), p. 129097. DOI: 10.1016/j.fuel.2023.129097.

[132] Pitsch, Heinz and Ihme, Matthias. “An unsteady/flamelet progress variable method for LES of nonpremixed turbulent combustion”. In: *43rd AIAA Aerospace Sciences Meeting and Exhibit*. 2005, p. 557.

[133] Kopp, Wassja A. et al. “Detailed kinetic modeling of dimethoxymethane. Part I: Ab initio thermochemistry and kinetics predictions for key reactions”. In: *Combustion and flame* 189 (2018), pp. 433–442. DOI: 10.1016/j.combustflame.2017.07.037.

[134] He, Tanjin et al. “A chemical kinetic mechanism for the low- and intermediate-temperature combustion of Polyoxymethylene Dimethyl Ether 3 (PODE3)”. In: *Fuel* 212 (2018), pp. 223–235. DOI: 10.1016/j.fuel.2017.09.080.

[135] Drost, Simon, Schießl, Robert, Werler, Marc, Sommerer, Jörg, and Maas, Ulrich. "Ignition delay times of polyoxymethylene dimethyl ether fuels (OME2 and OME3) and air: Measurements in a rapid compression machine". In: *Fuel* 258 (2019), p. 116070. DOI: 10.1016/j.fuel.2019.116070.

[136] Hiroyasu, Hiroyuki, Kadota, Toshikazu, and Arai, Masataka. "Development and Use of a Spray Combustion Modeling to Predict Diesel Engine Efficiency and Pollutant Emissions : Part 1 Combustion Modeling". In: *Bulletin of JSME* 26.214 (1983), pp. 569–575. DOI: 10.1299/jsme1958.26.569.

[137] Leung, K.M., Lindstedt, R.P., and Jones, W.P. "A simplified reaction mechanism for soot formation in nonpremixed flames". In: *Combustion and Flame* 87.3 (1991), pp. 289–305. DOI: 10.1016/0010-2180(91)90114-Q.

[138] Pachano, Leonardo et al. "A two-equation soot-in-flamelet modeling approach applied under Spray A conditions". In: *Combustion and Flame* 231 (2021), p. 111488. DOI: 10.1016/j.combustflame.2021.111488.

Chapter 3

Tools and methodology

Contents

3.1 Introduction

This chapter brings together both the tools and methodology used in this thesis. As mentioned earlier, the methodology is predominantly computational and includes a wide range of tools. Below, these will be described in the natural order of their independence within the general methodology, considering that studying combustion requires combining basic thermodynamics, chemistry, and

transport phenomena. Basic thermodynamics and chemistry are always present in the simplest form of studying combustion, while studying a flame necessarily involves including transport phenomena. These two extremes in the study of combustion will be represented in this thesis with homogeneous reactors at the simplest end and 3D CFD calculations at the most comprehensive end, passing through flamelets where diffusion phenomenon is taken into account.

Therefore, tools will begin by explaining the determination of the thermodynamic properties of the target fuels, followed by the representation of chemical kinetics through chemical mechanisms. Once the chemical kinetics is introduced, the phenomenon of chemiluminescence and how it can be considered through the coupling of its own sub-mechanism and the estimation of its thermodynamic properties will be described. Next, the models of canonical configurations used will be introduced, starting with the most basic, 0D – homogeneous reactors, then considering the diffusion with 1D – counterflow flamelets, and finally, the 3D CFD model used. Within this last model, both the liquid and gas phases are described, which are coupled using the nearest node approach to exchange mass, momentum, energy terms of a parcel (Lagrangian particle) with the fluid-phase (Eulerian field) values. At this point, in addition to numerical aspects and assessments of calibrations, adaptations and developed tools performance results, some fundamental knowledge must be introduced to comprehensively explain the entire workflow involved in spray combustion modelling as well as the selection of different frameworks to carry out this work.

Figure 3.1 shows how the different tools interact to each other, determining the general methodology outline of the research.

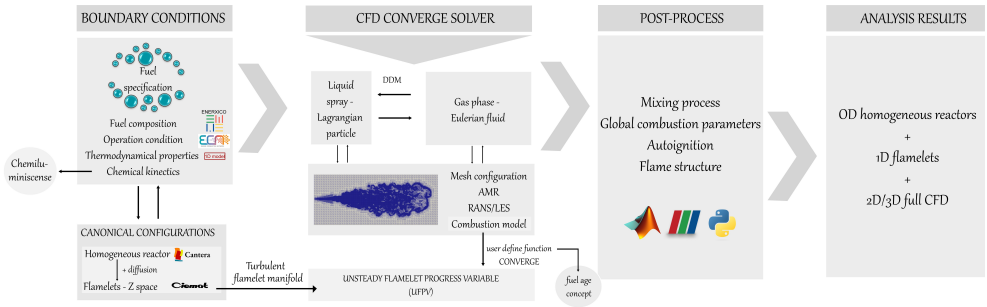

Figure 3.1: General methodology outline.

3.2 Physical properties

Ensuring accurate modelling of material properties is of utmost importance when configuring and conducting calculations in any kind of flow. The characteristics of the fluid, including density and viscosity, among others, can vary based on factors such as composition, pressure, and temperature. Obtaining precise values for these properties is essential, as they can significantly impact the design of devices and processes. In particular, in $CONVERGE$ when a spray combustion is calculated, liquid properties must be specified in order to complete the characterization of the fuel under study. For these properties, which includes density, viscosity, conductivity, surface tension, vapour pressure, heat of vaporization and specific heat, values must be known ideally from 0 K to the critical temperature, for the saturated liquid. Given these $OMEn$-type fuels novelty in modelling, very few studies on their properties are available. Specifically, there are the works of Boyd [1], Kulkarni et al. [2] and Burger [3]. On the one hand, Boyd conducted measurements of the vapour pressures of various Poly-Oxymethylene Dimethyl Ethers. However, these measurements were limited to their atmospheric boiling temperatures. On the other hand, Kulkarni et al. used force field simulation to predict the vapour pressures of $OMEn$ at temperatures up to 543.06 K for OME_3 and 582.21 K for OME_4. It is worth noting that Kulkarni et al. mentioned that they relied solely on Boyd's vapour pressure data set to develop their simulation. Additionally, Burger et al. [3] also employed Boyd's vapour pressure correlation in their study. For these reasons, a methodology based upon a cubic equation of state developed by Pastor et al. [4] was used to obtain all the properties in a wide range of temperatures according to the framework of the $CONVERGE$ CFD simulations. In that work, the Peng-Robinson equation of state (EoS) has been applied; this EoS can be expressed as Equation 3.1:

$$P = \frac{R_u T}{\vartheta - b} - \frac{a(T)}{\vartheta^2 + 2b\vartheta - b^2} \tag{3.1}$$

where T denotes the absolute temperature, R_u is the universal gas constant, ϑ represent the molar volume and a and b are obtained following mixing rules and are dependent on the critical properties (T_{ci} and P_{ci}) and the acentric factor ω. The equation for the fugacity coefficient of each component in the mixture has been used to solve the Liquid-Vapour equilibrium. For more details, refer to the work [4].

In the present work, the $OMEn$-type selected for simulations has been OME_1 as a single-component and a blend of OME_3 and OME_4 representing

a generic multicomponent $OMEn$; more details about this blend definition can be found in the following Chapter 4. Therefore, the critical properties for OME_1, OME_3 and OME_4 are listed in Table 3.1 which are obtained from Kulkarni et al. [2] and the acentric factor from $ASPEN$ database [5] and are used as input in the 1D real gas calculations.

Component	T_c[K]	ρ_c [kg/m^3]	p_c [bar]	ω
OME1	497.3	309.2	48.8	0.3080
OME3	621.5	322.1	30.2	0.3261
OME4	679.3	318.8	25.0	0.6918

Table 3.1: Critical properties of OME_1, OME_3 and OME_4 estimated by Kulkarni et al. [2] and acentric factor from ASPEN database [5].

The final thermophysical properties used are presented in Figure 3.2 for OME_1, OME_3 and OME_4, as well as for n-Dodecane, which is a reference hydrocarbon for the type of calculation in the present thesis. Both the vapour pressure, latent heat of vaporization and the liquid heat capacity were obtained from real-gas behaviour at saturation conditions using the Peng-Robinson EoS described before. Then, liquid density is directly used from Kulkarni results [2], because Peng-Robinson tends to overpredict this property. And finally, viscosity, surface tension and conductivity are from a fitting to $ASPEN$ database (273 to 373K), which has been extrapolated to the full liquid range.

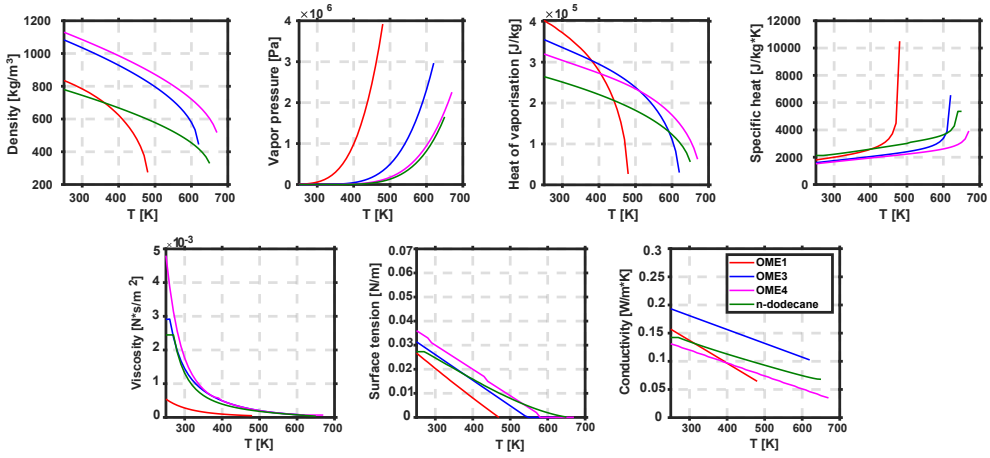

Figure 3.2: Relevant properties for liquid spray modelling.

OME_1 presents the most significant variations and differences in viscosity and surface tension compared to n-Dodecane, however conductivity values are in similar ranges. Besides, in general OME_3 and OME_4 have similar characteristics and OME_1 in most of the properties is closer to OME_3 than OME_4, consistent with the chain length. In $CONVERGE$, thermodynamic properties must be supplied for every single component fuel to be simulated. Then, the multi-component fluid is defined by specifying the mass fractions of each component. For that reason, Figure 3.2 illustrates the behaviour specific to each individual component.

3.3 Chemical mechanism

A chemical mechanism is a model that determines the species involved in characterizing the reacting mixture and defines the chemical reactions that convert reactant species into product species. Global reactions, assuming complete combustion, are commonly used to describe the chemical reactions involved in combustion processes, where the conversion of reactants into products of a general hydrocarbon can be described according to Equation 3.2,

$$\nu'_{C_mH_n} C_mH_n + \nu'_{O_2} O_2 \rightarrow \nu''_{CO_2} CO_2 + \nu''_{H_2O} H_2O \tag{3.2}$$

where ν'_k and ν''_k denotes the stoichiometric coefficient of species k for the reactants and products species, respectively. Nevertheless, it is important to note that global reactions are a significant simplification, it is too complex to solve by simple chemistry assumptions a complex reaction process, such as autoignition of hydrocarbons, reference fuels here (especially due to the presence of a Negative Temperature Coefficient effect [6]) and even $OMEn$-type fuels. For that reason, the use of more detailed chemistry is recommended. In the broad field of reaction kinetics, the development of reaction mechanisms can be categorized based on their complexity into detailed, skeletal, and reduced mechanisms. Under a more detailed chemistry model than a global reaction, like the ones mentioned before, a chemical system can be described by the general form of N_r elementary reactions that include N_c species,

$$\sum_{k=1}^{N_c} \nu'_{kj} M_k \rightleftharpoons \sum_{k=1}^{N_c} \nu''_{kj} M_k \qquad for \quad j = 1, ..., N_r \tag{3.3}$$

where M_k stand for species k. The objective of the reaction mechanism is to determine the rate at which the specified reactions take place. The rate of reaction ω_j of a reaction j is expressed as follows [7]:

$$\omega_j = k_{f,j} \prod_{k=1}^{Nc} c_k^{v'_{k,j}} - k_{b,j} \prod_{k=1}^{Nc} c_k^{\nu''_{k,j}} \qquad for \quad j = 1, ..., N_r \tag{3.4}$$

here, c_k is the molar species concentration, while k_{fj} and k_{bj} represent the rate coefficients of the forward and backward reactions, respectively. In general, these coefficients are dependent on temperature and may also be influenced by pressure and are usually modelled using Arrhenius Law (Equation 3.5) where, A_r is a pre-exponential constant, b_r the temperature exponent and E_a the activation energy associated with the reaction [8].

$$k_r = A_r T^{b_r} e^{-\frac{E_{ar}}{R_u T}} \tag{3.5}$$

The mass of species k produced per unit volume and unit time, which is the chemical source term $\dot{\omega}_k$, is the sum over all reaction in the mechanism, given by Equation 3.6,

$$\dot{\omega}_k = \sum_{j=1}^{N_r} (\nu''_{kj} - \nu'_{kj}) \omega_j = \sum_{j=1}^{N_r} \nu_{kj} \omega_j \tag{3.6}$$

Noting that due to the mass conservation, the sum over all source terms is equal to 0. Using the chemical source term (Equation 3.6) it is possible to compute the heat release rate following Equation 3.7,

$$\dot{\omega}_T = - \sum_{k=1}^{N_c} \Delta h^0_{f,k} \dot{\omega}_k \tag{3.7}$$

where, $\Delta h^0_{f,k}$ represent the enthalpy of formation of species k.

Finally, regarding the chemical mechanism, in addition to the definition of the chemical reactions, it is usually accompanied by the thermodynamic properties of the species involved in the mechanism. These thermodynamic data are typically represented by well-known NASA polynomial forms, namely specific heat (Equation 3.8), enthalpy (Equation 3.9), and entropy (Equation 3.10).

$$\frac{c^{\circ}_{p,k}}{R} = a_{1k} + a_{2k} T_k + a_{3k} T_k^2 + a_{4k} T_k^3 + a_{5k} T_k^4 \tag{3.8}$$

$$\frac{h^{\circ}_k}{R} = a_{1k} T_k + \frac{a_{2k} T_k^2}{2} + \frac{a_{3k} T_k^3}{3} + \frac{a_{4k} T_k^4}{4} + \frac{a_{5k} T_k^5}{5} + a_{6k} \tag{3.9}$$

$$\frac{s_k^\circ}{R} = a_{1k}ln(T_k) + a_{2k}T_k + \frac{a_{3k}T_k^2}{2} + \frac{a_{4k}T_k^3}{3} + \frac{a_{5k}T_k^4}{4} + a_{7k} \tag{3.10}$$

Currently, researchers in the field have conducted numerous experiments to explore the application of $OMEn$ in engines. The findings indicate that the use of $OMEn$ can replace hydrocarbons efficiently and with several advantages, as mentioned in Chapter 1. However, based on the literature review (Chapter 2), there is a scarcity of research focusing on fundamental investigations and detailed chemical kinetics models for $OMEn$. Table 3.2 summarizes the chemical kinetic reaction mechanism for $OMEn$. Furthermore, there are other mechanisms that model the chemical kinetics of $OMEn$ in blends with other fuels [9–12], primarily hydrocarbons such as n-heptane, iso-octane, or natural gas.

Mechanism	Fuel	Reaction mechanism	
		Species	Reactions
Sun 2016 [13]	OME3	274	1674
Sun 2018 [14]	OME1	524	2821
He 2018 [15]	OME1-3	225	1082
Li 2020 [10]	OME3	61	190
Cai 2020 [16]	OME2-4	322	1611
Jacobs 2019 [17]	OME1	530	2889
Niu 2021 [18]	OME1-6	92	389

Table 3.2: An overview of the research on the detailed chemical kinetics model of pure OMEn-type fuels.

In this work, the mechanisms used for OME_1 and OME_{34} were the ones developed by Jacobs et. al [17] and Cai et. al [16], respectively. Nevertheless, the mechanism presented by Niu et al. [18] includes the chemical kinetic to OME_{1-6}, for that reason, was also evaluated in terms of homogeneous reactor and laminar flamelets to compare a full OME_{1-6} fuel and the simplified OME_{34}, as well as to evaluate the performance of both mechanisms for the simplified OME_{34} fuel. These results will be shown in Chapter 4.

In terms of CFD tools, a first straightforward solution to directly integrate chemical reactions into reactive flow simulations consists of solving CFD

transport equations where averaged species source terms are derived directly from chemical kinetics mechanisms. This approach, usually denoted as 'direct chemistry integration', neglects turbulence effects on combustion. However, it can be pretty expensive in computational terms when applied to complex spray flow problems, with many cells to provide an adequate spatial resolution. The effort can be kept under acceptable limits either by mechanism reduction or by pre-tabulation of the chemistry, where look-up tables of the full chemical evolution are stored in terms of mixture fraction and progress variable and are later fed into CFD solver [19]. On the other hand, transport due to convection and diffusion occurs in flames together with chemical reactions, which can be adequately considered through the flamelet approach [7]. In brief, these pre-tabulated combustion models rely on canonical configurations. In the Diesel engine modelling literature, typically zero-dimensional (0D) homogeneous reactors and one-dimensional (1D) non-premixed igniting flamelets are used to tabulate chemistry. Both of them are used in the present work and will be discussed in the following section 3.5

3.4 Chemiluminescence

Luminescence due to chemical excitation is a phenomenon found in combustion processes, giving rise to light-emitting species. Due to its natural occurrence, it offers a useful diagnostic tool for flames and other combustion processes. Over the years, chemiluminescence measurement has gathered attention for its simple, non-intrusive techniques compared to expensive laser measurements. It has been identified that excited species such as OH* and CH* occur within the reaction zone, thereby providing identification of the reaction zone. Predicting chemiluminescent species by modelling their chemical kinetics has yet to be widely practised today. However, sub-mechanisms for these species already exist (chemical reactions and thermodynamic properties may be consulted in Appendix 3.A) [17, 20–23] and could significantly contribute to the characterization of a flame structure. Such contributions would be noteworthy for two main reasons. Firstly, it would be an additional tool to validate combustion models used in Computational Fluid Dynamics (CFD). Secondly, it would enable a more cost-effective approach to understanding the interaction between different species and their roles within a combustion process under different configurations. In hydrocarbon flames, the most used fuel type, the four significant emitters found are OH^*, CH^*, $C2^*$, and CO_2^* [24], here star (*) refers to electronically excited molecules. A typical flame spectrum obtained from hydrocarbon combustion is shown in Figure 3.3

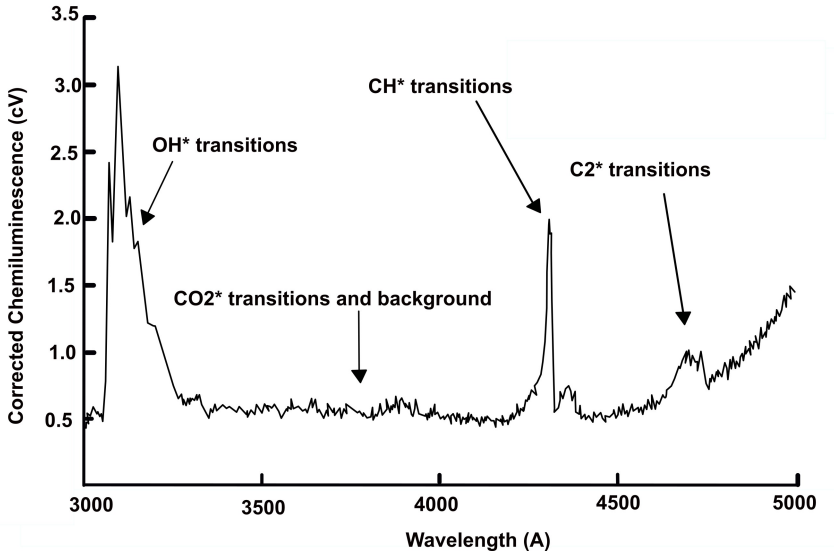

Figure 3.3: Flame spectrum of a hydrocarbon flame, showing the appearance of various excited species at different wavelengths [25].

As is well known from the study of Diesel sprays, which are characteristic of compression ignition engine combustion, soot production is impossible to avoid when it comes to hydrocarbons. Being a black body, soot emits and absorbs radiation across the entire spectrum. This aspect should be considered when analysing the results obtained by optical techniques, particularly those involving chemiluminescence, since the emitted light comes from both sources, excited species and soot, partly coinciding spatially.

Nowadays, several synthetic and renewable fuels are being studied in the decarbonization race. $OMEn$-type is one of the biggest attractions. Due to their oxygenated characteristics, they are non-sooting as it was exposed in Chapter 2, so all the observed radiation will be solely from the chemiluminescent species. For this reason, it is essential to know the spatial distribution of each of them.

In the present work, the main contribution lies in the coupling of the sub-mechanisms of the chemiluminescence species (OH^*, CH^* and $C2^*$), and the species involved in these, in the chemical mechanisms used for $OMEn$-type fuels and also for n-Dodecane [26], (Jacobs et al. [17] already included CH^* and OH^*). The last step was to determine the thermodynamic properties of these species, mainly for C_2^* that was not available in the mechanisms database.

Starting from the fact that the thermodynamic properties of the species in their ground state (OH, CH, C2) are known by the chemical mechanism thermodynamic data as it was stated in Section 3.3, the energy difference ΔE between a base species and its excited species can be quantified using Equation 3.11 [27].

$$\Delta E = \frac{hc}{\lambda} N_A \tag{3.11}$$

where h denotes Planck's constant (6.626 x 10^{-34} $J.s$), c is the speed of light (3 x 10^{8} m/s), λ represent the wavelength of the chemiluminescence transition, and N_A is Avogadro's number (6.022 x 10^{23} mol^{-1}).

This ΔE is represented in the thermodynamic properties through the coefficients of the polynomials. Taking OH and OH^* as an example, if one plots c_p and h as a function of temperature, it will be found that the c_p values for both species coincide, while there is a constant difference in h throughout the temperature range. Since c_p indicates no differences in thermal enthalpy, the difference in h tells that it corresponds to the formation enthalpy required to transition from a ground species to its excited species and vice versa.

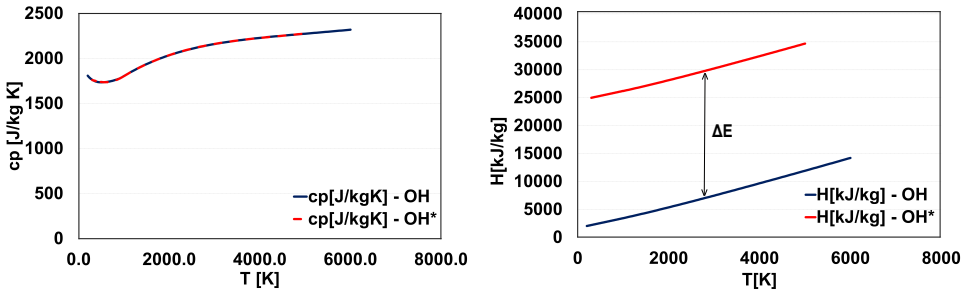

Figure 3.4: Evolution of specific heat and enthalpy of OH and OH^* versus temperature.

In terms of the coefficients of the polynomials represented by equations Equation 3.8, Equation 3.9, the difference between the species is represented by the coefficient a_6. Therefore, by knowing the enthalpy of the ground species (with all coefficients known) and calculating the corresponding ΔE for each species, it is possible to determine the coefficient a_6 of the excited species.

The wavelength used to calculate the ΔE of each species, correspond to 308 nm for OH^* and 401 nm for CH^*. While, due to the emission of C_2^* appearing between 436 nm and 564 nm, bands called Swan bands which are found in the visible region of flame spectra, hence, an average wavelength of 500 nm was used for the calculations [20, 27].

Finally, it is important to note that all the results presented using this tool are qualitative results, because not all precursors of chemiluminescent species have been calibrated as it is recommended in [20].

3.5 Canonical combustion configurations

Simulating reacting flows is a computationally demanding task, primarily because of the numerous thermochemical variables that need to be transported and the computationally expensive evaluation of chemical source terms and transport coefficients. Accurate chemical kinetics representation often necessitates incorporating hundreds of species and reactions, resulting in a significant computational cost. Global mechanisms that simplify the reaction mechanism to only a few species may not adequately capture essential combustion characteristics like two-stage ignition or pollutant formation. As presented in Table 3.2 the selected mechanism in this work also contains a considerable number of species and reactions. In this context, canonical configurations become meaningful and essential, as their computational cost is significantly lower in 0D and 1D simulations while still considering the simplifications compared to the complex phenomena occurring in a multi-species, multiphase, and highly turbulent combustion process.

However, in addition to its low computational cost, its usefulness in generating helpful tabulations for 3D or 2D CFD calculations make these modelling approaches interesting. The outcome of solving these configurations is intriguing in itself, as it allows for the resolution of canonical problem setups to evaluate the effect of chemical mechanisms on the combustion process and the formation of pollutant emissions.

Furthermore, it enables a comprehensive analysis of the process, gradually increasing the complexity of the phenomena encountered by a fuel during its combustion process, starting with a homogeneous reactor (the simplest case), moving on to laminar flamelets (including diffusion), and culminating in CFD simulations (where all transport phenomena are considered in the calculation). Thus allowing for a comprehensive understanding of how the flame structure is modified by introducing new physical elements into the auto-ignition process.

3.5.1 Closed homogeneous reactor

The homogeneous reactor cases involve the ignition of a sequence of independent closed constant-pressure reactors, where the initial conditions are determined based upon an adiabatic mixing process of two streams, namely fuel and air.

The changes in concentrations of chemical species in a homogeneous constant pressure reactor can be effectively modelled by employing the ordinary differential equation (ODE) system based on Equation 3.12, while assuming a constant pressure and enthalpy. A code to resolve the homogeneous reactor configurations was implemented in Python, considering multi-component fuel and using the *Cantera* package [28]. In *Cantera*, a reactor is the most basic representation of a chemically reacting system. It represents an extensive thermodynamic control volume where all state variables are uniformly distributed. The system is typically dynamic, meaning that all states are time-dependent, allowing for transient changes due to chemical reactions. However, it is assumed that thermodynamic equilibrium (but not chemical equilibrium) is maintained throughout the reactor at all times.

$$\frac{\mathrm{d}\rho Y_k}{\mathrm{d}t} = \dot{\omega_k} \tag{3.12}$$

Initial conditions are obtained from the adiabatic mixing between fuel and air streams in a range of equivalence ratios spanning both lean and rich conditions.

The time evolution of the chemical state can be tracked following a characteristic progress variable (Y_c). In the present study, Y_c (Equation 3.13) includes the evolution of three major species (CO_2, H_2O and CO) according to the definition which has been previously used in [29], and also respects the necessary condition of being increasingly monotonous for all the fuels objective of this work.

$$Y_c = 0.75Y_{CO} + Y_{CO_2} + Y_{H_2O} \tag{3.13}$$

Homogeneous reactor calculations show that the relative trends among fuels do not change much with other progress variable definitions, as will be shown in Appendix 4.A.

A version of the normalized progress variable (C) is used according to Equation 3.14.

$$C = \frac{Y_c - Y_c^{inert}}{Y_c^{eq} - Y_c^{inert}} \tag{3.14}$$

where Y_c^{inert} and Y_c^{eq} are the inert and equilibrium values for the progress variable, then C ranges between 0 and 1. Since in the autoignition process, two zones known as low and high temperature are distinguished, the ignition delay

corresponding to each zone is obtained from values of C = 0.1 and C = 0.9, respectively. These zones could be evaluated in terms of the intensity of the chemical source term as derived from the homogeneous reactor simulation for each mechanism. In Figure 3.5 an example of the time evolution of temperature, progress variable and heat release rate for one reactor case at stoichiometric conditions are presented. The chemical activity for the first 0.5 ms it is negligible, hence the time scales start at this timing to improve the clarity during autoignition. After that, there is a slight increase in temperature, and around 0.85 ms there is a first noticeable increase in temperature, corresponding to the low temperature ignition delay. Shortly after that, temperature rises again to reach the final equilibrium value. These two stages are reflected in time evolution of progress variable and heat release rate (HRR), which will be the most evident indicator of chemical activity. Evolution of progress variable and temperature are certainly similar, and for HRR it is possible to distinguish two peaks corresponding to the low and high temperature ignition process, respectively.

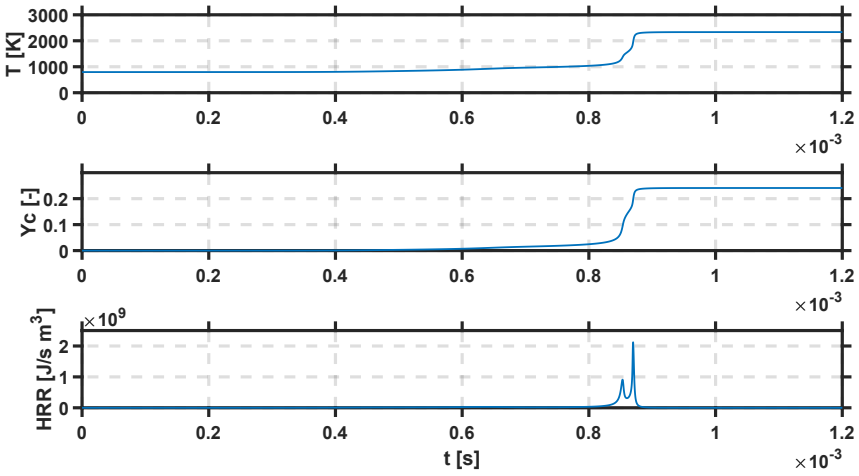

Figure 3.5: Temporal evolution of temperature, progress variable (Yc) and heat release rate (HRR) under homogeneous reactor simulation, for OME_1 with an equivalence ratio: ϕ = 1 and initial temperature = 900K and ambient density 22.8 kg/m^3

3.5.2 Laminar flamelets

Non-premixed flames, also known as diffusion flames, are characterized by diffusion being typically the rate-controlling process; this can be evaluated

using the dimensionless Damköler number (Da), already introduced in Section 2.2 to explain the ID during autoignition process, relates the characteristics chemical time τ_{chem} and the characteristic physical time τ_{physic} and is defined by Equation 3.15. This number proves valuable in general combustion scenarios for assessing the significance of physical phenomena (e.g., mixing) versus chemical processes. For premixed flames, where mixing plays a negligible role, this number approaches 0, but on the opposite, non-premixed flames result in larger values.

$$Da = \frac{\tau_{physic}}{\tau_{chem}} \tag{3.15}$$

The modelling of turbulent diffusion flames has proven to be quite successful, with one of the most commonly applied combustion models being the flamelet approach. Initially introduced by Peters [30], this approach builds upon the earlier ideas of Williams [31], suggesting that a turbulent diffusion flame can be conceptualized as an ensemble of laminar flamelets. The key advantage of the flamelet approach lies in its ability to decouple the complex chemical structure of the flame from flow dynamics, allowing for independent modelling [32]. Hence, a laminar flamelet formulation represents a canonical configuration of diffusion flames in combustion studies.

The flamelet formulation

The fundamental principle of the flamelet approach hinges on transforming variables from physical space to mixture fraction space Z, which describes the spatial and temporal evolution of temperature (T) and species mass fractions (Y_i) in terms of Z. The simplest way to express flame variables as functions of Z is through the Burke-Schumann solution [33], which assumes infinitely fast chemistry and an equilibrium state for all mixture fractions. This simplification reduces the reaction zone to an infinitely thin layer, where the two reactants never coexist. However, real flames exhibit finite reaction rates and non-equilibrium effects. The steady and unsteady formulations of laminar flamelet equations were developed by Peters in 1980 [34] and 1984 [30], respectively, based on local coordinate transformations and boundary layer arguments. Subsequently, Peters proposed a new method [7], a two-scale asymptotic analysis, to re-derive the flamelet equations.

Assuming combustion occurs within a thin layer surrounding the surface of stoichiometric mixture, a local coordinate transformation can be introduced, as depicted in Figure 3.6: the coordinate x_1, perpendicular to the iso-surface of stoichiometric mixture, is replaced by Z, while the remaining coordinates are tangential to that surface.

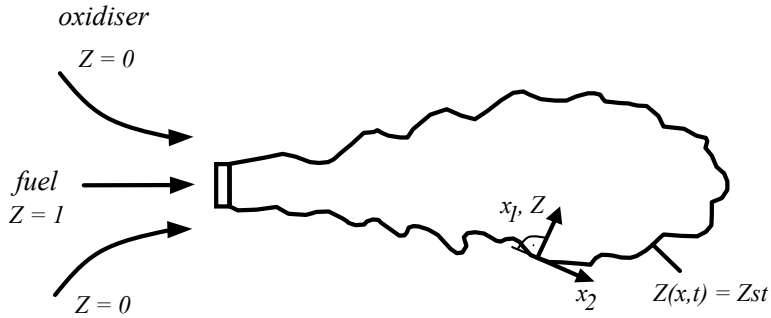

Figure 3.6: Representation of the coordinate transformation, from physical to mixture fraction space in a turbulent jet diffusion flame. Adopted from [35]

If it is assumed that any reactive scalar ψ depends solely on the coordinates (Z, t) in a reactive flow, the application of the coordinate transformation, leading to the formulation of the one-dimensional flamelet equation, Equation 3.16:

$$\frac{\partial \psi}{\partial t} = \frac{\chi}{2}\frac{\partial^2 \psi}{\partial Z^2} + \dot{\omega_k} \tag{3.16}$$

In physical terms, this transformation involves considering minor alterations in the tangent directions to mixture fraction level surfaces in comparison to the normal direction. In Equation 3.16, χ represents the scalar dissipation rate defined by Equation 3.17. It has the dimension of an inverse time and therefore represents the inverse of a flow residence time-scale.

$$\chi = 2D\frac{\partial Z}{\partial x_i}\frac{\partial Z}{\partial x_i} \tag{3.17}$$

χ measures the strength of convection and diffusion in the mixture fraction space, since it is related to the strain rate to which the flame is submitted. This parameter plays a very important role in flamelet models, which appears as a diffusion coefficient in the flamelet equations.

Analytical expressions for the scalar dissipation rate in the counterflow diffusion flame configurations have been derived under simplifying assumptions and can be described by Pitsch et al. [36] (Equation 3.18):

$$\chi(Z) = \chi_{st} f(Z) \tag{3.18}$$

where χ_{st} is the scalar dissipation rate at the stoichiometric mixture fraction Z_{st} and $f(Z)$ represents the scalar dissipation rate distribution profile in mixture fraction space. Two popular and well-established choices are:

- $erfc - profile$: Peters [30] proposed that, for a laminar counterflow diffusion flame with constant density and diffusion coefficients, χ can be described as:

$$\chi(Z) = \frac{SR}{\pi} exp\left\{-2\left[erfc^{-1}(2Z)\right]^2\right\} \tag{3.19}$$

  here, SR represent the strain rate, defined by the velocity gradient at the oxidizer side of the counterflow flamelet.

- $ln-profile$: Pitsch [37] investigated an unsteady, one-dimensional mixing layer with the fuel in the middle and pure oxidizer towards both sides, where the maximum mixture fraction decays over time, and proposed a scalar dissipation rate model:

$$\chi(Z) = -\frac{2Z^2}{t} ln\left(\frac{Z}{Z_R}\right) \tag{3.20}$$

where Z_R is the maximum mixture fraction on the symmetry line, where the strain is zero.

In this thesis, the first profile which is extensively used in the literature, and assumes that χ follows a steady profile is used.

The flamelet solution

The flamelet equation is first examined in the steady state by neglecting the transient term:

$$\frac{\partial^2\psi}{\partial Z^2} = -\frac{2\omega_k}{\chi} \tag{3.21}$$

It is possible to see the reaction rate depends on the scalar dissipation rate, which represents the inverse of the flow residence

- $\chi \to 0$: infinite chemistry and equilibrium, and behave similar to the homogeneous reactor equation 3.12 (at steady state).

- $\chi \to \infty$: Frozen mixing layer, no reaction.

The entire solutions of Equation 3.21 can be described by the so-called S-shaped curve, as it is usually represented temperature against Da, therefore, the curve takes the shape of an inverted S, here, the representation against χ_{st} is used, due to the significance of this parameter in the following turbulence-chemistry interaction approach. An example is presented in Figure 3.7, and it is commonly used to identify the flame states, such as non-reacting and steady burning situation, ignition and extinction limits.

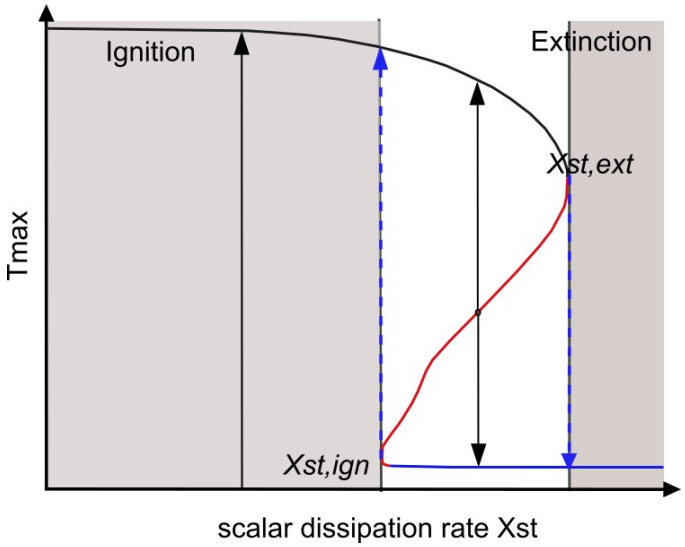

Figure 3.7: S-curve for autoigniting flamelets.

Different branches define the S-curve. At low values of strain or scalar dissipation rate (χ_{st}), a region is characterized wherein the flame transitions from inert conditions to the stable burning branch; this region is termed the auto-ignition range and is bounded by the ignition point at $\chi_{st,ign}$ (black line). The increase of the scalar dissipation rate implies higher diffusion and the eventual flame quenching at a given point along the stable burning branch, identified as the extinction point $\chi_{st,ext}$. A region defined by re-ignition and flame extinction is encompassed between the ignition and extinction points. In this range, the intermediate unstable burning or middle branch is found (red line), characterized by high sensitivity to small strain variations. Slight strain variations will immediately lead to the re-ignition to the stable burning branch or the extinction of the weakly reacting branch, also known as the lower branch (blue line). At even higher strain rates, the flame exhibits no chemical activity.

Once the S-curve is entirely computed, the unsteady or transient solutions are carried out. The auto-ignition region is the interesting one for the present work and would correspond to an unsteady transition, so unsteady solutions for this region are calculated, filling the Z, χ and C space. In the present work, the 1D laminar autoigniting flamelet are calculated using the LFLAM code [38] in the mixture fraction space.

3.6 CFD model implementation

In comparison to the traditional design of spray combustion systems, based on experimental knowledge and simple calculation algorithms, current computational fluid dynamics (CFD) tools have reached a point where it is possible to understand in detail the combustion process and flame structure, guiding the design and development of more efficient and cleaner applications.

CFD is recognized as the scientific discipline that generates quantitative of fluid-flow phenomena, encompassing heat transfer and chemical reactions, through computer-based numerical simulations. This approach is highly esteemed and regarded as powerful because it overcomes many limitations of experimental analysis. By reducing research time and cost, CFD complements experimental findings effectively.

The contribution of CFD is particularly noticeable in the case of liquid spray combustion, as it involves a series of simultaneous processes (spray atomization, dispersion, evaporation, and combustion) that are very difficult to isolate and, therefore, quantify accurately.

3.6.1 Description of the numerical model

Spray calculations in this thesis are carried out with the $CONVERGE$ code [39]. This software has gained broad acceptance within the Internal Combustion Engine (ICE), because of its integrated Adaptive Mesh Refinement (AMR) tool. The AMR tool enables the computational mesh to be adjusted during runtime. This capability of $CONVERGE$ allows for grid refinements based upon velocity, temperature, and fuel mass fraction gradients [39]. Figure 3.8 shows the computational domain generated in $CONVERGE$ where a realistic recreation of the flow field experimented by the free spray can be obtained with the combustion simulation.

The domain is a cylinder that reproduces the inner geometry of the high-pressure high-temperature vessel 102 mm and 140 mm for the SA and SD, respectively, in length and 50 mm in radius. The domain is large enough

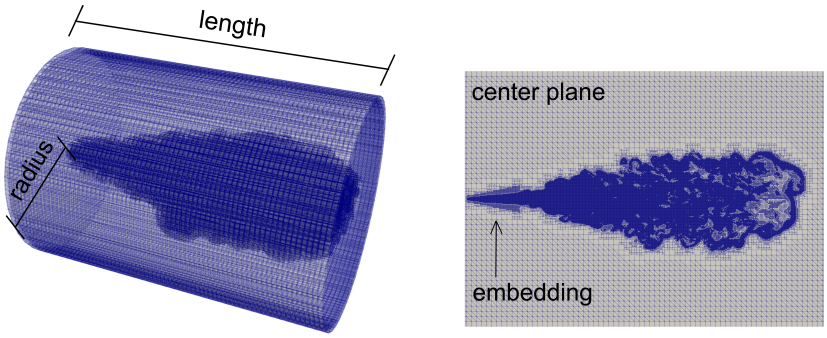

Figure 3.8: Computational domain and mesh details for an LES simulation. The image on the left displays the 3D domain, while the image on the right shows a cut of the central plane, where the work of the AMR and the embedded fixed cone can be observed.

to prevent spray-wall interaction. The base mesh grid is composed of 2 mm cubes, which is generated automatically by $CONVERGE$ cut-cell Cartesian method. Near the nozzle area, grid mesh resolution is added using a truncated cone-shaped fixed embedding. With the AMR a minimum cell size that ranges between 62.5 μm and 125 μm depending on the spray size or turbulence model are reached. Table 3.3 summarizes the mesh set-up characteristics for all the cases considered in that work.

The mesh independence and validation of the RANS spray model have been previously calibrated and optimized by Pachano [40] for the same computational environment, and they have been inherited and utilized in the present work. For LES, the RANS conditions have been taken as a starting point, and following the recommendations from the literature [41–43] for similar setup in $CONVERGE$ CFD solver, given the characteristics of an LES calculation where higher spatial resolution is required compared to RANS, a mesh with the characteristics presented in the Table 3.3 has been used. The mesh independence study with LES framework has achieved this final meshing setup. This study will be presented in the following. It is worth noting that naturally, the gradients found in Spray A, given its nozzle size, are smaller than those of SD, for that reason the mesh for the smaller injector is finer.

$CONVERGE$ code stands out for being based on the finite volume method to solve numerically the classical conservation equations in their integral form in each cell of the domain. The solution procedure is conducted in iterative form using a Pressure Implicit with Splitting of Operators (PISO) algorithm. The spatial discretization of the computational domain is performed with a

		Spray A	Spray D
RANS	base	2 mm	
	min cell size	125 μ m	
	length domain	102 mm	
	embedding level	3	
LES	base	2 mm	
	min cell size	62.5 μ m	125 μ m
	length domain	102 mm	104 mm
	embedding level	4	3

Table 3.3: Configuration of the computational mesh.

second-order central difference scheme, while a first-order implicit scheme was employed for temporal discretization.

Mesh independence study

The grid convergence analysis is conducted for the inert condition of the reference Spray A, the one that requires higher resolution due to its smaller nozzle size, resulting in larger velocity gradients. The recommendations from the literature and the methodology used in RANS have been followed, where the minimum cell size of the mesh for SD is defined to be twice the size of SA, considering the assumption that the flow structures can be scaled by the ratio of change in nozzle diameter [44], so once determined the mesh setup for SA, for SD is immediately obtained. In order to achieve this, global parameters are examined for three meshes with varying minimum cell sizes achieved through AMR. The characteristics of the meshes are summarized in Table 3.4. In all three scenarios, a truncated cone-shaped fixed embedding is employed, with a minor radius of 1 mm, a major radius of 5 mm, and a length of 10 mm. with a base mesh cell size of 2 mm and minimum cell sizes as shows Table 3.4, which align with the mesh configurations employed in the investigation of single-hole nozzle sprays, similar to those examined in this study [42, 43, 45]. The cell size of the embedding region, as well as the minimum cell size, are calculated knowing the base grid and embedding or AMR level using Equation 3.22 [39]. Mesh 0 represents the configuration with the typically smallest cell size employed in this type of studies. As such, it serves as a base or reference configuration, while the other two configurations represent variations achieved by adjusting the cell size either upwards or downwards through the use of Adaptive Mesh Refinement (AMR) levels.

$$scaled\ grid = dx_{base}/2^{grid_{scale}} \tag{3.22}$$

Name	Mesh 0	Mesh 1	Mesh 2
Nozzle		SA	
% O_2		0	
Fuel		C12	
T_{amb} [K]		900	
AMR level	5	4	6
Embedding level	4	3	5
Base grid [mm]		2	
Min. cell size [mm]	0.0625	0.125	0.03125
Nº of processors		144	
CPUh	2.6E4	7.3E3	5.7E4

Table 3.4: Characteristics of the studied meshes tested with the inert nominal condition for n-Dodecane.

Figure 3.9 shows the results for the three meshes regarding vapour penetration, which increase with time as the spray advances in the combustion chamber, and liquid length which reach a steady value after few micro seconds. For vapour penetration, the mesh named "Mesh 1" with a minimum cell size of 125 μm deviates significantly from the experimental penetration within a few microseconds. On the other hand, the other two meshes with cell sizes of 62.5 μm (Mesh 0) and 31.25 μm (Mesh 2) show minor differences. Mesh 0 (blue) slightly over-predicts between 0.1 and 0.5 ms but then closely matches the experimental evolution. The finer mesh (Mesh 2) exhibits better prediction in the initial stage and continues to evolve similarly to the experiment, with only a slight under-prediction at the spray tip.

Regarding liquid length, the trend is similar. The coarser mesh significantly over-predicts this parameter, while Mesh 0 and Mesh 2 are closer, with the finer mesh providing the best prediction for this parameter.

In summary, regarding vapour penetration, there are no significant differences between Mesh 0 and Mesh 2, as both provide acceptable predictions for this parameter. However, for liquid length, there is a clear preference for Mesh 2. Nevertheless, the computational cost of each mesh is shown in Table 3.4, highlighting the significantly higher cost of Mesh 2 due to its smaller cell size. Therefore, considering the same criterion followed throughout this thesis regarding the acceptance of a certain deviation in liquid length it has been decided that, based on the mesh independence study, Mesh 1 is discarded presenting the worst results. Between Mesh 0 and Mesh 2, Mesh 0 is chosen due to its lower computational cost, which is nearly half of that for Mesh 2

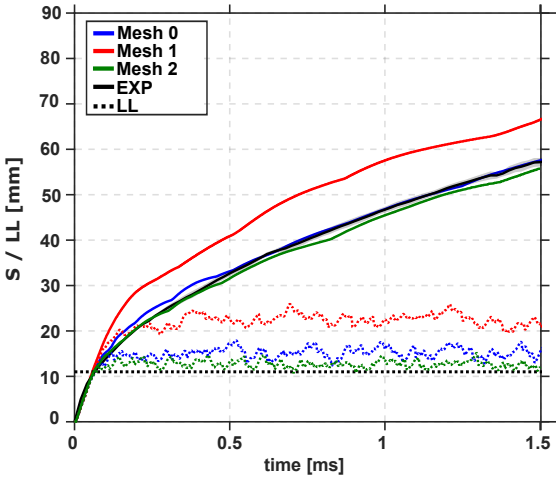

Figure 3.9: Liquid length and vapour penetration for experimental and the 3 different meshed used for simulations under inert nominal conditions for n-Dodecane, for the ECN SA. Results from the finer mesh is represented in blue, coarser in red and the intermediate one in green.

(Table 3.4), while still providing acceptable predicted results. Therefore, its definition is in line with the recommendations provided by different studies. For example, Celik et al. [46] proposes that the cell size (Δ) should be around $25\lambda_k$, where λ_k is the Kolmogorov length scale. Additionally, Pei et al. [47] mention that in SA, λ_k is on the order of 1 to 5 μm. By combining the findings of these two studies and taking an average value of λ_k as 2.5 μm, it can be concluded that for SA, Δ should be 62.5 μm, which coincides with the value used in Mesh 0.

Multiphase modelling

Multiphase modelling is done from a DDM (Discrete-Droplet Method) perspective, where the continuous liquid jet is discretized into 'blobs' or 'parcels', which consist of a number of droplets with the same characteristics, interacting with the gas (Eulerian) phase, in which the mixing and combustion processes occur.

During the injection process, when the fuel is injected into the combustion chamber, it undergoes different processes such as droplet atomization, collisions, drag, and evaporation. As it was phenomenologically explained in Chapter 2, this sequence of events leading to the vaporization of the fuel, ultimately resulting in gas-phase combustion, begins with atomization, which is responsible for breaking the liquid stream into droplets. This process is

caused by instabilities imposed on the liquid surface, mainly based on the linear instability theory proposed by Reitz and Bracco [48]. This break-up of the liquid vein takes a distance called break-up length. Fuel is detected downstream of the break-up length in droplets experiencing drag induced by the relative velocity with the air environment entrained by the spray. They suffer Kelvin-Helmholtz (KH) instabilities as well as Rayleigh-Taylor (RT) instabilities caused by aerodynamic forces. When these forces are higher than the internal forces, which uphold the cohesion of the droplet, specifically, when the Weber number surpasses a critical value, the droplet breaks up.

In terms of modelling, that phenomenon is accounted for by a modified version of the KH-RT model. In this modified KH-RT model, aerodynamic instabilities (i.e., KH waves) are responsible for the primary break-up of the injected liquid blobs (also known as parents). Child drops are created during this process, and the secondary break-up of these drops is modelled by examining the competing effects of the KH and RT mechanisms. In the spray modelling framework, the KH-RT approach has been successfully applied because it is computationally efficient and, at the same time, can provide reasonable agreements with experimental measurements. However, it usually requires extensive calibration for two main reasons. First, due to the semi-empirical nature of the liquid phase sub-models, a priori constants must be quantified, which is usually achieved by comparison with experiments. On the other hand, due to physical and numerical limitations in the description of the near nozzle dense region, a compromise in mesh resolution must be found [49, 50]. Table 3.5 presents the main constant of the model used in this thesis, both in RANS and LES context.

	RANS	**LES**
Number of parcels	2.7e+5	1.5e+6
Fraction of injected mass/parcel	0.05	0.05
Shed factor	1	0.1
KH - Model size constant, B_0	0.61	0.61
KH - Model velocity constant, C_1	0.188	0.188
KH - Model breakup time constant, B_1	5	3
RT - Model breakup time constant, C_I	1	1
RT - Model size constant, C_{RT}	0.1	0.1
Breakup length model	Off	Off
Spray cone angle	15	20

Table 3.5: Configuration of the spray model in CONVERGE for both RANS and LES simulations. Constants for RANS are the ones calibrated by Pachano in [40]. All the results are for an injection duration of 5.0 ms and injected mass of 0.0127 g.

Droplets products of atomization will experiment collisions, which are taken account with the no time counter model proposed by Schmidt and Rutland [51], which is based on techniques used in gas dynamics for Direct Simulation Monte Carlo (DSMC) calculations. It is presented as an alternative to the O'Rourke [52] algorithm since no time counter method involves stochastic (randomly determined) subsampling of the parcels within each cell, and this sampling potentially results in much faster collision calculations. Moreover, the droplet drag coefficient is determined dynamically, accounting for variations in the drop shape. Finally, vaporization is the last event, since the liquid spray is injected into the computational domain and converted from the liquid into gaseous vapour. This phenomenon is modelled using the Frossling correlation [53], with which the rate of droplet size changes over time is determined.

The spray model used to describe and determine the Lagrangian particle transport is coupled through source term of the mass, momentum, and energy transport equation terms with the fluid-phase (Eulerian field).

3.6.2 Equations of fluid motion

The dynamics of the multiphase fluid is governed by the classical Navier-Stokes conservation equations of mass, momentum, and energy. In the case of a combustion process, it involves multiple species reacting through multiple chemical reactions, for that reason it is necessary to add another transport equation, in this case the so-called species transport equation. In order to achieve numerical resolution, the equations are customized to suit the specific problem under investigation. This adaptation process often involves simplifying the equations by disregarding certain terms.

For a turbulent compressible flow, the instantaneous transport equations for mass and momentum can be expressed according to Equation 3.23 and Equation 3.24 respectively, where ρ represents the density, u corresponds to the velocity of the fluid. P is the pressure, μ denotes the viscosity, δ_{ij} represent the Kronecker delta and τ_{ij} reflects the Reynolds stresses of the system ($\tau_{ij} = \rho u_i^{'} u_j^{'}$) which need to be modelled to provide mathematical closure and to account for turbulence effects. S is a source term, i.e. evaporation for the mass conservation equation, mass sources for the momentum equation or spray coupling.

$$\frac{\partial \rho}{\partial t} + \frac{\partial (\rho u_i)}{\partial x_i} = S_{mass} \tag{3.23}$$

$$\begin{aligned}\frac{\partial(\rho u_i)}{\partial t} + \frac{\partial(\rho u_i u_j)}{\partial x_j} &= -\frac{\partial P}{\partial x_i} \\ + \frac{\partial}{\partial x_j}\left[\mu\left(\frac{\partial u_i}{\partial x_j} + \frac{\partial u_j}{\partial x_i}\right) - \frac{2}{3}\mu\frac{\partial u_k}{\partial x_k}\delta_{ij}\right] &+ \frac{\partial \tau_{ij}}{\partial x_i} + S_{mom}\end{aligned} \tag{3.24}$$

In conjunction with this, the expression for compressible energy transport in multi-phase flows, specifically in terms of internal energy, is derived from Equation 3.25.

$$\begin{aligned}\frac{\partial \rho e}{\partial t} + \frac{\partial(\rho u_i e)}{\partial x_j} &= -P\frac{\partial(\rho u_j)}{\partial x_j} \\ + \sigma_{ij}\frac{\partial(\rho u_i)}{\partial x_j} + \frac{\partial}{\partial x_j}\left(K\frac{\partial T}{\partial x_j}\right) &+ \frac{\partial}{\partial x_j}\left(\rho D\sum_k h_k\frac{\partial Y_k}{\partial x_j}\right) + S_e\end{aligned} \tag{3.25}$$

Being e the specific internal energy, σ_{ij} the stress tensor, K denotes the conductivity and T is temperature. In the fourth element on the right-hand side of the Equation 3.25 D correspond to the mass diffusion coefficient, h_k defines the species enthalpy, and Y_k represents the mass fraction of each specie in the cell.

As mentioned earlier, in the study of a combustion process, more than one species are involved, so an additional transport equation for species is defined as shown in Equation 3.26.

$$\frac{\partial \rho_k}{\partial t} + \frac{\partial(\rho_k u_j)}{\partial x_j} = \frac{\partial}{\partial x_j}\left(\rho D\frac{\partial Y_k}{\partial x_j}\right) + S_{mass} \tag{3.26}$$

3.6.3 Turbulence modelling

Turbulence poses a significant challenge in the field of fluid mechanics. In most case studies, the flow regime is turbulent, requiring appropriate turbulence models to approximate real-world results. Turbulence, through a convective and diffusive process, considerably enhances the momentum, energy, and species rate of the mixture [54].

Turbulent flow can be described as three-dimensional, time-dependent, dissipative, and influenced by boundary conditions. Exhibits velocity, pressure, and density fluctuations, often occurring at small scales and high frequencies.

Simulating these fluctuations computationally can be both costly and complex. Hence, the governing equations of the process are manipulated to remove the influence of minor scales, resulting in a simplified set of equations. Nevertheless, these modified equations introduce additional variables and turbulence models that are essential for determining the velocity field and other related variables.

Turbulence models are developed within the computational fluid mechanics framework, where the solution stability and simulation time are crucial parameters.

The primary criteria used to assess different models include: level of description, completeness, cost, and ease of use, range of applicability, and accuracy [55]. Taking these criteria into account, the depiction of turbulent combustion processes can be accomplished through three levels of computations. Figure 3.10 illustrates the three most significant methods used to address turbulence: RANS, LES and DNS.

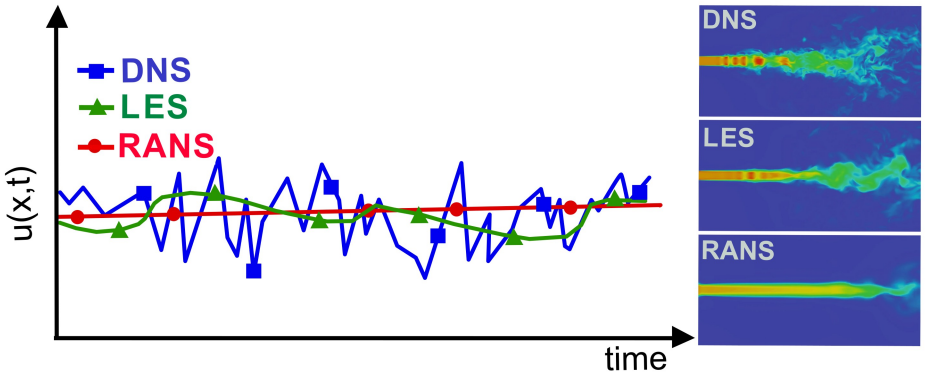

Figure 3.10: A comparison of instantaneous velocities predicted by RANS, LES and DNS turbulence approaches. Time evolution and spatial distribution. Adapted from [56].

- Reynolds Averaged Navier Stokes (or RANS) computations have historically been the first possible approach because the computation of the instantaneous flow field in a turbulent flame was impossible for numerous industrial application due to the computational cost. This approach requires closure rules: a turbulence model to deal with the flow dynamics in combination with a turbulent combustion model to describe chemical species conversion and heat release. From the balance equations of

Reynolds or Favre (i.e. mass-weighted), averaged quantities are obtained by averaging the instantaneous balance equations. Therefore, a RANS calculation does not reproduce a real flow, as mean flow is not able to replicate reality, considering the chaotic nature of combustion and the non-repeatability of events. A simple example case can be represented by the presence of hot spots typically found in industrial devices, which are crucial for design and material selection. A RANS calculation would be unable to detect these isolated hot spots in the domain. However, for well-known and well-defined problems, RANS calculations remain an interesting and reliable option, keeping in mind their limitations.

- The second level of computation corresponds to large eddy simulations (LES). In LES, the turbulent large scales are directly calculated, while smaller ones are modelled using sub-grid closure model, and this approach arises from the fact that at the scale where the sub-grid model is applied, there is only dissipation, which is more universal than turbulence production and therefore easier to model. By filtering the instantaneous balance equations 3.24, the balance equations for large eddy simulations are derived. In combustion problems, LES enables the determination of the instantaneous position of a "large scale" resolved flame front, but a sub-grid model is still necessary to consider the impact of small turbulent scales on combustion. LES is capable of capturing low-frequency variations in any quantity of interest, as Figure 3.10 shows for velocity.

- The third level of computation involves direct numerical simulations (DNS), where the complete set of instantaneous Navier-Stokes equations is solved without any model for turbulent motions. In DNS, all turbulence scales are explicitly resolved, allowing for the accurate capture of their effects on the physical problem. DNS is capable of predicting the precise time variations of temperature, velocity, species mass fraction, etc. (Figure 3.10), similar to how a high-resolution technique would measure them in an experimental setting. To achieve this, the mesh resolution must be selected in a manner that allows for the solution of even the smallest scales, known as Kolmogorov scales. However, it is important to note that this requirement poses a limitation on the method, and it is for that reason that DNS is not extended as RANS or LES.

Figure 3.11 provides an overview of the different turbulent approaches, as depicted in the energy spectrum. The RANS model perform the modelling of spatial frequencies corresponding to eddies of all sizes. In the middle, the LES

scheme resolves the larger turbulent scales above the spatial filter (Δc) and employs sub-grid models to represent the smaller energy eddies. Finally, DNS resolves all turbulent scales without the need for any turbulence model. In this thesis, both the RANS and LES approaches have been utilized for analysis purposes, and they will be discussed in the following sections.

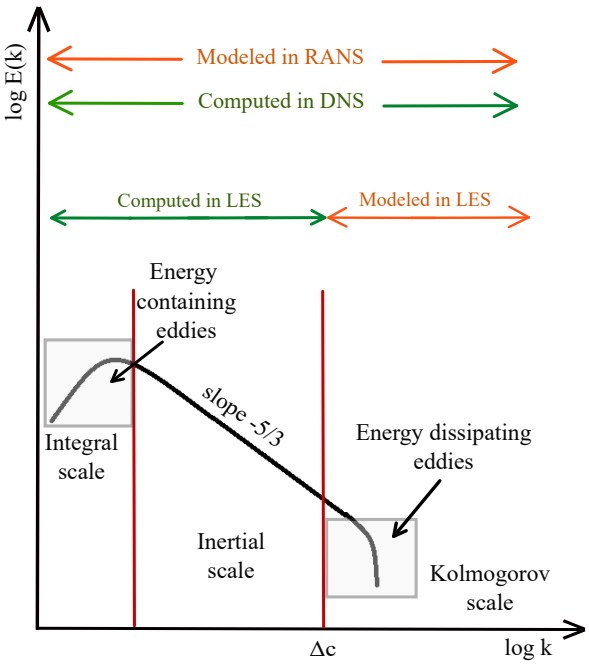

Figure 3.11: Sketch of Kolmogorov energy spectrum for all the approaches to consider turbulence resolution in the flow: RANS, LES and DNS turbulent schemes.

Reynolds Averaged Navier-Stokes approach

The first approach considered in this thesis is the Reynolds Averaged Navier-Stokes (RANS). Within this approach, the turbulent motion inflow that causes significant fluctuation of flow properties (i.e. velocity, pressure, temperature, and even density (if compressible flow) is treated by decomposing the flow properties, such as any velocity component u_i into an average value and a fluctuation component [57]. The equation for turbulence fluctuation is represented in Equation 3.27 where u_i is the instantaneous velocity, $\bar{u_i}$ is the ensemble mean and $u_i^{'}$ the fluctuating component.

$$u_i = \bar{u_i} + u_i^{'} \tag{3.27}$$

The ensemble averaging of the equations introduces an additional term in the classical conservation equation, and is known as Reynolds stresses (τ_{ij}), which account for the impact of turbulence. This is an unclosed term and has to be modelled. In order to determine it, additional transport equations need to be solved in conjunction with the governing Navier-Stokes equations. In this sense, most of combustion studies rely on classical turbulence models originally developed for non-reacting flows, such as the two-equation turbulence model based on the eddy viscosity concept, which are then reformulated in terms of Favre averaging [58]. Among this two-equation models, for Diesel-like spray applications the most used and generally accepted is the $k-\varepsilon$ model, which present several variants, such as the Standard *std* $k-\varepsilon$ and the renormalization group *RNG* $k-\varepsilon$. The former one is the selected model in the present work with $C_{\varepsilon 1} = 1.55$ to account for round jet correction [40, 59, 60].

For all two-equation k-ε models, the turbulence length scale ℓ is expressed in terms of the turbulent kinetic energy (k) and the dissipation rate of this energy (ε) according to Equation 3.28, with C_μ a constant defined by the user.

$$\ell_e = C_\mu^{3/4} \frac{k^{3/2}}{\varepsilon} \tag{3.28}$$

The *std* $k-\varepsilon$ model represents the modelled Reynolds stress as being proportional to the mean rates of deformation, following the proposal by Boussinesq [61] and is expressed as Equation 3.29.

$$\tau_{ij} = -\bar{\rho}\widetilde{u_i^{'}u_j^{'}} = 2\mu_t S_{ij} - \frac{2}{3}\delta_{ij}\left(\rho k + \mu_t \frac{\partial \widetilde{u_i}}{\partial x_i}\right) \tag{3.29}$$

where the tilde denotes the Favre average and the over-bar represents the ensemble mean. The turbulent kinetic energy k is defined as half of the trace of the stress tensor, according to Equation 3.30 and the turbulent viscosity μ_t is given by Equation 3.31. Turbulent mass and energy diffusivities are derived from turbulent viscosities based upon the dimensionless Prandtl and Schmidt numbers (Pr_t, Sc_t).

$$k = \frac{1}{2}\widetilde{u_i^{'}u_i^{'}} \tag{3.30}$$

$$\mu_t = C_\mu \rho \frac{k^2}{\varepsilon} \tag{3.31}$$

While the mean strain rate tensor S_{ij} is expressed by Equation 3.32

$$S_{ij} = \frac{1}{2}\left(\frac{\partial \widetilde{u_i}}{\partial x_j} + \frac{\partial \widetilde{u_j}}{\partial x_i}\right) \tag{3.32}$$

Therefore, two transport equations are established for the turbulent kinetic energy and its dissipation rate in order to calculate the turbulent viscosity and close Equation 3.29.

The turbulent kinetic energy transport equation is given by Equation 3.33

$$\frac{\partial \rho k}{\partial t} + \frac{\partial (\rho u_i k)}{\partial x_i} = \tau_{ij}\frac{\partial u_i}{\partial x_j} + \frac{\partial}{\partial x_j}\left(\frac{\mu + \mu_t}{Pr_k}\frac{\partial k}{\partial x_j}\right) - \rho\varepsilon + \frac{C_s}{1.5}S_s \tag{3.33}$$

While the transport equation for the kinetic energy dissipation (ε) is described in Equation 3.34

$$\begin{aligned}\frac{\partial \rho\varepsilon}{\partial t} + \frac{\partial (\rho u_i \varepsilon)}{\partial x_i} &= \frac{\partial}{\partial x_j}\left(\frac{\mu + \mu_t}{Pr_\varepsilon}\frac{\partial \varepsilon}{\partial x_j}\right) + C_{\varepsilon 3}\rho\varepsilon\frac{\partial u_i}{\partial x_i} \\ &+ \left(C_{\varepsilon 1}\frac{\partial u_i}{\partial x_j}\tau_{ij} - C_{\varepsilon 2}\rho\varepsilon + C_s S_s\right)\frac{\varepsilon}{k} + S\end{aligned} \tag{3.34}$$

In the given equation, S represents the user-supplied source term, while Ss represents the source term that represents interactions with the discrete phase (spray). The $C_{\varepsilon i}$ terms are model constants that consider compression and expansion effects [39].

The standard values for the model constants employed in this work, are listed in Table 3.6.

RANS std k-ε model					
C_μ	$C_{\varepsilon 1}$	$C_{\varepsilon 2}$	$C_{\varepsilon 3}$	$1/Pr_k$	$1/Pr_\varepsilon$
0.09	1.55	1.92	0	1	0.77

Table 3.6: Values of constants of the k-ε model, adopted from [40].

In the context of RANS framework simulations, results are adequate when trying to predict global phenomena such as evaporation, mixture preparation or heat release rate. But for highly local phenomena such as lift-off or the need

to predict typical intermittency in a combustion process, the prediction of an average flow or mixture field within sprays is not accurate enough. In that sense, and considering the purpose of this thesis, LES calculations have been done to go deeper in the analysis and using as a start point RANS results in order to optimize the matrix calculation and computational resources.

Large Eddies Simulations approach

The non-isotropic nature and intricate behaviour of eddies increase as their size grows larger. Larger eddies derive their kinetic energy from the overall fluid energy, containing a significant portion of the turbulent kinetic energy (80%). They transfer kinetic energy to smaller eddies through stretching and breaking, a process known as "cascading" Additionally, larger eddies play a crucial role in diffusive processes involving mass, momentum, and energy. Consequently, simulating large eddies is highly desirable. On the other hand, smaller eddies acquire kinetic energy from larger eddies and transfer it back to the fluid through viscous shear. In high Reynolds number flows, the small-scale turbulent eddies exhibit statistical isotropy. This characteristic makes them "more universal" and less dependent on boundary conditions and mean flow velocity compared to larger eddies. Therefore, simulating smaller eddies is also desirable [56].

LES models have been developed for several decades to capture these important eddy features. LES resolves integral and Taylor eddies up to a user- or mesh-defined minimum eddy size Δ. In this context, the scale Δ plays a critical role as it determines the minimum size at which eddies will be resolved, effectively acting as a filter for the sub-grid scale (SGS). Eddies smaller than Δ are modelled within the SGS model. And this is crucial, since the SGS model allows for the decay of turbulent kinetic energy at the appropriate spatial locations within the turbulent flow [62].

These characteristics of the LES approach are reflected when compared with RANS in how the fields are decomposed for modelling or resolving in the case of LES. As discussed in Section 3.6.3, RANS models decompose the field into a set average and a fluctuating component. On the contrary, in LES cases the field is decomposed into a resolved field and a sub-grid field [63], this can be represented also by Equation 3.27 considering the resolved component of the velocity as $\overline{u_i}$ and the sub-grid or modelled velocity as $u_i^{'}$. In contrast to the RANS approach, where the mean velocity field is obtained through an ensemble average of the mean velocity field, here, the velocity field that is resolved can be characterized as a spatial average of the actual velocity field.

Subsequently, when incorporating the LES decomposition into the traditional momentum conservation equation, the resulting expression is presented in Equation 3.35. In this scenario, the filtered parameters are indicated by the use of over-bars. The stress tensor σ_{ij} and τ_{ij} are given by Equation 3.36 and Equation 3.37 respectively.

$$\frac{\partial(\overline{\rho}\tilde{u}_i)}{\partial t} + \frac{\partial(\overline{\rho}\tilde{u}_i\tilde{u}_j)}{\partial x_j} = -\frac{\partial \overline{P}}{\partial x_i} + \frac{\partial \bar{\sigma}_{ij}}{\partial x_j} - \frac{\partial \tau_{ij}}{\partial x_j} \tag{3.35}$$

$$\overline{\sigma_{ij}} = \mu\left(\frac{\partial \widetilde{u_i}}{\partial x_j} + \frac{\partial \widetilde{u_j}}{\partial x_i}\right) - \frac{2}{3}\mu\frac{\partial \widetilde{u_k}}{\partial x_i}\delta_{ij} \tag{3.36}$$

$$\tau_{ij} = \overline{\rho}(\widetilde{u_i u_j} - \widetilde{u_i}\widetilde{u_j}) \tag{3.37}$$

The main focus of most LES models is to address the modelling of the sub-grid stress tensor τ_{ij}. To address this, in the context of the present work, a One-equation model, particularly the *Dynamic Structure* have been selected due to its successful application in Diesel spray calculations [64–67]. This model, deviates from using turbulent viscosity to represent the sub-grid stress tensor [68]. In order to maintain a balance in the energy transfer between the resolved and sub-grid scales, the model introduces a transport equation (represented by Equation 3.38) for the sub-grid kinetic energy.

$$\frac{\partial k}{\partial t} + \overline{u_i}\frac{\partial k}{\partial x_i} = -\tau_{ij}\frac{\partial \overline{u_i}}{\partial x_j} - \varepsilon + \frac{\partial}{\partial x_i}\left(\frac{\nu_t}{\sigma_k}\frac{\partial k}{\partial x_i}\right) \tag{3.38}$$

To that end, the sub-grid stress tensor models must be a function of the sub-grid turbulent kinetic energy. The modelled stress tensors, as in other models, are written for two filters, for Δ named *grid* level kinetic energy:

$$\tau_{ij} = c_{ij}k \tag{3.39}$$

and assuming that c_{ij} which are the elements of a tensor that has to be determined, does not change with the filter size, for the second filter Δ_2 states:

$$T_{ij} = c_{ij}K \tag{3.40}$$

where the K states for the *test* level kinetic energy. The *grid* and *test* level kinetic energies are related by the trace of the Leonard, hence, no additional

transport equation for K is required. Substituting these models for the two stress tensors into the Germano' identity, the following expression is established:

$$L_{ij} = T_{ij} - \widehat{\tau_{ij}} = c_{ij}K - \widehat{c_{ij}k} \tag{3.41}$$

This yields a set of six Fredholm integral equations of the second kind, given the symmetry of the stress tensor, which can be resolved through an iterative process. Alternatively, in an algebraic way, the tensor coefficient is eliminated from the integral, and the equation is solved directly for τ_{ij}. Consequently, the model for the sub-grid tensor is represented as:

$$\tau_{ij} = 2k\left(\frac{L_{ij}}{L_{ii}}\right) \tag{3.42}$$

In CFD simulations, the spatial filter of a LES model, which determines the scale of the largest eddies to be resolved, is directly linked to the size of the computational mesh by the following expression:

$$\Delta = \sqrt[3]{Vol} \tag{3.43}$$

where, Δ is the grid filter and Vol the cell volume.

Hence, the cells in the computational domain must be sufficiently small to resolve a significant amount of energy. This poses a significant challenge for the LES approach, as it is the case of a spray flow in a combustion process where the mesh used typically consists of millions of cells required to provide sufficient spatial resolution, leading to a substantial computational power requirement.

LES quality criteria

After conducting the mesh independence analysis and introduce the turbulence modelling, in order to continue with the numerical assessment of the model, it is necessary to perform an analysis of the quality of the LES calculations. This involves determining the percentage of turbulent flow energy that is resolved and modelled due to the spatial filtering associated with the sub-grid scales. The grid resolution is a crucial factor to take into account as it impacts not only the numerical discretization error but also the contribution of the sub-grid scale model, as mentioned earlier. A good LES approaches DNS, with a spatial resolution that tends to resolve the smallest scales, such as the Kolmogorov scales. To ensure sufficient resolution of the turbulent flow energy and accurate LES results, the application of these sub-grid models

necessitates a quality assessment [69–71]. Several authors have defined quality indexes to quantify the reliability of the implemented LES model, considering both numerical and model accuracy [46, 55, 71]. Following Pope's criterion, which is based on turbulent kinetic energy, it is established that the acceptable limit for a good LES is that the modelled kinetic energy should be around 20% or less of the total kinetic energy, which includes both modelled and resolved components. However, to apply this criterion, it is necessary (as recommended by [72]) to have temporal averaging as well as averaging across multiple realizations, given the intrinsic unsteadiness of the simulated spray combustion process. However, this is not feasible due to the computational cost associated with such calculations, which require a very fine grid resolution, as demonstrated in the mesh independence study. Another widely used criterion is the one proposed by Celik et al. [46], based on viscosity. Just like Martínez [73] has proposed, to deal with transient and stationary components consistently, the Celik et al. criterion will be used in this study to evaluate the quality of the LES. The Celik et al. quality index serves as a verification index for sufficient resolution but not as a validation index, as the latter requires a comparison with DNS calculations or experiments, as Celik et al. establishes in his work. Therefore, this index evaluates, according to Equation 3.44, the relative contribution of laminar viscosity, sub-grid viscosity, and numerical viscosity. The authors suggest that for the quality of the LES simulation to be acceptable, this index should fall between 0.75 and 0.85, indicating that at least 75% of the turbulent kinetic energy has been resolved.

$$IQ_\nu = \frac{1}{1 + \alpha_\nu(\frac{\nu_{sgs}+\nu+\nu_{num}}{\nu})^n} \tag{3.44}$$

where ν denotes the laminar viscosity, ν_{num} is the numerical viscosity associated with the numerical error and considered equal to ν_{sgs} [46, 74], and the constants α_ν and n are obtained from the outcomes of a DNS calculation [74].

The criterion has been applied to both inert and reactive calculations and for SA and SD, considering their differences in mesh size. In this section, the results of the reactive calculations will be presented, as they are the most critical and extensively used for analysis, aligning with the objectives of this study, which focus on the combustion process.

Figure 3.12 displays the results of the viscosity-based quality index for SA and SD, respectively. In both cases, the time evolution of the parameter is depicted for OME_1 in the 2D field of the spray's central plane. In both configurations, the quality index reaches the values stipulated by Celik et al. to meet the condition of a good LES, resolving 75% or more of the turbulent energy.

Emphasizing that, for the SD, where lower gradients are experienced due to its larger nozzle size, the quality index values throughout the spray are very high. In contrast, in the SA with higher gradients, despite its smaller cell size (Table 3.3), there are points close to or equal to the minimum accepted value. Nevertheless, the area occupied by these lower values is minimal compared to the rest of the domain.

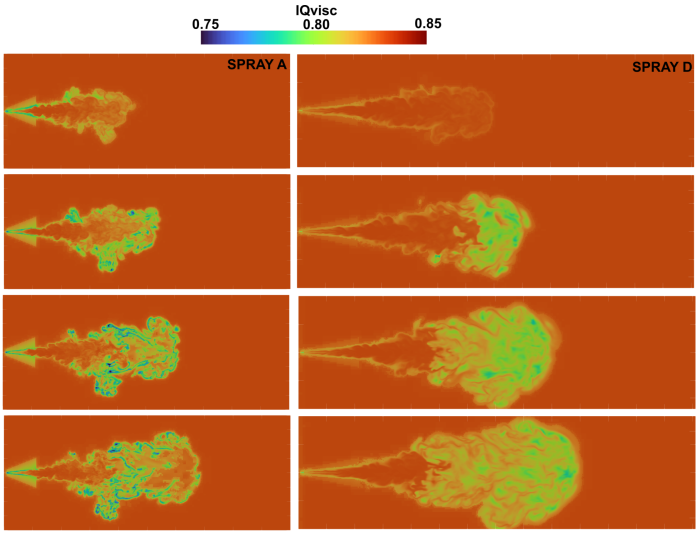

Figure 3.12: LES quality assessment using an index based on the viscosity evaluated in several time-steps for ECN SA (left) and SD (right) under reactive nominal condition for OME_1.

3.6.4 Turbulence chemistry interaction

Combustion is a complex process involves the interaction of multiple chemical species and reactions occurring at different time and length scales. Turbulence affects the mixing of fuel and oxidizer, which in turn influences the reaction rates and heat release. Ergo, in CFD combustion simulations, the turbulence-chemistry interaction plays a crucial role and has to be considered, which can be done in several ways. One of this is based on Conditional Momentum Closure [75, 76], which is based upon the observation that a significant correlation exists between reactive scalars and mixture fraction, and equations are solved using conditional averaging. However, even in cases involving direct chemistry interaction, it poses a high computational cost. Another way is using Probability Density Function (PDF) methods. Are powerful approaches and today widely adopted in combustion modelling. In these methods, transport

equations for joint scalar or joint velocity-scalar PDF are solved. The main advantage of PDF methods is that the chemical source term appears in closed form, and thus no modelling is required [77]. However, they are also computationally expensive to enable properly description of the mixing process. A second way to use PDF to build a numerical model is to presume the PDF shape through the information from available quantities, such as mean and variance of mixture fraction and scalar dissipation rate [8]. The main advantage of presumed PDF approaches is their relatively low computational effort, since the PDF shape is known a priori and does not have to be transported over the whole simulation run.

In this thesis, the Unsteady Flamelet Progress Variable (UFPV) combustion model has been used, it relies on a presumed PDF method to address the turbulence-chemical interaction for its implementation. This approach is based upon the description of a turbulent flame as a set of strained laminar counterflow flamelets. In various theses preceding this one from the same research group, more details regarding its implementation [66, 78] and/or application [40, 79] can be found. The general workflow presented in Figure 3.13 starts with an external tabulation of a laminar flamelet table or manifold, which is done offline. The temporal evolution of the chemical reactions is represented by the progress variable Y_C, with the same definition as shown above for both closed homogeneous reactors and flamelets. The time evolution in the flamelet is re-parametrized from a temporal basis to a normalized progress variable basis (Equation 3.14).

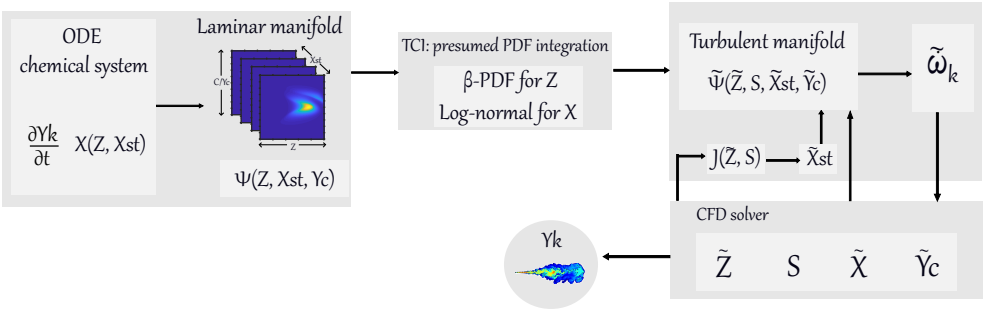

Figure 3.13: UFPV model workflow.

After laminar flamelets have been calculated, the influence of turbulence is accounted for to produce a turbulent manifold, i.e. a set of tables or manifold that are used interactively during the CFD calculation. The turbulence chemistry interaction is taken into account by considering that the mixture fraction and the scalar dissipation rate are statistical independent, using a

presumed PDF approach for these two variables. On the one hand, a β-PDF function is used for the mixture fraction, which is defined by the mean value of mixture fraction ($\tilde{Z}$) and the corresponding variance $\widetilde{Z''^2}$. This implies that a function $P_Z(Z, \tilde{Z}, S)$ exists, with the segregation factor S, which normalizes the mixture fraction variance according to the Equation 3.45.

$$S = \frac{\widetilde{Z''^2}}{\tilde{Z}(1-\tilde{Z})} \tag{3.45}$$

On the other hand, a log-normal function with $\sigma = \sqrt{2}$ is used for the scalar dissipation rate, according to $P_\chi = (\chi_{st}, \widetilde{\chi_{st}}, \sigma)$. This means that the mean value of the scalar dissipation rate $\tilde{\chi}$ can be obtained by the expression presented in Equation 3.46.

$$\widetilde{\chi} = \left(\int_0^\infty \chi_{st} P_\chi \left(\chi_{st}; \widetilde{\chi_{st}}, \sigma\right) d\chi_{st} \right) \left(\frac{1}{F(Z_{st})} \int_0^Z F(Z) P_Z(Z; \widetilde{Z}, S) \right) = \widetilde{\chi}_{st} J(\widetilde{Z}, S) \tag{3.46}$$

where J relates $\widetilde{\chi_{st}}$ and $\tilde{\chi}$, the former one used to parametrize the flamelet manifold, while the latter one is retrieved from the CFD calculation following Equation 3.47

$$\tilde{\chi} = C_\chi \frac{\varepsilon}{k} \widetilde{Z''^2} \tag{3.47}$$

Turbulent-averaged values of any variable ($\tilde{\psi}$) can be obtained according to Equation 3.48.

$$\tilde{\psi}(\tilde{Z}, S, \widetilde{\chi_{st}}, \tilde{t}) = \int_0^\infty \int_0^Z \psi(Z, \chi_{st}, \tilde{t}) P_Z(Z, \tilde{Z}, S) P_\chi(\chi_{st}, \widetilde{\chi_{st}}, \sigma)\, dZ\, d\chi_{st} \tag{3.48}$$

In particular, the turbulent manifold stores turbulent-averaged values of relevant 'k' species in terms of average and variance of mixture fraction, average stoichiometric scalar dissipation rate and average normalized progress variable, i.e. $\tilde{Y_k} = \tilde{Y_k}(\tilde{Z}, S, \widetilde{\chi_{st}}, \tilde{c})$ using the formulation presented in Equation.3.48. The lookup tables that compose the turbulent manifold are discretized with 51 points in $\tilde{c}$, 27 points in $\widetilde{\chi_{st}}$, 41 points in $\tilde{Z}$ and 17 points in S.

The coupling of UFPV and the CFD solver is performed by means of the chemical source term of the transport equation of any k species, which are

a reduced number of the total number of species presented on the detailed chemical mechanism, according to Equation 3.49.

$$\tilde{\dot{\omega}}_k = \frac{\tilde{Y_k^{tab}}(\tilde{Z}, S, \tilde{\chi_{st}}, \tilde{Y}_c(t+\Delta t)) - \tilde{Y_k}^{cell}(t)}{\Delta t} \tag{3.49}$$

where Δt is the CFD time-step, the species mass fraction at the cell is represented by $\tilde{Y_k}^{cell}$ and $\tilde{Y_k}^{tab}$ is the species mass fraction tabulated in the next time step, for which $\tilde{Y}_c(t+\Delta t)$ is calculated according to Equation 3.50.

$$Y_c(t+\Delta t) = \tilde{Y}_c(t) + \tilde{\dot{\omega}}_{Y_c}(\tilde{Z}, S, \tilde{\chi_{st}}, \tilde{Y}_c(t))\Delta t \tag{3.50}$$

To reduce the computational cost, as it was mentioned, only a reduced number of the species in the chemical mechanism are transported by the CFD solver [80–82]. Some sink species are selected following the method presented in [83] to close the atomic mass balance, as well as to keep similar mixture thermophysical properties. Detailed information and description regarding the methodology and accuracy of the selection of this sink species will be explained in the following lines.

As a final remark about the TCI model, it is important to mentioned that considering that chemical reactions occur where species are mixed at the molecular level, implying that combustion takes place at smaller scales of the flow, LES does not resolve the chemical source terms, but rather models them entirely. In this sense, both LES and RANS can use exactly the same combustion model.

Dummies species

While other approaches (e.g., FGM [84]) transport an equation for the progress variable, the structure of the CFD code here does not allow it. Instead, a limited number of species, referred to as "tabulated" or "transported" (9 or 10 in the present work, depending on the fuel if it is single-component or multi-component, as is the case of $OMEn$ in this work, composed by OME_3 and OME_4), are transported. Some of these species are used to reconstruct the progress variable and enter the tables. In this code, the transported species are: O_2, CO_2, CO, H_2O, OH, CH_2O, $FUEL$, H and C_2H_2. An exception is done when chemiluminescent species are included and increase the number of transported species, as stated in Section 3.4.

As the tables are generated with the detailed mechanism, it is necessary to compensate for the lack of species, which would impact the atomic balance (and consequently, the molecular weight of the mixture and density) and the local thermochemical properties (specific heat capacity, formation enthalpy). To address this, certain species must be selected that fully close the atomic balance of C, H, and O while providing reasonable thermochemical properties. These are the "reconstructed" species (as they do not come from a transport equation) or "dummy" species.

The starting point for reconstruction is always the C, H, O balance, hence, 3 species that close the balance are selected. For H, H_2 is used, and for O, O_2 is used (for more details refer to works by Winklinger [78], or Pérez-Sanchez [66]). For C, a species dependent on the fuel and mechanism is sought. It is logical to choose the one that has the greatest contribution to the mass balance, formation enthalpy, and specific heat capacity [85].

For the analysis presented below, it is important to remember that what is commonly referred to as $OMEx$ in this section is a mixture composed of OME_3 and OME_4, whose mass fractions will be used in the following reconstructed equations. More details about the $OMEx$ blend composition could be found in the following Chapter 4.

According to the previous discussion, the analysis is presented in detail in this section for $OMEx$. In the second one, the result obtained with this substitution is analysed for both fuels. This analysis has been done with the *Cantera* chemical kinetics code [28] both fuels, $OMEx$ and OME_1 using *Cai* and *Jacobs* mechanism respectively, through homogeneous constant pressure adiabatic reactor simulations, which start from an adiabatic mixing state and react until equilibrium for a number of equivalence ratio situations. The main goal is the comparison of a fully detailed mechanism solution to that obtained only with a limited number of such species present (the so-called "tabulated" species) and introducing three additional species to complete the mass and energy balance (i.e. "reconstructed" or "dummy" species). This simplified context will help evaluate the methodology used in the UFPV model when reducing the number of transported species.

The first step to define the reconstructed species is to quantitatively evaluate the differences in mass fraction, enthalpy of formation and total enthalpy between these two cases, namely using all the species and using only the tabulated species, without reconstructed species. Figure 3.14 shows the results of using the two cases mentioned above. In the case of the evaluation of mass, when all the species are considered, the addition of all mass fractions is equal to 1. In the other cases, a lower than one solution is obtained, meaning that

a residual is obtained due to the species that are not considered. In order to represent the different situations that appear in spray combustion, this analysis was done to three different equivalence ratio conditions, namely $\phi = 0.5$, 1 and 2; only the figures corresponding to the case of $\phi = 1$ will be presented. A similar situation is observed on the right plot for the enthalpy of formation, with the blue line corresponding to the case with the detailed mechanism and the other one to the case where only tabulated species are considered.

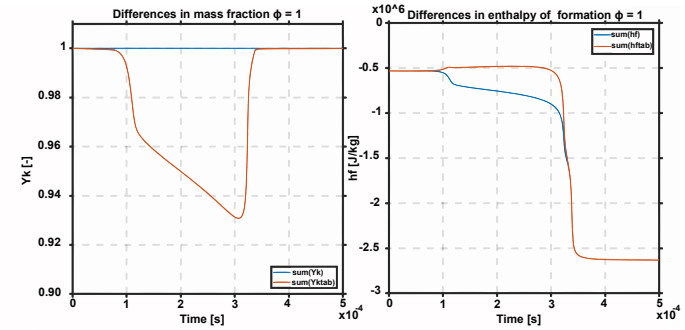

Figure 3.14: Differences in the summation of mass fractions (left) and enthalpies of formation (right) between a homogeneous reactor solution when using all species in the mechanism (blue line) or only tabulated species (orange line).

Once visualized the difference between working with all the species present in the chemical mechanism and only with the selected ones, the next step to take is to identify for each ϕ condition and for each instant of time, which of all the non-tabulated species has the higher contribution regarding mass and energy, so that it will be used to compensate mass and energy unbalances.

ϕ	Candidate species found					
0.5	$CH_3OCH_2OCH_2OCHO$	H_2O_2	HOCHO	CH4	HO2	O
1	$CH_3OCH_2OCH_2OCHO$	HOCHO	CH_4	H_2	O	
2	OME3XKET1X3	$CH_3OCH_2OCH_2OCHO$	HOCHO	CH_4	H_2	

Table 3.7: Summary of the candidate species to be used for reconstruction.

Table 3.7 shows the species with the highest influence on the mass and energy residual along the reactor time evolution; most species coincide in the three proposed ϕ conditions. However, to see the impact of each species on the total mass fraction residual, on the enthalpy of formation and on the sensible enthalpy (the latter represented by the specific heat Cp), representative plots of this effect are made in Figure 3.15.

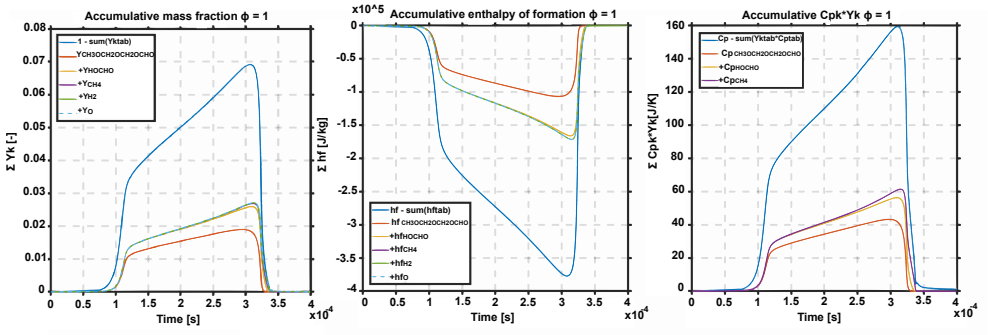

Figure 3.15: Contribution of each of the candidate species to the residuals of mass fraction (left), enthalpy of formation (centre) and cp (right). Plots show the total residual (blue line) as well as the major contributing species in cumulative terms, i.e. the individual contribution of the species is the distance between the corresponding line and the previous one.

As mentioned above, the study starts from the difference between working with all the species of the chemical mechanism and with only the tabulated species. Therefore, in Figure 3.15 is possible to see the mass, enthalpy of formation and Cp in cumulative terms. That means starting from the species with the most weight by mass and gradually accumulating its mass and enthalpies in descending order. As a reference, the blue line shows the total residual for each of the three cases when comparing the total of the species and only the tabulated species.

From the Figure 3.15 it follows that the candidate specie to use in the reconstruction of Carbon atomic mass, due to the high impact on the cumulative terms (mass, enthalpy of formation and Cp) are:

1. $CH_3OCH_2OCH_2OCHO$
2. $HOCHO$
3. CH_4

In that order of relevance, it is essential to note that there are four other species (H_2O_2, HO_2, O and H_2) appearing in the analysis. However, they do not have Carbon in their molecules, so they are discarded because the carbon element balance cannot be closed with them.

With the candidate species identified, the following equations (3.51, 3.52, 3.53) have been used to reconstruct and evaluate the most accurate species

to obtain the temperature. For Carbon reconstruction a general specie "Y_{RC}" composed by m number of carbon atoms, n of oxygen atoms and p hydrogen atoms, and corresponds to any of the three species selected before ($CH_3OCH_2OCH_2OCHO$, $HOCHO$, CH_4).

$$\begin{aligned} C_{reconstruct} = Y_{RC} = &- \frac{MW_{RC}}{2}\left[5\left(\frac{-Y_{fuel}^{OME3}\times Z - Y_{OME3}}{MW_{OME3}}\right)\right. \\ &- 6\left(\frac{Y_{fuel}^{OME4}\times Z - Y_{OME4}}{MW_{OME4}}\right) + \frac{Y_{CH2O}}{MW_{CH2O}} \\ &\left. + 2\frac{Y_{C2H2}}{MW_{C2H2}} + \frac{Y_{CO}}{MW_{CO}} + \frac{Y_{CO2}}{MW_{CO2}}\right] \end{aligned} \tag{3.51}$$

$$\begin{aligned} H_{2reconstruct} = &- \frac{MW_{H_2}}{2}\left[12\left(\frac{-Y_{fuel}^{OME3}\times Z - Y_{OME3}}{MW_{OME3}}\right)\right. \\ &- 14\left(\frac{Y_{fuel}^{OME4}\times Z - Y_{OME4}}{MW_{OME4}}\right) + 2\frac{Y_{H2O}}{MW_{H2O}} \\ &\left. + \frac{Y_H}{MW_H} + 2\frac{Y_{CH2O}}{MW_{CH2O}} + 2\frac{Y_{C2H2}}{MW_{C2H2}} + \frac{Y_{OH}}{MW_{OH}} + p\frac{Y_{RC}}{MW_{RC}}\right] \end{aligned} \tag{3.52}$$

$$\begin{aligned} O_{2reconstruct} = &- \frac{MW_{O_2}}{2}\left[4\left(\frac{-Y_{fuel}^{OME3}\times Z - Y_{OME3}}{MW_{OME3}}\right)\right. \\ &- 5\left(\frac{Y_{fuel}^{OME4}\times Z - Y_{OME4}}{MW_{OME4}}\right) + \frac{Y_{CH2O}}{MW_{CH2O}} + \frac{Y_{H2O}}{MW_{H2O}} \\ &\left. + \frac{Y_{CO}}{MW_{CO}} + 2\frac{Y_{CO2}}{MW_{CO2}} + \frac{Y_{OH}}{MW_{OH}} + n\frac{Y_{RC}}{MW_{RC}}\right] + (1-Z)Y_{O2\text{inf}} \end{aligned} \tag{3.53}$$

To evaluate the impact of the new 'dummy' species, after the reconstruction, three different scenarios are compared:

- Transporting all the species: $\sum Y_k = 1$

- Transporting only 10 tabulated species: $\sum Y_{k_{tab}} < 1$
- Transporting these 10 species and 3 reconstruct species: $\sum Y_{k_{tab+rec}} < 1$

Then, imposing the same thermodynamic state (h, P) defined by the first scenario where all species present in the mechanism are considered and the three respective compositions, it is possible to compare the true temperature (first case) to the other two simplified scenarios.

To conclude this section and evaluate the proposed methodology, from Figure 3.16 it follows that the first candidate $CH_3OCH_2OCH_2OCHO$ is which can reproduce the correct temperature evolution for the three different equivalent ratio studied. It is clear that using this species, the temperature is practically the same as using all the species present in the mechanism, capturing the low-temperature zone correctly. Regarding the other two dummy species under study, on the one hand, $HOCHO$ over-predicts the low-temperature zone; on the other hand, CH_4 cannot represent this problematic zone.

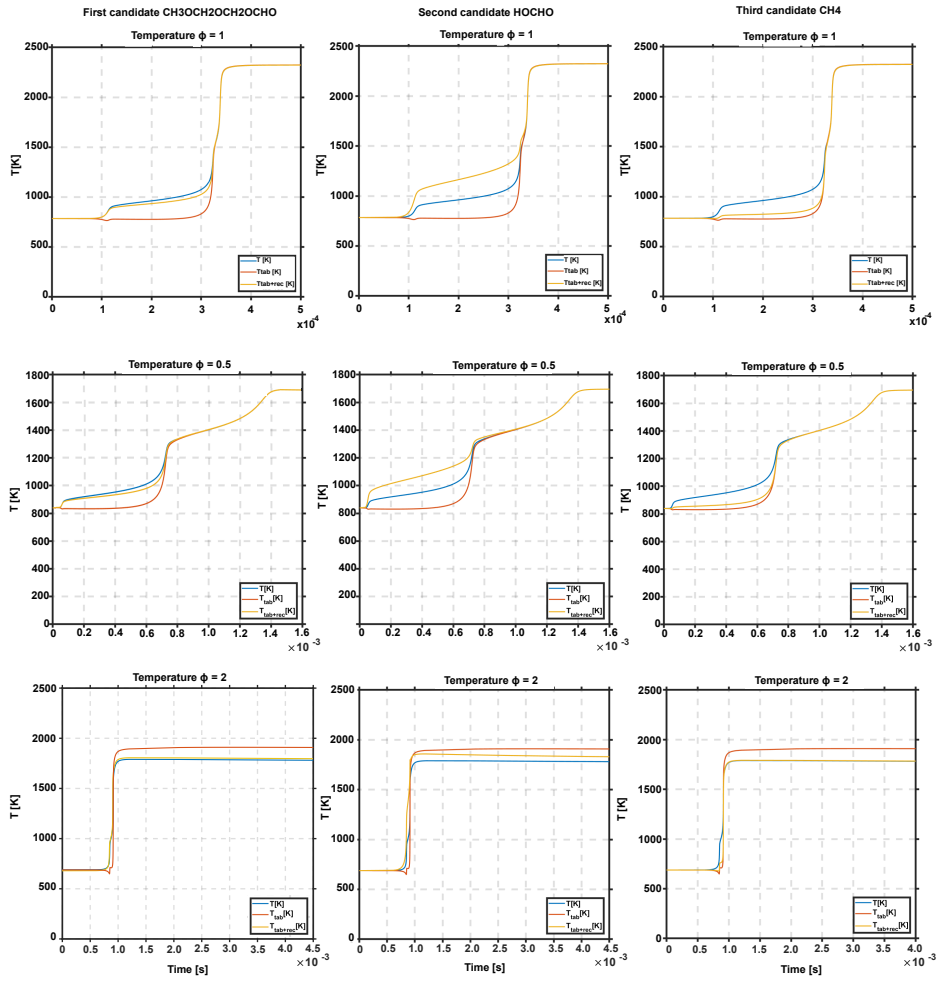

Figure 3.16: Temperature evolution with the three possible dummy species and the three different condition of equivalent ratio evaluated, ϕ= 1 (top), ϕ= 0.5 (middle), ϕ= 2 (bottom).

For OME_1, the same methodology as for OME_x has been followed. The final result is that the better species to reconstruct in this fuel, it is: CH_3OCHO. Figure 3.17 shows the main result of the reconstruction process, differences in temperature evolution between the three possible scenarios and the three levels of equivalent ratio, as in $OMEx$

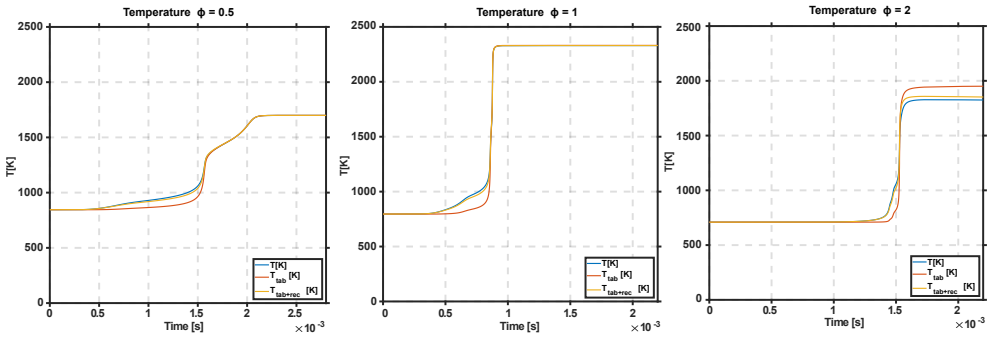

Figure 3.17: Temperature evolution for the three different condition of equivalent ratio evaluated, ϕ=0.5 (left), ϕ= 1 (middle), ϕ= 2 (right) for OME_1 when considering CH_3OCHO as dummy species.

3.7 Fluid Age

The residence time distribution is extensively used in the process industry as a fundamental tool for modelling the advancement of kinetically-limited processes within a specific system, and can be defined as the time any fluid particle has spent within a domain. In flows that involve complex kinetic processes, such as combustion, the degree of combustion reactions and the formation of pollutants can be associated with the residence time of the fluid. To assess this parameter, specific authors suggest employing a Lagrangian simulation of particles injected into the domain [86]. As this Lagrangian approach provides an estimate for a discrete number of particles, Ghirelli and Leckner [87] argue that this might be insufficient to describe all fluid flow and proposed a transport equation derived from an Eulerian formulation. The authors generalize the transport equation proposed by Sandberg [88], for different scenarios, including from cases of single species and non-diffusive flow to multiple species and turbulent flow, using the balance on a control volume. Therefore, in that context, the Eulerian fluid residence time a_M for the flow of a fluid comprising one or more chemical species with equal diffusivities reads:

$$\frac{\partial \rho a_M}{\partial t} + \frac{\partial}{\partial x_i}(\rho u_i a_M) = \frac{\partial}{\partial x_i}\left(\rho D \frac{\partial a_M}{\partial x_I}\right) + \rho \tag{3.54}$$

One of the scenarios presented by Ghirelli and Leckner involves a flow where different streams are considered, resulting in a new transport equation for a variable called stream age a_i, which can be interpreted as the age of material originating from the ith stream of fluid, weighted by its mass. This

variable is undefined when the mass fraction Y_i is equal to zero [89]. In order to avoid this singularity, Ghirelli and Leckner propose a transport equation for the mass-weighted stream age $\Phi_i = Y_i a_i$.

In the present work, where the objective is the study of Diesel-like sprays, mixers of two streams, fuel and air, this transport equation (3.55) was implemented in *CONVERGE* CFD package, and refers to the stream represented by the fuel, using the mixture fraction Z as Y_i, which is a passive scalar, therefore, without reaction and without source terms. Henceforth, the term Φ_i will be referred to as a_{mw-f} to facilitate comprehension, while a_i will be denoted as a_f, hence results, $a_{mw-f} = \mathrm{Z}\ a_f$

$$\frac{\partial \rho a_{mw-f}}{\partial t} + \frac{\partial}{\partial x_i}(\rho u_i a_{mw-f}) = \frac{\partial}{\partial x_i}\left(\rho D \frac{\partial a_{mw-f}}{\partial x_i}\right) + \rho Z \tag{3.55}$$

Thus, from the equations stated above, the fluid age which is the residence time of the mixture, is corresponded to by a_M; a_f represents the fuel age, the residence time solely of the fuel; and a_{mw-f} stands for the mass-weighted fuel age. These three parameters are related according to Equation 3.56.

$$a_M = a_{mw-f} + (1 - Z)a_{air} = Z a_f + (1 - Z)a_{air} \tag{3.56}$$

In the case of injection into the combustion chamber (as the configuration used in this work) where air was already present, a_{air} equals the time from the start of injection (SOI), and a_f represents the time (conservative) of the fuel present at a point from the moment it has been injected.

The relation between different definitions, exposed above, was evaluated carried out RANS simulations under inert conditions. Figure 3.18 shows the fields of the different quantities at 1.20 ms for those simulations. Also, the mixture fraction field is present because it impacts on the stream age definition.

At the top of the figure, the a_M (left) and a_f (right) are illustrated. From these, the physical significance of each aforementioned parameter can be observed. On one hand, the a_M clearly exhibits its maximum (corresponding to the physical time at which the image was taken, 1.20 ms) in the air present in the chamber since the SOI, while the minimums occur near the nozzle and along the spray axis, where the injected fuel begins to mix with the air. On the other hand, the a_f, in contrast, has its origin at zero in the air as it tracks the fuel, and its maxima occur at the peripheries of the spray (bearing in mind that this is a RANS calculation, hence everything appears smoother), where vortices are generated and recirculation takes more importance, favouring

longer residence times. In the bottom right, the a_{mw-f} is located, which, as the name suggests, is associated with the mass fraction of fuel, or in this study, the mixture fraction Z. For this reason, the a_{mw-f} exhibits a rise in the downstream direction along the centreline. This increase in a_{mw-f} indicates that, despite the decrease in Z downstream, the fractional increase in a_f exceeds the fractional decrease in mass fraction along the centreline. Conversely, in the radial direction, the a_{mw-f} decreases. This suggests that the radial decrease in Z outweighs the radial increase in a_f, as noted by Shin et al. in [89].

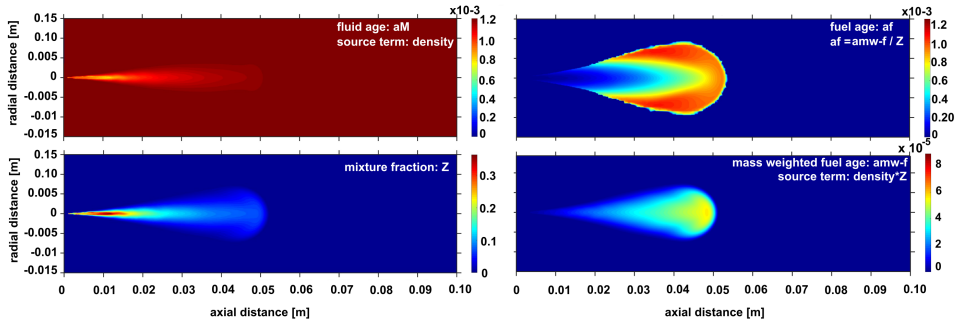

Figure 3.18: Fields of fluid age, fuel age, mass-weighted fuel age and mixture fraction at 1.20 ms for inert simulations of n-Dodecane with RANS approach.

If now the distribution at the centre line is evaluated, the different profiles are shown in Figure 3.19.

The Eulerian way to determine the fuel age produces the same residence time as the one determined by integrating the fluid particle velocity along the entire domain. From that, it is possible to determine the shape of the fluid age at the centreline ($a_{fuel_{cl}}$) Equation 3.57, based on the assumption that in a spray, along a trajectory where the ratio r/x is constant [40], the velocity is proportional to a constant multiplied by the velocity at the centre of the jet and the normalized profile of r/x named: PN(r/x).

$$a_{fuel_{cl}} = \int \frac{dx}{u} = \frac{1}{kPN(r/x)} \int \frac{dx}{u_{cl}} \cong \int \frac{xdx}{ku_0 d_{eq}} \cong \frac{x^2/2}{ku_0 d_{eq}} \tag{3.57}$$

where, u is the velocity, u_{cl} is the velocity at the centre line, u_0 defines the velocity at the nozzle output, the equivalent diameter defined in Equation 5.6 is represented by d_{eq}, x is the axial distance, k is the constant that comes from the trajectory idea explained before, and PN denotes the normalized profile.

And applying the well-known mixing law [90, 91] that relates the mixture fraction at the centre line (Z_{cl}) and the axial coordinate (x):

$$Z_{cl} \approx \frac{1}{x} \tag{3.58}$$

The relation between the different quantities follow that the mass weighed stream age (a_{mw-f}) is proportional to x, which is verified in the profiles presented in the Figure 3.19.

$$a_{mw-f} = a_f \times Z \rightarrow a_{mw-f\,cl} = a_{f\,cl} \times Z_{cl} \cong x \tag{3.59}$$

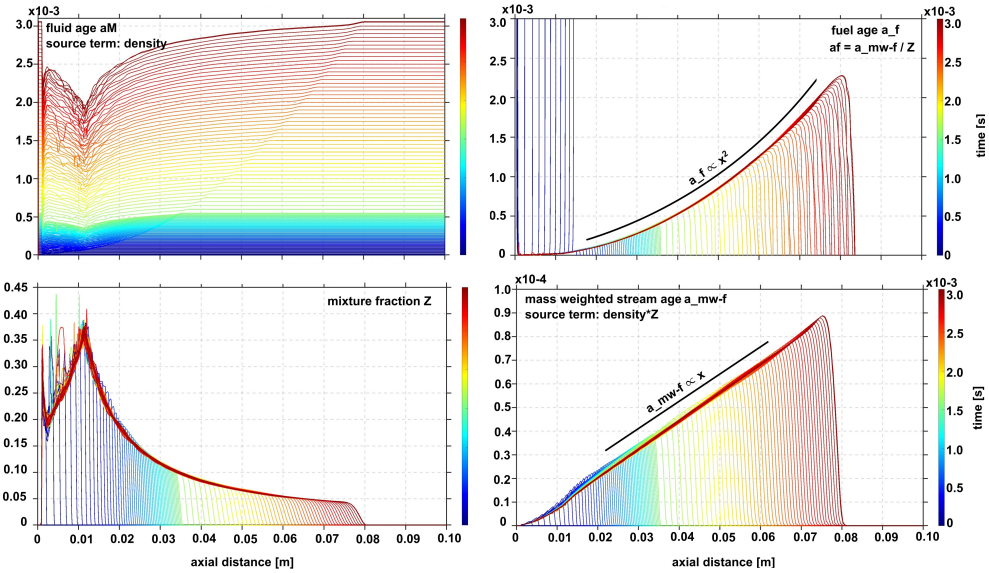

Figure 3.19: Axial variation of (top): the centreline of fluid age and fuel age, and (bottom): centreline of mixture fraction and mass-weighted fuel age. Coloured by simulation time from 0 to 3.06 ms. The colour-scale is the same for the four images. The strange behaviour from 0 to 0.01 m in all the parameters are related to the presence of liquid fuel (liquid length = 0.010 m).

These parameters, primarily the fuel age, will be utilized in Chapter 6, shedding light on both the analysis of the spray auto-ignition process and its differences from flamelet ignition due to the time constraints imposed by the mixing process of the spray, as well as in the comparison of ground and excited species related to the modelling of chemiluminescent species and its different chemical nature.

3.8 Summary

This chapter outlines the computational tools and methodology employed in this study to investigate the combustion process of synthetic and renewable oxygenated fuels of the $OMEn$-type, under ECN SA and SD configurations. To this end, the investigation starts from simpler configurations, referred to as canonical combustion configurations, specifically closed-homogeneous reactor, whose model has been implemented by the author for multicomponent fuels in *Cantera* [28], and counterflow flamelets modelled using the ZLFLAM code [38].

Regarding spray modelling, the description of the liquid phase the Lagrangian parcel Eulerian fluid approach has been used. Two approaches have been employed for turbulence modelling, with RANS serving as the starting point and LES representing high-fidelity simulations. Additionally, in the LES framework, a mesh independence has been achieved as well as, an acceptable quality of LES based on the viscosity-based index proposed by Celik et al. 3.44.

Concerning combustion modelling, an advanced flamelet-based model called UFPV was utilized. The chemical mechanisms employed all correspond to detailed mechanisms, namely Cai et al. [16] for $OMEx$ and Jacobs et al. [17] for OME_1.

Due to the novelty of these fuels, corresponding adaptations of codes and methodologies previously used for hydrocarbons have been carried out, including the determination of dummies species, which are fundamental in the UFPV model, responsible for closing the mass balance and representing the thermodynamic state of the actual mixture present in the spray.

Finally, other new tools have been developed, such as the modelling of major chemiluminescent species present and the fuel age. These tools allow for a deeper and more detailed and analysis of the CFD results, and also serve as a valuable complement to the experimental results found in the literature.

The results obtained under the modelling approach outlined in this chapter will be presented in the following three chapters, which present a continuity and are sort according to the complexity and approximation to the real behaviour found in a diesel-like spray.

References

[1] Boyd, Richard H. “Some physical properties of polyoxymethylene dimethyl ethers”. In: *Journal of Polymer Science* 50.153 (1961), pp. 133–141. DOI: 10.1002/pol.1961.1205015316.

[2] Kulkarni, Aditya et al. “A Force Field for Poly(oxymethylene) Dimethyl Ethers (OMEn)”. In: *Journal of Chemical Theory and Computation* (2020). DOI: 10.1021/acs.jctc.9b01106.

[3] Burger, Jakob, Ströfer, Eckhard, and Hasse, Hans. “Production process for diesel fuel components poly(oxymethylene) dimethyl ethers from methane-based products by hierarchical optimization with varying model depth”. In: *Chemical Engineering Research and Design* 91.12 (2013), pp. 2648–2662. DOI: 10.1016/j.cherd.2013.05.023.

[4] Pastor, J., Garcia-Oliver, Jose, Pastor, Jose, and Vera-Tudela, W. “One-Dimensional Diesel spray modeling of multicomponent fuels”. In: *Atomization and Sprays* 25 (2015), pp. 485–517. DOI: 10.1615/AtomizSpr.2014010370.

[5] Aspen Technology Inc. *https://www.aspentech.com*. 2020.

[6] Yang, Yi, Boehman, André L., and Simmie, John M. “Effects of molecular structure on oxidation reactivity of cyclic hydrocarbons: Experimental observations and conformational analysis”. In: *Combustion and Flame* 157.12 (2010), pp. 2369–2379. DOI: 10.1016/j.combustflame.2010.04.015.

[7] Peters, Norbert. “Turbulent combustion: The state of the art”. In: *Turbulent Combustion*. Cambridge Monographs on Mechanics. Cambridge University Press, 2000, pp. 1–65. DOI: 10.1017/CBO9780511612701.002.

[8] D. Veynante, L. Vervisch. “Turbulent combustion modeling.” In: *Prog. Energy Combust. Sci. Vol. 28, pp. 193-266* (2002). DOI: 10.1016/S0360-1285(01)00017-X.

[9] He, Tanjin et al. “Development of surrogate model for oxygenated wide-distillation fuel with polyoxymethylene dimethyl ether”. In: *SAE International Journal of Fuels and Lubricants* 10.3 (2017), pp. 803–814. DOI: 10.4271/2017-01-2336.

[10] Lin, Qinjie, Tay, Kun Lin, Zhou, Dezhi, and Yang, Wenming. “Development of a compact and robust Polyoxymethylene Dimethyl Ether 3 reaction mechanism for internal combustion engines”. In: *Energy Conversion and Management* 185 (2019), pp. 35–43. DOI: 10.1016/j.enconman.2019.02.007.

[11] Lv, Delin et al. “Development of a reduced diesel/PODEn mechanism for diesel engine application”. In: *Energy Conversion and Management* 199 (2019), p. 112070. DOI: 10.1016/j.enconman.2019.112070.

[12] Huang, Haozhong et al. "Construction of a reduced PODE3/nature gas dual-fuel mechanism under enginelike conditions". In: *Energy & Fuels* 33.4 (2019), pp. 3504–3517. DOI: 10.1021/acs.energyfuels.8b03926.

[13] Sun, Wenyu et al. "Speciation and the laminar burning velocities of poly (oxymethylene) dimethyl ether 3 (POMDME3) flames: An experimental and modeling study". In: *Proceedings of the Combustion Institute* 36.1 (2017), pp. 1269–1278. DOI: 10.1016/j.proci.2016.05.058.

[14] Sun, Wenyu et al. "Exploration of the oxidation chemistry of dimethoxymethane: Jet-stirred reactor experiments and kinetic modeling". In: *Combustion and Flame* 193 (2018), pp. 491–501. DOI: 10.1016/j.combustflame.2018.04.008.

[15] He, Tanjin et al. "A chemical kinetic mechanism for the low-and intermediate-temperature combustion of Polyoxymethylene Dimethyl Ether 3 (PODE3)". In: *Fuel* 212 (2018), pp. 223–235. DOI: 10.1016/j.fuel.2017.09.080.

[16] Cai, Liming et al. "Auto-ignition of oxymethylene ethers (OMEn, n = 2–4) as promising synthetic e-fuels from renewable electricity: shock tube experiments and automatic mechanism generation". In: *Fuel* 264 (2020), p. 116711. DOI: 10.1016/j.fuel.2019.116711.

[17] Jacobs, Sascha et al. "Detailed kinetic modeling of dimethoxymethane. Part II: Experimental and theoretical study of the kinetics and reaction mechanism". In: *Combustion and Flame* 205 (2019), pp. 522–533. DOI: 10.1016/J.COMBUSTFLAME.2018.12.026.

[18] Niu, Bo et al. "Construction of reduced oxidation mechanisms of polyoxymethylene dimethyl ethers (PODE1–6) with consistent structure using decoupling methodology and reaction rate rule". In: *Combustion and Flame* 232 (2021), p. 111534. DOI: 10.1016/j.combustflame.2021.111534.

[19] Pierce, Charles D. and Moin, Parviz. "Progress-variable approach for large-eddy simulation of non-premixed turbulent combustion". In: *Journal of Fluid Mechanics* 504 (2004), pp. 73–97. DOI: 10.1017/S0022112004008213.

[20] Kathrotia, Trupti. "Reaction Kinetics Modeling of OH*, CH*, and C2* Chemiluminescence". PhD thesis. 2011.

[21] Hall, Joel Meador and Petersen, Eric L. "An optimized kinetics model for OH chemiluminescence at high temperatures and atmospheric pressures". In: *International Journal of Chemical Kinetics* 38 (2006), pp. 714–724. DOI: 10.1002/kin.20196.

[22] Smith, Gregory P., Park, Chung, and Luque, Jorge. "A note on chemiluminescence in low-pressure hydrogen and methane–nitrous oxide flames". In: *Combustion and Flame* 140.4 (2005), pp. 385–389. DOI: 10.1016/j.combustflame.2004.11.011.

[23] Tamura, Masayuki et al. "Collisional Quenching of CH(A), OH(A), and NO(A) in Low Pressure Hydrocarbon Flames". In: *Combustion and Flame* 114.3 (1998), pp. 502–514. DOI: 10.1016/S0010-2180(97)00324-6.

[24] Gaydon, A. G. (Alfred Gordon). *The spectroscopy of flames.* eng. Second edition. London: Chapman and Hall, 1974.

[25] Haber, L. C. and Vandsburger, U. "A global reaction model for oh* chemiluminescence applied to a laminar flat-flame burner". In: *Combustion Science and Technology* 175.10 (2003), pp. 1859–1891. DOI: 10.1080/713713115.

[26] Yao, Tong et al. "A compact skeletal mechanism for n-dodecane with optimized semi-global low-temperature chemistry for diesel engine simulations". In: *Fuel* 191 (2017), pp. 339–349. DOI: 10.1016/j.fuel.2016.11.083.

[27] Kopp, M., Brower, M., Mathieu, Olivier, Petersen, Eric, and Güthe, Felix. "CO2* chemiluminescence study at low and elevated pressures". In: *Applied Physics B* 107 (2012). DOI: 10.1007/s00340-012-5051-4.

[28] David G. Goodwin, Raymond L. Speth, Harry K. Moffat, and Bryan W. Weber. *Cantera: An object-oriented software toolkit for chemical kinetics, thermodynamics, and transport processes.* URL: https://doi:10.5281/zenodo.1174508.

[29] Desantes, Jose M., García-Oliver, Jose M., Novella, Ricardo, and Pachano, Leonardo. "A numerical study of the effect of nozzle diameter on diesel combustion ignition and flame stabilization". In: *International Journal of Engine Research* (2019). DOI: 10.1177/1468087419864203.

[30] Peters, N. "Laminar diffusion flamelet models in non-premixed turbulent combustion". In: *Progress in Energy and Combustion Science* 10.3 (1984), pp. 319–339. DOI: 10.1016/0360-1285(84)90114-X.

[31] Williams, Forman A. "Recent Advances in Theoretical Descriptions of Turbulent Diffusion Flames". In: 1975. DOI: 10.1007/978-1-4615-8738-5_5.

[32] Cuenot, Bénédicte. "The Flamelet Model for Non-Premixed Combustion". In: *Turbulent Combustion Modeling: Advances, New Trends and Perspectives*. Ed. by Tarek Echekki and Epaminondas Mastorakos. Dordrecht: Springer Netherlands, 2011, pp. 43–61. DOI: 10.1007/978-94-007-0412-1_3.

[33] Burke, S. P. and Schumann, T. E. W. "Diffusion Flames". In: *Industrial & Engineering Chemistry* (1928). DOI: 10.1021/ie50226a005.

[34] Peters, N., Hocks, W., and Mohiuddin, G. "Turbulent mean reaction rates in the limit of large activation energies". In: *Journal of Fluid Mechanics* 110 (1981), pp. 411–432. DOI: 10.1017/S0022112081000815.

[35] Peter, Andreas et al. "Mixture formation analysis of polyoxymethylenether injection". In: *Atomization and Sprays* 30.11 (2020), pp. 843–859. DOI: 10.1615/AtomizSpr.2020035250.

[36] Pitsch, Heinz and Ihme, Matthias. "An unsteady/flamelet progress variable method for LES of nonpremixed turbulent combustion". In: *43rd AIAA Aerospace Sciences Meeting and Exhibit*. 2005, p. 557.

[37] Pitsch, Heinz Günter. "Modellierung der Zündung und Schadstoffbildung bei der dieselmotorischen Verbrennung mit Hilfe eines interaktiven Flamelet-Modells; 1. Aufl." Zugl.: Aachen, Techn. Hochsch., Diss., 1997. PhD thesis. Göttingen, 1998, VI, 148 S. : Ill., graph. Darst.

[38] Naud, Bertrand, Novella, Ricardo, Pastor, José Manuel, and Winklinger, Johannes F. "RANS modelling of a lifted H2/N2 flame using an unsteady flamelet progress variable approach with presumed PDF". In: *Combustion and Flame* 162.4 (2015), pp. 893–906. DOI: 10.1016/j.combustflame.2014.09.014.

[39] CONVERGE CFD Software. *https://convergecfd.com*.

[40] Pachano, Leonardo. "CFD Modeling of combustion and soot production in diesel spray". PhD thesis. Universitat Politecnica de Valencia, 2020.

[41] Senecal, P. K., Pomraning, E., Richards, K. J., and Som, S. "Grid-convergent spray models for internal combustion engine CFD simulations". In: 2012, pp. 697–710. DOI: 10.1115/ICEF2012-92043.

[42] Senecal, P. K., Pomraning, E., Richards, K. J., and Som, S. "An investigation of grid convergence for spray simulations using an les turbulence model". In: vol. 2. SAE International, 2013. DOI: 10.4271/2013-01-1083.

[43] Nguyen, Tuan M., Dahms, Rainer N., Pickett, Lyle M., and Tagliante, Fabien. "The Corrected Distortion model for Lagrangian spray simulation of transcritical fuel injection". In: *International Journal of Multiphase Flow* 148 (2022). DOI: 10.1016/j.ijmultiphaseflow.2021.103927.

[44] García-Oliver, J. M., Novella, R., Pastor, J. M., and Pachano, L. "Computational study of ECN Spray A and Spray D combustion at different ambient temperature conditions". In: *Transportation Engineering* 2.July (2020). DOI: 10.1016/j.treng.2020.100027.

[45] Senecal, P. K. et al. "Large Eddy Simulation of Vaporizing Sprays Considering Multi-Injection Averaging and Grid-Convergent Mesh Resolution". In: *Journal of Engineering for Gas Turbines and Power* 136.11 (2014), p. 111504. DOI: 10.1115/1.4027449.

[46] Celik, I. B., Cehreli, Z. N., and Yavuz, I. "Index of resolution quality for large eddy simulations". In: *Journal of Fluids Engineering, Transactions of the ASME* 127 (5 2005), pp. 949–958. DOI: 10.1115/1.1990201.

[47] Pei, Yuanjiang et al. "Large eddy simulation of a reacting spray flame with multiple realizations under compression ignition engine conditions". In: *Combustion and Flame* 162.12 (2015), pp. 4442–4455. DOI: 10.1016/j.combustflame.2015.08.010.

[48] Reitz, Rolf and Bracco, F. "Mechanisms of breakup of round liquid jets". In: *Encyclopedia of Fluid Mechanics* 3 (1986).

[49] J., Abraham. "What is Adequate Resolution in the Numerical Computations of Transient Jets?" In: *Transactions of the SAE, 106 (3), pp. 141–155* (1997). DOI: 10.4271/970051.

[50] Iyer V. A., Abraham J. "Penetration and Dispersion of Transient Gas Jets and Sprays". In: *Combust. Sci. Technol., 130, pp. 315–334* (1997). DOI: 10.1080/00102209708935747.

[51] Schmidt, David P. and Rutland, C.J. "A New Droplet Collision Algorithm". In: *Journal of Computational Physics* 164.1 (2000), pp. 62–80. DOI: 10.1006/jcph.2000.6568.

[52] O'Rourke, P J. "Collective drop effects on vaporizing liquid sprays". In: (1981).

[53] Anthony A. Amsden T. Daniel Butler, Peter J. O'Rourke. "The KIVA-II Computer Program for Transient Multidimensional Chemically Reactive Flows with Sprays". In: *SAE 1987 transactions: Fuels and Lubricants-V96-7* (1987). DOI: 10.4271/872072..

[54] Launder, B.E. and Spalding, D.B. "The numerical computation of turbulent flows". In: *Computer Methods in Applied Mechanics and Engineering* 3.2 (1974), pp. 269–289. DOI: 10.1016/0045-7825(74)90029-2.

[55] Pope, Stephen B. *Turbulent Flows*. Cambridge University Press, 2000. DOI: 10.1017/CBO9781316179475.

[56] Rodriguez, Sal. *LES and DNS Turbulence Modeling*. Springer International Publishing, 2019, pp. 197–223. DOI: 10.1007/978-3-030-28691-0_5.

[57] Che Sidik, Nor Azwadi, Yusof, Siti Nurul Akmal, Asako, Yutaka, Mohamed, S., and Aziz, Arif. "A Short Review on RANS Turbulence Models". In: *CFD Letters* 12 (2020), pp. 83–96. DOI: 10.37934/cfdl.12.11.8396.

[58] Favre, Alexandre. "Equations statistiques des gaz turbulents". In: *Compte-Rendus de l'Académie des Sciences Paris* 246.18 (1958), pp. 2576–2579.

[59] Pope, S. B. "An explanation of the turbulent round-jet/plane-jet anomaly". In: *AIAA Journal* 16.3 (1978), pp. 279–281. DOI: 10.2514/3.7521.

[60] Novella, R., García, A., Pastor, J.M., and Domenech, V. "The role of detailed chemical kinetics on CFD diesel spray ignition and combustion modelling". In: *Mathematical and Computer Modelling* 54.7 (2011), pp. 1706–1719. DOI: 10.1016/j.mcm.2010.12.048.

[61] Boussinesq, Joseph. *Essai sur la théorie des eaux courantes*. Bibliothèque nationale de France, 1877.

[62] Clark, Robert A., Ferziger, Joel H., and Reynolds, W. C. "Evaluation of subgrid-scale models using an accurately simulated turbulent flow". In: *Journal of Fluid Mechanics* 91.1 (1979), pp. 1–16. DOI: 10.1017/S002211207900001X.

[63] Sagaut, P. *Large eddy simulation for incompressible flows: an introduction*. Springer Science and Business Media, 2006.

[64] Bharadwaj, N, Rutland, Christopher, and Chang, S. "Large eddy simulation modelling of spray-induced turbulence effects". In: *International Journal of Engine Research* 10 (2009), pp. 97–119. DOI: 10.1243/14680874JER02309.

[65] Rutland, Christopher J. and Bharadwaj, Nidheesh. "A Large Eddy simulation study of sub-grid two-phase interaction in particle-laden flows and diesel engine sprays". In: *Atomization and Sprays* 20.8 (2010), pp. 673–695. DOI: 10.1615/AtomizSpr.v20.i8.20.

[66] Pérez-Sánchez, E.J. "Application of a flamelet-based combustion model to diesel-like reacting sprays". PhD thesis. Universitat Politecnica de Valencia, 2019.

[67] Mompó, Juan Manuel. "Engineering Large Eddy Simulation of Diesel Sprays". In: *Riunet* (2014). DOI: 10.4995/Thesis/10251/37345.

[68] Pomraning, Eric. "Development of Large Eddy Simulation Turbulence Models". PhD thesis. University of Wisconsin-Madison, 2000. DOI: 10.13140/2.1.2035.7929.

[69] Geurts, Bernard J and Fröhlich, Jochen. "A framework for predicting accuracy limitations in large-eddy simulation". In: *Physics of fluids* 14.6 (2002), pp. L41–L44. DOI: 10.1063/1.1480830.

[70] di Mare, Francesca, Knappstein, Robert, and Baumann, Michael. "Application of LES-quality criteria to internal combustion engine flows". In: *Computers and Fluids* 89 (2014), pp. 200–213. DOI: 10.1016/j.compfluid.2013.11.003.

[71] Brusiani F., Bianchi G. "LES Simulation of ICE Non-reactive Flows in Fixed Grids". In: *SAE Technical Paper* 2008-01-0959 (2008). DOI: 10.4271/2008-01-0959.

[72] Battistoni, Michele, Xue, Qingluan, and Som, Sibendu. "Large-eddy simulation (LES) of spray transients: start and end of injection phenomena". In: *Oil & Gas Science and Technology–Revue d'IFP Energies nouvelles* 71.1 (2016), p. 4. DOI: 10.2516/ogst/2015024.

[73] Martinez, María. "Computational study of the Injection Process in Gasoline Direct Injection (GDI) Engines". PhD thesis. 2022.

[74] Celik, I., Klein, M., and Janicka, J. "Assessment Measures for Engineering LES Applications". In: *Journal of Fluids Engineering* 131.3 (2009), p. 031102. DOI: 10.1115/1.3059703.

[75] Paola, G. De, Mastorakos, E., Wright, Y. M., and Boulouchos, K. "Diesel Engine Simulations with Multi-Dimensional Conditional Moment Closure". In: *Combustion Science and Technology* 180.5 (2008), pp. 883–899. DOI: 10.1080/00102200801894273.

[76] Klimenko, A.Y. and Bilger, R.W. "Conditional moment closure for turbulent combustion". In: *Progress in Energy and Combustion Science* 25.6 (1999), pp. 595–687. DOI: 10.1016/S0360-1285(99)00006-4.

[77] Pei Y. Hawkes E., Kook S. "A Comprehensive Study of Effects of Mixing and Chemical Kinetic Models on Predictions of n-heptane Jet Ignitions with the PDF Method". In: *Proc. Combust. Inst. 34* (2013). DOI: 10.1007/s10494-013-9454-z.

[78] Winklinger, Johannes Franz. "Implementation of a Combustion Model based on the Flamelet Concept and its Application to turbulent reactive Sprays". PhD thesis. Universitat Politecnica de Valencia, 2014.

[79] Pandal Blanco, Adrian. "Implementation and Development of an Eulerian Spray Model for CFD simulations of diesel Sprays". PhD thesis. Universitat Politècnica de València, 2016.

[80] Payri, F., Novella, R., Pastor, J.M., and Pérez-Sánchez, E.J. "Evaluation of the approximated diffusion flamelet concept using fuels with different chemical complexity". In: *Applied Mathematical Modelling* 49 (2017), pp. 354–374. DOI: 10.1016/j.apm.2017.04.024.

[81] Desantes, J.M., García-Oliver, J.M., Novella, R., and Pérez-Sánchez, E.J. "Application of an unsteady flamelet model in a RANS framework for spray A simulation". In: *Applied Thermal Engineering* 117 (2017), pp. 50–64. DOI: 10.1016/j.applthermaleng.2017.01.101.

[82] García-Oliver, J. M., Novella, R., Pastor, J. M., and Winklinger, J. F. "Evaluation of combustion models based on tabulated chemistry and presumed probability density function approach for diesel spray simulation". In: *International Journal of Computer Mathematics* 91.1 (2014), pp. 14–23. DOI: 10.1080/00207160.2013.770844.

[83] Pera, C., Colin, O., and Jay, S. "Development of a FPI Detailed Chemistry Tabulation Methodology for Internal Combustion Engines". In: *Oil and Gas Science and Technology - Revue de l'IFP* 64 (3 2009), pp. 243–258. DOI: 10.2516/ogst/2009002.

[84] Van Oijen, JA and De Goey, LPH. "Modelling of premixed laminar flames using flamelet-generated manifolds". In: *Combustion science and technology* 161.1 (2000), pp. 113–137. DOI: 10.1080/00102200008935814.

[85] Sanchis, Enrique. "Desarrollo y aplicacion de una metodologia para la tabulacion de la cinética química detallada asociada a la oxidación de hidrocarburos". In: *Universitat Politecnica de Valencia* (2012).

[86] Shin, Donghoon, Ryu, Changkook, and Choi, Sangmin. "Computational Fluid Dynamics Evaluation of Good Combustion Performance in Waste Incinerators". In: *Journal of The Air and Waste Management Association* 48 (1998), pp. 345–351. DOI: 10.1080/10473289.1998.10464046.

[87] Ghirelli, Federico and Leckner, Bo. "Transport equation for the local residence time of a fluid". In: *Chemical Engineering Science* 59.3 (2004), pp. 513–523. DOI: 10.1016/j.ces.2003.10.013.

[88] Sandberg, Mats. "What is ventilation efficiency?" In: *Building and Environment* 16.2 (1981), pp. 123–135. DOI: 10.1016/0360-1323(81)90028-7.

[89] Shin, Dong-hyuk, Sandberg, RD, and Richardson, ES. "Self-similarity of fluid residence time statistics in a turbulent round jet". In: *Journal of Fluid Mechanics* 823 (2017), pp. 1–25. DOI: 10.1017/jfm.2017.304.

[90] Chiu, W.S., Shahed, S.M., and Lyn, W.T. "A Transient Spray Mixing Model for Diesel Combustion". In: *SAE Transactions* 85 (1976), pp. 502–512. DOI: http://www.jstor.org/stable/44644055.

[91] Hermann Schlichtin, Klaus Gersten. *Boundary-Layer Theory*. Springer Berlin, Heidelberg, 2000. DOI: 10.1007/978-3-662-52919-5.

Appendix

3.A Reaction mechanism and thermodynamic properties of chemiluminescence species

This appendix contains the reaction mechanism used to model the chemiluminescence species, OH*, CH* and C2*. Depending on the original mechanism, additional intermediate species may be added, along with their chemical kinetics, to balance the overall chemical mechanism employed for modelling fuels oxidation. Furthermore, the thermodynamic properties calculated, as explained in chapter 3, are presented below.

Reaction mechanism:

OH*

Elementary reaction	Ar	br	Ea
CH+O_2=CO+OH*	$4.8E+16$	-1	5100
H+O+M=OH*+M	$3.8E+14$	0	1000
H+OH+OH=OHV+H_2O	$1.45E+15$	0	0
OH*+AR=OH+AR	$2.17E+10$	0.5	2057
OH*+H_2O=OH+H_2O	$5.9E+12$	0.5	$-8.61E+02$
OH*+CO_2=OH+CO_2	$2.75E+12$	0.5	$-9.67E+02$
OH*+CO=OH*CO	$3.23E+12$	0.5	$-7.87E+02$
OH*+H=OH+H	$1.5E+12$	0.5	0
OH*+H_2=OH+H_2	$2.95E+12$	0.5	$-4.44E+02$
OH*+O_2=OH+O_2	$2.1E+12$	0.5	$-4.82E+02$
OH*+O=OH+O	$1.5E+12$	0.5	0
OH*+OH=OH+OH	$1.5E+12$	0.5	0
OH*+CH_4=OH+CH_4	$3.36E+13$	0.5	$-6.35E+02$
OH*=OH	$1.4E+06$	0.5	0
OH*+N_2=OH+N_2	$1.08E+11$	0.5	-1238

CH*

Elementary reaction	Ar	br	Ea
CH*+AR=CH+AR	4.0E+11	5E-01	0
CH*+H_2O=CH+H_2O	5.3E+13	0	0
CH*+CO=CH+CO	2.44E+12	5E-01	0
CH*+CO_2=CH+CO_2	2.41E-01	4.3	-1.69E+03
CH*+O_2=CH+O_2	2.48E++6	2.14	-1.72E+03
CH*+H_2=CH+H_2	1.47E+14	0	1.36E+03
CH*+CH_4=CH+CH_4	1.73E+13	0	1.67E+02
CH*=CH	1.86E++6	0	0
CH*+N_2=CH+N_2	3.03E0+02	3.4	-3.81E+02
C+H+M=CH*+M	6.0E0+14	0	6.94E+03
C_2H+O_2=CO_2+CH*	2.17E+10	0	0
C_2H+O=CO+CH*	6.2E+12	0	0

C2*

Elementary reaction	Ar	br	Ea
CH_2+C=C_2^*+H_2	$2.4E+12$	0	0
C_3+O=C_2^*+CO	$5.2E+11$	0	0
C_2^*=C_2	$1.0E+07$	0	0
C_2^*+O_2=C_2+O_2	$4.8E+13$	0	0
C_2^*+CO_2=C_2+CO_2	$4.8E+13$	0	0
C_2^*+H_2O=C_2+H_2O	$4.8E+13$	0	0
C_2^*+CO=C_2+CO	$4.8E+13$	0	0
C_2^*+CH_4=C_2+CH_4	$4.8E+13$	0	0
C_2^*+H=C_2+H	$4.8E+13$	0	0
C_2^*+H_2=C_2+CH_4	$4.8E+13$	0	0
C_2^*+OH=C_2+OH	$4.8E+13$	0	0
C_2^*+Ar = C_2+Ar	$4.8E+13$	0	0

NASA Thermodynamic polynomials:

OH*		300	5000	1000
2.88E+00	1.01E-03	-2.28E-07	2.17E-11	-5.13E-16
5.03E+04	5.60E+00	3.64E+00	1.85E-04	-1.68E-06
2.39E-09	-8.43E-13	5.00E+04	1.36E+00	

CH*		300	5000	1000
2.20E+00	2.34E-03	-7.06E-07	9.01E-11	-3.86E-15
1.04E+05	9.18E+00	3.20E+00	2.07E-03	-5.13E-06
5.73E-09	-1.96E-12	1.04E+05	3.33E+00	

C2*		300	5000	1000
4.14E+00	6.53E-05	1.84E-07	-5.30E-11	4.71E-15
1.27E+05	7.47E-01	7.00E+00	-7.40E-03	3.23E-06
4.80E-09	-3.30E-12	1.26E+05	-1.39E+01	

Chapter 4

Canonical configuration results

Contents

4.1 Introduction

This chapter examines the modification of combustion when adding different layers of physical content. Different well-defined combustion canonical configurations have been used to achieve this, employing finite-rate chemistry solvers. These configurations allow evaluation of the fuel oxidation, shedding light on the chemical mechanism's role during combustion modelling.

In a first 0D analysis, the fuel oxidation was investigated with homogeneous constant-pressure adiabatic reactor simulations performed with *Cantera* [1], where only chemistry occurs without any transport. Then, in a second step, 1D laminar flamelet calculations are performed using the $ZLFLAM$ code [2]. Flamelets in counter-flow configuration are solved in mixture fraction space for any 'k' species in the chemical mechanism. The solutions of diffusion

laminar flamelets, where transport phenomena are introduced and coexist with chemistry, are evaluated. The influence of the interaction between diffusion and chemistry is assessed based on the previous solutions of homogeneous reactors.

The relationship between the two canonical configurations used lies in the fact that a homogeneous reactor is the limit of a flamelet when the strain rate tends to be null. In the absence of strain rate, there is no diffusion or convection, allowing mixtures to be solved separately. Hence, unlike a flamelet, each homogeneous reactor is solved independently, without being coupled with the rest of the mixtures. Consequently, their resolution requires significantly less time compared to a flamelet. Homogeneous reactors and flamelets are computed with the same initial and boundary conditions as those used in the experimental campaign and turbulent spray calculations, specifically at the fuel and oxidant streams. The initial state corresponds to the result of an adiabatic mixing between a fuel and an air stream, with the corresponding boundary conditions of the injected fuel and the chamber air. This work assumes no heat losses and imposes an adiabatic evolution with constant pressure to solve their chemical evolution.

Although in the context of the ENERXICO project [3], a wide range of boundary condition variations has been conducted during experimental campaigns, many of which will be replicated through CFD calculations (Chapters 5 and 6), in this chapter, only the nominal condition will be presented and analysed, which is defined for canonical configurations, by $T_{amb} = 900\ K$ and $\rho_{amb} = 22.8\ \mathrm{kg}/m^3$ with an ambient composition determined by 15 % O_2 and 85 % N_2.

Table 4.1 summarized the $OMEn$ composition in experiments as well as the different composition considered in this chapter, depending on the chemical mechanism used. Due to the extremely low percentage of OME_1 and OME_2 (Table 4.1), they have been omitted from the calculation. Their traces have been added to OME_3, as well as other components ($\sim$1.2 %) ($OMEn$ composition of the experiments is not equal to 100 %.)

		Chain length composition		
		OME_{34}	OME_{36}	OME_{exp}
weight %	OME_1	-	-	0.01
	OME_2	-	-	<0.01
	OME_3	59.14	59.14	57.90
	OME_4	40.86	28.87	28.87
	OME_5	-	10.08	10.08
	OME_6	-	1.91	1.91

Table 4.1: Composition of the different OMEn chains that have been calculated in this section. For the rest of the results chapters, the composition of OME34 has been used and referred as OMEx. Last column correspond to OMEn composition in ENERXICO experiments.

Originally, when the research associated with this thesis began in 2020, based on the literature review conducted then, only two chemical mechanisms were available to model $OMEn$-type fuels. On the one hand, Jacobs et al. [4] for OME_1, and on the other hand, Cai et al. [5] for OME_{34}, both belonging to research groups at the Aachen University. For this reason, they were initially selected for the comprehensive modelling associated with this thesis, including canonical configurations and CFD.

However, in 2021, Niu et al. [6] developed a new chemical mechanism for poly-oxymethylene Dimethyl Ethers, where all chains from OME_1 to OME_6 are included. Therefore, due to the possibility of incorporating all components of the real composition of $OMEn$ with the Niu et al. mechanism, an evaluation of the influence of the chain length on the development of chemical kinetics was conducted in a posteriori. This involved comparing results under canonical configurations of OME_3, OME_{34} (a simplification employed with the Cai mechanism), and OME_{36} (almost the same composition as in experiments, considering the negligible proportion of OME_1 and OME_2). However, it should be noted that there is no available experimental data for the chemical ignition delay time of pure OME_5 and OME_6. Therefore, in the Niu mechanism, these components' reaction rates are extrapolated using $OMEn$ data with lower chain lengths. Additionally, the predictions of the two mechanisms (Cai and Niu) were compared when modelling OME_3 or OME_{34}.

From this point forward, in this thesis, a generic mixture of polyoxymethylene dimethyl ether will be referred to as $OMEn$, and $OMEx$ will be used when the mixture corresponds to the typical one used in numerical simulations (OME_3 and OME_4, first column of Table 4.1).

The combustion canonical configurations are also beneficial for modelling the chemiluminescence phenomenon, which is commonly used experimentally to track the flame structure. Implementing the sub-mechanisms of these species in Cai and Jacobs mechanism and Yao et al. [7], the one used to model n-Dodecane chemical kinetics could shed light on the understanding of these excited species, their behaviour, and their relation with the ground species.

Therefore, in this chapter, the canonical configurations described previously will be extensively utilized to evaluate the following points as described below:

- A detailed analysis will be conducted under combustion canonical configurations to compare the chemical kinetics of the selected $OMEn$-type fuels (OME_1 and OME_{34}) with n-Dodecane, which will be used as a reference. Highlighting the role of the fuel in the development of the auto-ignition process under the configurations considered.
- Modelling of chemiluminescent species, OH^*, CH^*, and $C2^*$. Evaluation of the relationship between the three, as well as with the ground species.
- A comparison will be made between the Cai and Niu chemical mechanisms for OME_3 and OME_{34}, as well as between the Jacobs and Niu mechanisms for OME_1. Additionally, an analysis will be conducted to compare the effects of chain length when modelling $OMEx$, these results will be obtained using the Niu mechanism for OME_3, OME_{34}, and OME_{36}.

Finally, it is worth mentioning that these solvers also allow for the tabulation of chemistry, which, in this work, flamelets solutions are later used to reduce the computational cost of CFD calculations by using a transported PDF tabulated chemistry combustion model.

4.2 Closed homogeneous reactor

The first step in the detailed results analysis under canonical configurations, is the study of the chemical kinetics in closed homogeneous reactor conditions for all the fuels under investigation. This allows to compare the different chemical mechanism in terms of an ignition delay that is only influenced by chemical reactions. Ignition delay (ID) evolutions for three mechanism are shown in Figure 4.1 as a function of mixture fraction (Z) for baseline operating conditions (i.e. ambient temperature 900 K). Similarly to other hydrocarbon fuels, different zones can be identified along the ignition process

depending on the reactivity state, namely those corresponding to the low and high temperature zones.

High-temperature ignition delay (ID_{HT}) exhibits the typical v-shape for all three fuels as a function of mixture fraction, with a minimum value at the so-called "most reactive mixture fraction" [8], which is relatively rich for all cases (0.059, 0.123 and 0.112 for n-Dodecane, OME_x and OME_1 respectively). As for the low-temperature ignition delay (ID_{LT}), the v-shape is also visible spanning a wider mixture fraction range compared to the high-temperature one. However, differences among fuels are more evident, especially for n-Dodecane and OME_x, where the minimum ID_{LT} is reached for very low mixture fractions, well in the lean range. The time elapsed between low and high temperature ignition delay (ID_{LT} and ID_{HT}) is the cool flame period as defined e.g. in Payri [9]. This is relatively long for the latter two fuels in the lean region. For OME_1 this interval is overall short, hinting at a single-stage ignition process in most of the ignition delay results shown, which are in a relevant range in terms of spray ignition. Furthermore, OME_1 presents longer ignition delay values than the other two fuels for both low and high temperature regimes. Finally, calculated ignition delays at the most reactive mixture fraction follow the trend presented by the cetane numbers in Table 2.1, with n-Dodecane (0.23 ms) being the first one to ignite, closely followed by OME_x (0.32 ms), and finally OME_1 shows the longest ignition delay (0.82 ms).

The chemical analysis of homogeneous reactors is complemented by the source term for the progress variable $\dot{Y}_c$ over the mixture fraction – temperature map, left panel of Figure 4.2. These maps show different reactivity islands depending on the mixture fraction and the distance to the equilibrium temperature, i.e. the progress variable. The same figures have been included in the right panel in terms of equivalence ratio, so that mixture composition compared to stoichiometry can be better compared. For all three fuels three different regions have been identified and are described in the bullet points:

- Region I: This region presents a clear chemical activity, is found around stoichiometric locations and close to equilibrium temperatures. This island is narrower in terms of mixture fraction range for n-Dodecane, compared to the oxygenated fuels. Just as an example, maximum $\dot{Y}_c$ in this region is found at around 2000 K, ranging within $0.045 < Z < 0.060$ for n-Dodecane, while this range is $0.085 < Z < 0.145$ for OME_x and $0.085 < Z < 0.12$ for OME_1.

- Region II: This region represents a second intermediate island of reactivity. Is found at around 1100 K for n-Dodecane. While this happens at roughly

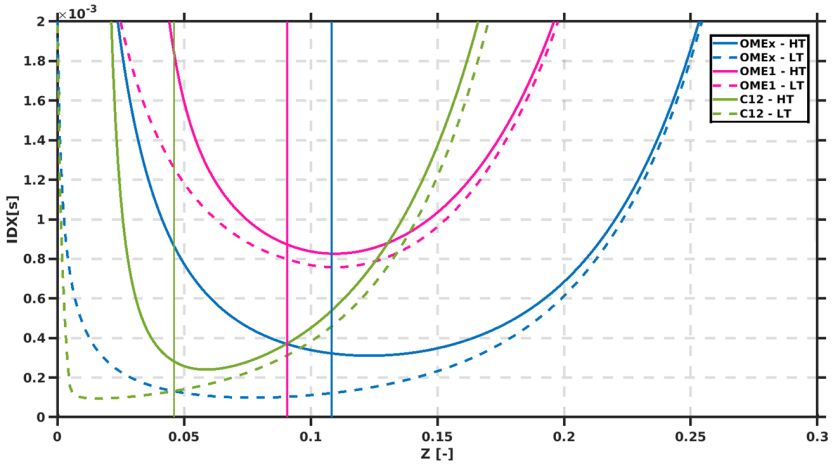

Figure 4.1: Ignition delay for OME_x, OME_1 and n-Dodecane (C12) for closed homogeneous reactors. Both low- (dashed line) and high-temperature stage (solid line) have been quantified. Starting conditions are obtained from an adiabatic mixing between fuel and air at nominal operating (ambient temperature 900 K). Vertical solid lines correspond to the stoichiometric mixture fraction Z_{st}.

below 1500 K for both OME_x and OME_1, it spans the mixture fraction range from almost zero to 0.3 for all three cases. This second reactivity island is very close to the initial adiabatic mixing curve for n-Dodecane, so this will be the trigger for initial reactions for the alkane fuel.

- Region III: This last region is found for the two oxygenated fuels, where the second island is further away from the initial inert state if compared with n-Dodecane, but this third island can still be found at or below 1000 K, with increasing $\dot{Y}_c$ values as one moves towards rich regions.

Some differences from the ID plots can be explained based upon the $\dot{Y}_c$ maps. As previously discussed, only two reactivity islands (Regions I and II) are observed for n-Dodecane, which overlap for slightly lean to and rich mixtures ($0.03 < Z < 0.1$), where ID_{HT} is shortest. Furthermore, the intermediate region between both islands, which would be representative of cool flame period, still exhibits a noticeable $\dot{Y}_c$ value, and hence short differences between ID_{LT} and ID_{HT} (Figure 4.1) are obtained within that range. Compared to the two other fuels, Region II extends well into the lean region and very close to the initial adiabatic mixing state, which results in a faster initiation of the low temperature reactions and hence in short ID_{HT} (Figure 4.1).

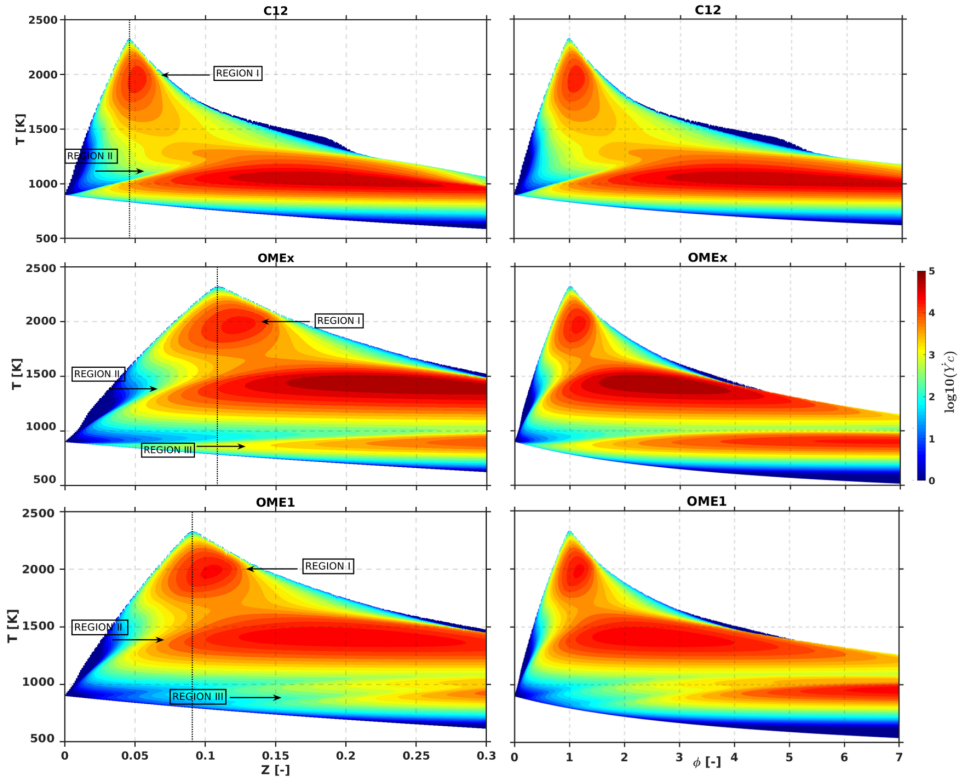

Figure 4.2: Chemical source term $\dot{Y}_c = dY_c/dt$ for homogeneous reactor calculations in terms of mixture fraction (left panel), equivalent ratio (right panel) and temperature.

For OME_x, Region III is close to adiabatic mixing in the $0.07 < Z < 0.15$ region, where low temperature ignition delay will be shortest (Figure 4.1). Furthermore, for this mixture fraction range there is an overlap of three reactivity islands resulting in the lowest ignition delay, and a short duration of the cool flame period. In spite of the difference in reactivity distribution, ID values in this region are quite similar to those of n-Dodecane, but the cool flame period is slightly longer due to the presence of a $\dot{Y}_c$ valley at around 1000 K. Finally, in the $Z < 0.07$ range (Region III) close to the adiabatic mixing line is similar to that of n-Dodecane, but the low reactivity at around 1000 K prevents from the transition to the high temperature ignition, and hence ID_{HT} is longer than for n-Dodecane.

Finally, OME_1 a Region III, i.e. the lowest temperature reactivity island, that is only active for very rich mixtures (Z>0.2, Phi> 3) compared to $OMEx$. $\dot{Y}_c$ values close to the adiabatic mixing line are lowest compared to the two

other fuels, resulting in a very late initiation of reactions, and hence the longest ID values. Most of the ignition occurs in the $0.05 < Z < 0.2$ range of relatively high temperature with an almost single step, as the short transition between ID_{LT} and ID_{HT} shows (Figure 4.1).

Most of the results in the analysis of homogeneous reactor have been plotted against mixture fraction. The purpose of using the mixture fraction axis was to highlight the important role of mixing on absolute terms, which is crucial in spray combustion. Furthermore, mixture fraction can be more easily compared to axial distance to the nozzle, as will be shown in CFD results, i.e. by the inert spray analysis (Figure 5.3). Using equivalence ratio as an independent variable is interesting from the chemical point of view. Note that the contour plots in the right panel of Figure 4.2 contain essentially the same information as the original ones in terms of mixture fraction, but they are re-scaled on the x-axis according to the fuel stoichiometry. In that sense, the relative location and intensity of the different high reactivity zones do not change compared to using mixture fraction, but the width of the contours in the equivalence ratio case look more similar between OME_x and n-Dodecane.

4.3 Laminar flamelets

The analysis of laminar igniting flamelets makes up the intermediate natural step to bridge the gap between the chemical analysis of homogeneous reactors and the spray problem. In fact, the initial evolution of a flamelet with the limit cases of a very low strain rate (SR) should be relatively close to a homogeneous reactor situation. As SR increases, the combustion process of the flamelet is increasingly affected by diffusion. Therefore, the relative roles of chemical reactivity and diffusion modify the ignition process.

Figure 4.3 shows the flamelet auto-ignition contour maps of $\dot{Y}_c$ similarly to the homogeneous reactor (Figure 4.2) for two different SR values, namely $SR = 10$ and 1000 $(1/s)$. A set of solid gray lines is superimposed on each case indicating instantaneous flamelet temperature with a constant 10 μs time-step increase between lines. In that way, the density of lines is indicative of the progression rate of the auto-ignition sequence, e.g. temperature increases fast in the less dense region of the contour map. A dotted line is drawn to identify the maximum temperature at every time step, starting at the location where this maximum temperature is equal or higher than, 905 K to identify the differences in the behaviour of the first reactors. A solid black line identifies the steady solution.

In general terms, the most intense reactivity island at stoichiometric mixtures and high temperature (previously described as Region I) is present for all cases, but clear differences can be observed in the intermediate and low temperature reactivity zones (Region II and III) compared to Figure 4.2. Starting with n-Dodecane at the lowest strain rate value, one can still find some remainders of the low temperature (Region II) from very lean up to rich conditions $0.025 < Z < 0.1$. Moving towards high temperature, a drop in reactivity is observed at around 1000 K, similarly to the homogeneous reactors, followed by the final high reactivity around stoichiometric conditions (Region I). The high reactivity island observed at rich mixtures ($Z > 0.1$) in homogeneous reactors (Region II) is not present here. This could be due to the effect of diffusion at richer mixtures in mixture fraction space, as the imposed profile of scalar dissipation rate increases with mixture fraction in the plotted range. Note that this diffusion effect is the result of both convection and diffusion in physical space.

For the OME_x case, a low intensity zone is observed close to the initial adiabatic mixing line, especially around the stochiometric-rich zones, which was already present in homogeneous reactors (Region III). Moving to higher temperature, the drop in chemical activity is seen up to $1000 - 1100K$, followed by a reactivity pattern similar to that of homogeneous reactors at high temperature, with two zones (Region I and II) separated by a small valley at around 1500 K leading up to the steady solution. The peak reactivity zone observed for homogeneous reactors at rich conditions ($0.15 < Z < 0.3$) and below 1500 K (Region II) vanishes at low SR, although it can again be observed at the high one.

When moving to OME_1 the reactivity zone observed in homogeneous reactors close to the adiabatic mixing line (Region III) disappears, consistently with the long ID_{LT}, and the middle zone island is narrower in terms of mixture fraction range compared to homogeneous reactors in Figure 4.2. Similarly to OME_x, no presence of this rich reactive zone (Region II) is seen for low SR, while it appears again at high SR.

In general terms, a higher strain tends to shift reactivity towards richer mixtures. This is specially evident for both oxygenated fuels and for the intermediate-high temperature reactivity islands, which tend to expand within the mixture fraction space.

The overlap of instantaneous and maximum temperature lines superimposed upon reactivity contours helps explain the temporal evolution of flamelet ignition. For all three fuels, ignition is seen to start at lean conditions, shifting towards rich mixtures along the low reactivity zone at around 1000 K with a

very small temperature increase. For low SR the flame reaches the intermediate reactivity island (Region II), after which a very steep temperature increase is observed towards the steady state, which is evidenced by the apparent decrease in the density of instantaneous temperature lines around the maximum temperature line. As SR increases, diffusion effects tends to propagate ignition from the most reactive mixture fraction to other mixtures, both on the rich and lean sides. This is evidenced by the wider profiles of the instantaneous temperatures in mixture fraction space.

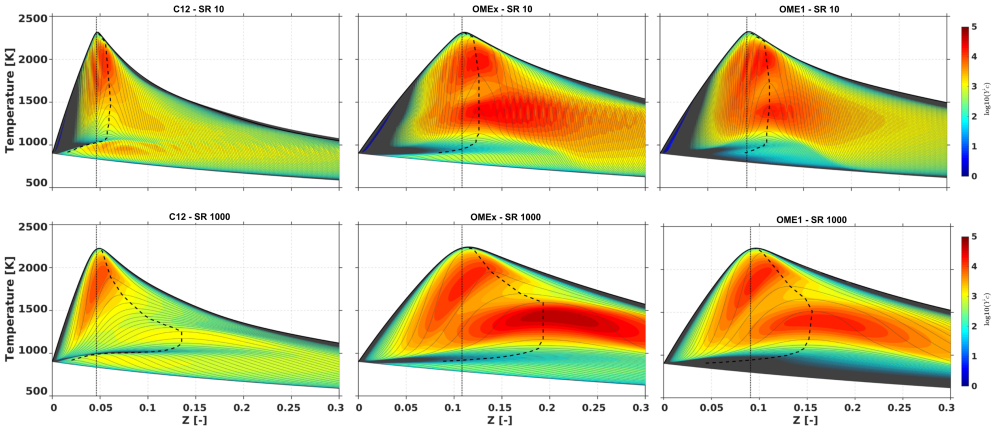

Figure 4.3: Contours of $\dot{Y}_c = \partial Y_c/\partial t$ from laminar flamelet solver in terms of mixture fraction and temperature. Superimposed on the contours, instantaneous flamelet temperature distributions (solid lines) with 10 μs time step have been plotted, together with the evolution of maximum temperature at every time step (dashed lines). Top row corresponds to $SR = 10(1/s)$, bottom row to $SR = 1000(1/s)$. Left column corresponds to n-Dodecane, middle OME_x and right OME_1.

Figure 4.4 compares the evolution of T_{max} against mixture fraction (left) and time (right). For n-Dodecane, one can observe the typical time evolution of a two-stage ignition process. The initial cool flame can be identified independently of SR by a clear drop in the slope of the maximum temperature for some period until the final jump at high temperature ignition timing occurs. This is not quite the case for OME_1, which aside from showing a later increase in temperature also features a more progressive initial temperature increase without an explicit drop in slope. After reaching around 1100 K, the second-high temperature increase is observed. OME_x shows an intermediate behaviour with a timing similar to that of n-Dodecane, and at the same time a more steady initial temperature increase. This evidences that such oxygenated fuels are closer to a single-stage ignition process.

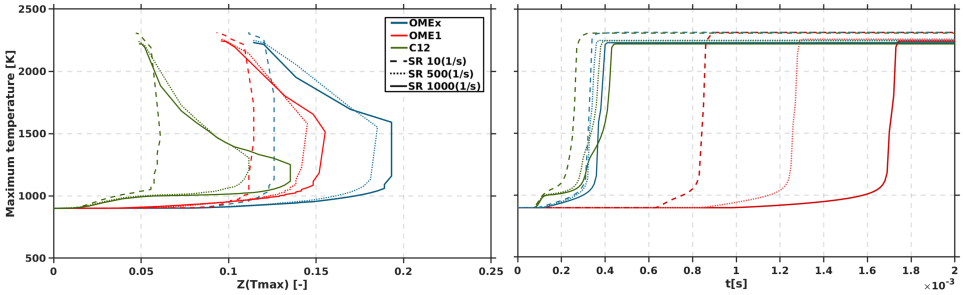

Figure 4.4: Evolution of maximum temperature in the flamelet during auto-ignition against time (right) and against the mixture fraction value at which it occurs for n-Dodecane, OME_x and OME_1 at three strain rate values, namely 10, 500 *and* 1000 $(1/s)$.

For n-Dodecane, increasing SR does not have any effect on the initial low temperature rise, while it tends to delay high temperature ignition. Another clear effect of increasing SR is the shift of the subsequent temperature rise towards rich mixtures. The steep temperature increase at constant mixture fraction only proceeds until reaching a point, from which maximum temperature shifts back towards lower mixture fraction values. This turning point coincides with the high temperature limit of the reactivity island at rich location ($0.1 < Z < 0.2$) (Figure 4.3). After that, maximum temperature eventually reaches the stoichiometric high reactivity region, where evolution becomes steady. For medium and high strain rate, this results in an apparent 3-stage ignition of maximum temperature versus time, namely the initial low temperature increase, the steep increase at constant mixture fraction in the rich region and the final temperature increase when reactivity shifts back towards stoichiometry. This behaviour is not observed for low strain rates, where high temperature ignition occurs almost at stoichiometric conditions.

Some of the previous effects can be discussed for the oxygenated fuels:

- Little effect of SR is observed on the timing of the low temperature ignition phase for OME_x, while it tends to delay the high temperature phase. In the early ignition stages, gradients of species are small and hence SR does not have a strong effect. It must be highlighted that a lower sensitivity of OME_x to strain is observed compared to n-Dodecane, which results in a faster high temperature ignition of the oxygenated fuel versus n-Dodecane at the highest SR, compared to the slower ignition at low SR. As for OME_1, the much lower reactivity results in a high sensitivity to strain for both the low and high temperature ignition stages.

- For both oxygenated fuels, maximum temperature evolution in the mixture fraction space also shows that ignition occurs at richer mixtures as SR increases. A similar behaviour to that of n-Dodecane is also observed, with also a steep increase to a constant mixture fraction followed by a shift of maximum temperature back to stoichiometric mixtures. However, for oxygenated fuels the latter phase starts at a higher temperature and closer to stoichiometric conditions, in agreement with the important reactivity island at rich locations (Figure 4.3).

In this section the auto-ignition process of the flamelets of the three fuels has been described. Important differences among them have been found, namely the absence of the zone of reactivity associated with low temperature in oxygenated fuels, as well as the presence of an important reactivity zone at intermediate temperature, not present in n-Dodecane. Ignition characteristics of OME_x are at an intermediate situation between n-Dodecane and OME_1.

4.4 Chemiluminescence species

The canonical configurations used in all sections of this chapter have also served as a tool for evaluating chemiluminescent species. As explained earlier in Section 3.4, their chemical sub-mechanisms [4, 10–13] have been added to the mechanisms used in this thesis, namely Cai, Jacobs, and Yao for n-Dodecane [7].

Figures 4.5 present the relationship between the ground species (in black) and the excited species (in red) under laminar flamelets with an SR = 500 $1/s$, for n-Dodecane, OME_x and OME_1, in row 1, 2 and 3 respectively. As usual, results for n-Dodecane are included as a reference. On the one hand, it is essential to mention that the motivation for modelling these species arises to compare with the results obtained experimentally, regardless of the fuel under study. On the other hand, especially in the case of $OMEn$-type fuels, it has been found that these fuels do not produce soot due to their oxygenated nature, unlike n-Dodecane, which is clearly associated with soot generation in its flame. This interference of soot can affect OH^* chemiluminescence experiments. Additionally, considering that OH^* is usually used for determining the location of the lift-off length in lifted flame combustion and that this species is not always available in numerical simulations, knowing the relationship between them is of great importance to avoid errors when comparing the lift-off length obtained from one species with that obtained from another, similarly, comparing OH fields (from CFD) with OH^* (from experiments), it should be noted that

experimentally, the chemiluminescence technique is much more straightforward and less costly than the laser-induced fluorescence (LIF) technique used for OH detection. Finally, knowing that not only OH^* is present in a flame, modelling the other chemiluminescent species with higher participation allows observing the behaviour of each one, the differences and similarities, and confirming which one results in a better flame tracer, which is the objective usually measured by optical techniques.

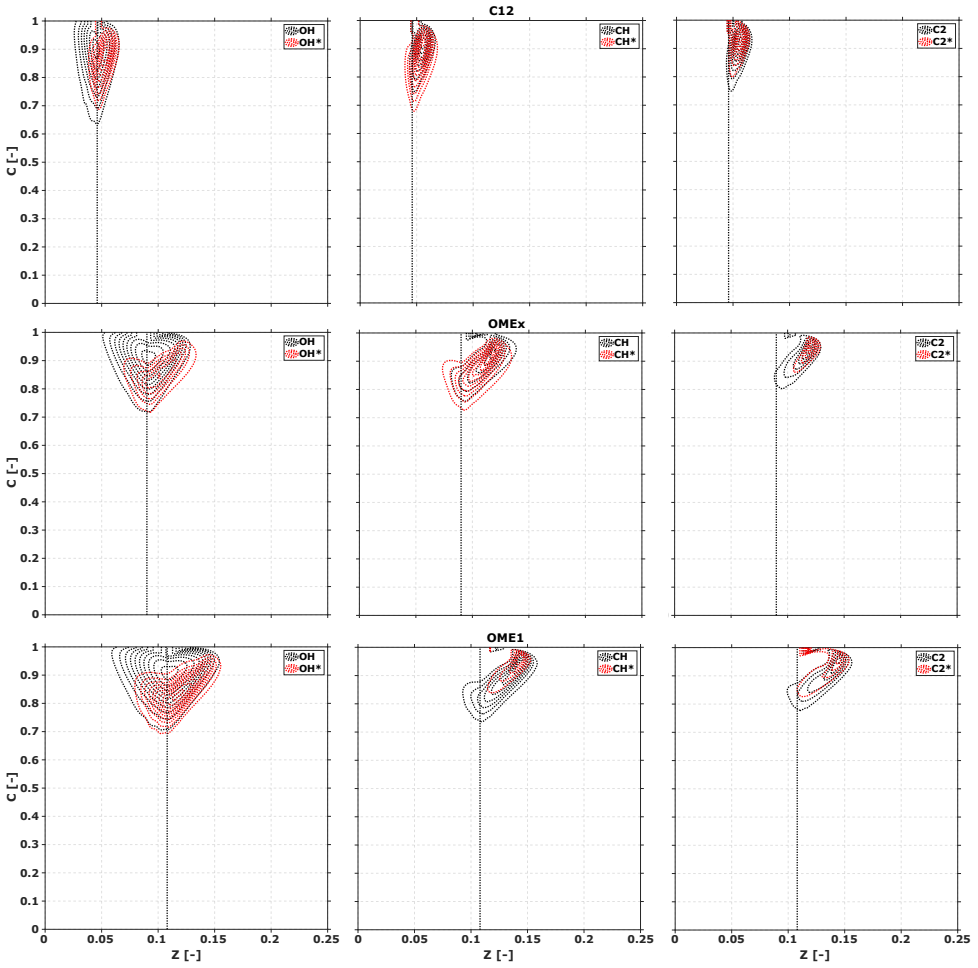

Figure 4.5: Distribution of the ground and excited species as a function of the normalized progress variable (C) and the mixture fraction field (Z) for laminar flamelets with $SR = 500\ 1/s$. The first row corresponds to the results for n-Dodecane, while rows 2, and 3 correspond to $OMEx$ and OME_1 respectively.

Generally, the ground-state OH species appear almost centred at stoichiometric conditions for all three fuels, while the excited OH^* species is slightly shifted towards richer conditions. Ground species is found at high values of the progress variable, close to chemical equilibrium (C = 1). However, it is observed that although the excited species shares its appearance zone with the ground species, it does not reach values of C = 1. This is more accurate in oxygenated fuels, which can be attributed to their distinct chemical nature. On the one hand, the lifetime of OH^* is limited and determined by the spontaneous emission rate. In contrast, OH is more long-lived and remains partially in equilibrium with the water generated during combustion [14].

For both CH^* and C_2^*, starting from n-Dodecane, a noticeable shift towards rich conditions of these species and their base species is observed. This effect is further enhanced in oxygenated fuels, where CH^* and C_2^* reach their maximum at Z values close to 0.14 for OME_x and 0.12 for OME_1. Furthermore, for all fuels, the production of both the base and excited species of CH and C_2 is lower than that of OH, and they are very similar.

From what is found with flamelets, it is expected that the fields of each species obtained through CFD will exhibit significant differences. This is primarily because OH is found at equilibrium or near-equilibrium values of C, while OH^* does not, indicating regions that are clearly differentiated within the spray. Additionally, species such as CH and C_2 do not extend into lean or even stoichiometric zones but are almost entirely in the rich region (especially for OME_1). This is likely to result in a minor extension within the spray for CH and C_2 compared to OH^*, leading to a less precise flame tracing from these species.

4.5 A comparison of chemical mechanism and OMEn chain length

As mentioned in Section 3.3, a new mechanism that includes from the shortest chain OME_1 to OME_6, was developed in 2021 by Niu et al. [6], from now on referred to as Niu which is a reduced chemical mechanism; From Table 3.2 it is possible to see that Niu present a small size compared to Jacobs [4] for OME_1 and Cai [5] for all other $OMEx$-type fuels, from now on referred to as Cai and Jacobs.

Although today, the use of the Niu mechanism is not so widespread in the community (partly given its novelty), which is reflected in the number of citations found on Google Scholar in October 2023, presented by the three

mechanisms 83 times for Cai, 87 Jacobs and 19 Niu [15]. However, as it was mentioned in the introduction of this chapter, its characteristics make it attractive to carry out a comparison under conditions of canonical configurations, on the one hand, to compare the performance of a reduced mechanism such as Niu against the mechanisms used in this work (Cai and Jacobs), and on the other hand, since Niu mechanism includes all the OME chains present in the composition of the fuel for experimental campaigns [16–20], which allows evaluating the effect of modelling OME_{34} (given the percentages presented in the fuel composition table) as representative of $OME_1 - 6$ as well as, quantify the effect of chain length in modelling the kinetico-chemical behaviour of OME_x.

The canonical configuration aforementioned will be used to understand fuel differences and chemical mechanism effects. Therefore, following the same methodology as the previous sections, the laminar flamelet configuration will also help to understand the interaction with diffusion. The results of these comparisons will be structured as follows:

1. Comparison of the Niu mechanism with Cai, which allows evaluating, on the one hand, the differences between the mechanisms by calculating homogeneous reactors and flamelets configurations for OME_3 and OME_{34} using both mechanisms. On the other hand, it evaluates the effect of the chain length considered. For these calculations, OME_{3-6} with the Niu mechanism will also be included and compared with OME_3 and OME_{34} results from the same mechanism.

2. Comparison of the Niu mechanism with Jacobs: This second part will present results of homogeneous reactors of OME_1 calculated using these two mechanisms.

Cai vs Niu: Chemical mechanism and chain length evaluation

The first point of this section presents the comparison of the chemical mechanisms of Cai and Niu, as well as the effect of chain length on modelling the chemical kinetics of the OME_x compounds.

It starts comparing the chain length. Figure 4.6 is an extension of Figure 4.1, including in shades of red the different OME chain lengths calculated with Niu and in shades of blue the ones from Cai. Focusing on the chains of either mechanism, it is clear that no significant differences are found from one to another mechanism, which happens throughout the spectrum represented, that is, for low- and high-temperature ignition delay and rich and lean mixture

fraction conditions. Some differences can be found between OME_3 and OME_{34} in both mechanisms, mainly in the ignition delay associated to high temperature, where for lean conditions, the single-component OME_3 tends to ignite a little before than OME_{34}, which is in line with Haspel et al. [21], the authors found that OME_4 ignite earlier than OME_3, hence, in the present work this is translated to earlier ignition of OME_{34} mix, and this changes as it shifts to higher mixture fractions, finding that at Z values close to stoichiometric, but still lean (~ 0.85), for Niu mainly, it is OME_{34} that has the lowest ignition delay. This corresponds to the cetane number, as the CN of OME_4 is higher than that of OME_3, but the difference is not too significant, 84 compared to 72 [22]. Therefore, the ignition delay of pure OME_3 is similar to the OME_{34} blend. As for Cai, although the trend is not reversed, OME_3 no longer ignites earlier and both OME_3 and OME_{34} chains have practically the same ignition delay at both low and high temperatures. However, comparing OME_{34} and OME_{36} with Niu, the behaviour is almost identical, with OME_{34} lines on top of OME_{36} ones throughout the mixture fraction space.

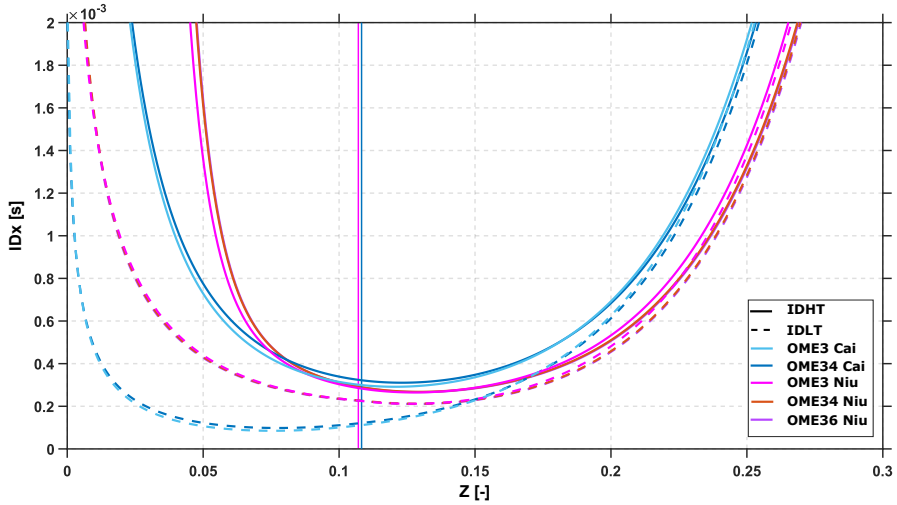

Figure 4.6: ID_{HT} for the different chains of OME_n calculated from Niu mechanism in red and Cai in blues, for closed homogeneous reactors. Both low- (dashed line) and high-temperature stage (solid line) have been quantified. Starting conditions are obtained from an adiabatic mixing between fuel and air at nominal operating (ambient temperature 900 K). Vertical solid lines correspond to the stoichiometric mixture fraction Z_{st}.

If now the focus is on comparing the two mechanisms in terms of ignition delay at high temperature, no significant differences are found around the

stoichiometric condition. Both have the most reactive mixture fraction in barely rich conditions, a little more rich Niu, but very close to each other. However, if moving to rich or lean, the Cai mechanism is shifted to lean condition respect Niu, presenting Cai with shorter high-temperature ignition delay for lean conditions than Niu's and longer ID_{HT} at rich conditions, and that happens for all the chain length considered (OME_3 and OME_{34}).

For ID_{LT}, Cai presents a behaviour similar to n-Dodecane, reaching very lean regions with the smaller ID_{LT}. Nevertheless, Niu ID_{LT} differs from n-Dodecane and Cai in this lean region, presenting higher ID_{LT} and with it minimum at stoichiometric or even rich conditions. Cai and Niu ignition delays show the same tendency at very rich conditions, almost matching ID_{HT} and ID_{LT} for mixture fractions above 0.22. These differences in low-temperature reactivity behaviour indicate a difference in the cool flame. Cai predicts a significantly more extended cool flame compared to Niu, which, as mentioned in previous section (4.2), influences the possibility of the fuel exhibiting a clearly differentiated two-step ignition, as observed in hydrocarbons, or rather a single-step ignition similar to the OME_1 behaviour.

Knowing that there are no differences between the chains lengths modelled and that the significant difference lies in the mechanism used, the differences observed in the ID will be evaluated in terms of T/Z/$\dot{Y}_c$, as in the previous section, comparing just OME_{34} results from Cai and Niu. Once again, the plots of the islands are categorized into 3 regions referring to the low, medium and high temperatures. In general terms, the islands have a highly similar structure. For this reason, isolines of $\dot{Y}_c$ have been added, as focusing on the different zones allows understanding the differences found in terms of ignition delay between mechanisms.

As mentioned earlier, the significant difference in high-temperature reactivity is given by a shift of Cai towards leaner regions compared to Niu, but with a minimum ignition delay found in slightly rich regions for both. This is reflected in the islands graph, where the high-temperature island (Region I) in both mechanisms peaks in Z values between 0.11 and 0.135, indicating similarity in the most reactive mixture fraction. On the other hand, the isoline with the level of $log(\dot{Y}_c)$= 4 that has been marked illustrates that Cai reaches leaner regions with higher levels of $\dot{Y}_c$, indicating more activity in this zone than Niu. A slight difference is also observed in this $log(\dot{Y}_c) = 4$ isoline towards the rich region, where Niu reaches Z = 0.15 with this level while Cai does not, explaining the shift in the ID_{HT} curves in Figure 4.6.

Regarding the intermediate temperature activity, represented by (Region II), both mechanisms exhibit the maximum intensity in this zone, although it

is slightly higher in Niu. In both cases, their highest intensity is between 1150 and 1500 K.

Finally, in (Region III), the differences seen in the ID_{LT} can be identified. In the lean regions, it can be seen in the ID curve (Figure 4.6) that Cai reaches very low ID values under very lean conditions, while Niu requires more ignition time for the same mixture fraction. This corresponds to the fact that in Region III of the islands plot (Figure 4.7), Cai extends towards values lower than 0.05 with the isoline of $log(\dot{Y}_c) = 2$, while Niu does not reach mixture fractions equal to 0.05 with this level of $\dot{Y}_c$. This indicates that the reactions under these conditions for this mechanism are very low and require more ignition time. Additionally, in rich regions, the medium or high activity of Niu remains closer to the inert mixture line, causing a reversal in the trend of the low-temperature ignition delay (ID_{LT}), with Niu igniting earlier in these regions.

Regarding the relationship between this region (Region II) and the low-temperature region (Region III), it is observed that in Cai, for values of Z between 0.9 and 0.12, there is lower activity compared to Niu. In other words, there is a decrease in activity when transitioning from low temperature to medium temperature, where the chemical activity increases again. This also aligns with what was mentioned about the greater cool flame in Cai, as defined by the IDx curves.

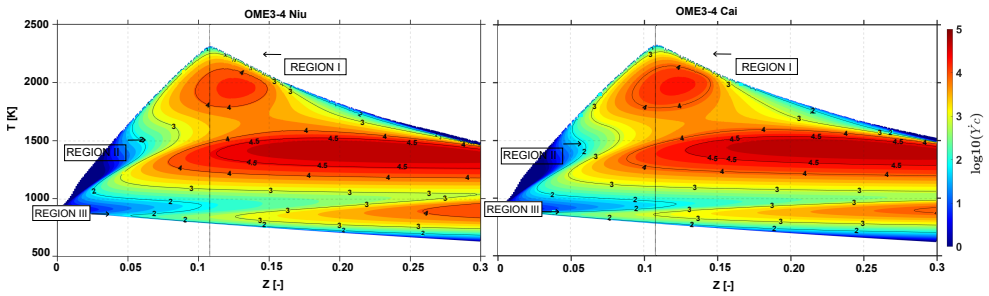

Figure 4.7: Chemical source term $\dot{Y}_c = dY_c/dt$ for homogeneous reactor calculations in terms of mixture fraction and temperature, for OME_{34} calculated from Niu mechanism (left) and Cai mechanism (right).

Therefore, considering that both mechanisms exhibit a similar ignition process, including the cool flame propagation, and taking into account that the turbulent cool flame wave occurs in sprays and promotes a reduction in ignition time compared to homogeneous flamelet ignition [23], Niu's ignition delay under spray conditions will be even lower and probably far from experiments.

The last step in the comparison is evaluating the ignition delay's sensitivity to strain rate variation. For that, results for three strain values encompassing the auto-ignition range are considered. Given the different auto-ignition characteristics of oxygenated fuels with n-Dodecane analysed in the previous section, the Figure 4.8 presenting the Ignition delay of the flamelets of the fuels for the different mechanisms also includes those of n-Dodecane. This is done to evaluate how each mechanism responds to diffusion and how it affects the previously conducted comparison.

Starting with the evolution of ignition delay at low strain (10 $1/s$), it can be said that regardless of the mechanism used for the OME_x fuels, n-Dodecane ignites earlier. If the "most reactive mixture fraction" is close to the stoichiometric condition of n-Dodecane, while for OME_x, both in Niu and Cai the most reactive mixture fraction is displaced towards slightly rich conditions, it indicates ignition under leaner conditions for n-Dodecane than the others as it was observed before. Now, focusing on the OME_x fuels, Niu predicts a lower ignition delay at low strain rate values than Cai for all the mixture fraction ranges.

As the strain rate increases, an apparent change in behaviour is observed in the relationship between the fuels. Starting with Niu, and speaking globally for both OME_{34} and OME_{36}, the ignition delay tends to decrease across the entire spectrum of mixture fraction. However, in the region of lower ignition delay, this value remains practically unchanged compared to the low-strain case for this same mechanism.

This phenomenon is not repeated for the other mechanisms that decrease their ignition time for lean conditions. However, stoichiometric or rich conditions tend to increase their ignition delay compared to the low strain rate case. At a strain rate of 500 $1/s$, the OME_{34} from Cai presents values very close to those of n-Dodecane in this range of mixture fractions. However, as we move towards the case of higher diffusion (SR = 1000 $1/s$), both Niu and Cai's OME_n experience a lower ignition time than n-Dodecane starting from a mixture fraction approximately equal to 0.6, which would correspond to a dosing of 1.33 for n-Dodecane and 0.6 for the OME_n fuels. Therefore, higher strain implies faster ignition for oxygenated fuels. The effect is more pronunced in Niu mechanism, aligning with the results presented by Rieth et al. at an ECN workshop [24], where an OME_{35} flamelet analysis with an imposed SR = 1000 $1/s$ had been compared with 0D simulations, using Niu mechanism, highlighting the diffusion effect on the ignition process.

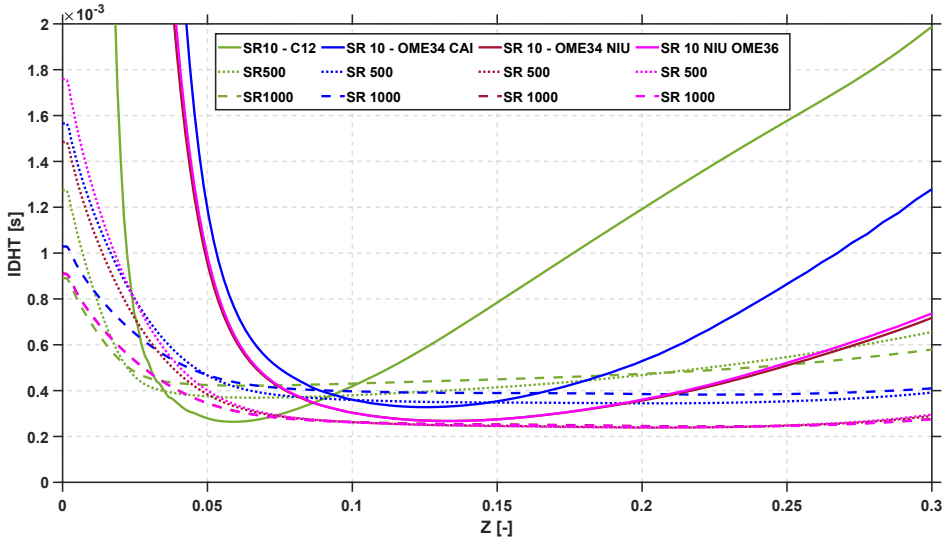

Figure 4.8: ID_{HT} for the different chains of OME_n calculated from Niu mechanism in red, Cai in blues and n-Dodecane (C12) in green, for laminar diffusion flamelet with three levels of strain rate values, 10, 500 and 1000 $1/s$ representatives of the auto-ignition range.

Jacobs vs Niu: Chemical mechanism evaluation

As stated in the introduction, the second point focuses on comparing Niu's mechanism with Jacobs's mechanism in modelling the shorter chain, OME_1. For this, a similar methodology to the one used to compare Cai and Niu has been followed, but simplified. This is because the effect of the chains is not at play here, but rather the effect of the mechanism itself.

Figure 4.9 presents the typical low-temperature and high-temperature ignition delay (ID) curves obtained using Jacobs and Niu mechanisms for OME_1. In this case, n-Dodecane has not been included due to the significant difference between these fuels already presented in the previous section, so a mechanism change will not alter these substantial differences. Regarding the two evaluated mechanisms, Niu also maintained the trend of low reactivity and single-step ignition due to the short cool flame. The significant difference is given by a lower ID obtained with Niu in almost the entire range of mixture fraction analysed, except for lean conditions, with Z values below 0.05 for low temperature and 0.06 for high temperature, where both mechanisms predict exactly the same ID.

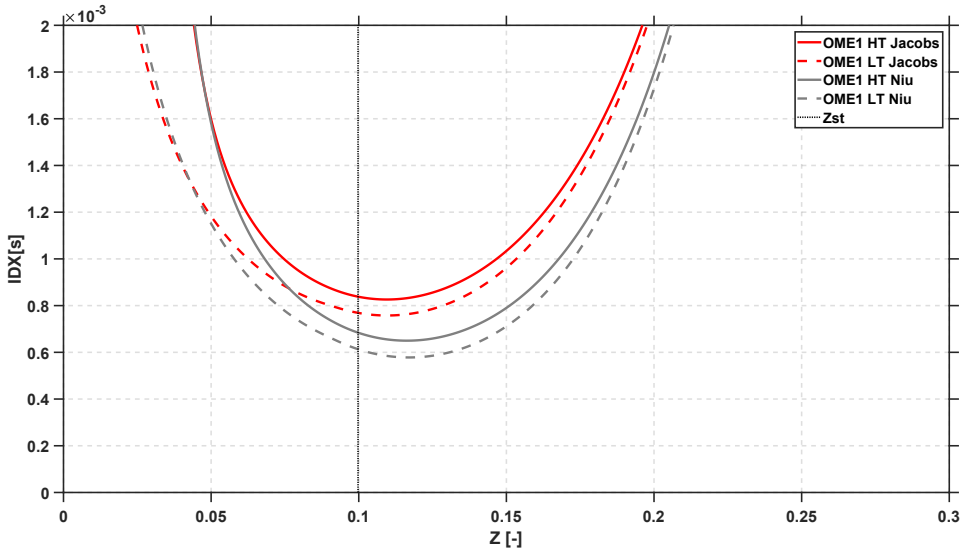

Figure 4.9: Ignition delay for the different chains of OME_1 calculated from Jacobs mechanism in red and Niu in greys, for closed homogeneous reactors. Both low- (dashed line) and high-temperature stage (solid line) have been quantified. Starting conditions are obtained from an adiabatic mixing between fuel and air at nominal operating (ambient temperature 900 K). Vertical solid line correspond to the stoichiometric mixture fraction.

Following the same reasoning, Figure 4.10 shows the reactivity islands obtained with the two mechanisms. The novelty with Niu is the presence of higher low-temperature activity (Region III) compared to Jacobs, which is very low. Similarly, in comparison with Cai, Niu exhibits higher activity near the inert mixture line than Jacobs for OME_1. Niu also shows a peak intensity in the intermediate region (Region II) of $log(\dot{Y}_c) = 4.5$, which is not reached in Jacobs. All these factors align with the lower ID (both low and high temperature) values presented by Niu across the entire range of mixture fractions. However, in Region I, Jacobs has higher intensity in high-temperature activity but with the same expansion in the Z space.

The last comparative analysis, similar to what was presented for Cai vs Niu, aims to evaluate the effect of diffusion on ID_{HT} in each mechanism. Figure 4.11 depicts the evolution of ID_{HT} in Z for three values of SR, as usual, 10, 500, and 1000 $1/s$ for OME_1. Consistent with the results from homogeneous reactor simulations, the ID obtained with Niu is lower than that obtained with Jacobs, regardless of the level of diffusion. In regions with low Z (< 0.085) and very rich conditions (> 0.15), the Niu mechanism for OME_1 behaves

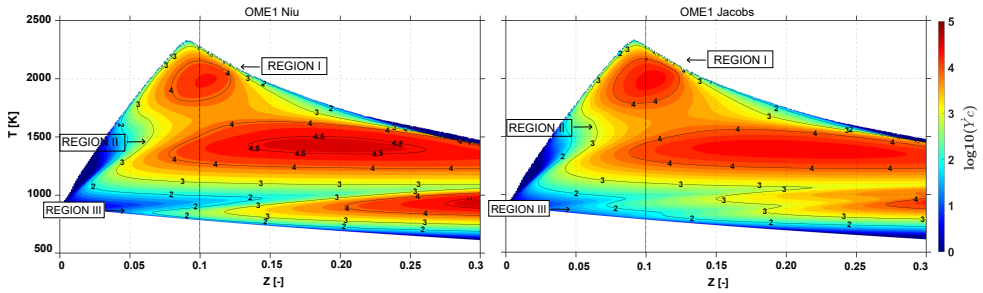

Figure 4.10: Chemical source term $\dot{Y}_c = dY_c/dt$ for homogeneous reactor calculations in terms of mixture fraction and temperature, for OME_1 calculated from Niu mechanism (left) and Jacobs mechanism (right).

similarly to the previously evaluated cases: higher SR leads to lower ID. In the most reactive zone of this fuel, with Z between 0.09 and 0.15, the Niu mechanism again appears to be minimally affected, predicting very similar IDs for all three SR values. However, a slight increase for the highest SR (1000 $1/s$) is visible compared to 10 and 500 $1/s$. This trend is notably pronounced in the ID_{HT} obtained with the Jacobs mechanism, where ignition delay time increases significantly as diffusion increases.

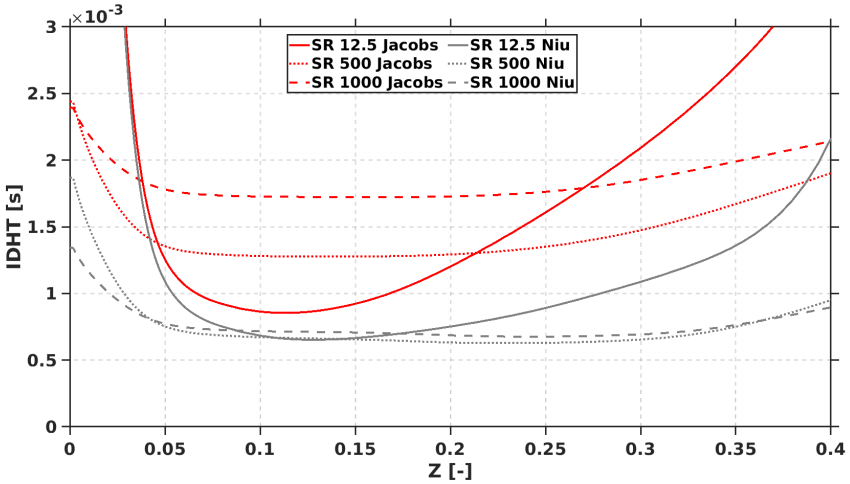

Figure 4.11: ID_{HT} for OME_1 calculated from Niu mechanism in grey and from Jacobs in red, for laminar diffusion flamelet with three levels of strain rate values, 10, 500 and 1000 $1/s$ representatives of the auto-ignition range.

4.6 Summary and conclusions

In this chapter, canonical configurations such as homogeneous reactors and laminar diffusion flamelets have been used to study the chemical kinetics of the fuels targeted in this thesis. On one hand, chemical kinetics has been analysed using homogeneous reactors, and then the influence of diffusion has been examined by considering different levels of strain rate in the flamelet calculations, allowing for the study of ignition sequence in different flamelets. Additionally, the effect of chemical mechanisms has been considered by comparing the Jacobs and Niu mechanisms for OME_1 and Cai and Niu mechanisms for OME_x. Since the Niu mechanism (recently developed) includes from OME_1 to OME_6, the influence of chain length has been evaluated when modelling an $OMEn$ mixture.

Finally, the canonical configurations have served as a tool for an initial comparison between chemiluminescent (or excited) species and their base species, which will be subsequently included in the CFD calculation of the spray. The main conclusions of the previously mentioned topics are presented below.

- Homogeneous reactors evidence differences in reactivity in terms of ignition delay and mixture fraction. Ignition delay for OME_x shows a similar behaviour to that of n-Dodecane, for both low and high temperature paths. OME_1 ignition, however, is slower than the other two, consistently with the lower cetane numbers. For both fuels, the most reactive mixture fraction is slightly rich, similarly to n-Dodecane.

- Laminar flamelets have shown the effect of diffusion on reactivity, which is later translated to the spray calculations. Compared to n-Dodecane, oxygenated fuels tend to show lower reaction rate close to the initial adiabatic mixing conditions. The ignition sequence, described in terms of maximum temperature, shows a similar path to n-Dodecane, with an initially lean low temperature ignition followed by the transition to high temperature ignition for rich conditions. Two important differences are to be noted. The first one is the absence of strong low temperature ignition for the oxygenated fuels, especially when compared to n-Dodecane. The second one is the effect of diffusion, which scales with strain rate and may eventually result in faster ignition for OME_x compared to n-Dodecane, although in the homogeneous reactor calculations the results were opposite. This highlights the effect of diffusion on ignition.

- From the modelling of chemiluminescent species, it can be concluded that the fuel does not have a significant influence in principle, as similar behaviour has been obtained in all three, with a distribution centred under rich conditions. However, in this regard, it can be observed that, on one hand, CH^* and $C2^*$ species are further shifted towards richness in oxygenated fuels compared to n-Dodecane, especially in the case of OME_1. On the other hand, it is anticipated that there are differences between the ground and excited species. For example, OH^* (mainly in oxygenated fuels) does not reach the C=1 condition, while OH does. This should be taken into account in CFD calculations, as these species are commonly used to determine the LOL, OH in CFD, and OH^* in experiments.

- From the comparison of the Cai and Niu mechanisms and the chain length for modelling the OME_x mixture, it can be concluded that the influence is more significant in the mechanism than in the chain length. Even with different levels of diffusion, it is not easy to distinguish the differences between OME_{34} and OME_{36}. Although there are differences between OME_3 and OME_{34}, they are tiny compared to the differences with the Niu mechanisms. In general, Niu exhibits lower ignition delays than Cai in homogeneous reactors and for the entire range of strain rates analysed in the flamelets. Regarding the effect of diffusion, it is interesting to note that the ID of OME_x is more influenced by the strain than n-Dodecane. At lower strain rates, n-Dodecane exhibits faster ignition, but OME_x ignites earlier as the strain rate increases. This diffusion effect on the advancement of ignition in OME_x is more accurately captured by the Niu mechanism. Change length finally does not influence so much in the results, and considering there is no available experimental data for the chemical ignition delay time of pure OME_5 and OME_6, and in Niu mechanism reaction rates of these components are extrapolated using data from $OMEn$ with lower chain lengths, Cai mechanism, more extended in the community research, is selected here to carry out the CFD simulations. On the other hand, concerning the comparison of mechanisms conducted on OME_1, while differences between Jacob and Niu exist with homogeneous reactors, they are not substantial, characterized by a lower ID with Niu. However, with flamelet results, both mechanisms predict very different trends, even at certain points, opposite ones. Jacobs demonstrates that with higher diffusion, the ID significantly increases, whereas with Niu, the diffusion effect is less pronounced, and there is no such trend regarding increased diffusion leading to a longer ignition delay time.

References

[1] David G. Goodwin, Raymond L. Speth, Harry K. Moffat, and Bryan W. Weber. *Cantera: An object-oriented software toolkit for chemical kinetics, thermodynamics, and transport processes.* URL: https://doi:10.5281/zenodo.1174508.

[2] Naud, Bertrand, Novella, Ricardo, Pastor, José Manuel, and Winklinger, Johannes F. "RANS modelling of a lifted H2/N2 flame using an unsteady flamelet progress variable approach with presumed PDF". In: *Combustion and Flame* 162.4 (2015), pp. 893–906. DOI: 10.1016/j.combustflame.2014.09.014.

[3] ENERXICO Project. *https://enerxico-project.eu/*. 2022.

[4] Jacobs, Sascha et al. "Detailed kinetic modeling of dimethoxymethane. Part II: Experimental and theoretical study of the kinetics and reaction mechanism". In: *Combustion and Flame* 205 (2019), pp. 522–533. DOI: 10.1016/J.COMBUSTFLAME.2018.12.026.

[5] Cai, Liming et al. "Auto-ignition of oxymethylene ethers (OMEn, n = 2–4) as promising synthetic e-fuels from renewable electricity: shock tube experiments and automatic mechanism generation". In: *Fuel* 264 (2020), p. 116711. DOI: 10.1016/j.fuel.2019.116711.

[6] Niu, Bo et al. "Construction of reduced oxidation mechanisms of polyoxymethylene dimethyl ethers (PODE1–6) with consistent structure using decoupling methodology and reaction rate rule". In: *Combustion and Flame* 232 (2021), p. 111534. DOI: 10.1016/j.combustflame.2021.111534.

[7] Yao, Tong et al. "A compact skeletal mechanism for n-dodecane with optimized semi-global low-temperature chemistry for diesel engine simulations". In: *Fuel* 191 (2017), pp. 339–349. DOI: 10.1016/j.fuel.2016.11.083.

[8] Mastorakos, Epaminondas. "Ignition of turbulent non-premixed flames". In: *Progress in Energy and Combustion Science* 35 (2009). DOI: 10.1016/j.pecs.2008.07.002.

[9] Payri, Francisco, García-Oliver, Jose M., Novella, Ricardo, and Pérez-Sánchez, Eduardo J. "Influence of the n-dodecane chemical mechanism on the CFD modelling of the diesel-like ECN Spray A flame structure at different ambient conditions". In: *Combustion and Flame* 208 (2019), pp. 198–218. DOI: 10.1016/j.combustflame.2019.06.032.

[10] Kathrotia, Trupti. "Reaction Kinetics Modeling of OH*, CH*, and C2* Chemiluminescence". PhD thesis. 2011.

[11] Hall, Joel Meador and Petersen, Eric L. "An optimized kinetics model for OH chemiluminescence at high temperatures and atmospheric pressures". In: *International Journal of Chemical Kinetics* 38 (2006), pp. 714–724. DOI: 10.1002/kin.20196.

[12] Smith, Gregory P., Park, Chung, and Luque, Jorge. "A note on chemiluminescence in low-pressure hydrogen and methane–nitrous oxide flames". In: *Combustion and Flame* 140.4 (2005), pp. 385–389. DOI: 10.1016/j.combustflame.2004.11.011.

[13] Tamura, Masayuki et al. "Collisional Quenching of CH(A), OH(A), and NO(A) in Low Pressure Hydrocarbon Flames". In: *Combustion and Flame* 114.3 (1998), pp. 502–514. DOI: 10.1016/S0010-2180(97)00324-6.

[14] Maes, Noud et al. "Characterization of Spray A flame structure for parametric variations in ECN constant-volume vessels using chemiluminescence and laser-induced fluorescence". In: *Combustion and Flame* 174 (2016), pp. 138–151. DOI: 10.1016/j.combustflame.2016.09.005.

[15] Google scholar. *https://scholar.google.es/*. 16 october 2023.

[16] Pastor, José V., García-Oliver, José M., Micó, Carlos, García-Carrero, Alba A., and Gómez, Arantzazu. "Experimental Study of the Effect of Hydrotreated Vegetable Oil and Oxymethylene Ethers on Main Spray and Combustion Characteristics under Engine Combustion Network Spray A Conditions". In: *Applied Sciences* 10.16 (2020), p. 5460. DOI: 10.3390/app10165460.

[17] Wiesmann, Frederik et al. "Numerical and Experimental Investigations on the Ignition Behavior of OME". In: *Energies* 15 (18 2022). DOI: 10.3390/en15186855.

[18] Preuß, Josefine, Munch, Karin, and Denbratt, Ingemar. "Performance and emissions of renewable blends with OME3-5 and HVO in heavy duty and light duty compression ignition engines". In: *Fuel* 303 (2021). DOI: 10.1016/j.fuel.2021.121275.

[19] Wiesmann, Frederik, Bauer, Esra, Kaiser, Sebastian A., and Lauer, Thomas. "Ignition and Combustion Characteristics of OME and N-Dodecane: A Comparison Based on CFD Engine Simulations and Optical Experiments". In: (2023). DOI: 10.4271/2023-01-0305.

[20] Pastor, Jose V., García-Oliver, Jose M., Micó, Carlos, and Tejada, Francisco J. "Characterization of the oxymethylene ether fuels flame structure for ECN Spray A and Spray D nozzles". In: *Applied Energy* 332 (2023). DOI: 10.1016/j.apenergy.2022.120475.

[21] Haspel, Philip et al. "Large eddy simulation of OME3 and OME4 spray combustion under heavy-duty conditions". In: *Fuel* 353 (2023), p. 129097. DOI: 10.1016/j.fuel.2023.129097.

[22] Wu, Yixuan, Ays, Isabelle, and Geimer, Marcus. "Analysis and Preliminary Design of Oxymethylene ether (OME) Driven Mobile Machines". In: *Preprint.* (2019).

[23] Dahms, Rainer N, Paczko, Günter A, Skeen, Scott A, and Pickett, Lyle M. *The role of cool-flame dynamics in high-pressure spray ignition.*

[24] Martin Rieth and Jackie Chen. *Spray A double injection DNS and OME flamelet analysis.* 2022. URL: https://ecn.sandia.gov/workshop/ECN8/ECN7.14.mp4.

[25] Akkurt, B. "Modelling multi-pulse diesel injection with flamelet generated manifolds". Phd Thesis (Research TU/e /Graduation TU/e). Mechanical Engineering, 2019.

Appendix

4.A Yc definition influence

In order to address whether the structure of the plots depends significantly on the chosen definition of Yc, and concurrently ascertain whether this would lead to different conclusions, an evaluation of the homogeneous reactor source term has been conducted for a different definition of the progress variable (Equation 4.1). This alternative definition includes CH_2O, a choice frequently made in similar approaches [25].

$$Yc = 2.7Y_{HO_2} + 1.5Y_{CH_2O} + 0.9Y_{CO} + 1.2Y_{H_2O} + 1.2Y_{CO_2} \tag{4.1}$$

Results for the three fuels under study are shown in Figure 4.12 below are very similar to the original formulation of Yc used in the study (Figure 4.2). Probably the log-scale may hide small differences at the low reactivity regions, especially where HO_2 and CH_2O may be present, but the overall extent of the different reactivity zones is the same.

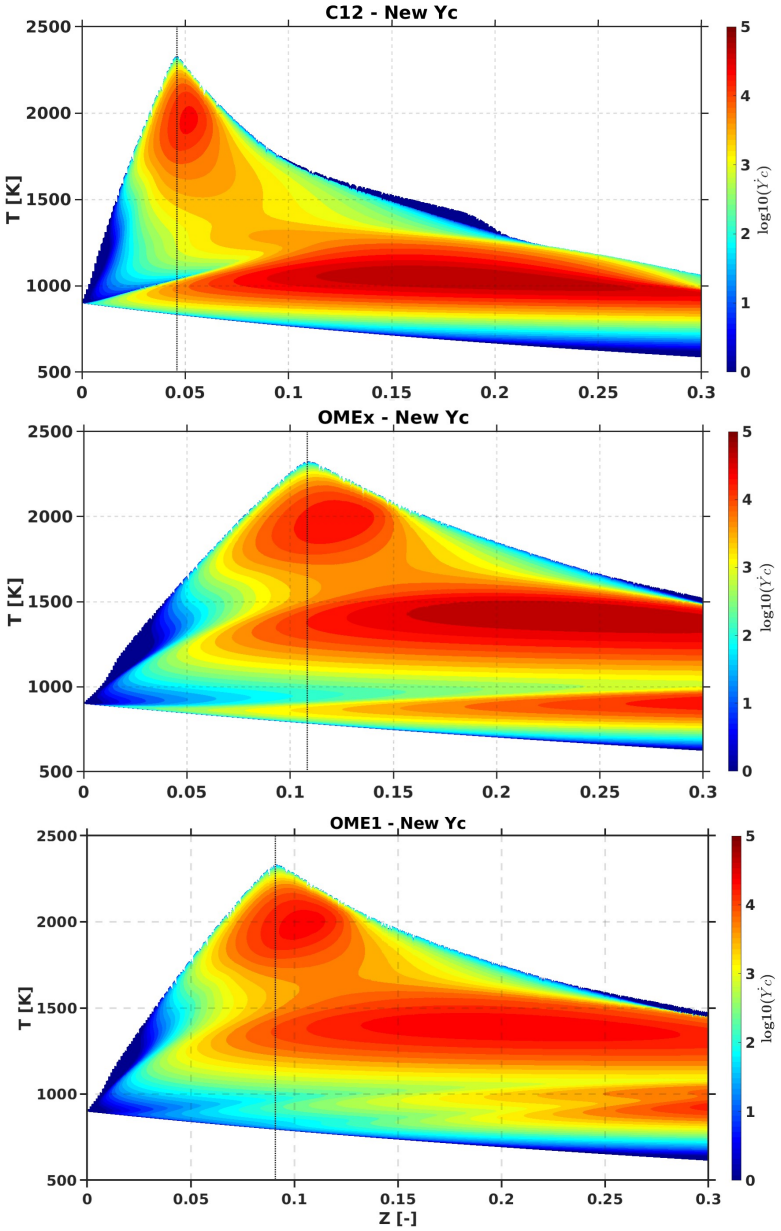

Figure 4.12: Chemical source term for homogeneous reactor calculations in terms of mixture fraction and temperature for the following definition of progress variable Yc = 2.7Yho2 + 1.5Ych2o + 0.9Yco + 1.2 Yh2o + 1.2Yco2.

Chapter 5

Analysis of fuel effects for Spray A within a RANS framework

Contents

5.1 Introduction

In this chapter, the analysis and understanding of the combustion process in a Diesel-type reactive spray is presented when a synthetic and renewable fuel such as $OMEn$-type is introduced. Special focus is laid on how the spray auto-ignites and the morphology and internal structure of the spray under quasi-steady conditions. To achieve this objective, an advanced combustion model, based on the flamelet concept, is applied within the framework of RANS turbulence models.

The large quantity of simultaneous complex processes that occur along the combustion of a Diesel spray (liquid spray atomization, dispersion, and

evaporation of droplets and heat release) are difficult to isolate and, therefore, to adequately quantify. Therefore, the design of a simplified experimental minimizes additional and unwanted effects that do not provide relevant information but only distort the measurements. These needs have led the Engine Combustion Network (ECN) [1], an internationally recognized research network in this field, already mentioned in Chapter 1 as it defines the context of this thesis, to develop a series of experiments specifically designed to measure Diesel-like sprays in dedicated combustion chambers. ECN has defined boundary conditions corresponding to those found within the combustion chamber of a Diesel engine at top dead centre. The fuel is injected at high pressure by single-hole injectors in a high-pressure and high-temperature environment. These single-hole injectors represent Diesel injection with different nozzle sizes, ranging from heavy-duty with SD to light-duty with SA.

In the context of calculations using the RANS framework, only SA simulations have been performed. However, RANS calculations carried out and presented in this chapter are considered of great importance. They represent a milestone within the thesis work plan, as they have generated know-how about the fluid-dynamic and chemical kinetic behaviour of novel $OMEn$-type fuels in the field of CFD. Furthermore, they will serve as a starting point for the LES calculations, facilitating model calibration, providing insights for result analysis, and optimizing the LES calculation matrix. This last point is crucial due to the high computational cost of LES, allowing for the selection of the most interesting conditions to study with LES based on the RANS results.

This chapter is structured as follows: First, penetration, evaporation and mixing process under inert condition for $OMEn$-type fuels and n-Dodecane is shown. After that, the analysis of the reactive spray for each fuel is presented. This analysis starts with global combustion parameters, followed by the autoignition sequence and eventually the flame structure at quasi-steady state. Although the main combustion analysis deals with $OMEx$ and OME_1, some results for n-Dodecane, which is the standard fuel for ECN studies, are included to highlight the differences between the oxygenated fuels and a more conventional hydrocarbon.

5.2 Simulation methodology

In this section, the simulation methodology within RANS calculations will be presented. A single hole spray injected into an ambient at steady conditions have been performed. Operating conditions coincide with those found in [2], where the corresponding experimental tests of the ENERXICO project [3]

are presented and serve as the validation source for all the spray calculations presented below, which were performed following ECN standards. Both experimentally and in simulations, SA injector corresponding to single-hole nozzle (reference 210675 [1]) with a diameter of 89.4 μm.

The computational domain corresponds to a cylinder representing the experimental combustion chamber, which has been meshed using the adaptive mesh refinement capabilities of $CONVERGE$. The mesh characteristics with their respective refinement levels are described in Section 3.6 Chapter 3. All the calculation have been carried out using $CONVERGE$ CFD solver [4] with the setup described in Section 3.6, the flamelets calculation results utilized in this chapter for the UFPV model were obtained using the LFLAM code [5]. As for the chemical mechanism, Jacobs et al. [6] was used to model the oxidation of OME_1, and the mechanism developed by Cai et al. has been used for OME_x blend, composed by 59.14 % of OME_3 and 40.86 % OME_4, referred as OME_x in this work.

A fuel injection rate, generated from a virtual injection rate generator [7], with an injection duration of 5 ms, is applied to achieve a quasi-steady state in a wide region of the spray as it shows in Figure 5.1. The virtual injector provides the rate shape for n-Dodecane. By combining the definition of mass flow, Equation 5.1, and injection velocity obtained through Bernoulli's principle Equation 5.2, an expression of the mass flow depending on injection pressure (ΔP_{inj}), area of the orifice (A) and density of the fuel is found. From this equation (Equation 5.3), it is possible, if the orifice area and injection pressure are kept constant, to determine the mass flow or injection rate of one fuel relative to a reference fuel just knowing the fuels densities (Equation 5.4).

$$\dot{m} = \int \rho u dA = \rho u C_A A \rightarrow u = \frac{\dot{m}}{\rho C_A A} \tag{5.1}$$

$$u = C_v \sqrt{\frac{2\Delta P_{inj}}{\rho}} \tag{5.2}$$

$$\dot{m} = \rho C_A C_V A \sqrt{\frac{2\Delta P_{inj}}{\rho}} \tag{5.3}$$

$$\dot{m}_{OMEn} = \dot{m}_{C12} \sqrt{\frac{\rho_{OMEn}}{\rho_{C12}}} \tag{5.4}$$

This approach assumes that the flow loss coefficients at the nozzle (C_A, C_V) are independent of the fuel, and the values used are those obtained

experimentally, $C_A = 0.98$, $C_V = 0.92$ [8, 9]. Aside from previous scaling law for $\dot{m}$, this assumption results in a fuel-independent momentum flux at the nozzle, as it is shown in Equation 5.5 in which the Equation 5.2 is used in the right part.

$$\dot{M} = \int \rho u^2 dA = \rho u^2 A \rightarrow \dot{M} = 2\Delta P_{inj} A \tag{5.5}$$

Table 5.1 present the density at 373 K used to calculate the injected mass of each fuel, starting for n-Dodecane values. The value of the density at this temperature was selected from the liquid properties' database used in CFD calculation presented in Section 3.2 to be consistent.

	ρ [kg/m^3] @373K	Injected mass [kg] (at 5ms)
n-Dodecane	679	1.27E-5
OME_x	960	1.50E-5
OME_1	681	1.28E-5

Table 5.1: Total mass injected of each fuel during 5 ms.

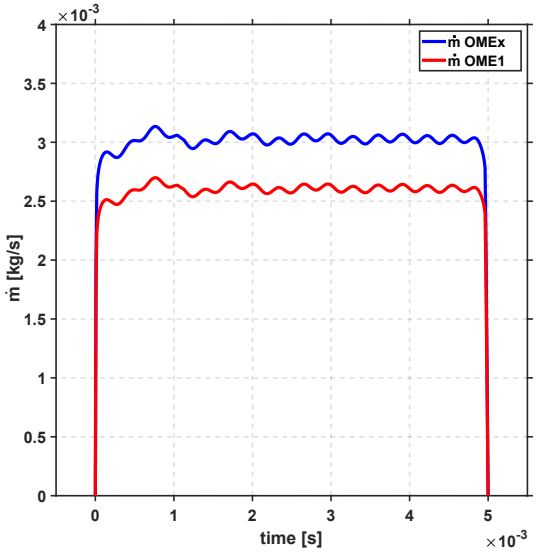

Figure 5.1: ROI profiles for the SA, for OME_x (blue) and OME_1 (red) obtained by adapting the results of the CMT virtual injection generator for n-Dodecane [7]

.

The nominal condition for SA is characterized by the following boundary conditions: an ambient temperature (T_{amb}) of 900 K, an oxygen molar

concentration (X_{O2}) of 0.15, and a density (ρ) of 22.8 kg/m^3. Table 5.2 summarizes the calculated CFD cases under reacting conditions. For each fuel, three calculation cases were carried out to assess the effect of varying ambient temperature of the combustion chamber into which the fuel is injected, while keeping constant density and oxygen content to evaluate the impact of boundary conditions on spray structure. Meanwhile, the mixing process studied under inert conditions is only conducted for the nominal condition (900 K). All the simulations within RANS framework have been done following previous work developed for the group, in which the validation of the model setup for n-Dodecane has been done using the ECN reference inert conditions, for which an extensive database is available, containing measurements of liquid and vapour penetration, mixture fraction and velocity field. The complete validation has been shown [10, 11]. Therefore, in the present study, only the injection conditions have been adapted to those of the ENERXICO project: the injection rate of each fuel and fuel properties.

Fuel	OME_x
	OME_1
Ambient Temperature	1000 K
	900 K
	800 K
Ambient density	22.8 kg/m^3
Ambient O_2 composition	15 %
Injection pressure	150 MPa
Fuel temperature	363 K
Nozzle diameter	SA - 89.4 μ m

Table 5.2: Thermodynamic and fuel injection conditions for the simulated reacting CFD cases within RANS framework, nominal temperature in bold.

5.3 Inert spray mixing characteristics

Simulating the inert spray, which means injecting it into an oxygen-free environment, allows for the separation of the simulation model from the fuel reactivity and enables the analysis of the main physical phenomena that occur in the spray, such as atomization, evaporation, and fuel-air mixing and the spray model validation, to validate global quantities according to ECN guidelines, the spray tip penetration is determined as the axial distance to the farthest point where the mixture fraction (Z) reaches a value of 0.001. The liquid length, on the other hand, is obtained at the axial position that encompasses

97% of the liquid mass. This validation is essential because the subsequent combustion process takes place within the multiphase flow analysed at this stage. Furthermore, under inert conditions, the study of grid independence is also conducted, this last point is not carried out in this work because, as mentioned earlier, the calculations with RANS turbulence modelling have been performed using a computational workflow, which was developed and validated for n-Dodecane sprays. [11].

However, Figure 5.2 shows how the computational setup reproduces the global parameters of mixture, vapour penetration is accurately predicted, for the $OMEx$ blend and the OME_1. Within the experimental campaign carried out in the context of the ENERXICO project, no tests were conducted under inert conditions. Therefore, the present validation has been performed using n-Dodecane inert results from CMT [7] database at the same condition (nominal SA) for this nozzle. Due to the fact that spray penetration while under inert conditions does not depend on the fuel, depends on the momentum flux [12] and as it was recently shown, momentum is independent of the fuel. Furthermore, this was clearly observed in the work presented by Garcia [13], where penetrations under reactive conditions overlap until each fuel ignites and experiences different accelerations influenced by the chemistry of each fuel. For this reason, the reactive case of the OME_1 900 K has been added, since it ignite late, at 1.3 ms, so it is possible to verify that the numerical result of vapour penetration up to that point of the inert cases aligns with this penetration, as well as with the n-Dodecane reference (under inert condition).

The other typical global parameter for validation is the liquid length, which is directly related to the fuel volatility properties, and hence it is not possible to use n-Dodecane results to validate $OMEx/OME_1$ predictions. For this reason, only the stabilized liquid length values obtained from tests under reactive conditions have been used as references. Both fuels show deviations from the experimental values. It is expected that an inert result would have a longer liquid length than a reacting one, which aligns with what is observed for OME_x. However, in the case of OME_1, the value obtained under inert conditions with CFD underestimates the experimental value observed under reactive conditions. In spite of that, given the very accurate prediction of vapour penetration and the well-known large Lift-off length exhibited by these fuels, it is considered that an imprecise prediction of the liquid length will not have significant effects on the combustion development. Considering the objectives of this study, these deviations in the liquid length are considered as acceptable.

Furthermore, from the inert cases performed in order to isolate the mixing

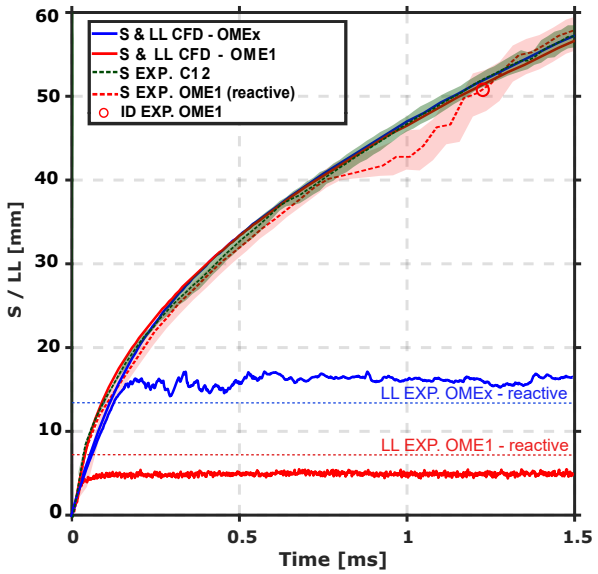

Figure 5.2: Spray tip penetration and liquid length for SA for OME_x and OME_1 under inert conditions, experimental tip penetration is for n-Dodecane, considering that under inert conditions fuels penetrate.

process of the combustion effects Figure 5.3a shows the evolution of the mixture fraction on the spray centreline for n-Dodecane [10], OME_x and OME_1 for nominal SA condition. Results show that the evolution is quite similar for all three fuels, with different plots peaking close to the location where the maximum liquid length is found, and dropping downstream with the typical x^{-1} law [14, 15]. Mixture fraction is very similar between n-Dodecane and OME_1 from 10 mm up to the tip of the jet, while OME_x shows slightly higher mixture fraction values. Figure 5.3b shows the mixture fraction evolution on the centreline versus the axial coordinate normalized by the equivalent diameter of each fuel, $x^* = x/d_{eq}$. The equivalent diameter is defined according to Equation 5.6.

$$d_{eq} = d_o \sqrt{\frac{\rho_f}{\rho_a}} \tag{5.6}$$

where d_o stands for the nozzle effective diameter, and ρ_f and ρ_a correspond to fuel and air density. Starting from n-Dodecane, fuel density increases 15% and 40% when moving to OME_1 and OME_x, respectively (Table 2.1), while all other parameters are constant. The normalized plot evidences that the scaling law is adequate, and that the only differences among mixture fraction

distribution downstream of the liquid length are due to the effect of fuel density, in agreement with previous knowledge from mixing-controlled turbulent sprays. Therefore, mixture fraction distribution for OME_1 is essentially coincident with that of n-Dodecane [10], and OME_x will have a slightly higher mixture fraction values due to the higher density. Inert calculations were not extended to other ambient temperature cases, but if one accounts for the scaling parameter, mixing distribution should be the same, as the temperature sweep has been carried out at constant ambient density. The only expected difference will be related to maximum liquid length, but due to the relatively high volatility of these fuels, no other major differences are expected.

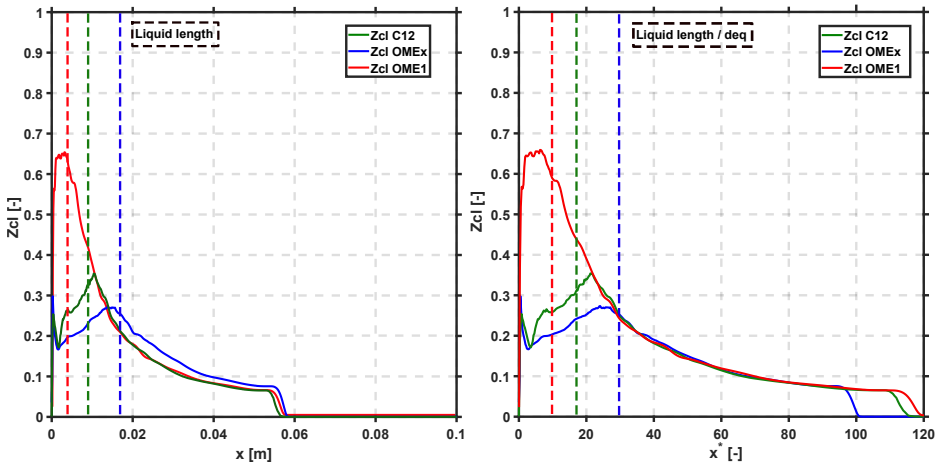

Figure 5.3: Mixture fraction profiles on the spray axis at 1.5 *ms vs axial distance* (*a*) *and vs normalized axial distance* (*b*). *Nominal inert condition.*

5.4 Global combustion parameters

In the present section, predicted combustion global parameters for OME_x and OME_1, namely tip penetration and lift-off length results are presented to give an overview of the prediction capabilities of the modelling approach. Numerical results are compared to those obtained from experiments for validation purposes. Tip penetration and ignition delay (ID) are determined from schlieren, and lift-off length (LOL) is obtained from OH^* chemiluminescence [2]. On the CFD side, ECN recommendations are followed. Similarly to the inert case, tip penetration is defined as the axial distance from the nozzle to the maximum location where mixture fraction reaches a value of 0.001, ID is defined as the time elapsed from the start of injection to the point where the maximum

derivative of the maximum of temperature in the domain is achieved, and LOL is defined as the minimum axial distance from the nozzle to the closest location where 14% of the maximum value of the mass fraction of OH in the domain is reached.

The time evolution of tip penetration and lift-off length for both fuels and the different temperature values is shown in Figure 5.4. Additionally, ignition delay and stabilized lift-off length value are presented in Table 5.3. Results show the steadily increasing tip penetration with time, while lift-off length is observed starting from ignition delay, with an initially decreasing evolution until a quasi-steady value is reached. Tip penetration evolution coincides with previous experimental and numerical results in the literature [16–19] progressing with the well-known inert evolution from the start of injection until some time after ID. At ignition timing, the jet expands radially, and there is a reorganization of the flow during which tip penetration does not depart from the inert one. Once this flow reorganization occurs, tip penetration accelerates and proceeds faster than the inert case.

For the investigated temperature sweep, tip penetration of all three temperature cases overlap for timings before ID. This parameter is governed by nozzle momentum flux and ambient density, which are all constant. The overlap continues until some period after ignition, from which tip penetration acceleration eventually occurs. This acceleration process is delayed with lower ambient temperature, concurrently with the stabilization of LOL further away from the nozzle [20]. For the OME_x 800 K case, ID is around 4 times longer than for 900 K and 6 times longer than for 1000 K. This results in an almost inert tip penetration until 1.2 ms for the 800 K case, at a much lower rate compared to the two other cases. A similar conclusion can be derived for OME_1 cases.

Predicted tip penetration for OME_x (Figure 5.4, left) agrees with experiments until ignition timing, after which a slight over-prediction is obtained for 900 and 1000 K, and satisfactory agreement is observed for the 800 K case. Lift-off length predictions for OME_x also match experimental values, especially in the quasi-steady state. ID and quasi-steady LOL values are presented in Table 5.3, confirming the good agreement between experiments and simulations for all temperatures values.

Figure 5.4 (right) also shows spray tip penetration and lift-off length for OME_1 at the three ambient temperature conditions. The overall evolution is essentially the same until ID, but this characteristic timing is reached later due to the lower reactivity of OME_1. After ID, spray tip acceleration is also observed, with differences among conditions depending on the ignition

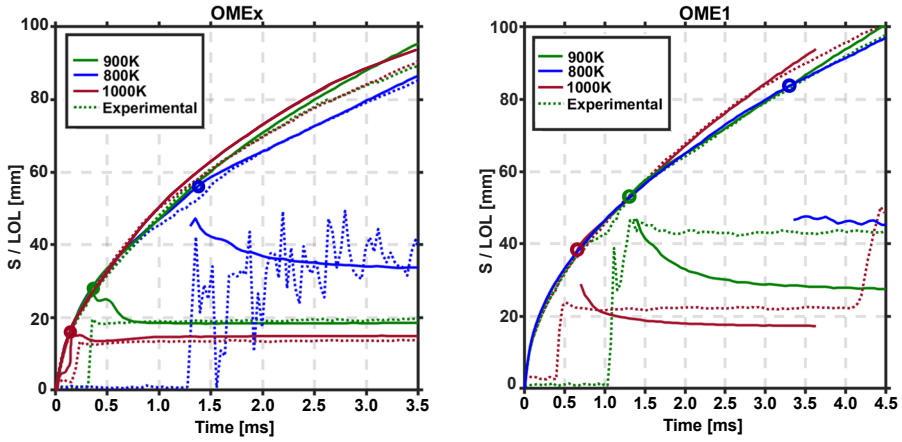

Figure 5.4: Time evolution of tip penetration and lift-off length for OME_x (left) and OME_1 (right). Solid and dashed lines correspond to CFD and experimental results, respectively. Marker shows the ID timing as derived from CFD calculations (5.3).

	800 K		900 K		1000 K	
	Exp.	CFD	Exp.	CFD	Exp.	CFD
ID $OMEx$ [ms]	1.21 ± 0.08	1.26	0.033 ± 0.02	0.34	0.19± 0.01	0.18
ID OME_1 [ms]	-	3.30	1.20 ± 0.08	1.31	0.45 ± 0.03	0.66
LOL $OMEx$ [m]	0.037 ± 0.022	0.034	0.019 ± 0.0008	0.020	0.0140 ± 0.0005	0.015
LOL OME_1 [m]	-	0.050	0.040 ± 0.002	0.030	0.020 ± 0.001	0.020

Table 5.3: Ignition delay and stabilized lift-off length for both experimental results and CFD calculations. Experimental data include both average and standard deviation.

timing. Lift-off length is also seem to stabilize further away from the nozzle compared to OME_x. Comparison between simulation and experimental results show excellent agreement for tip penetration, while predicted lift-off length presents a strong flame recession at 900 and 1000 K, which is not observed in experimental results. This results in an under-predicted stabilized value of the lift-off length, which is noticeable at the highest temperature and becomes much more evident at the nominal one. It must be noted that no ignition was obtained in experiments for 800 K due to the low ambient temperature together with the low fuel reactivity. This behaviour was not reproduced by the numerical results, where a very late ignition was obtained at 3.3 ms. However, numerical results for 800 K are still presented for substantiation of the obtained flame topology in later sections.

Differences between both fuels are obviously linked to the fuel reactivity characteristics, which have been discussed in previous sections at flamelet level

(Section 4.3). The subsequent section will discuss the spray ignition sequence to help draw an overall picture of the combustion characteristics of both fuels.

5.5 Spray autoignition sequence

This section describes the analysis of autoignition in terms of rate of heat release and mass species, both in terms of the spatial and temporal evolution. Previous results have shown that 1000 and 900 K exhibit a very similar tip evolution, ignition timing and LOL stabilisation. Therefore, only the sequence corresponding to 900 and 800 K is presented for both OME_x and OME_1. Starting for the nominal condition (900 K) for OME_x, Figure 5.5 shows the fields of local heat release rate (right panel) and mass fraction of CH_2O and OH (left panel). These two species are used as tracers for low and high temperature ignition, respectively. Keeping in mind that modelled ID for this case is 0.344 ms, several time instants have been selected around this timing to describe the autoignition sequence.

Contours show the appearance of CH_2O at the same time (0.22 ms) as the low temperature heat release rate begins to rise mildly. This is consistent with the concept of using CH_2O as a tracer of the low temperature ignition. As time advances, the spray is seen to grow both in axial and radial directions. Starting at 0.38 ms, which is the first frame after ID (0.344 ms), a noticeable increase in OH mass fraction can be observed, concurrent with a drop in total CH_2O as well as a sharp increase in heat release rate. Both OH and the most intense heat release are located at the tip of the spray.

Once ID timing is elapsed, the flame progress and develops into a typical diffusion structure, with CH_2O distributed around the centre of the spray and OH mainly on the stoichiometric reacting surface. Both the total mass of CH_2O and the heat release rate (showed in the bottom panel) stabilize, while OH mass increases due to the elongation of the diffusion flame front. The overall species distribution is similar to that presented in [10] for n-Dodecane at the same operating conditions, hinting at a very similar flame topology for OME_x and regular hydrocarbons.

Figure 5.6 shows the ignition sequence for the lower temperature case (800 K). Spray tip is observed to be longer than for the nominal case due to the later ignition timing. However, the stoichiometric surface does not increase with the spray tip, but becomes stabilized with a maximum length of 40 mm after 0.86 ms. This behaviour creates a lean region between the stoichiometric surface and the tip of the spray where ignition is seen to occur.

A very different distribution of species and heat release is found during ignition. CH_2O is seen to be relatively uniformly distributed throughout the whole spray width until 1.22 ms, after which both heat release and OH appear at the very tip of the jet. This ignition site later recedes towards the orifice, as seen both in heat release and OH along the different timings until 1.7 ms. At this latest timing, heat release rate is seen to start from a region at around $x = 35$ mm close to the spray radius and extends almost linearly towards the spray centre, which is reached at around $x = 47$ mm, where the maximum OH values are found. Note that a detailed inspection shows that maximum OH is not always coincident with maximum heat release locations. Heat release rate layer is close to the stoichiometric surface but clearly on the lean side. Compared to the nominal temperature, flame ignition occurs under lean conditions, which is rarely found in Diesel-like sprays.

Figure 5.7 shows the autoignition sequence for OME_1 at 900 K, which is quite different to the corresponding OME_x condition. Contours show actually more similar features to those of the low temperature 800 K OME_x case. CH_2O is uniformly distributed before 1.28 ms, with absence of low-temperature heat release. OH is first observed between 1.28 and 1.4 ms at the tip of the jet, concurrently with a sharp increase in both local and global heat release rate, from which it later recedes towards the nozzle. Similarly to the 800 K OME_x case, high temperature ignition is seen to occur in a lean region outside the stoichiometric surface, which remains steady from the first instant until being reached by the later heat release recession at 1.52 ms. After that, stoichiometric surface increases in length due to the lower entrainment linked to the drop in local density, and it ends up interacting with the heat release front. The last frame shows a heat release rate front anchored at the tip of the stoichiometric surface, with OH located further downstream under lean conditions.

Due to the particular flame structure developed by OME_1, it is also interesting to show the autoignition sequence of the case with the lowest ambient temperature, Figure 5.8. It is worth reminding the fact that, based on experimental results [2], OME_1 did not ignite at this operating condition, but CFD calculations predicted reaction onset. In this case, the analysis of species and local heat release shows a similar sequence to that at 900 K (CH_2O uniformly distributed, high temperature ignition occurring at the jet tip and the reaction zone receding towards the orifice until stabilization). However, both ignition and flame stabilization occur later in time and further away from the orifice. Furthermore, the observed recession of the reaction zone after ignition does not reach the stoichiometric surface, and hence the reaction zone always occurs under lean conditions.

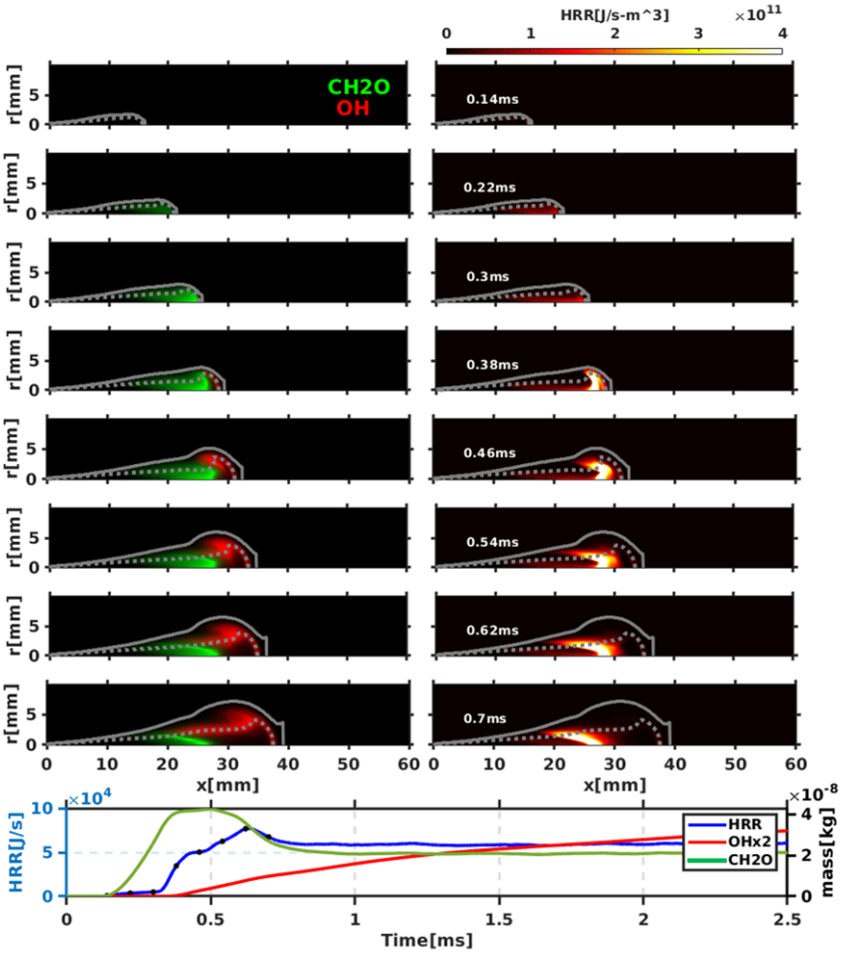

Figure 5.5: Time sequence of CH_2O and OH mass fraction (left panel) and local heat release rate (right panel) around ignition timing for OME_x at 900 K. Colorscales of species are normalized to the instantaneous maximum. Spray radius and stoichiometric mixture fraction iso-contour are marked with solid and dotted lines, respectively. Bottom plot shows the time-resolved total species mass and heat release rate.

Finally, Figure 5.9 shows the evolution of the maximum temperature in the CFD domain at each time step against the mixture fraction value at which this occurs. The layout is then very similar to the one used for the laminar flamelets (Figure 4.4). OME_x at 900 K presents a similar autoignition sequence as in flamelets, with an initially lean low temperature ignition that propagates to rich mixtures, where it eventually runs into the high temperature phase. This

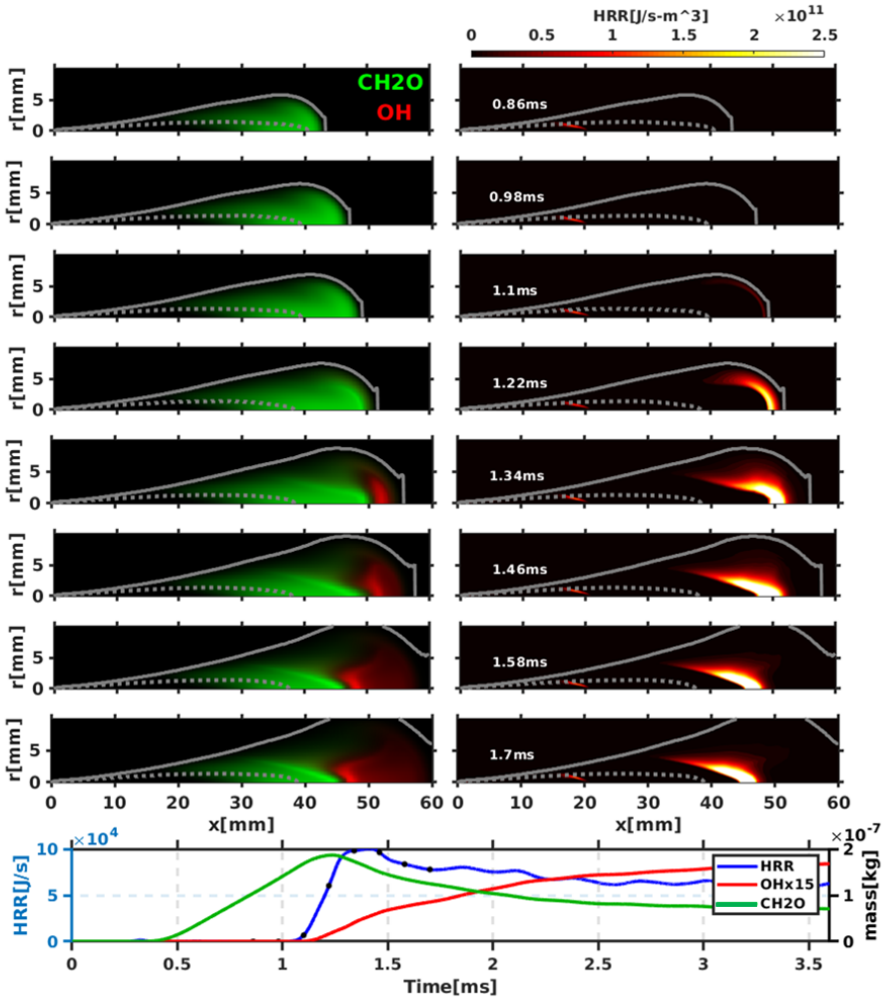

Figure 5.6: Time sequence of CH_2O and OH mass fraction (left panel) and local heat release rate (right panel) around ignition timing for OME_x at 800 K. Colorscales of species are normalized to the instantaneous maximum. Spray radius and stoichiometric mixture fraction iso-contour are marked with solid and dotted lines, respectively. Bottom plot shows the time-resolved total species mass and heat release rate.

is also similar to the typical ignition sequence for n-Dodecane. For all other three cases, namely OME_x at 800 K, and OME_1 at 800, 900 K, the evolution is quite different, with chemical activity always proceeding at lean conditions. These results evidence that spray ignition for these conditions is quite different from that of laminar diffusion flamelets.

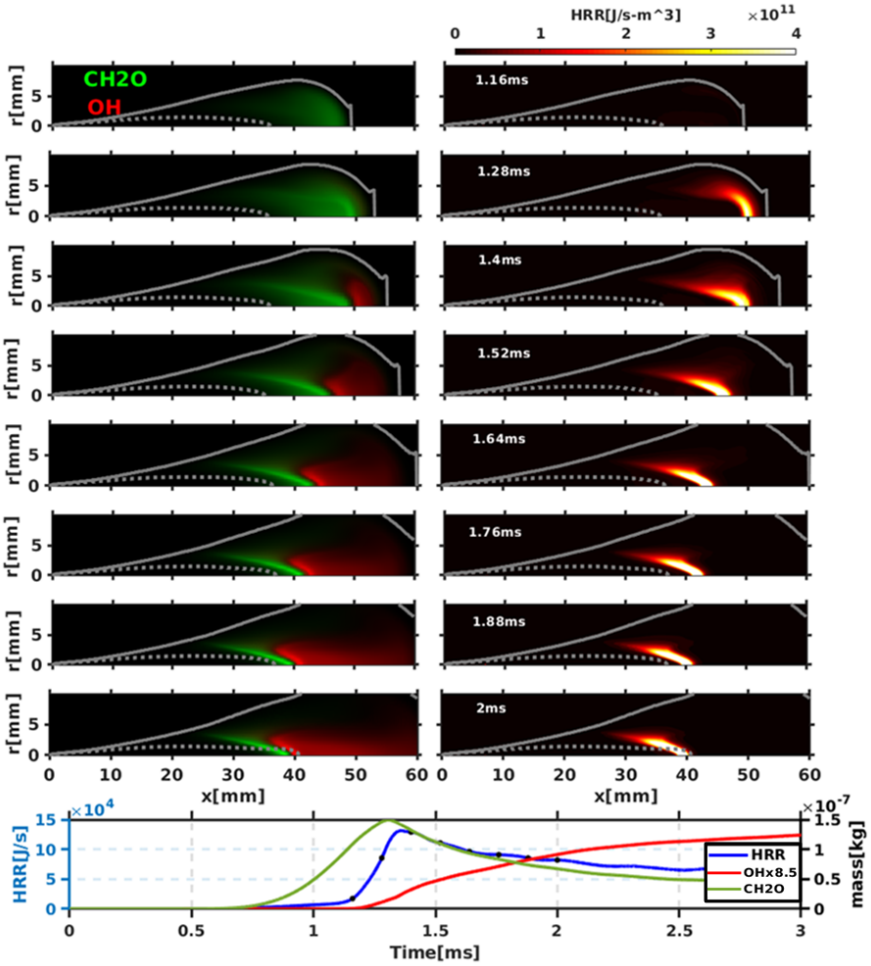

Figure 5.7: Time sequence of CH_2O and OH mass fraction (left panel) and local heat release rate (right panel) around ignition timing for OME_1 at 900 K. Colorscales of species are normalized to the instantaneous maximum. Spray radius and stoichiometric mixture fraction iso-contour are marked with solid and dotted lines, respectively. Bottom plot shows the time-resolved total species mass and heat release rate.

To give a first explanation of the difference in the ignition sequence between flamelets and sprays, one can resort to the amount of time spent by the fuel at a given mixture fraction/equivalence ratio value. The mixing field in flamelet space can be considered as having an initial time of a given mixture that is not zero, in the sense that all mixture fraction values exist due to the definition of the canonical configuration, while in the spray cases, the mixing field develops

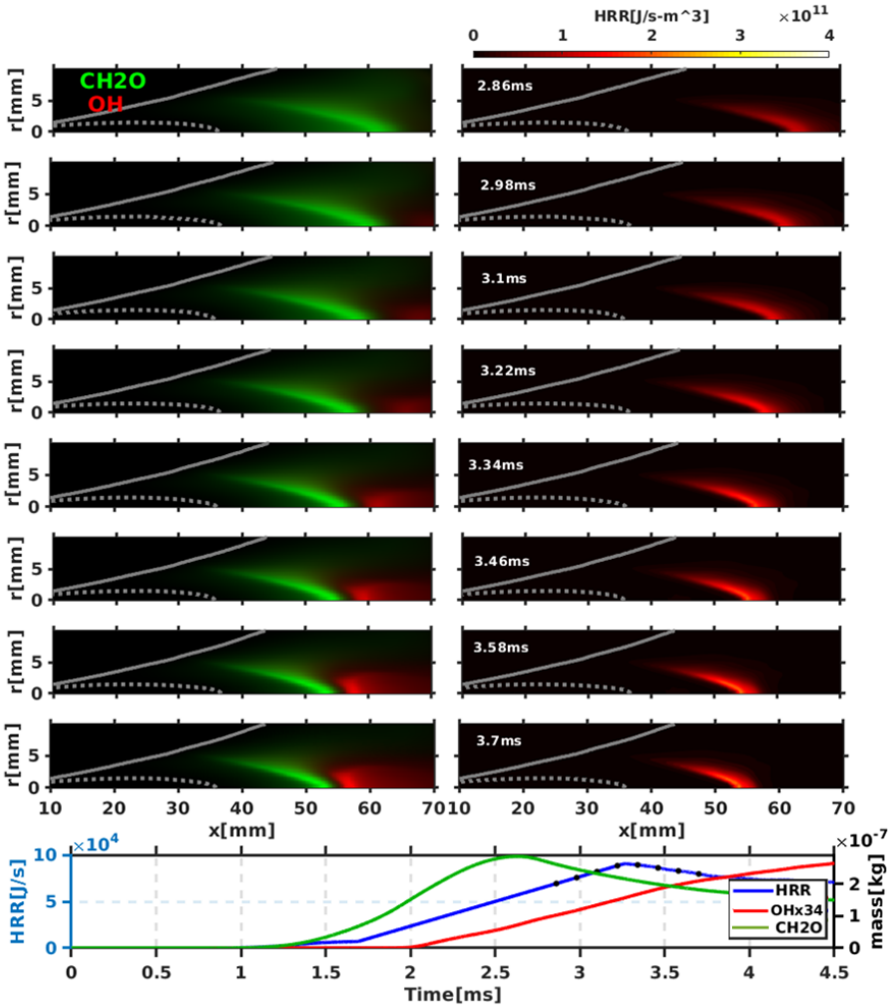

Figure 5.8: Time sequence of CH_2O and OH mass fraction (left panel) and local heat release rate (right panel) around ignition timing for OME_1 at 800 K. Colorscales of species are normalized to the instantaneous maximum. Spray radius and stoichiometric mixture fraction iso-contour are marked with solid and dotted lines, respectively. Bottom plot shows the time-resolved total species mass and heat release rate.

with time. As shown in [10], the amount of time spent by the fuel at a given mixture fraction changes along isolines of mixture fraction, and it increases when moving downstream and further way from the axis. This finite time spent by the fuel has strong implications on how reaction develops in mixture

fraction space versus spray calculations, and can be considered as a first factor explaining differences between Figure 5.9 and Figure 4.4.

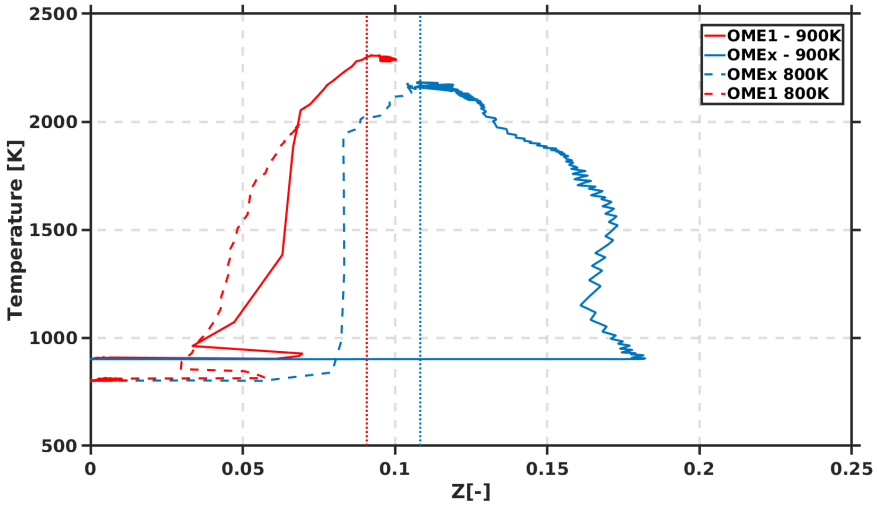

Figure 5.9: Evolution of instantaneous maximum temperature along ignition as a function of mixture fraction, as derived from CFD results for both oxygenated fuels at 800 *and* 900 K.

5.6 Flame structure at quasi-steady state

In this section, the effect of ambient temperature on the flame structure is analysed at quasi-steady state for both fuels and all temperature conditions. Figure 5.10 shows spatial distribution of heat release rate (top), scaled mass fractions of CH_2O and OH (middle) as well as normalized progress variable (bottom). The spray radius is plotted with gray solid line, the blue vertical line indicates the LOL position and the stoichiometric mixture fraction is plotted with a dashed gray line as in Figure 5.5. Note again that the OME_1 case at 800 K is just a hypothetical situation, as experiments show that ignition does not happen for this condition.

Consistently with the last frames of Figure 5.5, $OMEx$ results at 900 K show a heat release zone at the flame base upstream of the LOL region, which can be associated to the low temperature ignition stages. Then, an intense heat release zone is found at the lift-off location, and further downstream heat release is found on the stoichiometric surface. Note the log colour-scale for

HRR compared to previous Figures 5.5 to 5.8, which makes it possible to visualize the reaction zone around stoichiometric conditions. This structure is very similarly to n-Dodecane cases shown in [10]. As for species, CH_2O is first found slightly upstream of the lift-off length location and extending towards the spray centreline, always within rich mixtures, while OH is found on top of the stoichiometric surface, where the diffusion flame high temperature reaction occurs. The spatial distribution of species has good correlation with recent experimental results [21] obtained by measuring CH_2O and OH radical distributions using PLIF techniques. Moving to 1000 K, the quasi-steady flame topology remains very similar to that of the nominal temperature, except for the reduction in LOL. A typical diffusion flame is still observed, very similar to n-Dodecane case in [10].

On the other hand, the bottom row for $OMEx$ shows local heat release rate for the 800 K case. The long LOL and concurrently short stoichiometric surface implies that local heat release is only present at around the lift-off location, with no further reaction on the downstream part of the stoichiometric surface. This heat release structure can be seen to modify the spatial distribution of the relevant species. CH_2O is seen to be present much extensively upstream of the lift-off location, while OH is essentially located downstream of the CH_2O surface, instead of extending on the stoichiometric surface. The flame topology under quasi-steady conditions, hence, is governed by the presence of a highly premixed reaction front at the very tip of the stoichiometric surface.

Finally, at the bottom, the normalized progress variable C field is shown. This variable indicates when the reaction state reaches steady conditions. Similarly to both heat release and relevant species, no big differences are found between 900 K and 1000 K, where the transition towards equilibrium values occurs at the lift-off length throughout the whole radial cross-section. At 800 K, however, a fast transition is seen at the tip of the stoichiometric surface, but this transition is more gradual at radial locations higher than the stoichiometric ones, hinting at a lower reactivity within such lean locations.

Figure 5.10 also shows results at quasi-steady state for OME_1. Overall, the case at 1000 K is quite similar to those for OME_x at 900 and 1000 K, i.e. a typical lifted diffusion flame with the intense heat release rate starting at the lift-off and extending along the stoichiometric surface. For OME_1 the stoichiometric surface stabilizes closer to the nozzle compared to OME_x. This is mainly due to the lower fuel density, as the analysis of the inert spray distribution in Section 5.3 has shown. The distribution of both relevant species and progress variable is also overall similar to the corresponding OME_x cases.

On the other hand, results at 900 and 800 K are more similar to the

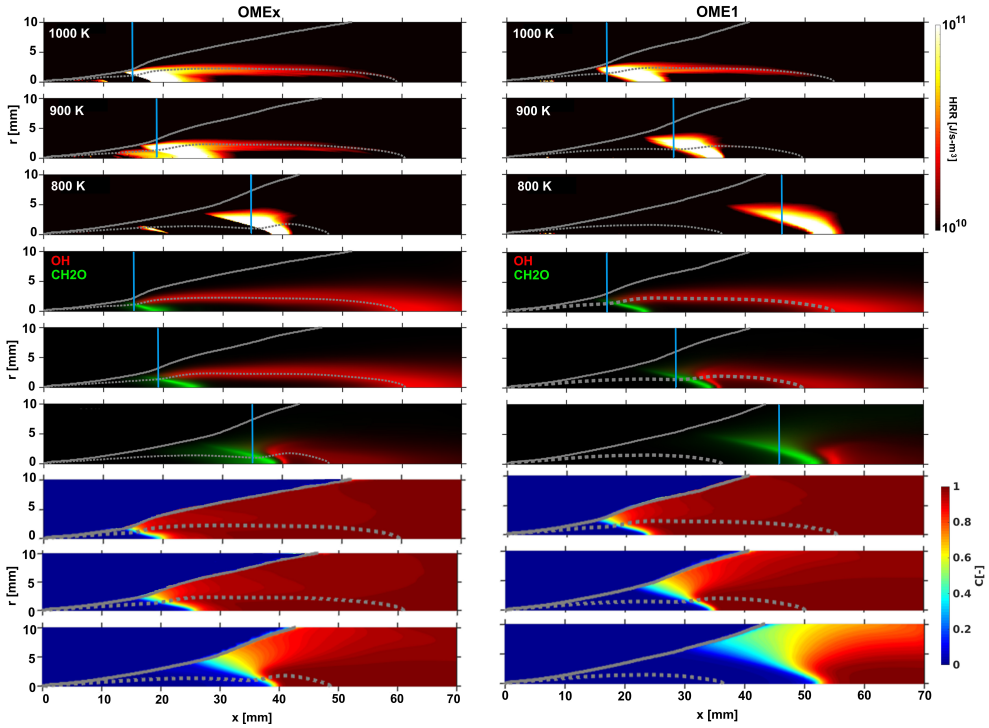

Figure 5.10: Quasi-steady local HRR contour (top), normalized CH_2O and OH mass fractions (middle) and normalized progress variable (bottom) at ambient temperature of 800K (bottom), 900K (middle) and 1000K (top) for OME_x in the left panel and OME_1 in the right one. Solid grey line represent the spray radius, dashed green line drawn at $\phi = 1$ and the corresponding lift-off length of each case is shown with the blue vertical line.

800 K OME_x case, showing a lift-off length stabilizing close to (900 K) or downstream (800 K) the tip of the stoichiometric surface. In fact, the OME_x case at 800 K seems to be an intermediate situation between the OME_1 cases at 900 K and 800 K. The reduction in reactivity due to a low ambient temperature or a low reactive fuel evidence similar effects, i.e. it shifts the lift-off length downstream, which for these oxygenated fuels strongly interacts with an intrinsically short stoichiometric surface. This displaces the main reaction zone further downstream and eventually, a lean mixing-controlled flame is obtained, with the reaction zone happening at equivalence ratio below 0.72. This behaviour is also reflected in the spatial distribution of relevant species and progress variable. In the latter case, the normalized progress has a more gradual transition towards steady conditions, quite different from the

typical diffusion flame. Although not shown here, the maximum temperature of the 800 K case will be dictated by that of the lean premixed front, which could have advantages in terms of NO_x formation.

For both fuels and all temperature cases, the evolution of the normalized progress variable around the lift-off location shows that CH_2O peak values are found at locations where progress variable starts to rise, while OH tends to occur in locations where progress variable is close to the steady value.

Figure 5.11 below shows scatter-plots of temperature (left) and local heat release (right) versus equivalence ratio at 4 ms with markers coloured in red for those locations where Y_{OH} and Y_{CH_2O} is larger than a 20 % of the maximum value for the cases of low temperature condition but also for OME_1 at 900 K, due to its also lean mixing-controlled flame structure. Results show that OH and CH_2O mark the high and low temperature stages (left), but, the highest heat release rate are not concurrent with peak OH, but rather with peak formaldehyde zones. This is evident for the 800 K cases, where the reaction front is fully in the lean region. Further detailed analysis Figure 5.11 indicates that for the low temperature cases, where the flame front is in fully lean regions, peak heat release rate occurs in locations concurrent with high CH_2O concentrations, and not with high OH, which is usually the case when a diffusion flame front exists.

5.7 Summary and conclusions

In this chapter, the combustion process and flame topology for isolated liquid sprays have been computationally studied for two oxygenated and renewable fuels, namely OME_x and OME_1, under ECN SA conditions. Three ambient temperature levels have been evaluated, and results have been compared to those available in experiments. Through the analysis of spray calculations, the following conclusions have been derived:

- In general terms, CFD modelling results are found to closely match experimental ones in terms of global combustion metrics, such as tip penetration, ignition delay and lift-off length. However, stabilization of lift-off length for OME_1 occurs at shorter distances to the nozzle, and CFD predicts ignition for OME_1 at the lowest ambient temperature, which does not occur in experiments.

- The combination of ambient temperature and different reactivity for both fuels has enabled the transition from a high reactivity typical diffusion

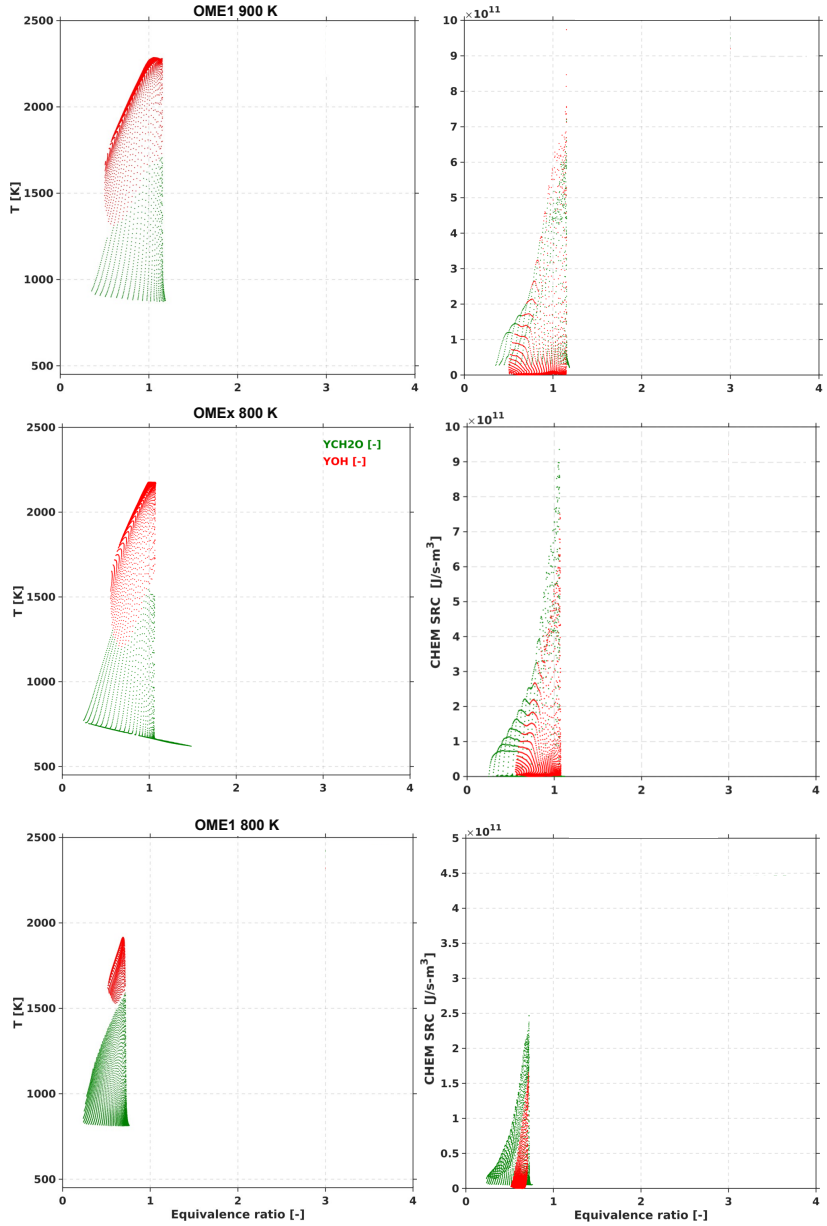

Figure 5.11: Scatter plots of local heat release rate (right) and temperature (left) versus equivalence ratio. Markers are coloured red or green when the local OH or CH_2O values are higher than the 20 % of the corresponding maximum, respectively.

flame structure (OME_x at $1000 - 900\ K$) towards lower reactivity cases, where lift-off length may eventually be longer than the length of the stoichiometric surface, and hence the flame stabilizes at very lean conditions, i.e. a type of lean mixing controlled flame is obtained. This is reflected in the spatial distribution of species. For the diffusion-flame topology, CH_2O is found at rich mixtures and low temperature, starting slightly upstream of the lift-off length location, while OH mainly occurs around the stoichiometric surface. For the lower reactivity conditions (OME_1 at $900 - 800\ K$), CH_2O is similarly found upstream of the lift-off length location, while OH is close to the axis at the flame lift-off length, and may also be found at stoichiometric conditions, but only if lift-off length is shorter than the maximum stoichiometric length.

- Laminar flamelet calculations, showed in Section 4.3 with OME_x-type fuels show a typical low temperature ignition on the lean mixtures, moving towards a high temperature ignition in the fuel-rich zone, similar to typical hydrocarbons. However, ignition in CFD configuration seems to occur on the lean side, especially for OME_1 as well as for the low temperature cases. This results from the finite residence time for relevant mixtures in the spray calculations, compared to the infinite one available for the flamelet ones.

- As a general conclusion, these oxygenated fuels can develop very different flames structures compared to conventional hydrocarbons, depending on the ambient temperature. The numerical approach followed here, which has been based upon igniting diffusion flamelets, is able to reproduce a lean mixing-controlled flame structure, although for those situations it under-predicts LOL.

References

[1] Engine combustion network. *https://ecn.sandia.gov/*.

[2] Pastor, José V., García-Oliver, José M., Micó, Carlos, García-Carrero, Alba A., and Gómez, Arantzazu. "Experimental Study of the Effect of Hydrotreated Vegetable Oil and Oxymethylene Ethers on Main Spray and Combustion Characteristics under Engine Combustion Network Spray A Conditions". In: *Applied Sciences* 10.16 (2020), p. 5460. DOI: 10.3390/app10165460.

[3] ENERXICO Project. *https://enerxico-project.eu/*. 2022.

[4] CONVERGE CFD Software. *https://convergecfd.com*.

[5] Naud, Bertrand, Novella, Ricardo, Pastor, José Manuel, and Winklinger, Johannes F. "RANS modelling of a lifted H2/N2 flame using an unsteady flamelet progress variable approach with presumed PDF". In: *Combustion and Flame* 162.4 (2015), pp. 893–906. DOI: 10.1016/j.combustflame.2014.09.014.

[6] Jacobs, Sascha et al. "Detailed kinetic modeling of dimethoxymethane. Part II: Experimental and theoretical study of the kinetics and reaction mechanism". In: *Combustion and Flame* 205 (2019), pp. 522–533. DOI: 10.1016/J.COMBUSTFLAME.2018.12.026.

[7] CMT, Clean Mobility and Thermofluids. *https://www.cmt.upv.es*. 2020.

[8] CMT, Clean Mobility and Thermofluids - Nozzle characterization. *https://www.cmt.upv.es/#/ecn/download*. 2022.

[9] Payri, R., García, J.M., Salvador, F.J., and Gimeno, J. "Using spray momentum flux measurements to understand the influence of diesel nozzle geometry on spray characteristics". In: *Fuel* 84.5 (2005), pp. 551–561. DOI: https://doi.org/10.1016/j.fuel.2004.10.009.

[10] Desantes, Jose M., García-Oliver, Jose M., Novella, Ricardo, and Pachano, Leonardo. "A numerical study of the effect of nozzle diameter on diesel combustion ignition and flame stabilization". In: *International Journal of Engine Research* (2019). DOI: 10.1177/1468087419864203.

[11] Pachano, Leonardo. "CFD Modeling of combustion and soot production in diesel spray". PhD thesis. Universitat Politecnica de Valencia, 2020.

[12] Kook, Sanghoon and Pickett, Lyle M. "Liquid length and vapor penetration of conventional, Fischer–Tropsch, coal-derived, and surrogate fuel sprays at high-temperature and high-pressure ambient conditions". In: *Fuel* 93 (2012), pp. 539–548. DOI: 10.1016/j.fuel.2011.10.004.

[13] Garcia-Carrero, Alba. "Experimental study of the fuel effect on diffusion combustion and soot formation under diesel engine-like conditions". PhD thesis. Universitat Politecnica de Valencia, 2021.

[14] Hermann Schlichtin, Klaus Gersten. *Boundary-Layer Theory*. Springer Berlin, Heidelberg, 2000. DOI: 10.1007/978-3-662-52919-5.

[15] Chiu, W.S., Shahed, S.M., and Lyn, W.T. "A Transient Spray Mixing Model for Diesel Combustion". In: *SAE Transactions* 85 (1976), pp. 502–512. DOI: http://www.jstor.org/stable/44644055.

[16] Desantes, José M., Pastor, José V., García-Oliver, José M., and Briceño, Francisco J. "An experimental analysis on the evolution of the transient tip penetration in reacting Diesel sprays". In: *Combustion and Flame* 161 (8 2014), pp. 2137–2150. DOI: 10.1016/j.combustflame.2014.01.022.

[17] Payri, Raul, García-Oliver, Jose M., Xuan, Tiemin, and Bardi, Michele. "A study on diesel spray tip penetration and radial expansion under reacting conditions". In: *Applied Thermal Engineering* 90 (2015), pp. 619–629. DOI: 10.1016/j.applthermaleng.2015.07.042.

[18] Desantes, J. M., Pastor, J. V., García-Oliver, J. M., and Pastor, J. M. "A 1D model for the description of mixing-controlled reacting diesel sprays". In: *Combustion and Flame* 156 (1 2009), pp. 234–249. DOI: 10.1016/j.combustflame.2008.10.008.

[19] Desantes, J. M., García-Oliver, J. M., Xuan, T., and Vera-Tudela, W. "A study on tip penetration velocity and radial expansion of reacting diesel sprays with different fuels". In: *Fuel* 207 (2017), pp. 323–335. DOI: 10.1016/j.fuel.2017.06.108.

[20] Benajes, Jesús, Payri, Raúl, Bardi, Michele, and Martí-Aldaraví, Pedro. "Experimental characterization of diesel ignition and lift-off length using a single-hole ECN injector". In: *Applied Thermal Engineering* 58 (1-2 2013), pp. 554–563. DOI: 10.1016/j.applthermaleng.2013.04.044.

[21] Pastor, Jose V., Garcia-Oliver, Jose M., Micó, Carlos, and Tejada, Francisco J. "Comparison of the Diffusive Flame Structure for Dodecane and OMEXFuels for Conditions of Spray A of the ECN". In: *SAE Technical Papers* 2020 (2020), pp. 1–10. DOI: 10.4271/2020-01-2120.

Chapter 6

Analysis of fuel and nozzle effects within a LES framework

Contents

6.1 Introduction

A Diesel-like spray was examined using RANS simulations to understand the temporal and spatial structure of the flame in chapter 5. RANS turbulence models can offer numerous advantages for engineering problems due to their ability to generally provide a favourable balance between accuracy and computational efficiency. While all turbulence scales are modelled, which could pose a challenge if the turbulence model is unsuitable for a specific problem,

the computational cost is notably low in comparison to other approaches. In this context, the continuous increase in computational power experienced over decades encourages the exploration of alternative approaches. Despite incurring a computational resource penalty, these approaches offer a new spectrum of possibilities. In this regard, LES calculations have gained increasing attention, particularly in the current research field. Two factors contribute to an anticipated enhancement in computational accuracy for LES calculations. Firstly, the largest eddies are not modelled but directly solved. Secondly, in accordance with classical turbulence theory, vortexes tend to become isotropic as they decrease in size. Therefore, the modelling of small eddies is expected to be more universal and less influenced by specific flow boundary conditions. Another notable strength of LES is its capacity to replicate flow intermittency, which can be crucial in addressing problems characterized by high variability.

In the case of Diesel sprays, which constitute a specific type of free shear flows, transport phenomena are primarily governed by the motion of large scales, resolved in LES simulations [1]. However, chemical reactions occur at the smallest scales of the flow, taking place when species are mixed at the molecular level. As a result, LES simulations cannot directly solve chemical reactions but need to model them [1, 2], enabling the direct extension of RANS combustion models to LES as it was stated in Chapter 3. Furthermore, it is anticipated that the shape of the filtered probability density function has a smaller effect on results than in RANS [2].

Given all the context outlined above, this chapter presents a study of the ignition process and flame structure of the target fuels within this thesis, namely $OMEx$[1] and OME_1. This complements the results obtained with RANS and the experiments carried out in the ENERXICO project, as this chapter covers a significant portion of the experimental matrix conducted in the mentioned project.

6.2 Simulation methodology

In chapter 5, temperature sweeps ranging from 800 K to 1000 K were computed using RANS simulations for the SA. In this chapter, where turbulence will be considered with an LES approach using the *Dynamic structure* model [3–6] for the sub-grid scales as it was described in Section 3.6, and considering the computational cost of that implies, a careful selection has been made regarding which calculations would be performed under this framework. Initially, the

[1] OME_3 and OME_4 blend with the composition presented in the first column of Table 4.1

focus has been on two nozzle sizes, namely ECN SA and SD, extending the study from the automotive-size nozzle to the larger heavy-duty one, which was not included in Chapter 5. Subsequently, the chosen temperature sweep includes the nominal 900 K and the low temperature (800 K), based upon findings from both RANS and experiments, which showed that there was not so much difference between the nominal and the 1000K high temperature case, developing in both cases a diffusion flame structure very similar to that of n-Dodecane, the reference hydrocarbon used in this thesis.

Inert simulations have been carried out as before the reacting ones in order to validate the spray model calibration and characterize the mixing process of each fuel and nozzle. Table 6.1 summarizes the cases calculated under inert and reacting conditions. All the simulations has been done under ECN reference condition, with $\rho = 22.8\ kg/m^3$.

0 % O_2		
	$OMEx\ OME_1\ C_{12}$	
Nozzle	SA	
	SD	
T_{amb}	900 K	
15 % O_2		
	$OMEx\ OME_1$	
Nozzle	SA	
	SD	
T_{amb}	900 K	
	800 K	

Table 6.1: Thermodynamic and fuel injection conditions for the simulated CFD cases in LES framework.

In LES framework, the ECN guidelines have been followed as in the chapter 5 to determine numerically the global combustion parameters. For completeness, they are recalled below:

- Vapour tip penetration (S): The axial distance to the farthest point where the mixture fraction (Z) reaches a value of 0.001.
- Liquid length (LL): The axial position that encompasses 97% of the liquid mass.

- Ignition delay (ID): The time elapsed from the start of injection to the point where the maximum derivative of the maximum of temperature in the domain is achieved,
- Lift-off length (LOL): The minimum axial distance from the nozzle to the closest location where 14% of the maximum value of the mass fraction of OH in the domain is reached.

6.3 Inert spray mixing characteristics

For the RANS cases (chapter 5), the model had been calibrated and validated for n-Dodecane for both inert and reacting conditions, and therefore only the validation of global combustion parameters is presented in this work. However, in this chapter, where LES calculations have been performed, the model was calibrated beforehand. The calibration under inert conditions has been performed in such a way that the results are acceptable for both SA and SD by simply modifying the flow rate and nozzle diameter (final tuned constants can be found in Table 3.5). In this section, the corresponding validation of the spray model calibration will be presented. It will be structured as follows: first, the results of both SA and SD from the CFD using n-Dodecane as the reference fuel in the ECN will be presented, contrasted with the extensive database available for this fuel, mainly for SA. Then, the validation (more concise, given the availability of experimental information) will be presented with results obtained for the target fuels of this thesis, also referred to as ENERXICO fuels, for both nozzles.

n-Dodecane ECN reference inert conditions (SA/SD)

The database used to validate the spray model under inert conditions relies on a comprehensive experimental database. Various parameters are necessary for an accurate validation process. For this reason, as mentioned, the validation has been performed using n-Dodecane fuel, which has an extensively characterized and widely used literature reference, and it is the same one Pachano [7] used to calibrate the spray model employed here within the RANS framework. However, there may be variations in the nozzle characteristics depending on the different sources used. Table 6.2 presents the experimental results used for validation, explicitly indicating the difference in the orifice size of each nozzle used experimentally, depending on the source. All CFD calculations performed in this thesis of SA have been conducted using the 210675 nozzle, which was the one used within ENERXICO measurements. Therefore, for local quantities validation, spatial coordinates are normalized

by the nozzle equivalent diameter Equation 5.6 (x^*=x/deq) in order to adjust variations in the nominal diameter between the simulated nozzle and the nozzles used in experimental measurements.

For SD, there is no available information other than the vapour penetration. Therefore, only the validation of this parameter for the larger spray is presented.

ECN Spray	Parameter	Experiment	Nozzle	Source
SA	Tip penetration	SCH	210675 d_0 = 89.4 μm	[8]
	Liquid length	DBI	210675 d_0 = 89.4 μm	[8]
	Mixture fraction	Rayleigh	210677 d_0 = 83.76 μm	[9]
			SA3 d_0= 94 μm	[10]
	Velocity	PIV	210678 d_0 = 88.6 μm	[11]
SD	Tip penetration	SCH	209135 d_0 = 189.4	[12]

Table 6.2: Experimental database for inert spray validation for n-Dodecane SA and SD.

The validation of the spray model for LES calculations under inert conditions begins, presenting for SA and SD the comparison of the vapour penetration and liquid length as shown in Figure 6.1 (obtained following the definitions of the ECN). Starting for SA, despite there being a slight over-prediction of the liquid length, the agreement for the vapour penetration is excellent and following the same criteria as in the RANS inert validation (section 5.3) where considering the spatial separation between the liquid zone and the combustion region is quite large, it can be stated that the slight over-prediction of the liquid length is not critical for the objectives of this thesis. Furthermore, this deviation is in the same order of magnitude as other LES simulations of the same ECN cases [13, 14]. However, for SD the spray tip penetration from simulations tend to overpredict the experimental one from 0.25 to 1.5 ms and then recover the experimental spray acceleration; it is important to note that the same spray model calibration has been used for both nozzles in order to achieve a robust model capable of predicting acceptable results independent of the nozzle size. For liquid length, there is no information for the SD.

The inert spray validation proceeds by comparing simulated profiles for the mean mixture fraction and its variance at the centre line (Z_{cl} and $Zvar_{cl}$) at a quasi-steady state (4.5 ms). Figure 6.2 on the left shows the evolution of the time average (from 1 to 4.5 ms) mixture fraction along the spray symmetry axis. The first notable observation is the difference between experiments. The recent results from the SA3 nozzle conducted by SNL [10] show a significantly lower value for the mixture fraction compared to the historically used result [9]. On the CFD side, capturing this parameter has always been challenging

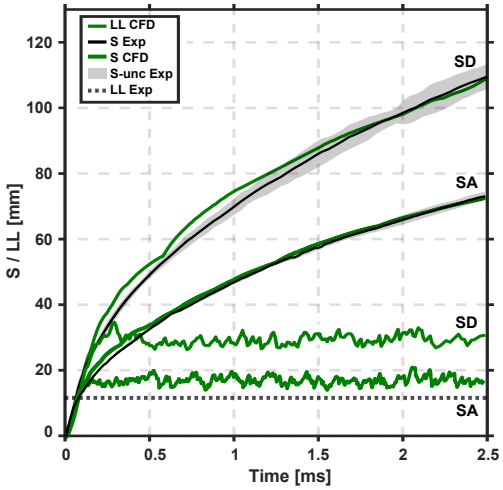

Figure 6.1: Liquid length and vapour penetration for experimental and simulated inert nominal conditions for n-Dodecane, used as reference fuel for the ECN SA and SD.

with LES, often resulting in an under-prediction of Z at the centre line and, therefore, a higher mixture obtained through LES calculations compared to experimental measurements. Xue et al., [14] obtained independently of the sub-grid model, a constant over-prediction of the mixture fraction at the centre line, using, as in the present work, *CONVERGE* CFD code. Furthermore, *OpenFOAM* simulations present similar behaviour regarding this prediction [13].

From this comparison, it can be concluded that the LES is in line with the new experimental measurements from SA3, considering the corresponding normalization of the axial coordinate due to the nozzle parameter differences.

On the right side of Figure 6.2, the variance of Z is shown, both the sub-grid and the total (sub-grid plus resolved) one, for LES calculations. Regarding the relationship between the sub-grid and the total variance, the results align with previous studies [15], where the resolved part is significantly larger than the modelled part, particularly when moving downstream. This is an additional indirect validation of the LES quality. In conclusion, these findings serve as a positive validation of the LES simulation, as it effectively resolves a significant portion of the mixture fraction.

To further validate the mixing process, radial profiles have been extracted at distances of 20, 30, and 45 mm from the nozzle, normalized by their values along the central axis. The results from the CFD simulations (in green) have been compared once again with the two experimental sources (in black). In

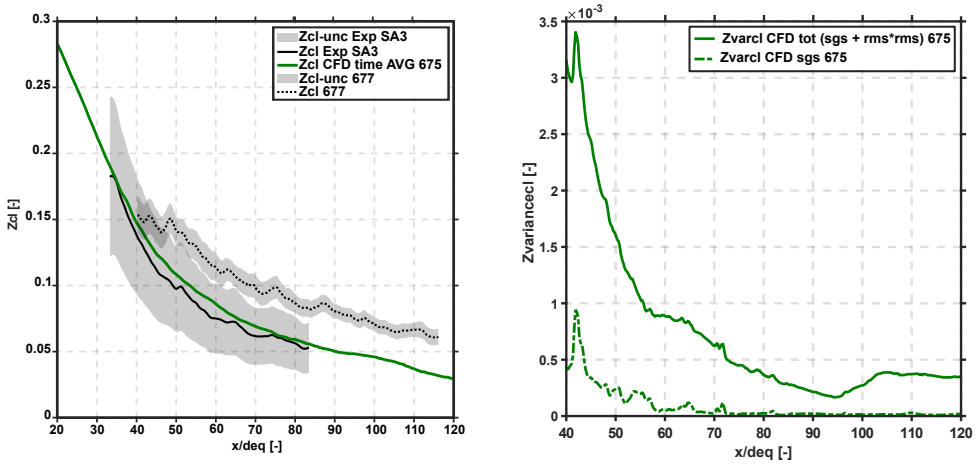

Figure 6.2: Mixture fraction validation at advanced time (4.5 ms). Left: Evolution of mean mixture fraction at the centre line. Right: Mixture fraction variance, total and sub-grid at the centre line.

this case, the CFD results show a very good agreement with both experimental sources, this time showing a concordance between experiments. Due to the similarity between the two experimental measurements, error bars are omitted for clarity.

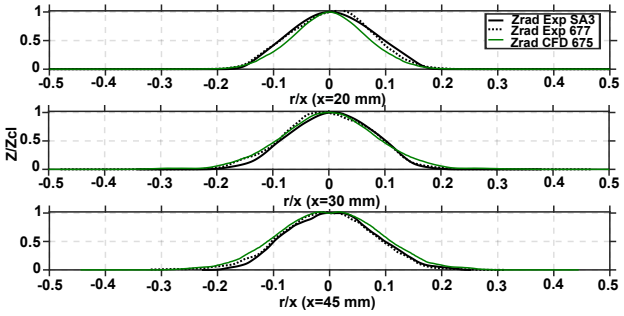

Figure 6.3: Spray validation at quasi-steady state. Radial profiles for the mixture fraction normalized at the centre line, at three different axial stations, 20, 30 and 45 mm, for inert nominal conditions for n-Dodecane, used as reference fuel, for the ECN SA.

Additionally, the axial velocity is compared with experimental results in Figure 6.4 at 1.5 *ms*; it should be noted that at this time, a mean value has not been calculated, as in the case of the mixture fraction at 4.5 *ms*, as it

is still a very transient period in the spray development. The model also demonstrates success in accurately matching the experimental measurements for axial velocity, with an abrupt and early drop in the velocity value in the CFD result, possibly due to differences in tip penetration.

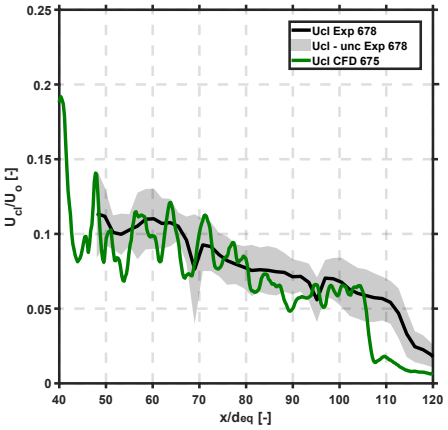

Figure 6.4: Spray validation at 1.5 ms in terms of the normalized velocity profile along the central axis relative to the nozzle exit velocity, given the differences between the experimental and simulated nozzle diameters, for inert nominal conditions for n-Dodecane, used as reference fuel for the ECN SA. Experimental results are represented in black, and CFD in green.

ENERXICO fuels study under inert conditions (SA/SD)

In order to extend the validation of the mixing process to $OMEn$-type fuel, LES simulations under inert conditions have been carried out for the fuels objectives of this thesis ($OMEx$ and OME_1). For those, an extensive database has been provided within ENERXICO project framework [16].

The measurements of vapour tip penetration within the ENERXICO project have been carried out in the same facilities as the one presented for n-Dodecane in the previous section but five years later. Therefore, for both SA and SD, a comparison between n-Dodecane ECN reference conditions and ENERXICO fuels the mass flow rates has been done in order to ensure that the injectors behaviours remains unchanged. Table 6.3 present the mass flow rate measured in each instance. For SA, it has been found that the rate remains unchanged when comparing the two experimental campaigns results. However, for SD, a change in the injector behaviour has been found, resulting in a modification of the mass flow rate, hence when moving to ENERXICO fuels, mass flow rate must be modified respecting ECN reference condition.

On the CFD side, the mass flow rate and its shape have been determined for SA with a virtual injector (ref CMT), already mentioned in chapter 5. While for SD, the mass flow rate was obtained from an "educated injection rate", in both cases the tools are available for n-Dodecane. However, through the Equation 5.4 mass flow rate for $OMEx$ and OME_1 have been derived.

	C12	
	SA	SD
$\dot{m}_{ECN}$ [g/s]	2.56	11.30
$\dot{m}_{ENERXICO}$ [g/s]	2.61	10.63

Table 6.3: Differences in mass flow rate measurements from ECN inert reference condition and ENERXICO project, for n-Dodecane and SA and SD.

Figure 6.5 presents a comparison for SA of the penetrations obtained with CFD for the two oxygenated fuels: $OMEx$ and OME_1. These are compared with two experimental sources, the OME_1 vapour penetration from experimental ENERXICO results [17], besides it was measured under reacting conditions, it ignites very late (at 1.2 ms, red circle in the figure) consequently, until this time is considered as inert. And, with experimental measurement of n-Dodecane [8] under inert condition (the same presented in Figure 6.1), bearing in mind that the mass flow rate is exactly the same in both experimental campaigns and, under inert conditions, they should penetrate in the same manner due to the vapour penetration being governed by momentum flux, which is independent of fuel type as it was demonstrated in Chapter 5. The first thing to highlight it is the matching from both experiments, confirming the information presented in Table 6.3. Also, a good correlation it can be observed between CFD and both experimental results. Despite a slight deviation after 1 ms, where both oxygenated fuels exhibit a slight decrease in spray acceleration compared to the experiment. However, $OMEx$ manages to recover the acceleration of the experiment before 2 ms, while OME_1 continues to underestimate the penetration slightly. Additionally, the liquid length is compared once again with the experimental values obtained under reactive conditions, as in chapter 5 and shows reasonably good agreement.

To conclude the validation of SA under inert conditions with the mixture fraction distribution, for which only inert measurements from SNL with the SA3 nozzle are available, but just for $OMEx$ no for OME_1, Figure 6.6 displays, on the left, the mixture fraction along the central line, similarly to n-Dodecane. Regarding the validation, the Zcl of $OMEx$ also exhibits acceptable behaviour, closely matching the experimental value from the SA3 injector results. Likewise, on the right, Figure 6.6 illustrates the radial distribution of the mixture fraction

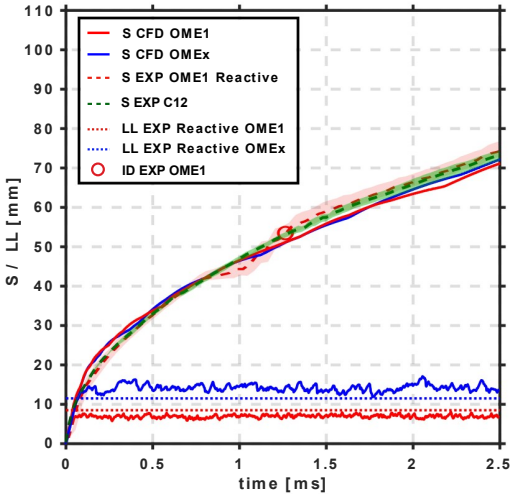

Figure 6.5: Liquid length and vapour penetration for simulated inert nominal conditions, vapour penetration of experiment is for n-Dodecane under inert condition and for OME_1 under reacting nominal conditions, which ignites at 1.2 ms. Also, liquid length of experimental are from reacting conditions for $OMEx$ and OME_1. All results correspond to ECN SA.

within the spray at different axial positions. It can be observed that closer to the nozzle, the CFD results predict a slightly smaller radial expansion compared to the experimental result, which is then resolved at a distance of 30 mm to be in perfect agreement with the experiments. At 45 mm, the difference observed on the left side (negative values in r coordinates) is due to an asymmetry in the experimental result.

The validation of the spray model calibration, when $OMEx$ and OME_1 are used, now extends to the larger spray, SD. In this case, it will be a less extensive validation as in n-Dodecane ECN inert reference condition section and even for $OMEx$-SA, recently presented. The low-temperature (800K) cases of OME_1 from the ENERXICO database that ignite very late (2.53 ± 0.181 ms) have been solely used to validate inert simulations of SD. Additionally, the liquid length will be contrasted against the ones measured under reacting conditions for ENERXICO fuels, considering that the difference in these parameters is minimal between inert and reacting conditions. Although the vapour penetration of n-Dodecane has also been validated under ECN conditions, in this work, the currently measured rate (ENERXICO Table 6.3) in SD has been chosen since the reactive experimental results of oxygenated fuels will be used with this rate to carried out and validate the whole reacting

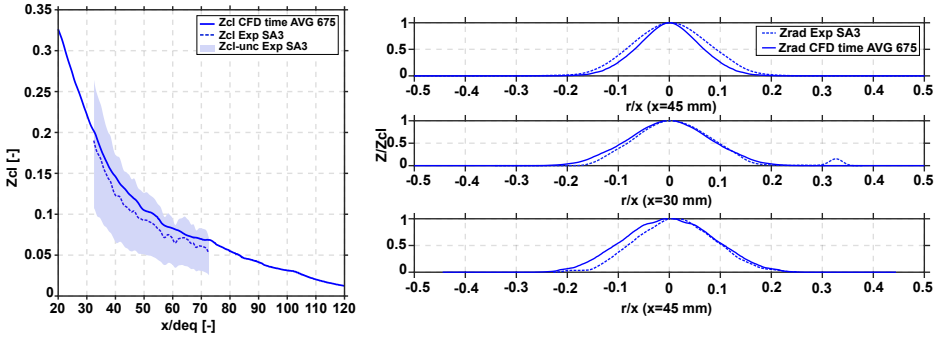

Figure 6.6: Spray validation at quasi-steady state. On the left, axial profiles at the centre line for the mixture fraction versus a normalized axial distance. On the right, radial profiles for the mixture fraction normalized at the centre line, at three different axial stations, 20, 30 and 45 mm also normalized. Results are for inert nominal conditions for OMEx, for the ECN SA.

cases. For this reason, n-Dodecane CFD simulations are also included here, in order to visualize that changing the mass flow rate, the spray model properly predicts the spray evolution.

Figure 6.7 shows the evolution of vapour and liquid penetration as a function of time. The results are shown up to 2.5 ms prior to the ignition delay of the case used as inert. The calibration used is the same as that of SA, to establish a robust model that can be used for different spray sizes. While it is observed that the vapour penetration evolution was more accurate in SA, acceptable results are obtained for SD, with an over-prediction between 0.2 ms and 0.7 ms that the CFD later adjusts to match the experimentally observed spray acceleration. For the liquid length, using the 97% criterion, as in RANS and LES SA, the prediction for OME_1 is excellent, and for n-Dodecane and $OMEx$, although slightly over-predicted, the deviation is low and acceptable.

6.4 Global combustion parameters validation

Once the calibration of the spray model is completed, which involves validating the global parameters of the inert spray, such as vapour penetration and liquid length, the mixing process through mixture fraction and velocity fields, as well as evaluating the relationship between the resolved mixture fraction and the sub-grid is evaluated, the validation of the model will proceed to reactive conditions. This includes the validation of global combustion parameters and flame structure, and this last step has been directly done for the target fuels

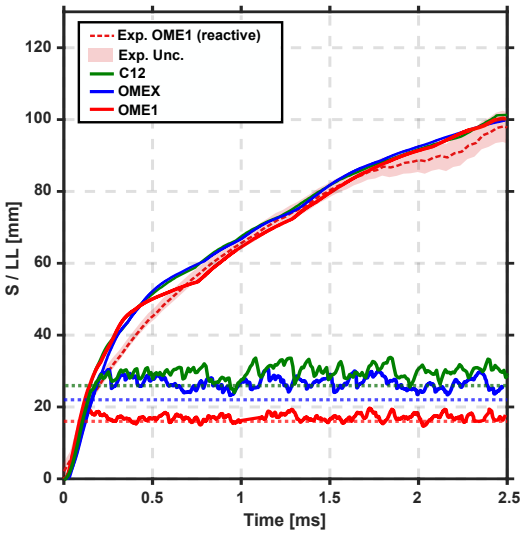

Figure 6.7: Liquid length and vapour penetration for experimental and simulated inert nominal conditions (except liquid length of experimental results that were taken from reactive conditions) for n-Dodecane, $OMEx$ and OME_1 for the ECN SD. Vapour penetration result from the experiment is represented in black, while CFD result is in green for n-Dodecane, blue for $OMEx$ and red for OME_1. In the case of liquid length, the same colour code is used, and the experimental results are drawn with a doted line.

of the thesis, OME_x and OME_1, as the ENERXICO project has provided a comprehensive database for the validation of these fuels in terms of global combustion parameters and flame structure under reactive conditions. For the global combustion parameters, the same experimental results previously presented in the chapter 5 have been used [16–18]. However, the validation of flame structure is a novelty in this work, and will be done with the LES calculations using its more realistic approach. For this purpose, chemiluminescence results of OH^* and PLIF of OH and CH_2O have been used, which are published by Pastor et al. [19].

Figure 6.8 shows the results of vapour penetration, lift-off length (LOL), and ignition delay for the two fuels and two nozzle sizes, SA and SD. CFD results are represented in blue and red for $OMEx$ and OME_1, respectively, while the experimental results are shown in black. Additionally, the mixture fraction field has been included to illustrate the representation of each parameter within the spray, but mainly to highlight the difference in equivalence ratio (ϕ) at the LOL position in each case. This effect will have a significant impact on the subsequent development of the flame structure and will be taken into account in the combustion process analysis, the values of ϕ at LOL is a mean value at the

lift-off length position corresponding to the time represented. Furthermore, the cases $OMEx$-SD and OME_1-SA (the extremes in terms of equivalence ratio at LOL) show two colour dotted lines, which represent a different post-processing workflow that will be explained in the following.

Given that the chaotic nature of a Diesel spray is largely captured by LES simulation, and symmetry cannot be assumed a priori, as in RANS framework, where a central plane can be used directly to compute global combustion parameters, the processing of the results and the correct acquisition of parameters must be done with certain care in an LES approach. The subfigures of $OMEx$-SD and OME_1-SA, contain, in addition to what has already been described, a dashed coloured line in the evolution of penetration and LOL. This is because, for these two cases, which represent the extremes in diffusive or non-diffusive behaviour (according to the equivalence ratio at the LOL), these global parameters have been processed both from the 3D CFD results and from a central plane. It has been found that there are practically no differences between the two ways of processing the results. Therefore, due to the difference in processing time between 3D and 2D, for the rest of the cases, the processing of the global combustion parameters has been done from a central plane of the spray.

Similar to the inert results, the penetration shows an excellent agreement with the experiments, with some deviations but within acceptable ranges. The most notable deviation is observed in the $OMEx$-SD case, where starting from the ignition delay, the experiment shows a higher penetration than the simulation throughout the entire range. However, numerical simulations results maintain the same slope as the experiment, indicating that the CFD well captures the spray acceleration and, therefore, the momentum.

Regarding the ID, which is represented as a dashed vertical line, in all cases, the difference between the CFD and experimental values is slight, less than 10 % in all the cases. For $OMEx$, the CFD predicts a shorter ID than the experimental value, while for OME_1, the CFD shows a delay compared to the experimental value.

Finally, the validation of the LOL evolution over time shows a strong agreement in $OMEx$, both for SA and SD. However, for OME_1, the CFD is unable to capture the correct behaviour of this parameter, especially for SA, where the CFD exhibits a significant backward movement that is not observed in the experiment. This results in a difference of approximately 10 mm between the modelling and experimental values, similar to what was observed in RANS. The SD also experiences some backward movement, but to a lesser extent, resulting in a stabilized value that is not too far from the experimental value.

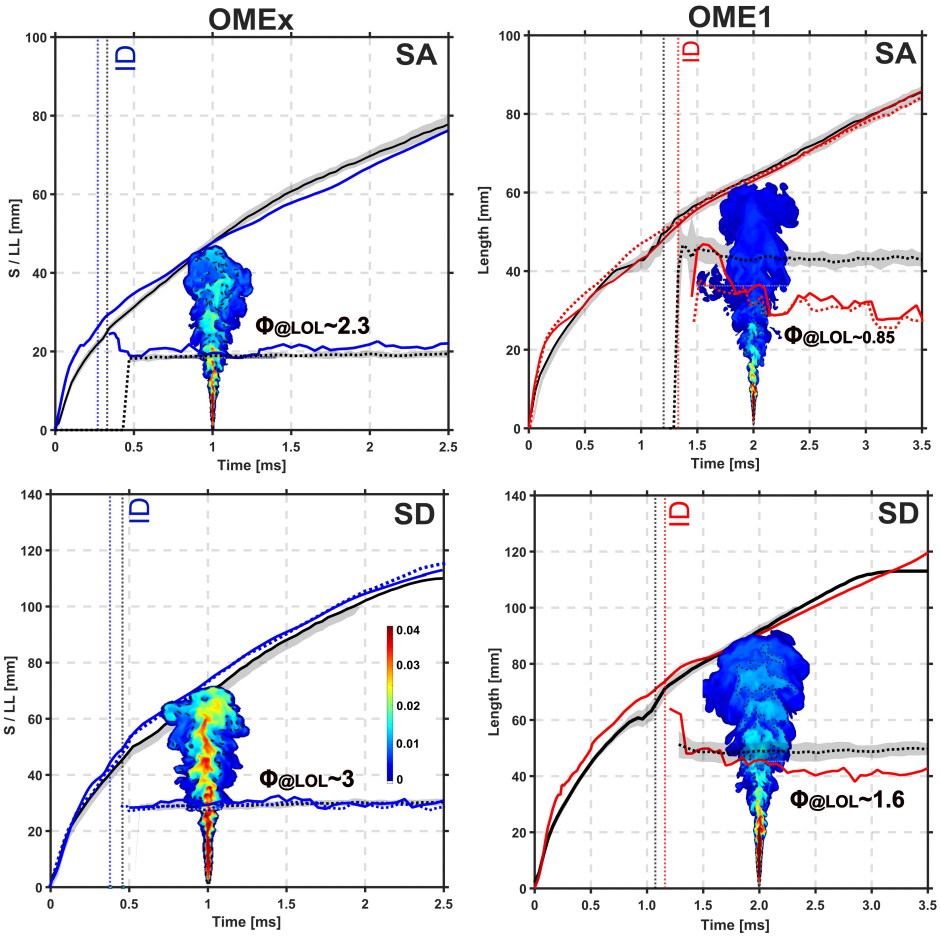

Figure 6.8: Time evolution of tip penetration and lift-off length for OME_x (left) and OME_1 (right), for the ECN SA in the top panel, and SD in the bottom for the nominal reactive condition. Vertical lines show the ID timing as derived from CFD calculations and from experiment. Mixture fraction field is superimposed with the same colour-scales in all cases.

To conclude the validation of the global combustion parameters, Figure 6.9 includes all the results of ignition delay and stabilized average LOL value for the 4 cases, allowing for a comparison of the effect of fuel and nozzle size in addition to the experiments and CFD. OME_1 exhibits a much higher ignition delay than $OMEx$ for both nozzle sizes, even exceeding or equalling double the ignition delay of $OMEx$ for the same nozzle size. Another particularity is that $OMEx$, as expected, ignites earlier in SA than in SD for the same thermodynamic condition. In contrast, OME_1 shows the opposite trend, and the larger nozzle achieves earlier ignition than the smaller one and that happens for both CFD and experiments. This behaviour can be explained in terms of mixture fraction and scalar dissipation rate. OME_1-SA ignite at very lean mixtures (equivalence ratio at LOL is 0.85, Figure 6.8); Meanwhile, the OME_1-SD ignites under conditions close to stoichiometric, implying that, considering the shape of the ignition delay versus Z of flamelets or homogeneous reactors, the most reactive Z is close to Z_{st}. However, if it shifts towards rich or lean equivalence ratios, the ignition delay increases (see Figures 4.1 and 4.9). For this reason, given the conditions of one spray versus the other, the SD will exhibit a lower ignition delay. More details on this could be found in Appendix 6.A.

Regarding the stabilized average LOL value, Figure 6.9 shows that, as expected given the geometry of each nozzle, in both fuels, SA stabilizes closer to the orifice than SD. In OME_1, despite the CFD predicting a higher ignition delay than the experimental value, there is no correlation with the LOL prediction. In this case, the CFD value is shorter than the experimental one.

6.5 Validation of CFD spray combustion evolution by means of experimental diagnostics

To conclude this validation, an extensive comparison of flame structure between CFD and the experiment has been carried out. In the first part, a qualitative comparison of OH and CH_2O fields[2] from CFD and the PLIF technique [19] has been performed. In the experiment, as the name suggests, a laser cuts through a plane of the spray (ideally the central plane) and collects information related to the molar density of the corresponding species. Information is recorded from different injection events, and hence the final result is a sample-averaged value. In the case of CFD, since conducting multiple realizations of such a calculation is computationally expensive, an azimuthal averaging of the results

[2]CFD fields are $Y_i.\rho$ in order to make a faithful comparison with experiments.

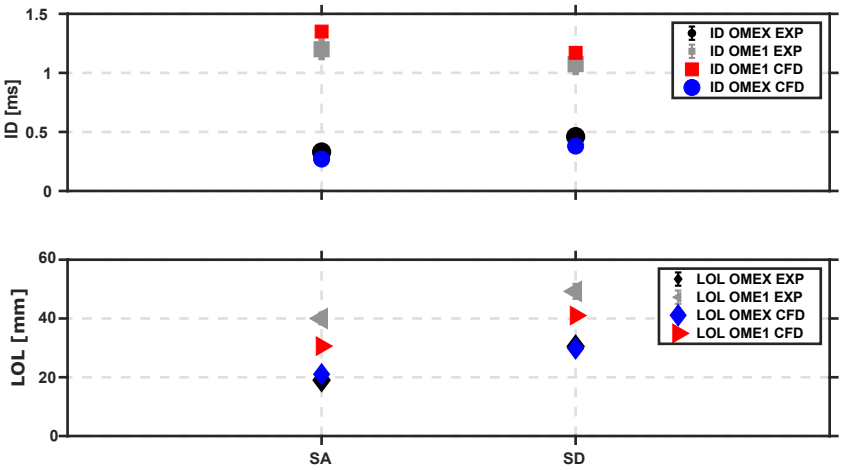

Figure 6.9: Ignition delay and stabilized lift-off length for both experimental results and CFD calculations for the nominal reactive condition. Experimental data include both average and standard deviation. The figure include results of $OMEx$ and OME_1 and the two nozzle sizes.

from a single realization has been performed. Both the experimental and CFD results have been normalized by the maximum value for every species and time, which results in a qualitative description of the spatial distribution of the corresponding species.

Next, the OH^* fields will also be qualitatively compared, modelling the chemiluminescence as introduced in Chapter 3 from the numerical modelling side and using the OH^* chemiluminescence optical technique in the experimental one. In this case, the experimental post-processing assumes azimuthal symmetry and delivers the symmetry plane from the original line-of-sight integrated images. Therefore, in the case of CFD, an azimuthal averaging has also been performed, resulting in these results in the central plane of the spray.

Figure 6.10 shows the flame structure from ignition to the quasi-steady state of $OMEx$ represented by CH_2O and OH species, which are tracers of low and high-temperature reactions, respectively, already used in the RANS framework (Chapter 5) to analyse the combustion process.

For SA, the temporal and spatial evolution of both species is particularly well captured, with slightly larger OH spread at the initial moment due to the earlier ignition delay in the CFD. CH_2O is located in the richer regions along the spray axis and near the nozzle orifice, as expected. OH is observed downstream, surrounding the tip of the CH_2O at 535 μs and 735 μs, and then

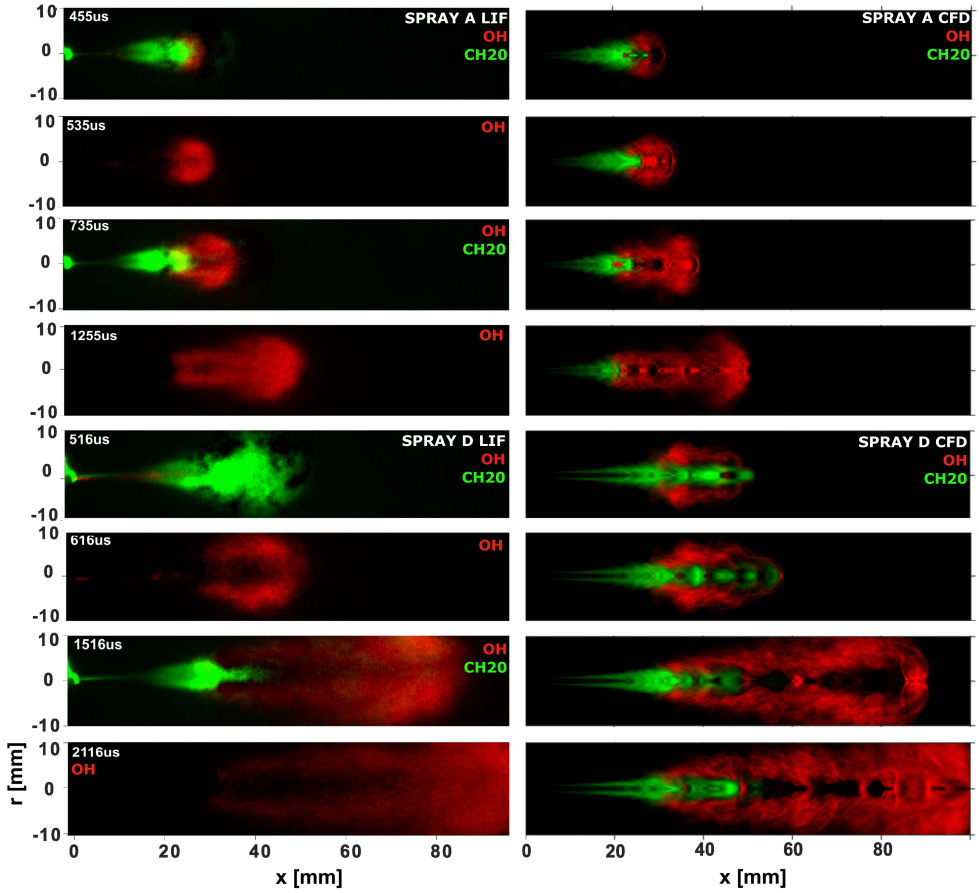

Figure 6.10: Comparison between experiments and CFD of the normalized signal of Formaldehyde (green) and OH (red) for OMEx. Left panel correspond to experimental results obtained from PLIF [19] and right panel from CFD, while the first four rows are for ECN SA and the last four for ECN SD.

at 1255 μs, it forms a relatively flat base instead of a W shape. Although the CH_2O is not recorded in this shot, the shape of the base is very similar to that of the CFD, where it no longer shares the region with CH_2O. Additionally, at this quasi-steady state time, CFD successfully predicts the typical spray head shape observed in the experiment, which is characteristic of Diesel sprays.

For SD of the same fuel (bottom part of Figure 6.10), during ignition, CH_2O distribution predicted by the LES is concentrated along the spray axis, while experimentally it appears more radially expanded. Axially, CH_2O spreads axially up to approximately 50 mm for both CFD and experiments. At 1516 μs, the shape developed by this species is similar in CFD and experiment, but in the CFD, it is more expanded axially, which is due to the overestimation of penetration by the CFD as Figure 6.8 shows (which is also reflected in the OH field, discussed below).

The flame structure prediction can be considered adequately validated in terms of OH and CH_2O fields. The differences mentioned earlier are due to the greater vapour penetration in the CFD. However, the base of the OH is perfectly predicted by the simulation, as seen previously in the LOL presented in Figure 6.8. It is worth mentioning that at times close to ignition (616 μs), where the OH is recorded in the experiment, the shape developed by the LES differs from the experiment, although it still exhibits its typical lobes and maximum intensity at the sides of the spray.

In the same manner, Figure 6.11 illustrates the flame structure of OME_1 for the two nozzle sizes. In this figure, the effect of the previously mentioned equivalence ratio at the lift-off length is already noticeable, as the structure developed by this fuel differs from that of $OMEx$. However, there is also a discernible difference between OME_1-SA (first four rows) and SD (last four rows). Starting with SD, which still retains certain diffusive characteristics, the interaction between species is presented for the first timing, where only CH_2O is visible; CFD mainly predicts the spatial distribution, but it is shorter than experiments in which CH_2O appears closer to the nozzle. These differences are represented then at a quasi-steady state, in which for CFD, the low-temperature species is almost consumed while, in experiments, remains in considerable quantities, effect that can be understood by the fact of the recession of OH in the CFD, which is not observed in the experiment. Therefore, in the simulations, this specie moves towards the nozzle and attacks CH_2O, consuming it, whereas in the experiments, both species remain stationary in their respective regions. Nevertheless, the spatial manner in which the species interact corresponds between simulation and experiment, as well as where their maxima occur.

Now moving to the SA, the comparison begins at 1.335 ms where only

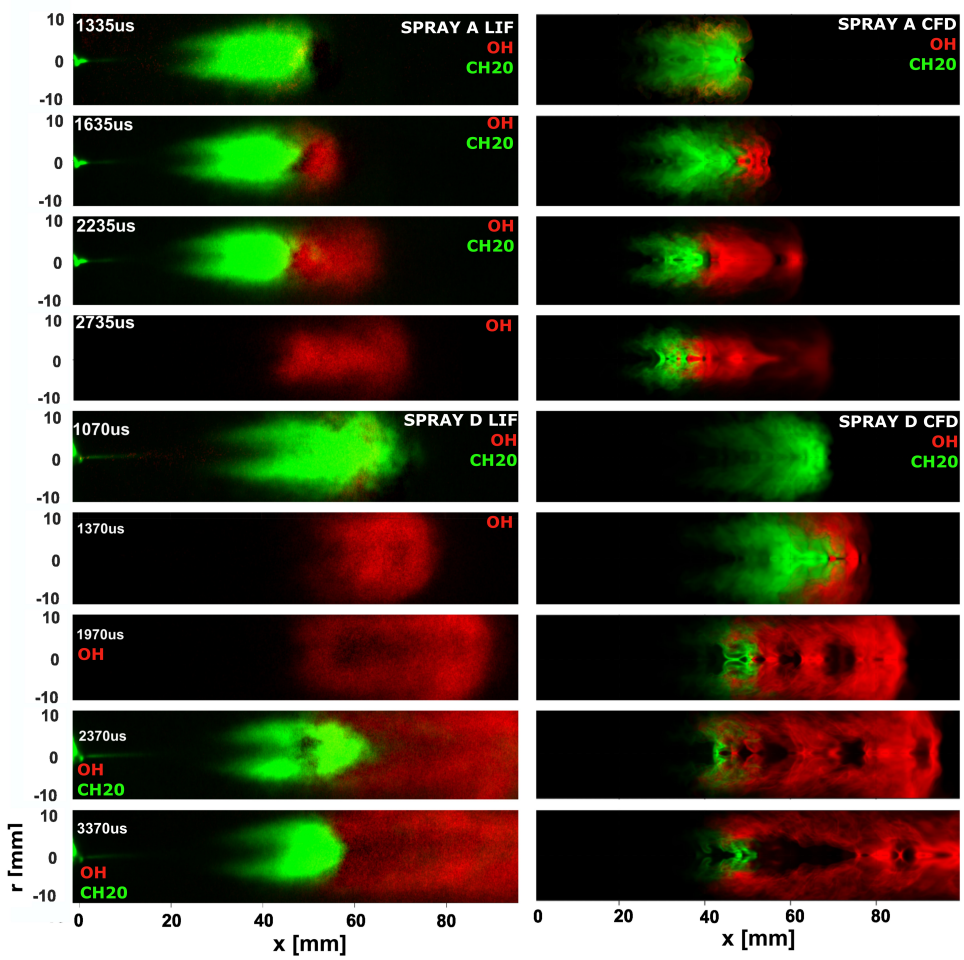

Figure 6.11: Comparison between experiments and CFD of the normalized signal of Formaldehyde (green) and OH (red) for OME_1. Left panel correspond to experimental results obtained from PLIF [19] and right panel from CFD, while the first four rows are for ECN SA and the last four for ECN SD.

CH_2O is observed, given the proximity to the injection point. At 1.635 ms, the CFD accurately reproduces the appearance of OH in both time and space, with an intense region of activity for CH_2O that starts being affected by OH. By 2.235 ms, in a quasi-stationary state, what determines the short LOL of the CFD compared to the experimental is the recession towards the nozzle experienced by OH in the simulation in agreement with Figure 6.8. Despite this peculiar behaviour obtained in the calculation, the relationship between species is correctly predicted, with a reasonably flat OH attack zone and intense OH activity over the central area of the spray.

As mentioned earlier, the flame structure of both sprays under nominal conditions has been validated using OH and CH_2O fields, as recently presented, as well as the OH^* field, which is a chemiluminescent species commonly used as a flame tracer due to its simple and non-intrusive measurement techniques compared to expensive laser measurements. In this thesis, chemiluminescent species have been modelled, as explained in Chapter 3, allowing for the determination of the flame structure using this species, and these results can be directly compared with experimental data, as shown in Figures 6.12 and 6.13.

Figure 6.12 shows the fields of OH^* from experiments and CFD for $OMEx$ for both nozzle sizes, with SA on the first six rows and SD on the last five. It should be noted that the figures do not correspond precisely to the same time instants in SA and SD, but in both cases, they depict the evolution of the spray after ignition until reaching a quasi-steady state. The differences between the structure of both sprays are noticeable and clearly associated with the influence of nozzle size. However, in both cases, CFD can accurately reproduce the OH^* structure within each case, with a common feature of having a maximum intensity at the base of the spray and decreasing intensity downstream.

In the SD case, which had a higher equivalence ratio at the LOL (Figure 6.8), the intensity of OH^* is maintained more strongly than in SA, particularly on the sides of the spray, typically on the stoichiometric surface as commonly observed in conventional hydrocarbons. This effect is partly due to the size of the orifice in this spray and also influenced by the oxygenated nature of these fuels, In any case, CFD also captures these differences, including the disappearance of the typical spray head observed at 1255 μs and also at 2655 μs.

Figure 6.13 shows, similar to the case of $OMEx$, the distribution of OH^* in both sprays for OME_1, including experimental and CFD results, as well as their temporal evolution. In the case of OME_1, as seen in the validation based on PLIF results, its flame structure is different from what is expected

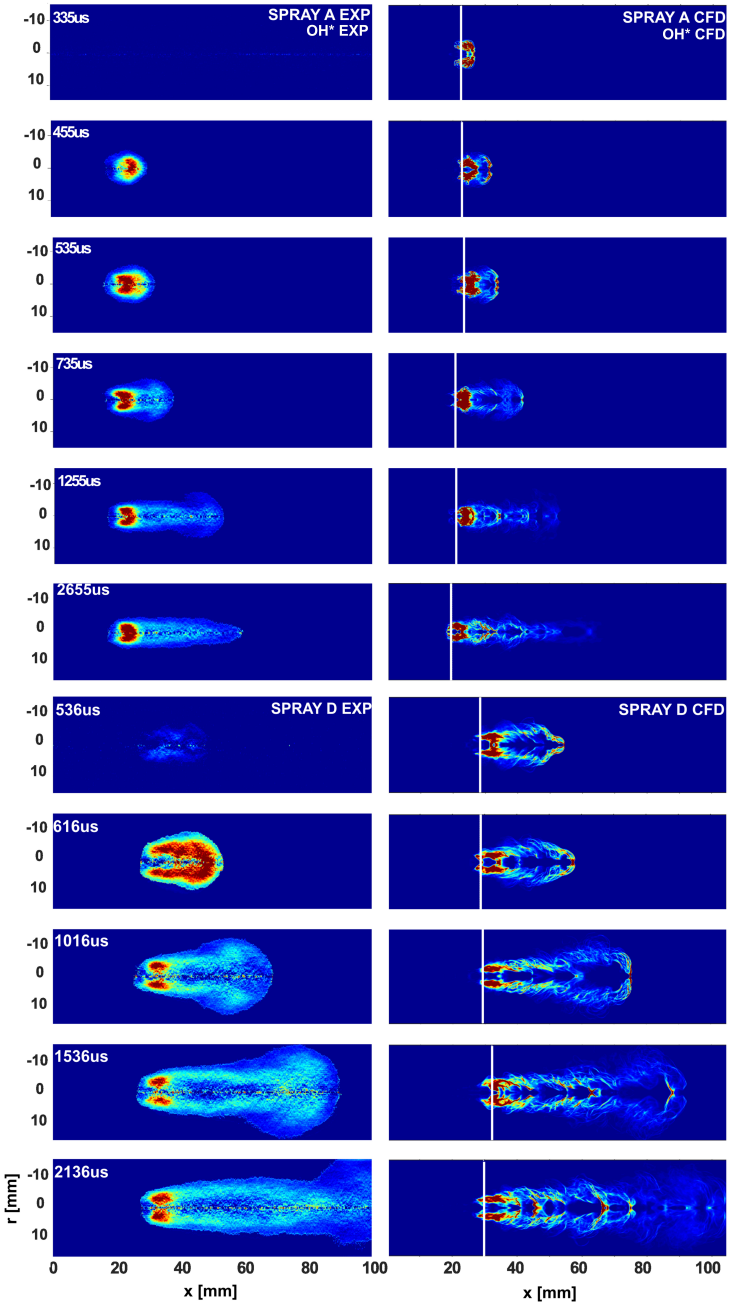

Figure 6.12: Spatial and temporal evolution of OH^* for OMEx. The first six rows correspond to ECN SA and the last five to ECN SD. In each block of two columns, the first one presents the deconvoluted signal at the symmetry plane of the flame obtained with OH^* chemiluminescence optical technique from [19], and the second present the azimuthal average result of modelling the OH^* chemiluminescence.

in a diffusion flame. This is clearly reflected in the OH^* structure, which is consistent with the extremely low equivalence ratio at LOL (Figure 6.8).

While the structure is the most striking aspect of this figure, especially in the case of SA, this section will focus on validation, leaving detailed analysis for later. However, it can be observed that this behaviour is consistent with the results obtained from RANS (see Chapter 5), which could be considered close to a premixed or partially premixed flame. Here, it can be seen that for both sprays, the intensity of OH^* is concentrated at the LOL position and extends only slightly downstream for SD and not at all for SA. CFD perfectly predicts this behaviour of a simple spot in the SA, although CFD predicts a movement towards the nozzle by OH^* once it ignites, which is translated into a recession towards the nozzle of the LOL. However, this backward movement is not observed in the experiment, consistently with PLIF OH. This indicates that the chemiluminescence is correctly modelled, although the lift-off stability proves challenging to be capture by CFD.

Continuing the exploration of chemiluminescence, after its successful validation through modelling, its data will be used with the aim to answer two questions related to the main chemiluminescent species involved in a combustion process. Firstly, it aims to identify the differences between the ground species OH and the excited species OH^* through CFD simulations. These species have different chemical natures, and often, due to the uncommon modelling of the excited species and the fact that it is more economical to quantify OH^* than OH experimentally (as it requires advanced optical techniques like PLIF), erroneous comparisons can be made. Therefore, false conclusions can be drawn when validating OH fields from CFD with OH^* fields from experiments.

Secondly, the relationship between typical chemiluminescent species in hydrocarbon flames (used as a reference and starting point here) will be analysed. This is interesting because, although these species are formed at different wavelengths as it was shown in Figure 3.3, there may be doubts in experimental conditions about whether some species, such as OH^*, may be recorded due to issues with optical filters, etc. However, what stands out in the target fuels of this thesis is that, due to their oxygenated nature with a high degree of oxygen bound and absence of C-C bonds, as shown in the literature review (chapter 2), they do not produce soot. This has a significant influence on experimental measurements since, in regular hydrocarbon fuels, resulting in sooting flames, soot incandescence overlaps with chemiluminescence, and hence the actual source of the recorded radiation in images cannot be distinguished.

Figure 6.14 shows a compilation of experimental results for $OMEx$, where the recently mentioned issues are addressed. The first row contains the OH^*

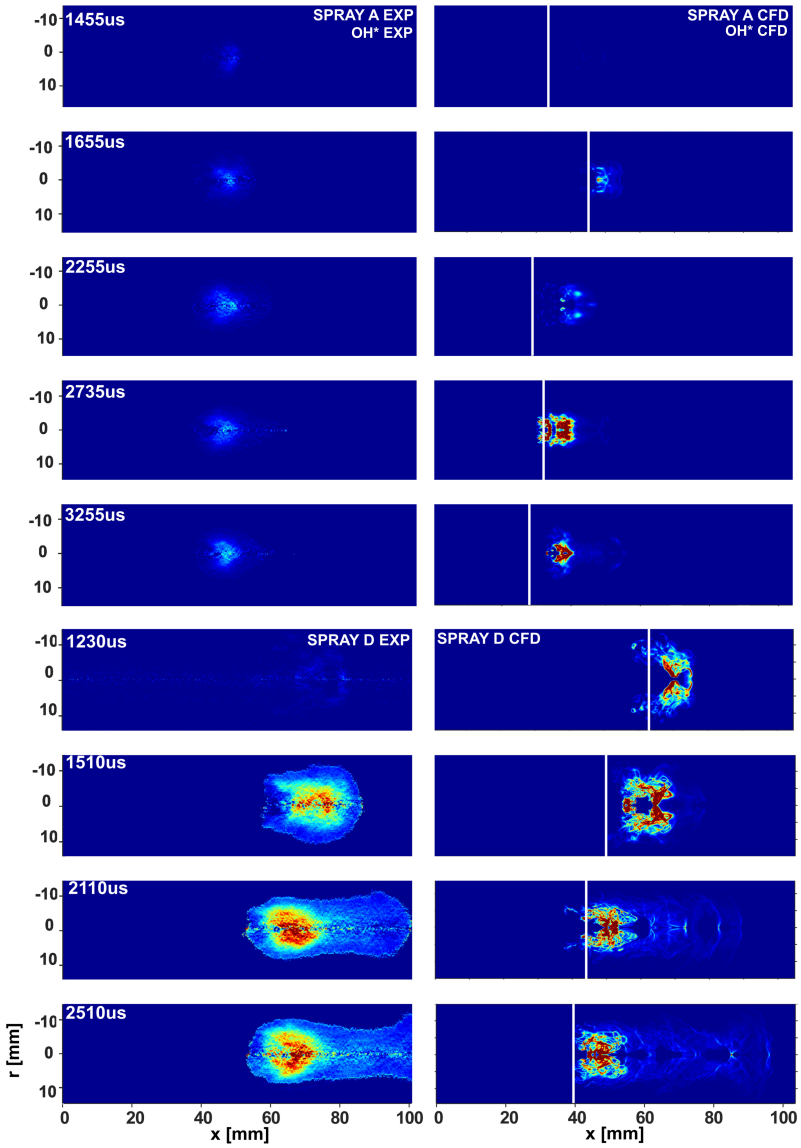

Figure 6.13: Spatial and temporal evolution of OH^* for OME_1. The first five columns correspond to ECN SA and the last four to ECN SD. In each block of two columns, the first one presents the deconvoluted signal at the symmetry plane of the flame obtained with OH^* chemiluminescence optical technique from [19], and the second present the azimuthal average result of modelling the OH^* chemiluminescence.

field obtained through chemiluminescence [19] (deconvoluted to be consistent when comparing with PLIF measurements in the second row). The second row presents the OH field obtained with PLIF [19], illustrating the relationship between both species. Finally, the third row contains DBI results demonstrating that no soot generation is observed with this fuel [17, 18]. Therefore, with these fuels, by recognizing the relationship between the chemiluminescent species and considering that ideally, they should not interfere with each other, one can be confident about the source of the recorded signal, which will be used to validate the models.

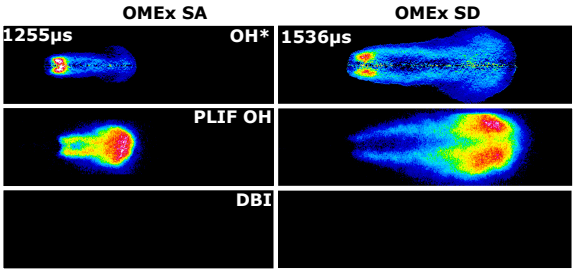

Figure 6.14: Results of flame structure for $OMEx$ with ECN SA and SD obtained by means of three different optical techniques. The first row correspond to the OH chemiluminescence deconvoluted signal at the symmetry plane of the flame [19], the second one depicts the OH PLIF signal [19], and the third row the average soot KL values obtained with DBI [17, 20].*

Based on the results obtained with flamelets and homogeneous reactors presented in Chapter 4 regarding chemiluminescent species, it was observed that the fuel type did not influence the distribution of these species (mainly comparing $OMEx$ and OME_1) but instead exhibited similar characteristics in terms of the conditions where they were found, regardless of the mechanism used. In this section, for brevity, the results of the $OMEx$-SD case will be presented and analysed. Then, Figure 6.15 shows the temporal evolution of the three modelled chemiluminescent species: OH^*, CH^*, and $C2^*$, in the third, fourth, and fifth columns, respectively. The second column displays the evolution of OH, while the first column corresponds to fuel age, a parameter that helps understand how the different chemical nature affects the spatial distribution within the spray, primarily of OH and OH^*, although the other two excited species follow the same trend as OH^*. All the presented fields result from azimuthal averaging of the instantaneous fields.

Starting with comparing OH and the OH^*, the first thing to mention is the LOL distance. The white vertical lines, solid and dashed, represent

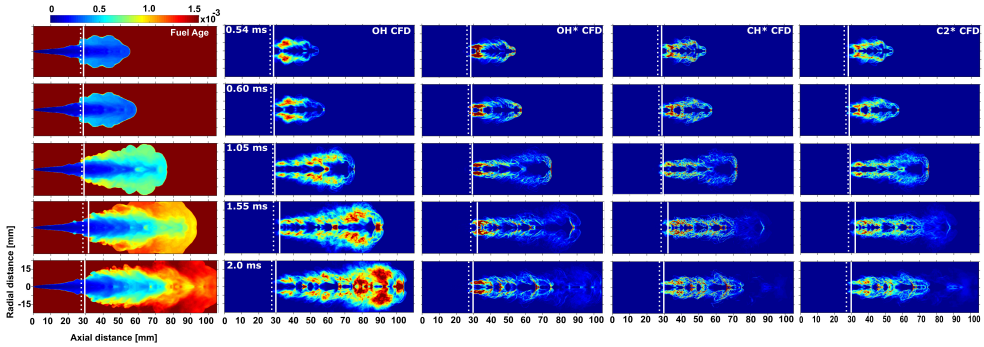

Figure 6.15: Comparison of the azimuthal average field of the fuel age field (first column), OH (second column) and chemiluminescence species fields, OH, CH* and C2* in the second, third, and fourth columns, respectively, and the for several time steps. Results correspond to OMEx SD.*

the LOL obtained from the OH and OH^* fields, respectively. For almost all time instances, it can be observed that the LOL obtained from OH is longer than that obtained from OH^*. The difference is small, but it is noteworthy and should be considered. Furthermore, the significant difference between these two species lies in their spatial distribution within the spray. While OH concentrates its maximum intensity at the head of the spray, OH^* it does so at the flame LOL position. This is directly related to the chemical nature of each species. OH^* has a limited lifetime determined by the spontaneous emission rate, while OH, as Maes et al. [21] states, is more long-lived and remains partially in equilibrium with the water produced during combustion.

These aspects are consistent with the findings from the flamelets and homogeneous reactors (section 4.4), where OH expands towards both lean and rich regions around the stoichiometric condition, typically between normalized progress variable (C) values of 0.7 and 1, consistently with their role as an equilibrium combustion product. On the other hand, the excited species OH^* is preferentially distributed towards rich regions, with a smaller portion towards lean regions. It is also noteworthy that in oxygenated fuels, OH^* is not found at C = 1; although it may be close to this value, it never reaches the equilibrium condition, consistently with its role as an intermediate species or rather a marker of chemical activity at around the LOL zone.

Fuel age, also known as residence time, supports these characteristics here. By comparing the fields of these species with the fuel age, it can be observed that, as expected, the region near the LOL, where the mixture fractions are higher, generating a rich region with high velocities, corresponds to a smaller

fuel age value. There is a clear correlation between OH and the regions where the fuel age increases significantly, possibly where the species are already or close to equilibrium. This can be seen at all time instances presented in Figure 6.15, but it is particularly noticeable later. For example, at 2 ms and 75 mm from the nozzle, the fuel age increases significantly, OH^* loses intensity sharply, and OH increases intensity, expands and invades that region at the head of the spray.

Focusing now on the relationship between the three modelled chemiluminescent species, OH^*, CH^*, and $C2^*$, it can be seen that they share the same spatial region and even have a similar distribution in terms of species intensity within the spray, especially in the first three-time instances shown. However, as the conditions become quasi-steady, CH^* and $C2^*$ experience a decrease in intensity downstream, becoming almost negligible after 80 mm. This is not the case for OH^*, which maintains its distribution and reaches the peak of the spray even at these time instances, with diminished intensity, yet still appreciable.

This observation aligns with the findings of Liu et al. [22], who used experimental techniques to compare OH^* and CH^* for a methane flame. They found that the distribution of OH^* can be divided into three regions: an intense section near the nozzle, a transition section in the middle of the flame, and a secondary section downstream. On the other hand, CH^* only exists in the first two regions defined above. The noteworthy aspect of these observations is that, as seen in the figure, OH^* extends throughout the spray and follows its temporal evolution, making it the best flame tracer regarding chemiluminescent species. Tracking CH^* or $C2^*$ would result in losing information about the downstream spray structure as time progresses.

6.6 Spray autoignition sequence

In this section, similar to Chapter 5, the analysis of auto-ignition is presented. It focuses on the heat release rate and mass species, examining spatial and temporal evolution. Furthermore, the study is extended to the mixture fraction space, where fuel age and heat release rate are used to describe the phenomenon. Figures 6.16 and 6.17 show the auto-ignition sequence of $OMEx$ for SD and SA, respectively. These figures display the normalized tracer species OH and CH_2O at each time step and the HRR, with the dashed green line representing the stoichiometric surface in each case. In this chapter, these panels will provide insights into the auto-ignition characteristics associated with the effect of the change in orifice size. Additionally, especially for SA, it will be possible

to visualize the features identified in LES but not discernible in RANS due to its averaged nature, which complements the experiments and helps understand the distribution of species and HRR within the spray.

Starting with $OMEx$, in both SD and SA, Figures 6.16 and 6.17 respectively, show that the maximum of heat release occurs at the LOL position, and consistently with the previously mentioned trend of ϕ at LOL values (Figure 6.8), the same pattern is observed downstream in each case. For SD, which had the highest ϕ at LOL value among the four cases, the heat is still being released over the stoichiometric surface downstream (in Figure 6.16, the stoichiometric surface and the HRR are superimposed, however it can be notice the yellow tone of the HRR underneath), similar to what happens in hydrocarbons under Diesel spray conditions [7]. This phenomenon is not so evident in the SA of $OMEx$, in which the effect of the decrease in equivalence ratio on the LOL position is already evident concerning the larger spray, resulting in a release of heat with high intensity at this position, but very little or almost negligible around the stoichiometric surface further downstream.

Another aspect to highlight from the nozzle sizes comparison, is the different distribution of OH with in the spray, which could be related with the mixing process and its stoichiometric conditions in each spray, and finally determines the interaction with CH_2O. In SD (Figure 6.16), the stoichiometric surface is clearly defined, delineating the rich zone in the core of the spray from the lean zone within the spray, which subsequently defines or is closely related to species distribution. In this case, OH is found on the stoichiometric surface, not within the spray, encompassing the upstream formaldehyde. However, in SA, OH does not contain formaldehyde but is in a reaction zone and faces each other. This effect, returning to the stoichiometric surface, can be explained in SA as the lean (periphery) and rich (centre of the spray) zones are not clearly delimited, unlike in the larger nozzle spray in which the bigger nozzle diameter determine a faster mixing, hence, larger stoichiometric surface. Instead, in SA, irregularities in the mixture fraction distribution are observed, creating folds and pockets inside and outside the "main" stoichiometric surface. This leads to the expansion of OH within the spray, also close to the centre, as there is no clear separation zone between rich and lean areas.

To finish the comparison between SA and SD, the plots of accumulated values of species shows that, for both cases, the time evolution of the production of CH_2O and OH in both sprays is very similar, and the ID is also. However, due to the mixing process that governs each spray, the flame structure during ignition presents the above-mentioned differences, which have been visualized through experiments. At this point, the contribution of LES is highlighted

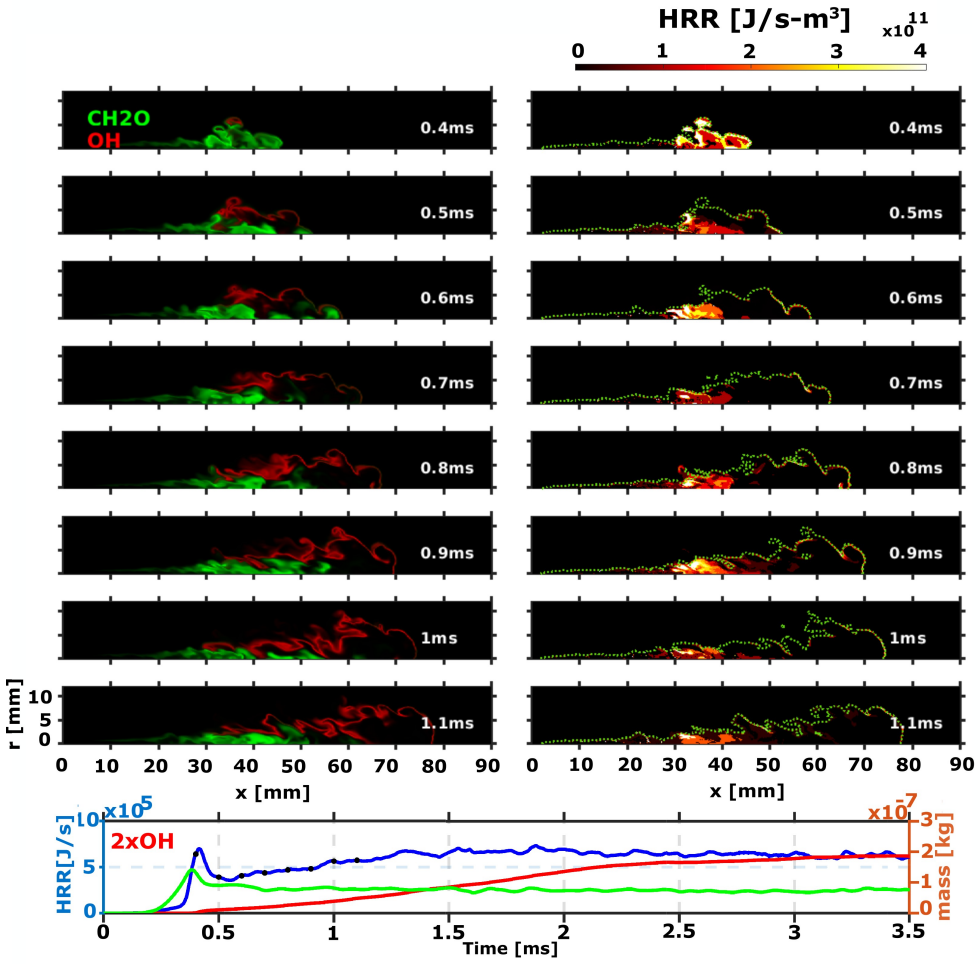

Figure 6.16: Time sequence of CH_2O and OH mass fraction (left panel) and local heat release rate (right panel) around ignition timing for OME_x at 900 K for the ECN SD injector. Colorscales of species are normalized to the instantaneous maximum. Stoichiometric mixture fraction iso-contour are marked with dotted lines. Bottom plot shows the time-resolved total species mass and heat release rate.

once again, as it can capture this mixture influenced by the oxygen content of the fuel.

Moving on to OME_1 and following the same reasoning as for $OMEx$, considering the fuel low reactivity and high ignition delay with the shorter chain within the $OMEn$ family, the fuel has more time to mix. Moreover,

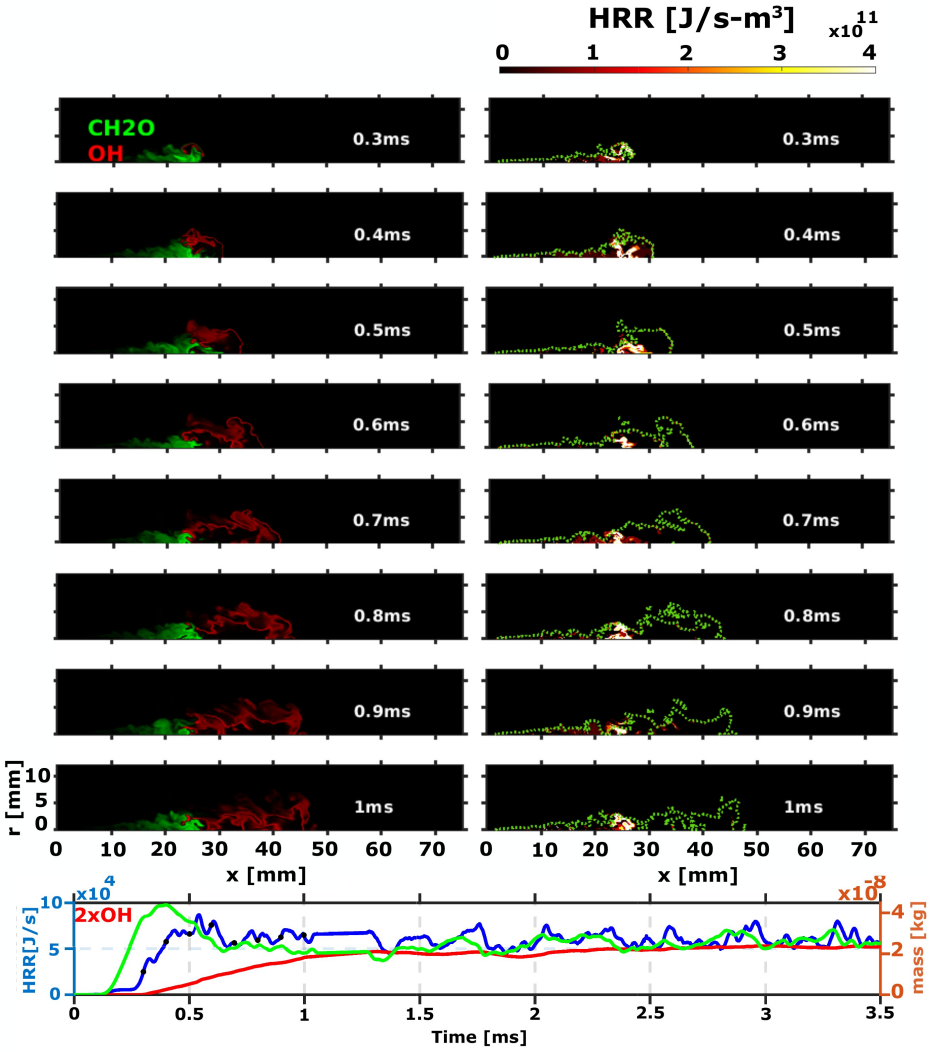

Figure 6.17: Time sequence of CH_2O and OH mass fraction (left panel) and local heat release rate (right panel) around ignition timing for OME_x at 900 K for the ECN SA injector. Colorscales of species are normalized to the instantaneous maximum. Stoichiometric mixture fraction iso-contour are marked with dotted lines.Bottom plot shows the time-resolved total species mass and heat release rate.

due to its low boiling point (short liquid length), the stoichiometric surface is extremely short in SA and completely irregular. However, for SD, the situation is closer to that of $OMEx$. Following the trend of Figure 6.8 where the ϕ at

LOL values are shown, OME_1-SD and $OMEx$-SA are the intermediate cases, which are also explained in this section consecutively.

Therefore, OME_1 with the larger nozzle also develops a stoichiometric surface that advances downstream over time but internally has rich and lean zones, sharply separating the spray between rich and lean regions, as $OMEx$-SD does in its typical diffusion flame. As a result, OH extends throughout the spray from a certain axial distance, rather than just being present on the periphery. The quantitative relationship between species is similar to that of $OMEx$, with significant production of OH, which consumes CH_2O and moves upstream.

For OME_1-SA, heat release occurs under lean conditions, creating conditions that are not conducive to the production of OH, which indicates faster combustion. Unlike the previous cases, in OME_1-SA, a considerable amount of time is required to observe OH after the ignition delay (300 μs approximately). Auto-ignition is strongly governed/characterized by an extensive presence of CH_2O, which, due to the low production of OH, is not consumed and persists in significant quantities throughout the auto-ignition process.

Furthermore, with the LES results, it is observed that the stoichiometric surface does not exceed 20 mm throughout the auto-ignition process. Instead, some pockets detach and move with the downstream flow, disappearing over time. Consequently, heat release always occurs under lean conditions.

To continue with the auto-ignition process of $OMEx$ and OME_1 in the two considered nozzle sizes, Figures 6.20 and 6.21 present the evolution of this process, but unlike the previous figures, in the mixture fraction space instead of physical space. Specifically, the temperature versus mixture fraction map is shown. The structure of the figures is as follows: in each panel, the first two rows correspond to SA, and the last two rows correspond to SD. For each nozzle, the upper row is colour-coded by fuel age and with HRR in the lower row. For each fuel and nozzle size, the initial time shown corresponds to a time very close to the ignition delay. Subsequently, intervals of 0.10 ms are used, and the last and fourth-time interval is slightly longer to observe a more advanced state, closer to the quasi-steady state. It allows for a connection with the Z-T maps of canonical configurations. It explains, through the concept of fuel age, the differences in ignition between a flamelet model and the spray. This was previously discussed in the RANS chapter by tracking maximum temperature and its corresponding mixture fraction (Figure. 5.9), mentioning the fuel age concept but without any result about it, since the fuel age transport equation approach was included for the calculation of the LES simulations matrix.

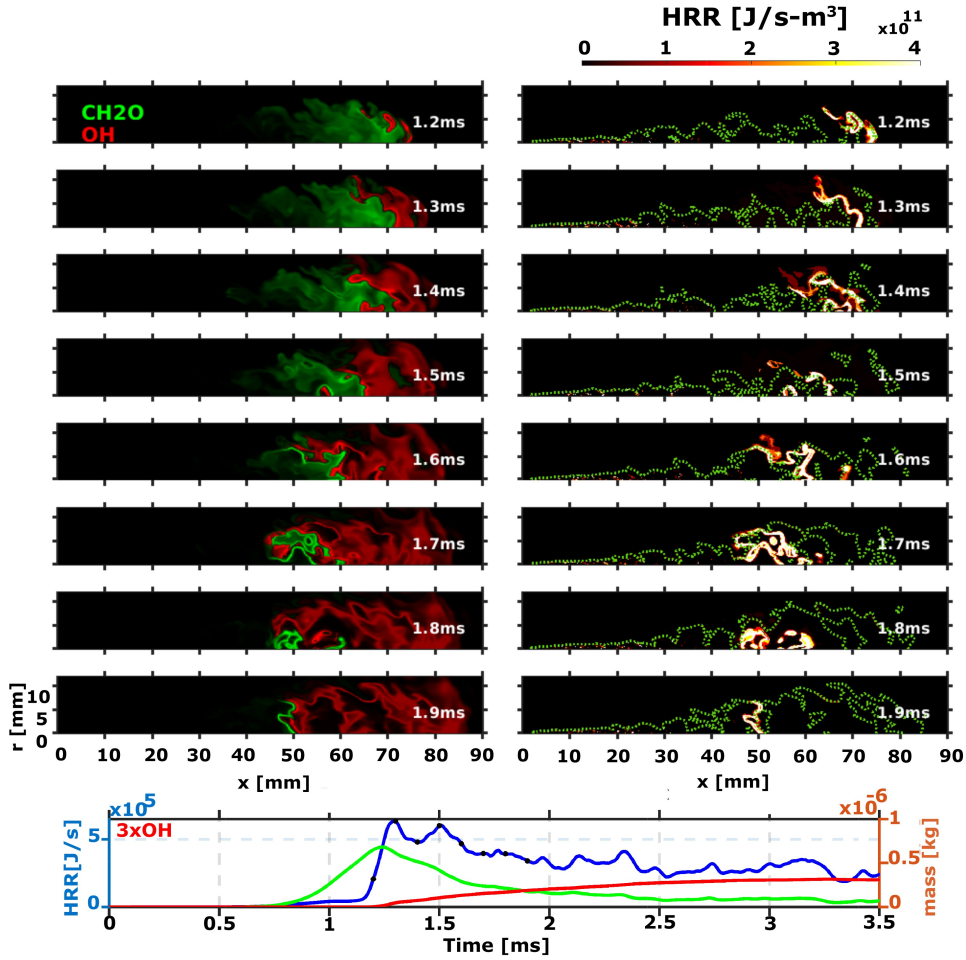

Figure 6.18: Time sequence of CH_2O and OH mass fraction (left panel) and local heat release rate (right panel) around ignition timing for OME_1 at 900 K for the ECN SD injector. Colorscales of species are normalized to the instantaneous maximum. Stoichiometric mixture fraction iso-contour are marked with dotted lines. Bottom plot shows the time-resolved total species mass and heat release rate.

In the case of $OMEx$ (Figure 6.20), ignition begins in rich zones and then propagates towards the stoichiometric region under both nozzle conditions. The rich zones that each nozzle size can ignite are clearly distinguished. Given the mixing process imposed by each orifice size, the SD nozzle reaches richer values of mixture fraction (0.3 - 0.4) with higher average temperatures than SA (max 0.2). In both SA and SD, the three zones of chemical activity or

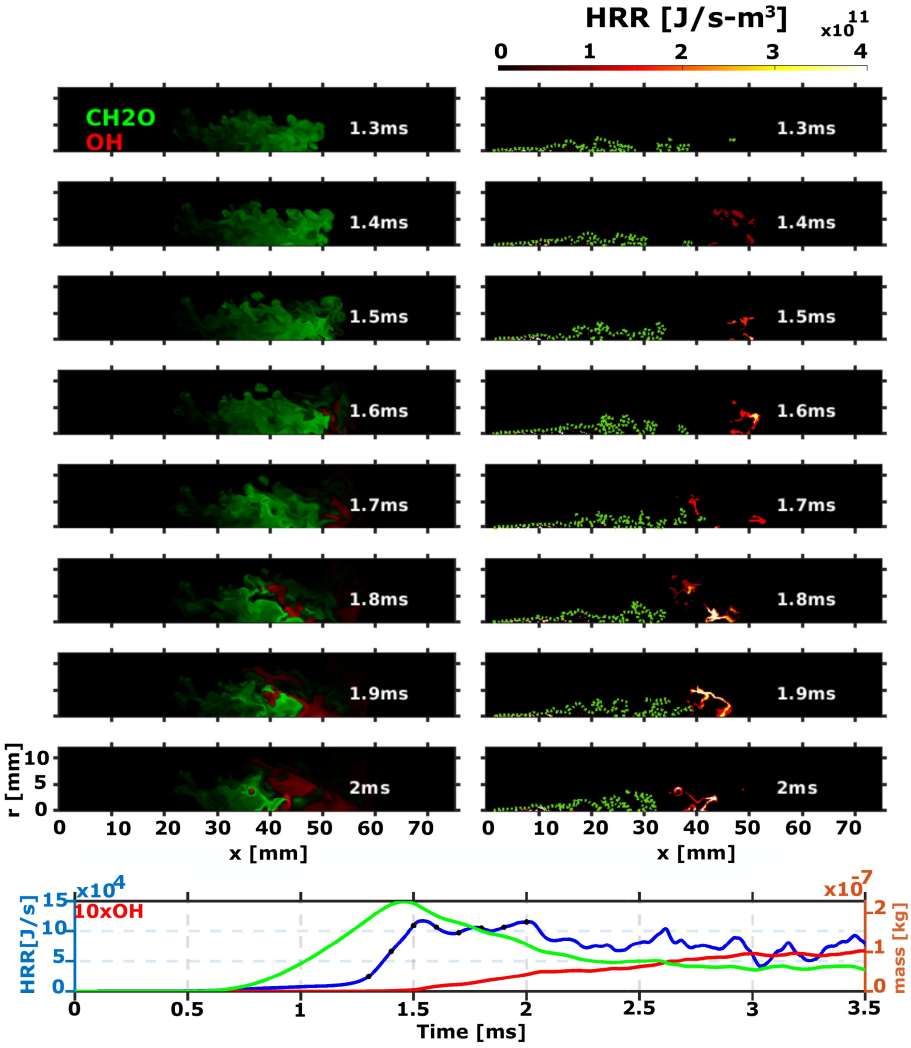

Figure 6.19: Time sequence of CH_2O and OH mass fraction (left panel) and local heat release rate (right panel) around ignition timing for OME_1 at 900 K for the ECN SA injector. Colorscales of species are normalized to the instantaneous maximum. Stoichiometric mixture fraction iso-contour are marked with dotted lines. Bottom plot shows the time-resolved total species mass and heat release rate.

heat release are observed: low, medium, and high temperature. However, the high-temperature zone tends to disappear in the SD as time progresses. While heat is released in both rich and lean zones, it is much higher in the rich zone

in both sprays, consistently with what was observed in the representation of the process in physical space. These zones precisely correspond to mixtures with a lower fuel age. Indeed, this is expected in this type of flame. This leads to the observation that this fuel exhibits a similar ignition sequence between flamelets and the spray. The fact that a mixture can persist for a longer time in flamelets compared to the spray, which is governed by the mixing process and its timescales, does not affect the release of heat in regions with low fuel age. These mixtures, characterized by low fuel age, are also present and "available" in the spray.

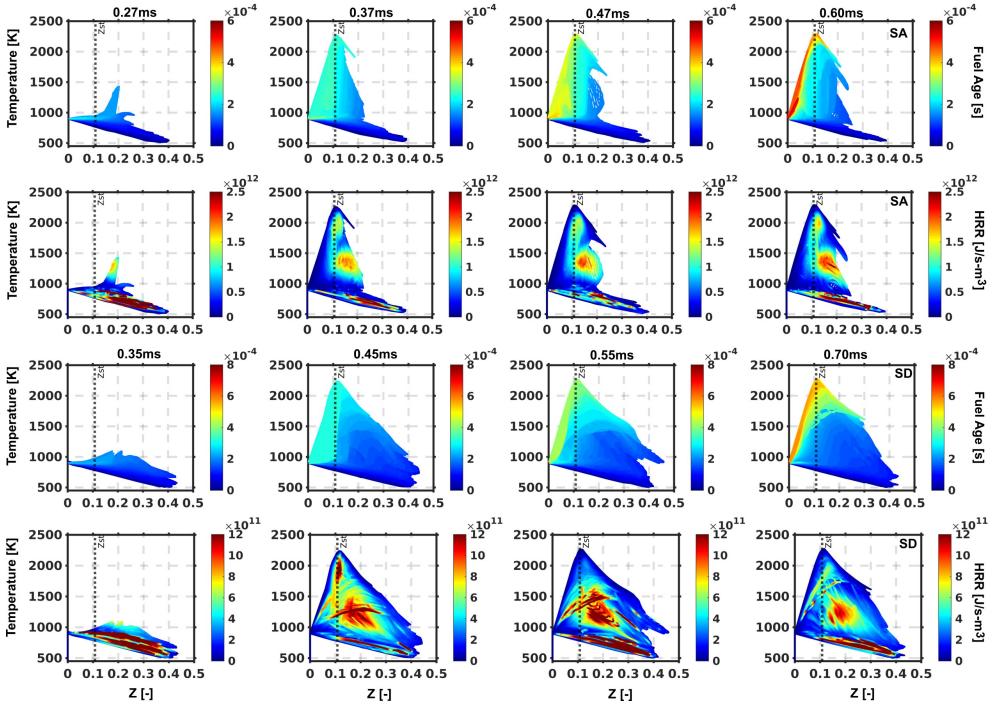

Figure 6.20: Spray flame structure of OMEx under nominal condition, represented by the temperature versus mixture fraction maps. The two top rows are for the ECN SA injector. The first one shows temperature coloured as the fuel age, and in the second row is coloured as the heat release rate. The last two rows have the same structure but for the ECN SD injector.

The main difference between flamelets and sprays arises when a long time is needed for auto-ignition, a condition that may not affect the flamelets but does determine (given the finite mixing times) the ignition of the spray; this effect is clearly seen in the OME_1, given its low reactivity and therefore, high ID. Moving on to this fuel and considering the results from canonical

configurations, RANS calculations, and the autoignition process in physical space, it is clear that in the SD case, OME_1 exhibits an intermediate behaviour between diffusive and premixed flames. On the other hand, in the SA case, the process is far from a diffusion flame. This is reflected in Figure 6.21, where ignition occurs in completely lean mixtures for SA, not reaching temperatures as high as in the SD case and with minimal heat release. This low heat release occurs in the regions closer to stoichiometry, which, similar to $OMEx$. This point can help understand the differences in ignition between flamelets and the spray in the case of OME_1. While in flamelets, OME_1 ignites and experiences a significant temperature increase under rich conditions (Figure 4.4), this cannot happen in the spray. The spray mixing process imposes a residence time for injected mass at different mixture conditions. This is represented in Figure 6.21, if compare the fuel age of the mixture at stoichiometric conditions in each spray, for SA, the mixture present really low values, below 0.35 ms, while in SD, the fuel age values are higher than 0.5 ms. Therefore, stoichiometric and even, rich mixtures spend more time at this conditions in SD than in SA, allowing to react in the larger spray. The spray is a set of different flamelets with a decreasing equivalence ratio over time due to fuel dilution with air. Due to the combined effect of reactivity and residence time within the spray, combustion does not occur over all equivalence ratio values as in a homogeneous reactor or flamelets configurations, even though the entire range of equivalence ratio is present in the spray. In the SD case, where a more considerable amount of mass is injected with a larger diameter, allowing richer zones to ignite, it develops a structure more similar to the $OMEx$ cases over time.

For OME_1-SA, the local peak in heat release/chemical activity occurring at stoichiometric/rich conditions cannot be reached in spray configurations simply because such mixtures are not able to react.

In summary, taking account the concept of fuel age and comparing two oxygenated fuels, one can state that fuel reactivity and mixing characteristics, depending on fuel and boundary conditions as nozzle diameter (i.e. stoichiometry) have a major role in chemistry development and hence flame structure.

6.7 Analysis of lift-off length stabilization

In order to analyse the flame stabilization of the presented cases, the two most extreme scenarios in terms of ϕ at LOL value classification, representing the most diffusive and least diffusive flames, were selected for brevity. Specifically, the $OMEx$-SD case (diffusive) and the OME_1-SA case (non-diffusive).

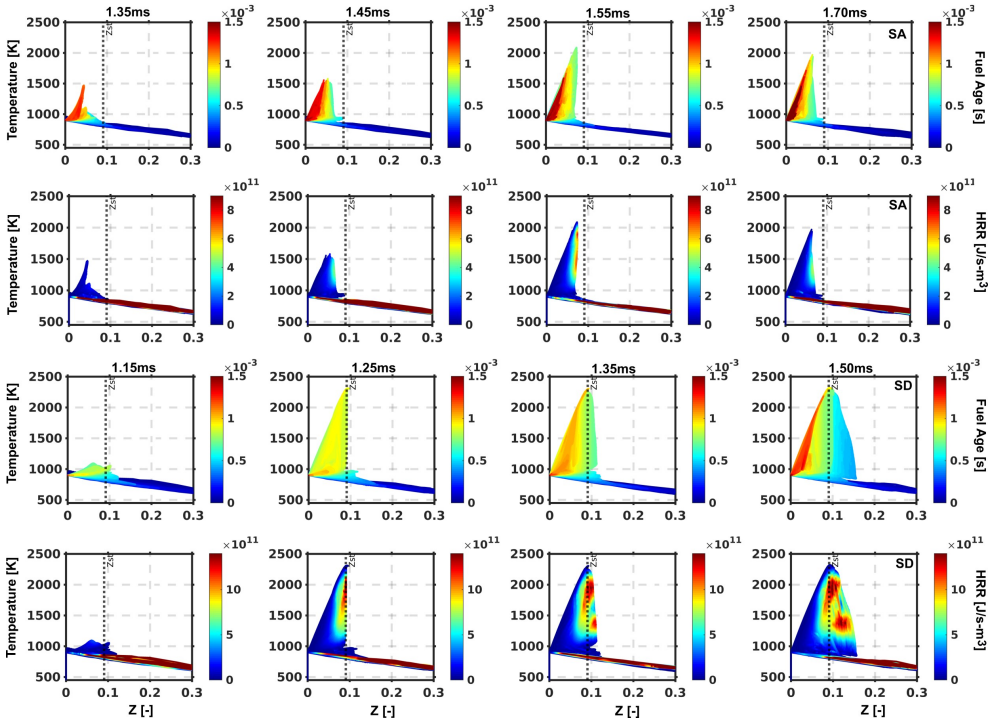

Figure 6.21: Spray flame structure of OME_1 under nominal condition, represented by the temperature versus mixture fraction maps. The two top rows are for the ECN SA injector. The first one shows the temperature coloured as the fuel age, and in the second row is coloured as the heat release rate. The last two rows have the same structure but for the ECN SD injector.

As illustrated in Figure 6.22, the flame stabilization of OME_1-SA is markedly different from what is observed in $OMEx$-SD, representing a typical diffusive flame. As mentioned earlier, flame stabilization is globally characterized by the LOL evolution over time. To study in more detail the flame stabilization of these fuels, Figure 6.22 depicts the OH field in combination with an isotherm of T = 1900 K (red line), in addition to the stoichiometric surface (black line) and the spray radius (white line) to visualize the central aspect that defines de flame stabilization, similar to the scheme presented by Tagliante et al. [23], where a detailed study and a proposal of a conceptual model of flame stabilization mechanisms for a lifted Diesel-type flame from DNS and experimental results. Thus, with this figure scheme, it can be clearly observed that the flame stabilization mechanism differs significantly between the two cases. The OME_x SD can be perfectly interpreted as a lifted-diesel-type flame, with two lobes on either side of the spray, creating rich zones (centre) and lean

regions (periphery). Small pockets of autoignition also exist, contributing to sustaining the flame.

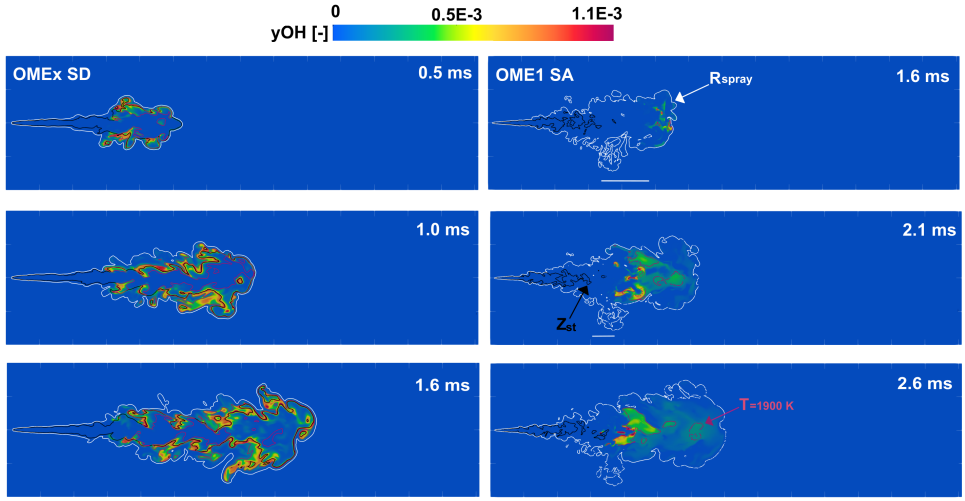

Figure 6.22: OH fields at several time-steps after the main ignition. Left image correspond to OMEx-SD case, and right to OME_1-SA. Spray radius determined from mixture fraction field is represented with a white line and stoichiometric surface with a black one. An iso-line of temperature at 1900 K (red line) is showed.

However, if now focus on the scheme developed by OME_1, it can be observed that the stabilization mechanism is very different, resulting in oscillations and backward movement of the LOL. These differences are similar to those explained by Perez-Sanchez in [24], where the flame stabilization of n-dodecane was studied at three different temperature levels: 750 K, 800 K, and 900 K. The study found that as the ambient temperature and reactivity decrease, the fuel loses the typical W-shaped form of the partially premixed combustion region (due to the presence of a rich mixture along the axis inhibits reaction and needs a radial displacement of combustion.) experienced at 900 K. This shape is flattened as the ambient temperature decreases. In the present work, a similar effect is found when comparing $OMEx$-SD and OME_1-SA. The similarity is even more remarkable when examining the LOL behaviour. Perez found that a greater recession of the LOL is observed at lower ambient temperatures. Here, a similar relationship can be established depending on the fuel, where $OMEx$ exhibits a very stable LOL both in SA and SD, while OME_1, regardless of the spray, once ignited, moves towards the nozzle, attempting to stabilize closer to it. Nevertheless, it should be noted that this movement towards the nozzle is

not observed in the experiments, so an assessment of the numerical effect on this behaviour must be considered.

As mentioned before and presented in the reactive validation section, both RANS and LES predict a recession towards the nozzle of the LOL in OME_1 (especially pronounced in SA) that is not observed in the experiment. However, the first conclusion is that LES approach cannot address this deficiency from the numerical simulation perspective. Given the irregularities in the OH field (Figure 6.22), which is used to determine LOL, three different LOL calculations have been performed for the OME_1 case. This is done to eliminate the hypothesis that the movement towards the nozzle obtained in the simulation is due to the post-processing of CFD results rather than the calculation itself. The three post-processing methods are: LOL obtained from the instantaneous OH field in a central plane (as in the other reactive validation cases); LOL obtained from the 3D instantaneous OH field; and finally, LOL obtained from azimuthal averaging of the OH field, the latter aimed at identifying whether the infinite planes in the domain could influence LOL position detection. A fourth and interesting approach would be to obtain LOL by averaging different LOL values obtained in different realizations, a path that could not be pursued in this thesis due to the computational cost associated with these calculations and the extensive matrix of conditions carried out.

Figure 6.23 (left) depicts the LOL evolution obtained through the three procedures mentioned above, along with the vapour penetration derived from considering the mixture fraction field in a plane and evaluating the 3D field. Regarding LOL, all three approaches exhibit remarkably similar behaviour, consistently manifesting a distinct backward motion and reaching a relatively stable value upstream of the ignition point.

As mentioned earlier, this particular OME_1-SA 900 K case experiences a combination of effects and events that may account for the predicted flame stabilization behaviour in simulations based on the employed models. The events and effects include the low reactivity of the fuel (Table 2.1), resulting in delayed ignition; the presence of oxygen in the fuel, which shortens the stoichiometric surface; and the low boiling point (Table 2.1), leading to a short liquid length, creating ample space (and time due to the high injection duration) to mix the evaporated fuel with air, resulting in a leaner mixture. This combination is mitigated, both in the case of SA 1000 K (Chapter 5) and SD 900 K (Section 6.3). In the former case, the high temperature in the atmosphere where the fuel is injected compensates the low reactivity of the fuel. In the latter case, the mixing process imposed by the SD, where more mass is injected, causes the stoichiometric surface to reach areas farther from

the orifice, similarly affecting the liquid length.

Considering that the reaction zone of this fuel under these conditions exhibits characteristics of a lean mixture, it is plausible to speculate that using the UFPV combustion model (based on counterflow flamelets) may influence the CFD results. Considering those above, the same case has been computed using another combustion model, namely, the Well-Mixed SAGE (WM). This combustion model is based on the well-mixed SAGE detailed kinetics solver, available in the CONVERGE CFD code [25]. The net production rate of each species is derived from the chemical mechanism, which is then used to solve the source term corresponding to the species transport equations at each computational cell and time step. Unlike the UFPV model, the WM model has no pre-imposed structure. Due to the high computational cost associated with solving transport equations for each species in the extensive mechanism used to model the chemical kinetics of this fuel, the case has been simulated using the RANS framework.

Figure 6.23 (right) presents the post-processed results of this case, comparing it with the UFPV cases (RANS and LES). The first notable observation is that, from UFPV combustion model point of view, RANS and LES predicts exactly the same recession effect on the LOL. Furthermore, the WM model (RANS calculation) does not exhibit LOL recession; instead, it maintains a moderately constant distance, resembling the experimental behaviour. However, it over-predicts the stabilized LOL value. Interestingly, both models ignite at a very similar distance from the orifice, quite close to the experimental ignition point. Nevertheless, their evolution over time is markedly different. Despite over-predicting the stabilized value, the WM model manages to reproduce stabilization at a nearly constant distance, akin to the experimental outcome. Suggestion that an LES simulation using WM would predict a better LOL time-evolution. Figure 6.23 (right) also includes the vapour penetration evolution from both combustion models, suggesting that, unlike LOL position, vapour penetration is not affected by the considered combustion model.

Given all that has been outlined above and considering the workflow employed in this thesis, the step preceding the CFD calculation is the generation of tables from diffusive flamelets. In order to identify the structure to which the CFD solver resorts, Figure 4.3 from the canonical configurations chapter, compiles information from laminar flamelets (after integration to account for TCI) for representative strain rate values during the ignition process of OME_1 flamelets. The figures present the information in the form of Yc-Z maps coloured by $\dot{Y}_c$, representing the chemical activity. It is evident that under the counter-flow flamelet condition, chemical activity predominantly occurs in

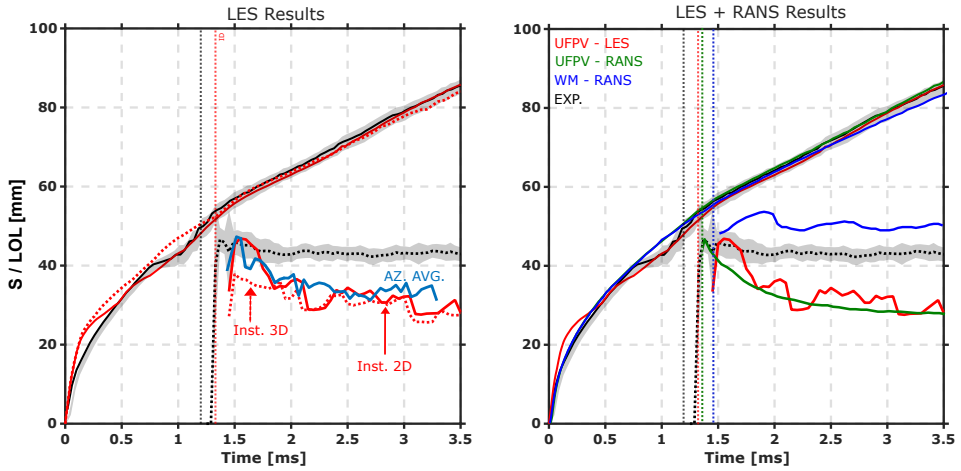

Figure 6.23: Time evolution of tip penetration and lift-off length for OME_1 for the ECN SA. On the left side, results obtained from LES and three different post-process are shown, and in the right a comparison between two combustion models and the two frameworks considered in this are presented. Vertical doted lines represent the ID.

rich zones, a tendency that is accentuated as the strain rate increases and also near the stoichiometric region. In contrast, there is minimal activity in lean zones. This observation might indicate that the combustion model tends to move towards the orifice in search of more reactive conditions to sustain flame stabilization.

In order to open a discussion and based on those above about the flamelets reactivities zones depending on the configuration, Figure 6.24 shows the normalized progress variable (C) and the mixture fraction (Z) fields for the two cases. Also, the LOL is represented with the white dashed line at each time. Results are shown at two timings, namely the main ignition and the at quasi-steady state.

The choice to represent these two parameters to visualize the possible flame structure of OME_1-SA is based on the classification proposed by Masri [26], where the concept of premixed flame and stratified flame is differentiated primarily based on the values of Z and C. Given the conditions presented by these two cases, on the one hand, $OMEx$-SD, where Z values cover the entire spectrum, typical of a non-premixed flame, and on the other hand, OME_1-SA would be close to what is considered a stratified flame, as in the ignition zone, Z always falls within a lean-stoichiometric range (clearly visible with the blue tone in the color scale). This flame displays premixed characteristics;

however, it spans a narrow range of flammable equivalence ratios due to the non-premixed nature of the flow. Mastorakos [27] refers to this scenario as premixed flame propagation in a stratified mixture, noting that low gradients of mixture fraction describe the reaction zone. Additionally, it can be observed that at the moment just after ignition (first row), the value of C in OME_1-SA compared to $OMEx$-SD is not as high, nor is it as widespread within the spray in the vicinity of equilibrium. Furthermore, this qualitative analysis aligns with the proposal by Bilger et al. [28] describing the stratified flames as a subgroup within the partially premixed turbulent combustion. In conclusion, the UFPV seems unable to predict adequate behaviour of mixture-controlled flames in case of low reactivity and ignition/stabilization in lean equivalence ratio, probably because it always tries to go towards a stoichiometric diffusion flame. However, the model succeeds in accurately replicating the distribution and interaction between species, CH_2O and OH, as well as the production of chemiluminescent species, both spatially and temporally.

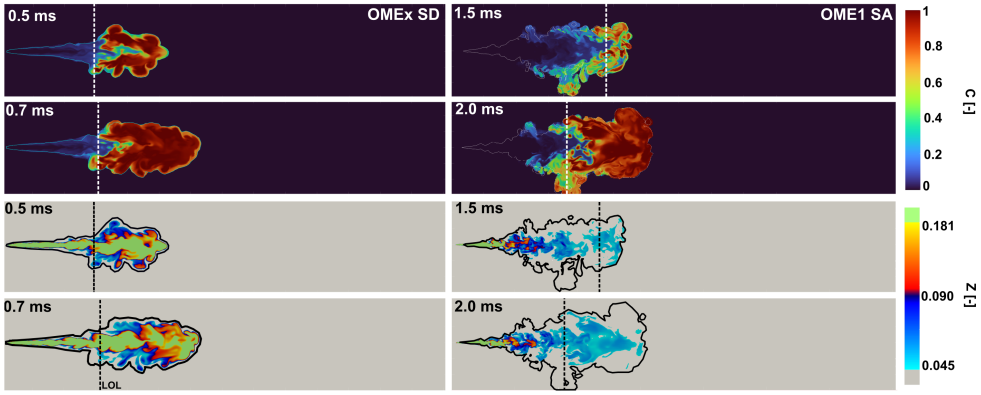

Figure 6.24: Normalized progress variable (top) and mixture fraction fields (bottom) for $OMEx$-SD (left) and OME_1-SA (right), after ignition and close to quasi-steady state

Finally, after the lift-off length stabilization analysis, and knowing that one of the significance of LOL lies in its close association with soot production. The increase in the lift-off length implies that the flame stabilizes in locations with leaner mixtures, resulting in a flame less prone to producing soot to the extent that soot becomes practically non-existent. Beyond the differences highlighted earlier between the two extreme cases analysed, it is now interesting for the four simulated nominal cases to emphasize and study through numerical results one of the novel and significant advantages of $OMEn$-type synthetic and renewable fuels, as discussed in the literature review Chapter 2, their negligible

or almost non-existent soot production, despite their different lift-off length. Although this thesis does not include particulate matter modelling, verifying this characteristic of soot-free production is essential. For this purpose, two conditions that determine the ability of a fuel to develop a soot flame have been visualized.

The well-known trade-off conditions between soot and NOx have been used. This trade-off provides guidelines for engine operating conditions in order to avoid soot and NOx emissions, in an engine, it is more complex, and both islands soot and NOx should be avoided; it is well-known that achieving this is challenging, given the low temperatures and the high equivalence ratio. The Low-temperature combustion (LTC) mode is an advanced engine technology capable of concurrently decreasing nitrogen oxides and soot emissions, all while preserving elevated thermal efficiency [29–31]. LTC is primarily accomplished through diverse methods, including homogeneous charge compression ignition, premixed charge compression ignition, partially premixed combustion, reactivity-controlled compression ignition, and gasoline compression ignition. Nonetheless, significant challenges in LTC include managing combustion across a broad range of loads, heightened combustion noise, and comparatively elevated emissions of carbon monoxide (CO) and hydrocarbons (HC) [32].

However, oxygenated fuels have emerged as a potential solution to soot production, regardless of the technology utilized in the engine, and as a characteristic purely associated with the fuel. Furthermore, Kitamura et al. [33] have studied the mechanism of smokeless Diesel combustion with oxygenated fuels, finding that the island is narrowed, particularly for DME ($OMEn$ with n = 0). The main difference is the size of the particles. To find particles with 40 nm in DME or OME_1, the equivalence ratio should be 4.5 and 5.5, respectively, while for n-heptane, 2.5. However, smaller particles with 5 nm may be found at an equivalence ratio of 2 or 2.5 for oxygenated fuels and from 1700 K. Nguyen et al. [34] have presented in an ECN workshop a study where they compare the potential of soot production of $OMEx$ and n-dodecane for the nominal condition of SA3, imposing the traditional conditions of temperature higher than 1400 K and equivalence ratio richer than 2, and under these conditions the differences were evident while for n-dodecane, these temperature and equivalence ratio conditions spatially coincide, facilitating soot production, the situation differs for $OMEx$ being completely separate.

This thesis, besides the finding of Kitamura, adopts the same criteria as Nguyen et al. in order to compare with hydrocarbon results and also given that it is the most conservative criteria if considered that $OMEx$ could present

differences with the island founded by Kitamura for DME and OME_1.

Figure 6.25 (top) visualizes the sooting-conditions results for each fuel ($OMEx$ and OME_1) for the smallest nozzle size (SA), representing the contour of an equivalence ratio equal to 2 (conditions higher than two are typically found within this contour) in red, and an iso-temperature contour of 1400 K in blue, for quasi-stationary conditions in each spray. This comparison shows that due to the oxygenated nature of these fuels, the $\phi = 2$ surface is short for these fuels. Additionally, in the case of OME_1, its low reactivity means that in the quasi-stationary state, the fuel has had too much time to mix with the air, resulting in a $\phi = 2$ surface even smaller than that of $OMEx$. In addition to the fact shown in Figure 6.19, the low production of OH (a tracer of high temperature) by OME_1 indicates that high temperatures are not reached in many regions of the spray.

Combining these characteristics results in the high-temperature region and the regions rich in oxygenated fuels being separated spatially, avoiding soot production, without any regions in the domain simultaneously fulfilling the sooting conditions.

Additionally, Figure 6.25 (bottom) shows the mass fraction of acetylene at the same instant of time as the condition of $\phi = 2$ and T = 1400 K. Acetylene is the most basic precursor of soot and is available in all chemical mechanisms. Therefore, even without modelling soot (out of the scope of this thesis), its production in each spray complements the findings mentioned earlier and the information available in the literature regarding these fuels. The results in Figure 6.25 demonstrate that oxygenated fuels produce orders of magnitude less acetylene than n-dodecane under these boundary conditions (nominal SA) if compared with literature results [35] for n-dodecane, where the yC_2H_2 mass fraction was in order to 1.5e-2 for different chemical mechanism and different combustion models evaluated. Also, Figure 6.25 show that the extension of the C_2H_2 within the spray is very compacted. This is associated with the chemical composition of each fuel. Both $OMEx$ and OME_1 share the basic structure, with the chain length being the differing factor. Neither of these fuels has carbon-carbon bonds, which translates to the difficulty of these fuels in generating species like C_2H_2 (acetylene).

Moving to the SD, Figure 6.26 shows that the scenario changes, mainly for the $OMEx$. The different mixing processes experienced by this spray, where more mass is injected and increased momentum flux resulting in a faster penetration, are responsible for this change in terms of the necessary conditions for soot production, finding that with greater penetration, rich conditions with $\phi \geq 2$, reach the high-temperature zone (T=1400 K). However, the situation

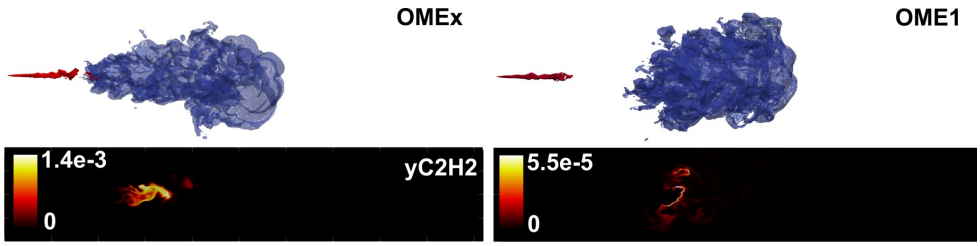

Figure 6.25: LES results at quasi-steady state of each case. Top image: iso-contour of equivalence ratio condition equal to 2 in red, and iso-contour of temperature of 1500 K. Bottom image: acetylene fields. Results are for $OMEx$ and OME_1, ECN SA.

remains far from the appearance presented by n-dodecane, also highlighting that the production of acetylene remains an order of magnitude lower in the $OMEx$ than in n-dodecane SA, where naturally, it is expected that for the same fuel in the SD the production would be even higher as it is presented by Zhang et al. [36] where a comparison of soot production between SA and SD is made. Therefore, after putting it into context by comparing it with highly sooty flames, it can be understood that despite the indications from figures 6.25 and 6.26, there are minimum conditions for soot production and bearing in mind the looser limits for oxygenated fuels presented by Kitamura et al., it is still challenging for this to occur, as evidenced by an experimental study using optical techniques by Pastor et al. [20] from the results of DBI, they conclude that oxygenated fuels do not produce particulate matter under any condition, neither in SA nor in SD. Finally, for OME_1, as expected, there are insufficient conditions according to the typical restriction on equivalence ratio and temperature proposed by Akihama et al. [37], even though acetylene production has increased due to the higher amount of injected mass. Although there is no longer such a large zone between $\phi = 2$ and T = 1500 K, these conditions do not spatially overlap, resulting in a situation similar to that of $OMEx$ in SA. This is consistent with the value of the equivalent ratio at the LOL position shown in Figure 6.8.

6.8 Analysis of low temperature conditions

As previously stated, the LES cases were selected based on the results of the RANS calculations and experimental results. For this reason, the high-temperature cases (1000 K) have been discarded as they do not present much novelty, developing a typical diffusion flame in both fuels, similar to any hydrocarbon. On the other hand, the low-temperature cases have shown that

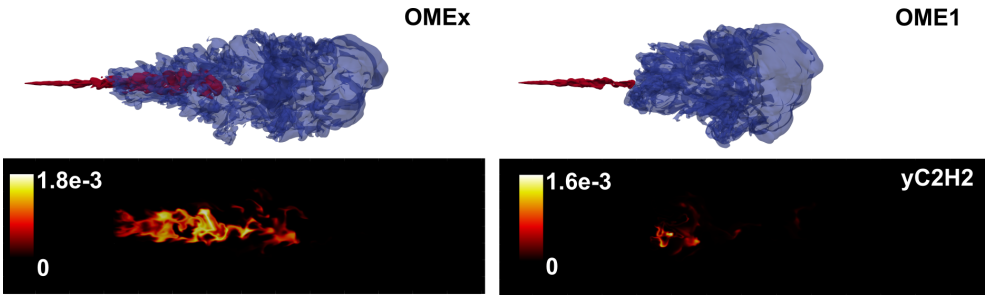

Figure 6.26: LES results at quasi-steady state of each case. Top image: iso-contour of equivalence ratio condition equal to 2 in red, and iso-contour of temperature of 1400 K. Bottom image: acetylene fields. Results are for $OMEx$ and OME_1, ECN SA.

these fuels can develop a different type of flame, especially OME_1, where its low reactivity combined with a low-temperature environment increases the differences already observed under nominal conditions. Just as in the nominal condition, the cases for both spray sizes have also been calculated at low temperatures to evaluate how the combustion model performs under these atypical flame behaviour and the chemical mechanism under low ambient temperature conditions. The global combustion parameters for both fuels in SA and SD are presented in Figure 6.27, where the simulation times are different depending on the ID value of each case, considering in all the cases that the quasi-steady state is achieved with the simulated time. It is important to note that in the experimental campaigns, the OME_1-SA case at 800 K did not ignite, so no information is available regarding ID and LOL, but the penetration measurement is available. In this section, the evaluation of model performance under low temperature conditions will be the focused, prioritizing the case of OME_1-SA due to its non-ignition characteristics (experimentally), a comparison between RANS, LES and experiments will be presented.

Concerning vapour penetration, it can be seen that the CFD well predicts all four cases. It is worth noting that in the SD cases where the penetration is greater, the experimental results are limited by the size of the optical window, while in the CFD, the domain has been increased compared to the SA case in order to obtain a more accurate evolution of the spray tip penetration. Now, focusing on $OMEx$ (left panels in Figure 6.27), the ID is significantly under-predicted for both sprays, approximately 50% lower than the experimentally obtained value. This did not occur in the nominal cases, indicating some inaccuracy in predicting the ignition of this mechanism under low-temperature conditions when an LES framework is used, with RANS under the same operating conditions, the ID was accurately predicted (Section 5.4). This

discrepancy is also reflected in the under-prediction of the LOL in the SD case. On the other hand, in the SA case, despite the large experimental variation in LOL, with error margins on the order of the LOL measurement, the LOL predicted by the CFD is very close to the instantaneous experimental value.

Regarding the OME_1 cases, due to the SA 800 K experimentally did not ignite, so the goal of the CFD calculation is not validation but rather to observe what the CFD predicts for this case with such low reactivity. It has already been presented in the RANS chapter, so a comparison between the two frameworks, LES and RANS, will be provided here. Nevertheless, the vapour penetration is available experimentally, corresponding to an inert case. Concerning this parameter, Figure 6.27 shows that both for SA and SD, the evolution of the vapour penetration predicted by the CFD is correctly aligned with the experimental result. As for the LOL, experimental values for OME_1-SD show a significant scattering, corresponding to a highly unstable operating condition. This means that validation from CFD is quite challenging. LOL predictions for OME_1-SD starts (2.4 ms) far from the experiment value, but rapidly (2.9 ms) fall within this high uncertainty interval.

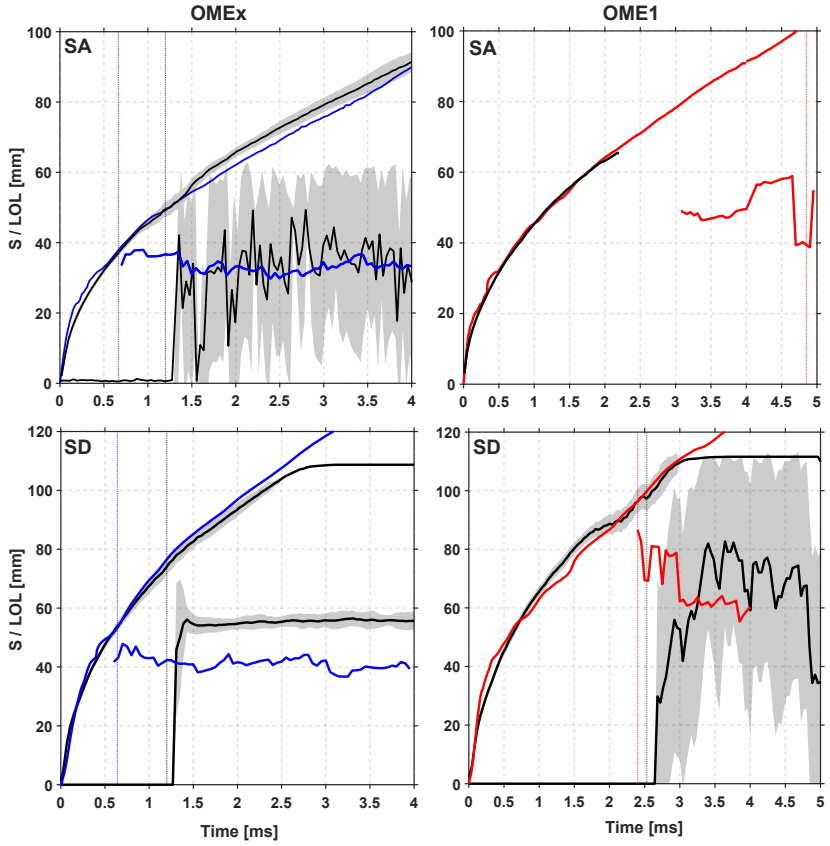

Figure 6.27: Time evolution of tip penetration and lift-off length for $OMEx$ and OME_1 for ECN SA and SD for the low temperature conditions (800 K). Vertical lines show the ID as derived from CFD and from experiments. There is no experimental information available about OME_1-SA penetration uncertainty.

For OME_1-SA, according to the maximum value of the temperature derivative, the main ignition delay occurs at 4.8 ms, even so, the derived LOL is presented after 3 ms due to the maximum temperature time evolution, which start to increase at this time (presented in Figure 6.29 and further commented in the following).

As in the nominal condition section, Figure 6.28 includes the results of ignition delay and stabilized average LOL values. In $OMEx$ cases, the experimental ignition under low temperature conditions is almost at the same timing for both sprays and also for CFD, despite the remarkable under-prediction, the trend is captured. Regarding OME_1, SD (the only that ignite experimentally), at 800 K the ID doubles the nominal value, igniting very late, but even so,

the Jacobs mechanism continue predicting correctly the ignition timing of this fuel. If now the ignition of $OMEx$-SD is compared with OME_1-SD, the tendency is the same as in nominal conditions, if compare experiments, $OMEx$ igniting on in half-time of OME_1 and this difference increase in CFD due to the under-prediction

Regarding the stabilized average LOL value, Figure 6.9 shows that, the LOL of $OMEx$-SA and $OMEx$-SD are closer to each other (36 mm and 41 mm respectively) than in the nominal case (20 mm for SA vs 30 mm for SD). Regarding stabilization, low temperature causes both to stabilize further apart. As for OME_1-SD, as seen in Figure 6.27, the recession persists, but at low temperatures, it stabilizes at the mean of the experimental value.

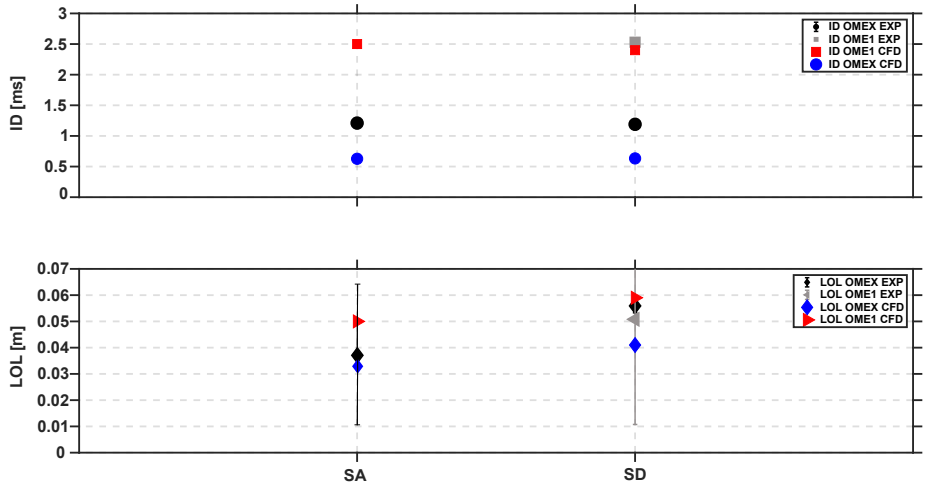

Figure 6.28: Ignition delay and stabilized lift-off length for both experimental results and CFD calculations for the low temperature conditions (800 K). Experimental data include both average and standard deviation. The figure include results of $OMEx$ and OME_1 and the two nozzle sizes.

Focusing on OME_1-SA, Figure 6.29 shows the evolution of the comparison of the spray tip penetration between RANS, LES and experiments, finding that great accuracy is achieved from the three sources, for that parameter is essential to highlight that the effect of the chemical mechanism is minimum in simulation, due to the late ignition timing. However, ID is far from RANS to LES and is null in experiments. Differences in ID influence the prediction of LOL, which is calculated simultaneously as in RANS for LES. However, the ID determined from the maximum derivative of temperature results in 4.8

ms; therefore, the length obtained is not strictly the LOL, but reflects the behaviour when the flame tries to stabilize under this challenging low reactivity condition. The differences between RANS and LES frameworks in terms of ID, are explained by examining Figure 6.29 (right), which illustrates, in the middle, the evolution of the maximum temperature across the entire domain. The LES calculation exhibits strong oscillations, consistently remaining below the maximum temperature reached by the RANS simulation. Even at 3.8 ms, it stays approximately 300 K lower, reaching the RANS temperature at nearly 5 ms and experiencing its maximum derivative there. Typically, when considering the same case simulated with both LES and RANS approaches, the LES would yield a higher maximum temperature, or at the very least, equal to that of RANS due to the strong influence of turbulence and the ability to reproduce intermittency, allowing to find hot spots within the spray. In the case of OME_1-SA at 800 K, the lower maximum temperature reached by the LES reflects its closer approximation to reality, where the fuel cannot autoignite under these low reactivity conditions. Furthermore, the right panel of Figure 6.29 shows the instantaneous field of temperature at 3 ms and 4.95 ms where it can be seen that the temperature in general is much lower than what the T_{max} vs time plot (middle panel) illustrates, and those maximum temperature values (1510 K for 3 ms and 2010 K for 4.95 ms) are only small spots (marked with a red star) but not indicative of sustained high temperature ignition. Reaffirming the closeness to the situation obtained in the experiments.

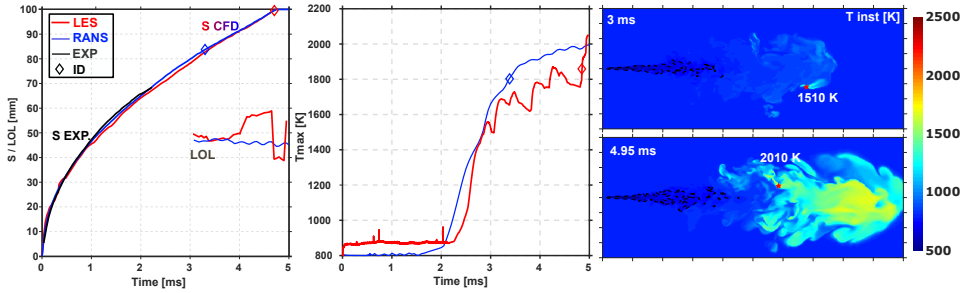

Figure 6.29: Left figure present the vapour tip penetration in solid lines and the lift-off length time evolution in dashed lines. Middle figure, display the time evolution of the maximum temperature within the domain, for CFD cases. Black lines correspond to experiments, red to LES results and blue to RANS. All results are for OME_1 ECN SA under 800 K condition. Left figure shows the instantaneous temperature field from LES simulations.

Figure 6.30 displays the temperature, CH_2O, and OH fields obtained through RANS and LES simulations. Additionally, the dashed line indicates

the stoichiometric surface. For both approaches, the shown fields result from azimuthal averaging over 25 planes in order to perform a fair comparison. Correlating them with Figure 6.29, the first row depicting the temperature field reflect the predictions made by tracking the maximum temperature, in LES due to the azimuthal average applied it can be noticed that the temperature in Figure 6.30 are lower than the instantaneous one (Figure 6.29), indicating the hot spot are the responsible for the high T_{max}. In averaged terms, temperature values in LES throughout the spray are significantly lower than those obtained with RANS. Even at 3 ms, the LES exhibits inert characteristics, whereas in RANS, the temperature increase is already noticeable. Regarding CH_2O, although the orders of magnitude obtained in both frameworks are similar, the spatial distribution is significantly different. In LES, CH_2O expands more within the spray, associated with the lower temperatures obtained with this approach. Additionally, it is related to the third presented field, OH, whose spatial distribution also differs, along with differences in orders of magnitude, LES field is multiplied by 10 in order to obtain similar magnitude and even so, is remarkably lower than the OH mass fraction obtained in RANS. Therefore, in the absence or low presence of radicals associated with low temperature, CH_2O will persist, similar to what occurred with OME_1-SA under nominal conditions.

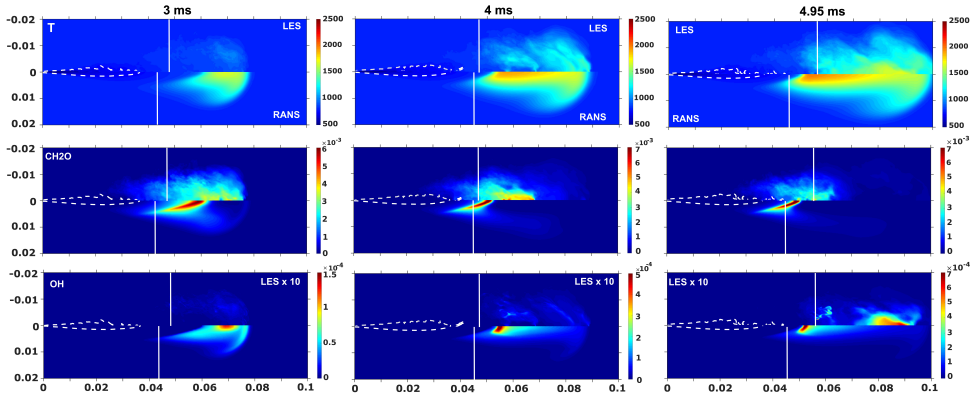

Figure 6.30: Temperature (top panel), CH_2O (middle panel) and OH (bottom panel) fields for three different instants. In each panel, top figure corresponds to LES results and bottom to RANS, in both cases an azimuthal average of the instantaneous fields is shown. Results for OME_1 ECN SA at 800 K.

Final considerations

To finalize this section where the behaviour in terms of global combustion parameters of the low-temperature cases have been presented, completing the analysis of the nominal conditions discussed earlier, Figure 6.31 summarizes the ignition process in terms of maximum temperature and mixture fraction for all the cases coloured by fuel age. This complements the findings presented in both the flamelets (Figure 4.4) and the RANS calculations (Figure 5.9).

Once again, the ignition process differs mainly due to the conditions in which it occurs for each fuel. For all four $OMEx$ cases, ignition is seen to occur with a similar sequence to that found in flamelets, with an initial low temperature propagating to rich mixtures, where it finally experiences a significant increase in temperature always under rich conditions until reaching the maximum temperature in mixtures close to or equal to stoichiometric. One first difference between RANS and LES is that, while for the former ignition at 800 K occurs under lean conditions, for LES the pathway happens under rich mixtures. These differences are clearly associated with the underestimation of the ID by the LES, which causes the stoichiometric surface is still close to the spray tip at the moment of ignition, hence, rich mixtures can auto-ignite. While in RANS, where the ID is 1.2 ms (exactly the same as the experiment), a separation of stoichiometric surface and the tip of the spray is already created (Figure 5.6), therefore, the spray auto-ignite in lean conditions and then stabilize at the stoichiometric surface. Given the oxygenated nature of the fuel, the stoichiometric surface has separated from the spray tip, creating a lean region where ignition occurs.

Moving on to the OME_1 cases, all cases exhibit a complete auto-ignition process under lean conditions with high fuel ages. There is a particularity in the case of the OME_1-SA nominal, where at high temperatures, the maximum temperature is found in regions with low fuel age compared to the rest. This is due to the pockets of stoichiometric regions that detach and move downstream, naturally having a much lower fuel age than the rest of the lean mixture. Although the maximum temperature has yet to be identified within these pockets since it corresponds to a low Z value, they are influenced by the proximity to these fresh mixtures existing in the maximum temperature zone, which generate large gradients of mixture fraction within the spray.

Regarding the other OME_1 cases, it is interesting to highlight the relationship between the nominal cases of SA and SD with the low-temperature SD case. The effect of the larger nozzle, where the flame tends to exhibit a more diffusive structure, and the low temperature associated with the low reactivity of the fuel lead to a flame that is more of a premixed or partially premixed

type. This results in an intermediate between the two nominal cases of both sprays.

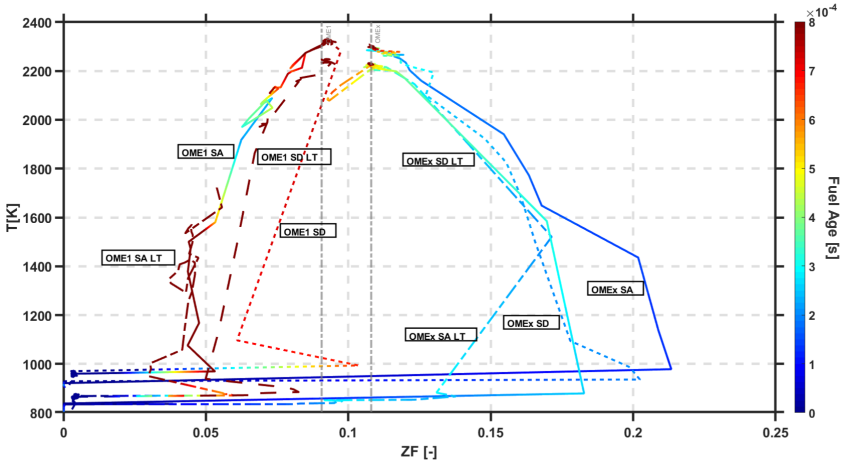

Figure 6.31: Evolution of instantaneous maximum temperature along ignition as a function of mixture fraction, as derived from LES results for both oxygenated fuels at 800 and 900 K, and ECN SA and SD.

At this point, explaining the ignition process presented in this figure (6.31) for the nominal OME_1-SD case is necessary. At low temperatures, it reaches a rich zone (Z = 0.11) and then, through a single point at 1100 K, it transitions to lean regions and automatically reaches a temperature of 2300 K in slightly rich mixture fractions. This is because the auto-ignition starts within small pockets of stoichiometric surface, presenting a steep slope for maximum temperature evolution within the domain. The temperature field goes from being at low temperatures to autoigniting at a point with temperatures close to adiabatic conditions. Indeed, this behaviour would be impossible to identify through a RANS calculation where everything is averaged, and the stoichiometric surface does not exhibit discontinuities. The reproduction of these pockets is possible thanks to the LES approach, which allows for a more detailed representation of the flow and combustion processes. LES captures the small-scale turbulent structures and provides a more accurate description of the local phenomena, such as the formation and evolution of stoichiometric pockets, which play a crucial role in ignition, mainly in these fuels.

6.9 Summary and conclusions

In this chapter, ECN SA and SD have been modelled in the frame of LES simulations using the Dynamic structure turbulence model and the UFPV combustion model. The most interesting cases from the point of view of the combustion behaviour have been selected based upon RANS and experimental results. LES analysis has focused on the effect of fuel and nozzle diameter. Both nominal (900 K) and low temperature (800 K) cases have been selected in terms of ambient temperature.

A robust calibration of the spray model has been achieved, meticulously validating the mixing process for SA and SD (with fewer parameters and experimental sources for this nozzle). This is noteworthy, given that the subsequent combustion process occurs over the multiphase flow predicted at this stage.

Extensive validation of the reactive cases has been conducted, obtaining good predictions for the global combustion parameters and flame structure of the studied nominal cases. Under nominal conditions, the ignition delay is well captured as the penetration value for both fuels and both nozzles. However, for OME_1, predicting LOL is challenging due to the flame structure developed by this fuel, especially with SA.

The flame structure has been properly described, revealing a clear trend between reactivity and non-premix/premix flame structures, which can be globally classified based on the equivalence ratio value at the LOL position, ranging from more diffusive to less diffusive: $OMEx$-SD / $OMEx$-SA / OME_1-SD / OME_1-SA. Correct prediction of chemiluminescence is observed using the sub-mechanisms and thermodynamic properties employed. OH^*, CH^*, and $C2^*$ exhibit similar structure within the flame, with OH^* aligning well with experimental data. Furthermore, it is found that OH^* is the best tracer due to the larger extent along the flame. Regarding the relation between ground and excited species, OH appear downstream than OH^* and presents their maximum intensity at the head of the spray. In contrast, OH^* present their maximum at the LOL. It is crucial to note that the validation of CFD using OH^* images cannot be carried out with OH fields.

From the study of the autoignition process in these cases, the oxygenated character of these fuels in the species distribution within the spray is highlighted. Fuel pockets downstream of the stoichiometric surface modify the typical two-lobed structure presented by hydrocarbons, even in $OMEx$-SD, the most diffusion flame structure.

A comparison between flame stabilization in the extreme cases, $OMEx$-SD and OME_1- SA, has been conducted, revealing novel mechanisms within a Diesel-like spray for OME_1, which develops a flame that is challenging to classify but could be close to partially premixed or, more specifically, stratified. However, given those mentioned above, the UFPV model may exhibit deficiencies in predicting the evolution of LOL for this case, as this combustion model imposes a pre-defined model of diffusion flamelets directly influencing the CFD result.

Regarding the non-sooting nature of polyoxymethylene dimethyl ethers flames, it has been demonstrated that, in addition to the low production of C_2H_2, a major soot precursor and the high degree of bound oxygen, which also inhibits soot formation, the necessary conditions for favourable soot formation in terms of mixture and temperature are also not met.

Finally, incorporating the low-temperature cases and considering the significant instability observed in most of these experimental scenarios, it is evident that the Cai mechanism for $OMEx$, which accurately predicted ID and LOL under nominal conditions, fails to do so correctly under low reactivity conditions when LES is considered. On the other hand, the case of OME_1-SA, which did not ignite experimentally, exhibits ignition in CFD; however, LES yields results more closely aligned with reality than RANS results. The ignition occurs very late, with significantly low production of OH and maximum temperatures within the spray much lower than those observed in Chapter 5.

References

[1] Pope, Stephen B. “Ten questions concerning the large-eddy simulation of turbulent flows”. In: *New Journal of Physics* 6.1 (2004), p. 35. DOI: 10.1088/1367-2630/6/1/035.

[2] Pitsch, Heinz. “Large-Eddy simulation of turbulent combustion”. In: *Annual Review of Fluid Mechanics* 38.1 (2006), pp. 453–482. DOI: 10.1146/annurev.fluid.38.050304.092133.

[3] Pomraning, Eric and Rutland, Christopher J. “Dynamic one-equation nonviscosity large-eddy simulation model”. In: *AIAA journal* 40.4 (2002), pp. 689–701. DOI: 10.2514/2.1701.

[4] Mompó, Juan Manuel. “Engineering Large Eddy Simulation of Diesel Sprays”. In: *Riunet* (2014). DOI: 10.4995/Thesis/10251/37345.

[5] Bharadwaj, N, Rutland, Christopher, and Chang, S. "Large eddy simulation modelling of spray-induced turbulence effects". In: *International Journal of Engine Research* 10 (2009), pp. 97–119. DOI: 10.1243/14680874JER02309.

[6] Bharadwaj, Nidheesh and Rutland, Christopher. "A large-eddy simulation study of sub-grid two-phase interaction in particle-laden flows and diesel engine sprays". In: *Atomization and Sprays* 20 (2010), pp. 673–695. DOI: 10.1615/AtomizSpr.v20.i8.20.

[7] Pachano, Leonardo. "CFD Modeling of combustion and soot production in diesel spray". PhD thesis. Universitat Politecnica de Valencia, 2020.

[8] Payri, Raul, García-Oliver, Jose M., Xuan, Tiemin, and Bardi, Michele. "A study on diesel spray tip penetration and radial expansion under reacting conditions". In: *Applied Thermal Engineering* 90 (2015), pp. 619–629. DOI: 10.1016/j.applthermaleng.2015.07.042.

[9] L., Pickett, J., Manin, C., Genzale, and al., Siebers D. et. "Relationship Between Diesel Fuel Spray Vapor Penetration/Dispersion and Local Fuel Mixture Fraction". In: *SAE Int. J. Engines 4(1):764-799, 2011* (2011). DOI: 10.4271/2011-01-0686.

[10] Wiesmann, Frederik et al. "Numerical and Experimental Investigations on the Ignition Behavior of OME". In: *Energies* 15 (18 2022). DOI: 10.3390/en15186855.

[11] García-Oliver, José M., Malbec, Louis-Marie, Toda, Hubert Baya, and Bruneaux, Gilles. "A study on the interaction between local flow and flame structure for mixing-controlled Diesel sprays". In: *Combustion and Flame* 179 (2017), pp. 157–171. DOI: 10.1016/j.combustflame.2017.01.023.

[12] Pastor, Jose, Garcia-Oliver, Jose, Antonio, Garcia, and López, Andrés. "An Experimental Investigation on Spray Mixing and Combustion Characteristics for Spray C/D Nozzles in a Constant Pressure Vessel". In: *SAE, International Powertrains, Fuels & Lubricants Meeting* (2018). DOI: 10.4271/2018-01-1783.

[13] Pérez-Sánchez, E.J. "Application of a flamelet-based combustion model to diesel-like reacting sprays". PhD thesis. Universitat Politecnica de Valencia, 2019.

[14] Xue, Qingluan, Som, Sibendu, Senecal, Peter K., and Pomraning, E. "Large Eddy simulation of fuel-spray under non-reacting IC engine conditions". In: *Atomization and Sprays* 23.10 (2013), pp. 925–955. DOI: 10.1615/AtomizSpr.2013008320.

[15] Pérez-Sánchez, Eduardo J, Garcia-Oliver, Jose M, Novella, Ricardo, and Pastor, Jose M. "Understanding the diesel-like spray characteristics applying a flamelet-based combustion model and detailed large eddy simulations". In: *International Journal of Engine Research* (2019). DOI: 10.1177/1468087419864469.

[16] CMT, Clean Mobility and Thermofluids - ENERXICO database. *https://www.cmt.upv.es/#/ecn/download/Enerxicodata*. 2022.

[17] Garcia-Carrero, Alba. "Experimental study of the fuel effect on diffusion combustion and soot formation under diesel engine-like conditions". PhD thesis. Universitat Politecnica de Valencia, 2021.

[18] Pastor, José V., García-Oliver, José M., Micó, Carlos, García-Carrero, Alba A., and Gómez, Arantzazu. "Experimental Study of the Effect of Hydrotreated Vegetable Oil and Oxymethylene Ethers on Main Spray and Combustion Characteristics under Engine Combustion Network Spray A Conditions". In: *Applied Sciences* 10.16 (2020), p. 5460. DOI: 10.3390/app10165460.

[19] Pastor, Jose V., García-Oliver, Jose M., Micó, Carlos, and Tejada, Francisco J. "Characterization of the oxymethylene ether fuels flame structure for ECN Spray A and Spray D nozzles". In: *Applied Energy* 332 (2023). DOI: 10.1016/j.apenergy.2022.120475.

[20] Pastor, José V, García-Oliver, José M, Micó, Carlos, and García-Carrero, Alba A. "An experimental study with renewable fuels using ECN Spray A and D nozzles". In: *International Journal of Engine Research* 23.10 (2022), pp. 1748–1759. DOI: 10.1177/14680874211031200.

[21] Maes, Noud et al. "Characterization of Spray A flame structure for parametric variations in ECN constant-volume vessels using chemiluminescence and laser-induced fluorescence". In: *Combustion and Flame* 174 (2016), pp. 138–151. DOI: 10.1016/j.combustflame.2016.09.005.

[22] Liu, Yao, Tan, Jianguo, Wan, Minggang, Zhang, Lang, and Yao, Xiao. "Quantitative Measurement of OH^* and CH^* Chemiluminescence in Jet Diffusion Flames". In: *ACS Omega* 5 (26 2020), pp. 15922–15930. DOI: 10.1021/acsomega.0c01093.

[23] Tagliante, Fabien et al. "A conceptual model of the flame stabilization mechanisms for a lifted Diesel-type flame based on direct numerical simulation and experiments". In: *Combustion and Flame* 201 (2019), pp. 65–77. DOI: 10.1016/j.combustflame.2018.12.007.

[24] Desantes, J.M., García-Oliver, J.M., Novella, R., and Pérez-Sánchez, E.J. "Application of a flamelet-based CFD combustion model to the LES simulation of a diesel-like reacting spray". In: *Computers and Fluids* 200 (2020), p. 104419. DOI: 10.1016/j.compfluid.2019.104419.

[25] CONVERGE CFD Software. *https://convergecfd.com*.

[26] Masri, A.R. *Turbulent Combustion Modeling*. Springer, Netherlands, 2011, pp. 355–380.

[27] Mastorakos, Epaminondas. "Ignition of turbulent non-premixed flames". In: *Progress in Energy and Combustion Science* 35.1 (2009), pp. 57–97. DOI: 10.1016/j.pecs.2008.07.002.

[28] Bilger, R.W., Pope, S.B., Bray, K.N.C., and Driscoll, J.F. "Paradigms in turbulent combustion research". In: *Proceedings of the Combustion Institute* 30.1 (2005), pp. 21–42. DOI: 10.1016/j.proci.2004.08.273.

[29] Niemeyer, Kyle E, Daly, Shane R, Cannella, William J, and Hagen, Christopher L. "Investigation of the LTC fuel performance index for oxygenated reference fuel blends". In: *Fuel* 155 (2015), pp. 14–24. DOI: 10.1016/j.fuel.2015.04.010.

[30] Hossam A., El-Asrag and Yiguang, Ju. "Direct numerical simulations of NOx effect on multistage autoignition of DME/air mixture in the negative temperature coefficient regime for stratified HCCI engine conditions". In: *Combustion and flame* 161.1 (2014), pp. 256–269. DOI: 10.1016/j.combustflame.2013.07.012.

[31] Kukkadapu, Goutham, Kumar, Kamal, Sung, Chih-Jen, Mehl, Marco, and Pitz, William J. "Autoignition of gasoline surrogates at low temperature combustion conditions". In: *Combustion and Flame* 162.5 (2015), pp. 2272–2285. DOI: 10.1016/j.combustflame.2015.01.025.

[32] Pachiannan, Tamilselvan et al. "A literature review of fuel effects on performance and emission characteristics of low-temperature combustion strategies". In: *Applied Energy* 251 (2019), p. 113380. DOI: 10.1016/j.apenergy.2019.113380.

[33] Kitamura, T, Ito, T, Senda, J, and Fujimoto, H. "Mechanism of smokeless diesel combustion with oxygenated fuels based on the dependence of the equivalence ration and temperature on soot particle formation". In: *International Journal of Engine Research* 3.4 (2002), pp. 223–248. DOI: 10.1243/146808702762230923.

[34] Tuan Nguyen, Fabien Tagliante, Julien Manin, Lyle Pickett, Hyung-Sub Sim, Kevin Wan and Angela Wu. *Investigation of Formaldehyde and PAH Behavior Using LES of N-dodecane and OME*. 2022. URL: https://ecn.sandia.gov/workshop/ECN9/ECN8.1.mp4.

[35] Chishty, Muhammad A., Bolla, Michele, Hawkes, Evatt R., Pei, Yuanjiang, and Kook, Sanghoon. "Soot formation modelling for n-dodecane sprays using the transported etodel". In: *Combustion and Flame* 192 (2018), pp. 101–119. DOI: 10.1016/j.combustflame.2018.01.028.

[36] Zhang, Min, Ong, Jiun Cai, Pang, Kar Mun, Bai, Xue-Song, and Walther, Jens H. "Large eddy simulation of transient combustion and soot recession in the ECN Spray A and D flames". In: *Fuel* 329 (2022), p. 125384. DOI: 10.1016/j.fuel.2022.125384.

[37] Akihama, K., Takatori, Y., Inagaki, K., Sasaki, S., and Dean, Anthony M. "Mechanism of the Smokeless Rich Diesel Combustion by Reducing Temperature". In: *SAE Technical Paper 2001-01-0655* (2001). DOI: 10.4271/2001-01-0655.

Appendix

6.A Particularities of OME1 ignition - SA vs SD

As has been shown throughout this document, OME_1 exhibits a very particular ignition process and flame structure under diesel spray conditions to which it is exposed. This leads to several aspects that are different from what is expected and are being explained in this thesis. From the LES calculations, which have been used to evaluate the two nozzle sizes, it is found that for OME_1, the SD ignites earlier than the SA, which is contrary to what is expected, considering only the effect of increasing the nozzle diameter (and its implications in terms of injected mass, velocity, etc.). However, this finding is consistent with what was experimentally observed by Garcia [17] under the same conditions. This section aims to explain why this phenomenon occurs. To do this, the first step is to detect the ignition point within the spray, identified by high temperature. Figure 6.32 presents the fields of mixture fraction (top), scalar dissipation rate (middle), and temperature (bottom) for SA (left) and SD (right). In each sub-figure, the ignition point is indicated for each spray. From the mixture fraction field, it is clear at first glance that the SD develops a richer spray than the SA, as usual, while regarding the scalar dissipation rate, since both ignite far from the orifice, the value of this parameter is very low and close between both sprays.

The combination of the mixture fraction condition and the scalar dissipation rate during ignition helps explain this reverse trend in the ignition delay of the sprays. To do this, it is necessary to consider the ignition delay of the flamelets, which are parameterized by the strain rate (directly related to the scalar dissipation rate). Figure 6.33 shows the evolution of the ignition delay of the flamelets versus mixture fraction for three different strain rate values. The vertical lines indicate, in red, the mixture fraction at ignition for SA; in blue, the mixture fraction at ignition for SD; and in black, the stoichiometric mixture fraction for OME_1. The ignition delay of the flamelets typically has a V-shaped curve for lower (or nearly zero) strain rates, where diffusion is not too important and tends towards homogeneous reactor behaviour. As diffusion

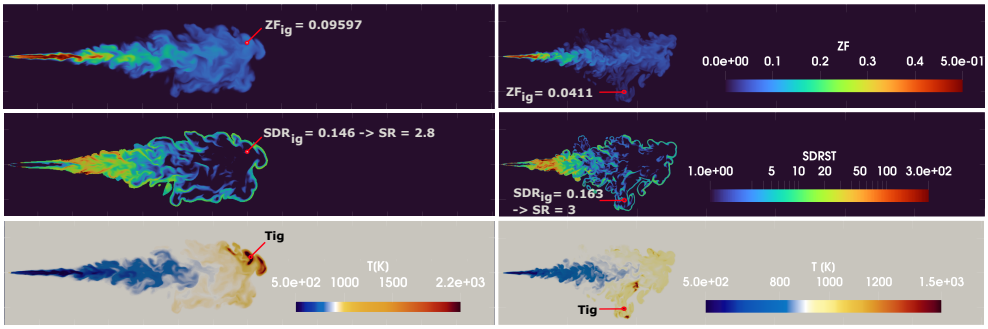

Figure 6.32: Fields of mixture fraction, scalar dissipation rate and temperature, in the first, second and third row respectively, for OME_1 and ECN SD (left panel) and SA (right panel). Results are taken at the ignition delay time and correspond to the nominal condition

increases, meaning higher strain rate values, this V-shaped curve shifts towards higher ignition delays and widens, losing its V-shape and becoming flatter over a wide range of mixture fractions, as shown in Figure 6.33. This behaviour is crucial in determining the ignition delay of SA and SD. Although both occur at very low strain rate values, the mixture conditions are very different. SD ignites under stoichiometric conditions, where the ignition delay reaches its minimum, while SA ignites under extremely lean conditions, where the ignition delay curve has a steep slope and its value increases drastically. As a final remark, this inverse behaviour in the ID of SA and SD may be more challenging to capture with the *Niu* mechanism, as demonstrated in Chapter 4, where it exhibits a less pronounced V-shape, so quite similar values of ID could be found in a wide range of Z, eliminating the differences between sprays.

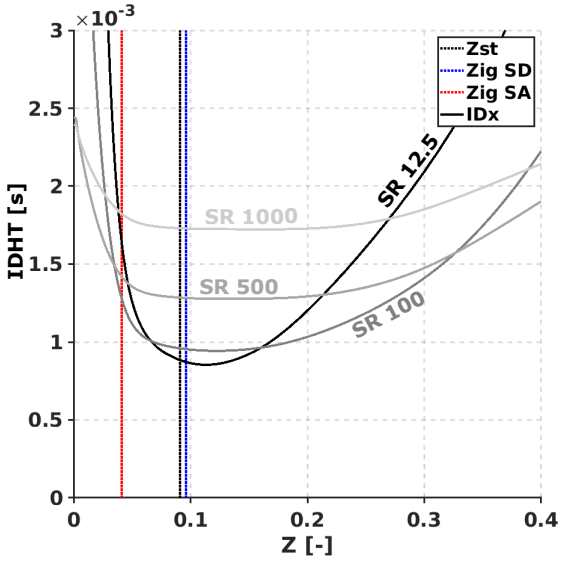

Figure 6.33: IDHT from flamelets results for OME_1 considering three different levels of SR (12.5, 100, 500 and 1000 1/s). The black vertical line correspond to the Z_{st}, and blue and red to the ignition mixture fraction (Z_{ig}) for ECN SD and SA, respectively.

Chapter 7

Conclusions and future works

Contents

7.1 Introduction

Recalling the discussion of Chapter 1 and in light of escalating concerns regarding global warming, there is a concerted effort to promote the development of renewable technologies to mitigate carbon dioxide emissions within the transportation sector, which significantly contributes to greenhouse gas emissions through the combustion of fossil fuels. The prevailing strategy within the transportation industry, in addition to electrification, entails shifting away from fossil fuels towards employing renewable resources for fuel, a paradigm referred to as defossilization. From the literature review presented in Chapter 2, $OMEn$-type fuels have emerged as candidates on this defossilization career, several advantages of the use of these fuels in ICEs have been presented, however, mainly numerical fundamental studies are an important gap in the literature. Based on this, the present thesis aims to achieve various objectives defined in Chapter 1, to contribute to filling these gaps and developing a more sustainable sector. This chapter will present the conclusions achieved through the whole work, along with guidelines for future work that the current research has opened up. These guidelines could enhance the findings already obtained and take a step further in the proposed trajectory.

7.2 Conclusions

The results obtained in this thesis have aided in improving the understanding of the combustion process of a Diesel-like spray when a synthetic and renewable fuel is used instead of a hydrocarbon, specifically the $OMEn$-type characterized in Chapter 2. The methodology proposed has been of great significance for the completeness of the results obtained, both from a scientific point of view and from an educational standpoint for the author. Studying a combustion process, and particularly a flame, is highly complex, and characterizing it is always a significant challenge, both experimentally and numerically.

Therefore, a path was traced that first led through 0D modelling to evaluate the chemical kinetics, then progressed to 1D using counterflow flamelets to consider the effect of diffusion and create the tabulation to feed the UFPV combustion model later, allowing for the study of the completeness of the problem. This process finally enabled the understanding of each phase of the process and the characterization of the new fuels, ultimately resulting in the examination of their flame structure during autoignition and in a quasi-steady state under different boundary conditions, all of which were defined following the ECN guidelines.

In the context described in Chapter 1, the calibration of a spray model for use in LES, in conjunction with an adaptation of an advanced combustion model such as the UFPV, has been regarded as a great final milestone within the thesis. This milestone was achieved as a result of all the previous steps taken, making extensive use of these high-fidelity simulation tools for the first time in the context of Diesel-like spray combustion with $CONVERGE$ and novel fuels in CMT. Moreover, several complemented tools have been developed and evaluated, highlighting the following points:

- Implementation of homogeneous reactor model in *Cantera*, considering multicomponent fuels.
- Generation of a physical properties database for $OMEn$-type fuels, which have been helpful for other PhD theses within CMT and in ECN8 Workshop as well.
- Chemiluminescence species modelling, allowing to understand the interaction between ground and excited species and enabling to make fair comparisons between CFD and experiments from these species.
- Fluid age, stream age and fuel age concepts implementation, tools that can shed light on understanding the differences between canonical config-

urations and spray combustion, given its inherent mixing process, can also be valuable for many future applications, i.e. the study of pollutant emissions.

Furthermore, based on the literature review, emphasis has been placed on attempting to address the gaps that exist regarding these fuels, which are primarily identified in fundamental studies. The main conclusions have already been formulated in their respective chapters; however, it is worthwhile to present them here from a more global perspective of the entire work. They will be outlined below, organized first by those obtained through the use of canonical configurations to understand the ignition of the fuels studied, followed by conclusions associated with spray combustion, within RANS and LES frameworks, and the influence of imposed boundary conditions.

Canonical configuration:

To assess the chemical kinetics of the mechanisms used, Cai for $OMEx$ and Jacobs for OME_1, 0D tools were employed. Homogeneous reactors implemented in *Cantera* facilitated the evaluation of the oxidation of each fuel with the respective chemical mechanism under consideration. Subsequently, 1D flamelet simulations have been conducted to assess the diffusion effect, evaluating both steady and transient regimes. Moreover, the significance of thoroughly analyzing the structure predicted by flamelets lies in studying the diffusion effect when compared with homogeneous reactor results and in the fact that these are the kinetic tables that the CFD will subsequently read to feed the UFPV combustion model. With these two combustion canonical configurations, chemical kinetics of $OMEx$ and OME_1 have been deeply investigated and compared with a reference fuel as n-Dodecane. Furthermore, an assessment of chemiluminescence species behaviour has also been conducted for the three fuels mentioned above. Moreover, the effect of the chemical mechanism used in the ignition has been evaluated for $OMEx$ and OME_1. Furthermore, for $OMEx$, the chain length utilized has been evaluated, comparing from the single-components OME_3 and OME_4 to variations ranging from OME_{34} to OME_{36}. In the following, the main conclusions obtained by these studies will be presented.

- Homogeneous reactors provided initial evidence regarding the reactivity of the fuels, particularly when compared to typical hydrocarbons like n-Dodecane. While $OMEx$ exhibits ignition delays similar to n-Dodecane at low and slightly longer at high temperatures, OME_1 already reveals that its low cetane number is decisive in its delayed ignition. Based on

the homogeneous reactor results, it is inferred that the equivalence ratio corresponding to the most reactive mixture fraction for all three fuels is quite similar, namely a slightly rich value.

- Flamelets evaluation shows that the oxygenated fuels present a practically negligible low-temperature ignition stage compared with n-Dodecane, and in turn, the presence of a medium-temperature zone absent in hydrocarbons, resulting in a faster attainment of high temperature at fixed mixture fraction. Therefore, when diffusion increases, the trend regarding ignition delay between $OMEx$ and n-Dodecane is reversed, causing $OMEx$ to exhibit lower ignition delays than hydrocarbon at high strain rates (500 and 1000 1/s). This last one is highlighted because experiments also show lower ID for $OMEx$ than for n-Dodecane, despite the cetane number exhibiting the opposite trend.

- The assessment of three major chemiluminescent species (OH*, CH* and C2*) shows that within the $OMEn$-type fuels there are no qualitative differences in terms of the distribution of these species regarding mixture fraction and normalized progress variable. This subsequently allows for selecting one of the fuels for further analysis in the spray combustion. Additionally, it has been observed that the main difference between the OH ground and OH* excited species lies in their respective locations, with the ground species being closer to C=1. In contrast, the excited species, consistent with its chemical nature, does not reach these values associated with equilibrium.

- The effect of $OMEx$ chemical mechanism and chain length has been evaluated, concluding that the influence of the mechanism is much more significant than the chain length. This results in the differences between modelling OME_{34} and OME_{36} being nearly impossible to identify. Although differences were observed between considering OME_3 or OME_{34}, the influence of using Niu is much more significant, showing lower ID than Cai in homogeneous reactors and flamelets, regardless of the SR. Therefore, the effect of diffusion on the ignition of $OMEx$ mentioned earlier is even more pronounced with Niu.

- OME_1 chemical mechanism comparison shows that although variations between Jacobs and Niu are observed in homogeneous reactors, they are not significant, typically manifesting as a lower ID with Niu. However, in the case of flamelet results, both mechanisms exhibit markedly different patterns, sometimes even exhibiting opposite trends. Jacobs indicates

that increased diffusion leads to a significant increase in ID. In contrast, with Niu, the diffusion effect is less prominent, and there is no clear trend suggesting that increased diffusion results in a shorter ignition delay time.

Spray combustion:

In the case of spray combustion, two turbulence modelling frameworks have been employed: RANS and LES. Within the RANS framework, an extension of a previously calibrated spray model for n-Dodecane has been conducted for $OMEn$-type fuels, simulating three temperature levels (1000, 900 and 800 K) for the ECN Spray A. On the other hand, within the LES framework, the calibration of the spray model, as well as the evaluation of mesh independence and the assessment of LES quality, has been carried out within the context of this thesis. In this second stage, the matrix calculation has been extended, addressing ECN Spray A and Spray D. However, based on RANS and experimental results, two temperature levels have been selected representing the nominal and low-temperature conditions. Furthermore, the autoignition process, lift-off length stabilization and quasi-steady state have been addressed under different boundary conditions. The following bullet points highlight general conclusions obtained from both frameworks regarding spray combustion:

- The global combustion parameters derived for SA and three ambient temperature levels closely align with experimental data for $OMEx$ and OME_1 within the RANS framework. Moreover, when boundary conditions are extended from SA to SD with LES under nominal conditions, the behaviour of the global combustion parameters also demonstrates good agreement for both nozzle sizes. However, predicting LOL for OME_1-SA remains challenging for the two frameworks considered. Under low temperature conditions, LES frameworks present worse predictions for $OMEx$, for which there is a consistent underprediction of the LOL and ID. Considering the case of OME_1-SA at 800 K, which has not ignited experimentally, comparing the two numerical frameworks used allows to conclude that LES tends to approach reality more closely. It shows a less pronounced temperature increase than in RANS and significantly less OH produced, indicating that it is not a perfectly defined ignition.
- An extensive and successfully validation of the flame structure for all the nominal conditions and both sprays has been achieved. The evaluation has been done during autoignition and quasi-steady state by comparing

OH and CH_2O with PLIF and OH^* with chemiluminescence optical techniques within the more realistic LES approach.

- OH^* serves as the most effective tracer among the considered chemiluminescent species, due to the larger extent along the flame. Regarding the relationship between OH and OH^*, it can be asserted that validating CFD using OH^* images cannot be accomplished with OH fields, since OH typically appears slightly downstream of OH^*. Furthermore, while OH^* reaches its maximum at the LOL, OH does so at the head of the spray, aligning consistently with the chemical nature of each species.

- The distribution of species within the spray in each nominal condition, along with the equivalence ratio values at the location of the Lift-Off Length (LOL), has allowed the establishment of a classification from more diffusive to less diffusive considering the two nozzle sizes: $OMEx$-SD, $OMEx$-SA, OME_1-SD, OME_1-SA. Furthermore, if the parametric variation of temperature is considered, the high temperature (1000 K) is placed at the very diffusive flame structure, while 800 K represent the opposite front, with OME_1-SA 800 K as extremely far from the typical Diesel-like spray structure. At this extreme lean mixing-controlled case (OME_1 800 K), the LOL may eventually be longer than the stoichiometric surface.

- The distribution of CH_2O and OH exhibits significant differences between cases with diffusion flame structure and those with more partially premixed conditions during the autoignition process. It has been demonstrated that the oxygenated nature of the fuels dictates species distribution within the spray. This behaviour of the mixture fraction was not detectable with RANS due to its averaged nature. However, LES demonstrates that fuel pockets downstream modify the typical two-lobed structure observed in hydrocarbons and are characteristic of diffusion flames.

- The comparison of autoignition sequence of flamelets calculation and spray calculation reveals that the mixing process imposed by the spray have great influence, moving the ignition from rich or stoichiometric conditions to lean conditions. Furthermore, evaluating the LOL stabilization of the two extreme cases under nominal conditions, $OMEx$-SD and OME_1-SA reveals that a novel mechanism within Diesel-like spray occurs for OME_1, developing a flame that is challenging to classify and could be close to partially premixed or, more specifically, stratified.

- As a general conclusion, the oxygenated fuels evaluated in this thesis can exhibit significantly different flame structures compared to hydrocarbons, depending on the boundary conditions. Larger nozzle diameters and higher temperatures tend to establish a diffusion flame, while smaller nozzle diameters and/or lower temperatures shift the flame structure away from typical diffusion flame characteristics. The combustion model employed in this study is capable of reproducing the distribution of species such as OH and CH_2O and their interactions, sometimes resulting in a lean mixing-controlled flame structure. However, it fails to accurately reproduce the stabilization of the LOL in these cases. This limitation arises from the combustion model used, UFPV, which imposes a predefined model of diffusion flamelets.

With the results obtained in this study, previous works claims about the role of the mixing process in oxygenated fuels during their autoignition process and quasi-steady state have been confirmed. Moreover, the matrix of calculations and boundary conditions evaluated has been significantly extended compared to existing literature, presenting for the first time variations in temperature and nozzle for $OMEx$ spray combustion simultaneously with an LES approach. Additionally, for OME_1, which according to the literature review has great potential for blending with Diesel, this is the first study of its kind. The extensive validation conducted by linking CFD and experiments under ECN conditions represents a strong synergy between modellers and experimentalists, generating new guidelines regarding validation methodologies.

7.3 Future works

Simulation, alongside theory and experimentation, has emerged as the third fundamental component in scientific inquiry, and a step further can always be taken due to its inherent high potential. Continuing to pursue excellence in high-fidelity simulations and their extensive use within the academic field should contribute to more and better research quality. Based on the outcomes of this work, subsequent research endeavours could enhance and extend the findings obtained here. Suggestions to address in future investigations include:

- Extend the calculations to other boundary conditions, such as variations in injection pressure. With this variation, important effects have been observed on the flame structure of primary reference fuels (PRF) and may affect a low reactive fuel such as OME_1. Additionally, evaluating

the combustion process while varying the oxygen content could also be of great value, given the conditions of a CI engine.

- Study, from a fundamental perspective, potential blends of $OMEn$-type fuels with hydrocarbons. This is because the cost of $OMEn$ fuels may currently be prohibitively expensive for operating with 100% pure fuels, in addition to being technically impossible for OME_1.

- Conduct an in-depth study of emissions resulting from the combustion of $OMEn$ fuels, primarily hydrocarbons, carbon monoxide, and nitrogen oxides. To achieve this, fuel age, to track the species would be highly beneficial, as pollutant formation may occur on larger time scales, and thus, residence time is crucial.

- Applying methodologies to identify local flame regimes in oxygenated fuels would be interesting, especially for conditions of low reactivity where it was found that these fuels develop flame structures that differ from those of a diffusion flame, so probably different flame regimes govern the whole process. This even involves the nominal condition of OME_1-SA.

- Evaluate other types of tabulation, such as premixed flamelet tabulation, for CFD-UFPV calculations of OME_1 to assess the behaviour of the lift-off length if a non-premixed flame structure is not imposed.

- Expanding the methodology employed to explore novel fuels such as hydrogen or ammonia for both representative terrestrial and maritime transportation conditions. This will certainly contribute to the development of environmentally sustainable technologies.

Global Bibliography

A., Krisman, E., Hawkes, and J., Chen. "A parametric study of ignition dynamics at ECN Spray A thermochemical conditions using 2D DNS". In: *Proceedings of the Combustion Institute* 37.4 (2019), pp. 4787–4795. DOI: 10.1016/j.proci.2018.08.026 (cited on pages 25, 26).

Akihama, K., Takatori, Y., Inagaki, K., Sasaki, S., and Dean, Anthony M. "Mechanism of the Smokeless Rich Diesel Combustion by Reducing Temperature". In: *SAE Technical Paper 2001-01-0655* (2001). DOI: 10.4271/2001-01-0655 (cited on page 223).

Akkurt, B. "Modelling multi-pulse diesel injection with flamelet generated manifolds". Phd Thesis (Research TU/e /Graduation TU/e). Mechanical Engineering, 2019 (cited on page 155).

Anthony A. Amsden T. Daniel Butler, Peter J. O'Rourke. "The KIVA-II Computer Program for Transient Multidimensional Chemically Reactive Flows with Sprays". In: *SAE 1987 transactions: Fuels and Lubricants-V96-7* (1987). DOI: 10.4271/872072. (cited on page 88).

Aspen Technology Inc. *https://www.aspentech.com*. 2020 (cited on page 68).

Assen, Niklas von der, Müller, Leonard J, Steingrube, Annette, Voll, Philip, and Bardow, André. "Selecting CO2 sources for CO2 utilization by environmental-merit-order curves". In: *Environmental science & technology* 50.3 (2016), pp. 1093–1101. DOI: 10.1021/acs.est.5b03474 (cited on page 29).

Awad, Omar I. et al. "Overview of polyoxymethylene dimethyl ether additive as an eco-friendly fuel for an internal combustion engine: Current application and environmental impacts". In: *Science of the Total Environment* 715 (2020). DOI: 10.1016/j.scitotenv.2020.136849 (cited on pages 29, 31).

Bamgboye, A.I. and Hansen, A.C. "Prediction of cetane number of biodiesel fuel from the fatty acid methyl ester (FAME) composition". In: *International Agrophysics* 22.1 (2008), pp. 21–29 (cited on page 32).

Barrientos, Eduardo J, Lapuerta, Magín, and Boehman, André L. "Group additivity in soot formation for the example of C-5 oxygenated hydrocarbon fuels". In: *Combustion and Flame* 160.8 (2013), pp. 1484–1498. DOI: 10.1016/j.combustflame.2013.02.024 (cited on page 34).

Barro, Christophe, Parravicini, Matteo, and Boulouchos, Konstantinos. "Neat polyoxymethylene dimethyl ether in a diesel engine; part 1: Detailed combustion analysis". In: *Fuel* 256 (2019), p. 115892. DOI: 10.1016/j.fuel.2019.115892 (cited on page 4).

Barro, Christophe, Parravicini, Matteo, Boulouchos, Konstantinos, and Liati, Anthi. "Neat polyoxymethylene dimethyl ether in a diesel engine; part 2: Exhaust emission analysis". In: *Fuel* 234 (2018), pp. 1414–1421. DOI: 10.1016/j.fuel.2018.07.108 (cited on page 4).

Battin-Leclerc, Frédérique. "Detailed chemical kinetic models for the low-temperature combustion of hydrocarbons with application to gasoline and diesel fuel surrogates". In: *Progress in Energy and Combustion Science* 34.4 (2008), pp. 440–498. DOI: 10.1016/j.pecs.2007.10.002 (cited on page 25).

Battistoni, Michele, Xue, Qingluan, and Som, Sibendu. "Large-eddy simulation (LES) of spray transients: start and end of injection phenomena". In: *Oil & Gas Science and Technology–Revue d'IFP Energies nouvelles* 71.1 (2016), p. 4. DOI: 10.2516/ogst/2015024 (cited on page 98).

Baumgarten, C. *Mixture Formation in Internal Combustion Engines*. Heat and Mass Transfer. Berlin; New York: Springer, 2006 (cited on pages 19, 20).

Benajes, Jesús, García, Antonio, Monsalve-Serrano, Javier, and Guzmán-Mendoza, María. "A review on low carbon fuels for road vehicles: The good, the bad and the energy potential for the transport sector". In: *Fuel* 361 (2024), p. 130647. DOI: 10.1016/j.fuel.2023.130647 (cited on pages 37, 40).

Benajes, Jesús, Payri, Raúl, Bardi, Michele, and Martí-Aldaraví, Pedro. "Experimental characterization of diesel ignition and lift-off length using a single-hole ECN injector". In: *Applied Thermal Engineering* 58 (1-2 2013), pp. 554–563. DOI: 10.1016/j.applthermaleng.2013.04.044 (cited on page 165).

Bharadwaj, N, Rutland, Christopher, and Chang, S. "Large eddy simulation modelling of spray-induced turbulence effects". In: *International Journal of Engine Research* 10 (2009), pp. 97–119. DOI: 10.1243/14680874JER02309 (cited on pages 96, 182).

Bharadwaj, Nidheesh and Rutland, Christopher. "A large-eddy simulation study of sub-grid two-phase interaction in particle-laden flows and diesel engine sprays". In: *Atomization and Sprays* 20 (2010), pp. 673–695. DOI: 10.1615/AtomizSpr.v20.i8.20 (cited on page 182).

Bilger, R. W. "The Structure of Diffusion Flames". In: *Combustion Science and Technology* 13.1-6 (1976), pp. 155–170. DOI: 10.1080/00102207608946733 (cited on page 22).

Bilger, R.W., Pope, S.B., Bray, K.N.C., and Driscoll, J.F. "Paradigms in turbulent combustion research". In: *Proceedings of the Combustion Institute* 30.1 (2005), pp. 21–42. DOI: 10.1016/j.proci.2004.08.273 (cited on page 220).

Blanquart, G, Pepiot-Desjardins, P, and Pitsch, H. "Chemical mechanism for high temperature combustion of engine relevant fuels with emphasis on soot precursors". In: *Combustion and Flame* 156.3 (2009), pp. 588–607. DOI: 10.1016/j.combustflame.2008.12.007 (cited on page 47).

Bongartz, Dominik et al. "Comparison of light-duty transportation fuels produced from renewable hydrogen and green carbon dioxide". In: *Applied energy* 231 (2018), pp. 757–767. DOI: 10.1016/j.apenergy.2018.09.106 (cited on page 31).

Borghesi, Giulio, Krisman, Alexander, Lu, Tianfeng, and Chen, Jacqueline H. "Direct numerical simulation of a temporally evolving air/n-dodecane jet at low-temperature diesel-relevant conditions". In: *Combustion and Flame* 195 (2018), pp. 183–202. DOI: 10.1016/j.combustflame.2018.02.020 (cited on pages 25, 26).

Borghesi, Giulio, Mastorakos, Epaminondas, and Cant, R. Stewart. "Complex chemistry DNS of n-heptane spray autoignition at high pressure and intermediate temperature conditions". In: *Combustion and Flame* 160.7 (2013), pp. 1254–1275. DOI: 10.1016/j.combustflame.2013.02.009 (cited on page 25).

Boussinesq, Joseph. *Essai sur la théorie des eaux courantes*. Bibliothèque nationale de France, 1877 (cited on page 93).

Boyd, Richard H. "Some physical properties of polyoxymethylene dimethyl ethers". In: *Journal of Polymer Science* 50.153 (1961), pp. 133–141. DOI: 10.1002/pol.1961.1205015316 (cited on page 67).

Brennan, John W. and Barder, Timothy E. *Battery Electric Vehicles vs Internal Combustion Engine Vehicles : A United States-Based Comprehensive Assessment*. Tech. rep. 2016 (cited on page 4).

Bruneaux, Gilles. “Liquid and vapor spray structure in high-pressure common rail diesel injection”. In: *Atomization and Sprays* 11 (2001), p. 24. DOI: 10.1615/AtomizSpr.v11.i5.40 (cited on page 22).

Brusiani F., Bianchi G. “LES Simulation of ICE Non-reactive Flows in Fixed Grids”. In: *SAE Technical Paper* 2008-01-0959 (2008). DOI: 10.4271/2008-01-0959 (cited on page 98).

Burger, Jakob, Siegert, Markus, Ströfer, Eckhard, and Hasse, Hans. “Poly(oxymethylene) dimethyl ethers as components of tailored diesel fuel: Properties, synthesis and purification concepts”. In: *Fuel* 89.11 (2010), pp. 3315–3319. DOI: 10.1016/j.fuel.2010.05.014 (cited on pages 29, 33).

Burger, Jakob, Ströfer, Eckhard, and Hasse, Hans. “Production process for diesel fuel components poly(oxymethylene) dimethyl ethers from methane-based products by hierarchical optimization with varying model depth”. In: *Chemical Engineering Research and Design* 91.12 (2013), pp. 2648–2662. DOI: 10.1016/j.cherd.2013.05.023 (cited on page 67).

Burke, S. P. and Schumann, T. E. W. “Diffusion Flames”. In: *Industrial & Engineering Chemistry* (1928). DOI: 10.1021/ie50226a005 (cited on page 78).

Cabra, R et al. “Simultaneous laser Raman-Rayleigh-LIF measurements and numerical modeling results of a lifted turbulent H2/N2 jet flame in a vitiated coflow”. In: *Proceedings of the Combustion Institute* 29.2 (2002), pp. 1881–1888. DOI: 10.1016/S1540-7489(02)80228-0 (cited on page 25).

Cai, Liming et al. “Optimized reaction mechanism rate rules for ignition of normal alkanes”. In: *Combustion and Flame* 173 (2016), pp. 468–482. DOI: 10.1016/j.combustflame.2016.04.022 (cited on page 47).

Cai, Liming et al. “Auto-ignition of oxymethylene ethers (OMEn, n = 2–4) as promising synthetic e-fuels from renewable electricity: shock tube experiments and automatic mechanism generation”. In: *Fuel* 264 (2020), p. 116711. DOI: 10.1016/j.fuel.2019.116711 (cited on pages 43, 47, 48, 71, 113, 129, 140).

Calcote, HF and Manos, DM. “Effect of molecular structure on incipient soot formation”. In: *Combustion and Flame* 49.1-3 (1983), pp. 289–304. DOI: 10.1016/0010-2180(83)90172-4 (cited on page 34).

Canadell, Josep G and Jackson, Robert B. *Ecosystem collapse and climate change*. Springer, 2021 (cited on page 2).

Celik, I., Klein, M., and Janicka, J. "Assessment Measures for Engineering LES Applications". In: *Journal of Fluids Engineering* 131.3 (2009), p. 031102. DOI: 10.1115/1.3059703 (cited on page 98).

Celik, I. B., Cehreli, Z. N., and Yavuz, I. "Index of resolution quality for large eddy simulations". In: *Journal of Fluids Engineering, Transactions of the ASME* 127 (5 2005), pp. 949–958. DOI: 10.1115/1.1990201 (cited on pages 86, 98).

Che Sidik, Nor Azwadi, Yusof, Siti Nurul Akmal, Asako, Yutaka, Mohamed, S., and Aziz, Arif. "A Short Review on RANS Turbulence Models". In: *CFD Letters* 12 (2020), pp. 83–96. DOI: 10.37934/cfdl.12.11.8396 (cited on page 92).

Ching-Hua Wang, Kung-Hui Shy and Lieu, Liang-Chi. "An Experimental Investigation on the Ignition Delay of Fuel Droplets". In: *Combustion Science and Technology* 118.1-3 (1996), pp. 63–78. DOI: 10.1080/00102209608951972 (cited on page 24).

Chishty, Muhammad A., Bolla, Michele, Hawkes, Evatt R., Pei, Yuanjiang, and Kook, Sanghoon. "Soot formation modelling for n-dodecane sprays using the transported etodel". In: *Combustion and Flame* 192 (2018), pp. 101–119. DOI: 10.1016/j.combustflame.2018.01.028 (cited on page 222).

Chiu, W.S., Shahed, S.M., and Lyn, W.T. "A Transient Spray Mixing Model for Diesel Combustion". In: *SAE Transactions* 85 (1976), pp. 502–512. DOI: http://www.jstor.org/stable/44644055 (cited on pages 112, 163).

Clark, Robert A., Ferziger, Joel H., and Reynolds, W. C. "Evaluation of subgrid-scale models using an accurately simulated turbulent flow". In: *Journal of Fluid Mechanics* 91.1 (1979), pp. 1–16. DOI: 10.1017/S002211207900001X (cited on page 95).

CMT, Clean Mobility and Thermofluids. *https://www.cmt.upv.es*. 2020 (cited on pages 159, 160, 162).

CMT, Clean Mobility and Thermofluids - ENERXICO database. *https://www.cmt.upv.es/#/ecn/download/Enerxicodata*. 2022 (cited on pages 188, 192).

CMT, Clean Mobility and Thermofluids - Nozzle characterization. *https://www.cmt.upv.es/#/ecn/download*. 2022 (cited on page 160).

CO2 Emissions in 2022, IEA, Paris https://www.iea.org/reports/co2-emissions-in-2022. Tech. rep. IEA, Paris, 2023 (cited on page 3).

CONVERGE CFD Software. *https://convergecfd.com* (cited on pages 8, 43, 82, 84, 94, 159, 218).

Cuenot, Bénédicte. “The Flamelet Model for Non-Premixed Combustion”. In: *Turbulent Combustion Modeling: Advances, New Trends and Perspectives*. Ed. by Tarek Echekki and Epaminondas Mastorakos. Dordrecht: Springer Netherlands, 2011, pp. 43–61. DOI: 10.1007/978-94-007-0412-1_3 (cited on page 78).

Cuoci, Alberto, Frassoldati, Alessio, Faravelli, Tiziano, and Ranzi, Eliseo. “Numerical modeling of auto-ignition of isolated fuel droplets in microgravity”. In: *Proceedings of the Combustion Institute* 35.2 (2015), pp. 1621–1627. DOI: 10.1016/j.proci.2014.06.035 (cited on page 24).

Cuoci, Alberto et al. “Autoignition and burning rates of fuel droplets under microgravity”. In: *Combustion and Flame* 143 (2005), pp. 211–226. DOI: 10.1016/j.combustflame.2005.06.003 (cited on page 24).

D. Veynante, L. Vervisch. “Turbulent combustion modeling.” In: *Prog. Energy Combust. Sci. Vol. 28, pp. 193-266* (2002). DOI: 10.1016/S0360-1285(01)00017-X (cited on pages 70, 100).

Dageförde, Toni, Gröger, Karsten, Kawaharada, Noritsune, and Dinkelacker, Friedrich. “Velocity Field Measurements with High Speed Structural Image Velocimetry in the Primary Atomization Region of Future Diesel Fuels”. In: *SAE International Journal of Advances and Current Practices in Mobility* 3 (2020). DOI: 10.4271/2020-01-2112 (cited on page 44).

Dahms, Rainer N, Paczko, Günter A, Skeen, Scott A, and Pickett, Lyle M. *The role of cool-flame dynamics in high-pressure spray ignition* (cited on page 144).

Dahms, Rainer N., Paczko, Günter A., Skeen, Scott A., and Pickett, Lyle M. “Understanding the ignition mechanism of high-pressure spray flames”. In: (2017). DOI: 10.1016/j.proci.2016.08.023 (cited on page 25).

David G. Goodwin, Raymond L. Speth, Harry K. Moffat, and Bryan W. Weber. *Cantera: An object-oriented software toolkit for chemical kinetics, thermodynamics, and transport processes.* URL: https://doi:10.5281/zenodo.1174508 (cited on pages 76, 103, 113, 127).

Dec, J. “A Conceptual Model of DI Diesel Combustion Based on Laser-Sheet Imaging”. In: *SAE International* (1997) (cited on page 26).

Desantes, J. M., García-Oliver, J. M., Xuan, T., and Vera-Tudela, W. “A study on tip penetration velocity and radial expansion of reacting diesel sprays with different fuels”. In: *Fuel* 207 (2017), pp. 323–335. DOI: 10.1016/j.fuel.2017.06.108 (cited on page 165).

Desantes, J. M., Pastor, J. V., García-Oliver, J. M., and Pastor, J. M. "A 1D model for the description of mixing-controlled reacting diesel sprays". In: *Combustion and Flame* 156 (1 2009), pp. 234–249. DOI: 10.1016/j.combustflame.2008.10.008 (cited on page 165).

Desantes, J.M., García-Oliver, J.M., Novella, R., and Pérez-Sánchez, E.J. "Application of an unsteady flamelet model in a RANS framework for spray A simulation". In: *Applied Thermal Engineering* 117 (2017), pp. 50–64. DOI: 10.1016/j.applthermaleng.2017.01.101 (cited on page 102).

Desantes, J.M., García-Oliver, J.M., Novella, R., and Pérez-Sánchez, E.J. "Application of a flamelet-based CFD combustion model to the LES simulation of a diesel-like reacting spray". In: *Computers and Fluids* 200 (2020), p. 104419. DOI: 10.1016/j.compfluid.2019.104419 (cited on page 216).

Desantes, JM, Pastor, JV, García-Oliver, JM, and Pastor, JM. "A 1D model for the description of mixing-controlled reacting diesel sprays". In: *Combustion and Flame* 156.1 (2009), pp. 234–249. DOI: 10.1016/j.combustflame.2008.10.008 (cited on page 46).

Desantes, José M, García-Oliver, José M, Xuan, Tiemin, and Vera-Tudela, Walter. "A study on tip penetration velocity and radial expansion of reacting diesel sprays with different fuels". In: *Fuel* 207 (2017), pp. 323–335. DOI: 10.1016/j.fuel.2017.06.108 (cited on page 46).

Desantes, Jose M., García-Oliver, Jose M., Novella, Ricardo, and Pachano, Leonardo. "A numerical study of the effect of nozzle diameter on diesel combustion ignition and flame stabilization". In: *International Journal of Engine Research* (2019). DOI: 10.1177/1468087419864203 (cited on pages 76, 161, 163, 164, 167, 172, 174).

Desantes, José M., Pastor, José V., García-Oliver, José M., and Briceño, Francisco J. "An experimental analysis on the evolution of the transient tip penetration in reacting Diesel sprays". In: *Combustion and Flame* 161 (8 2014), pp. 2137–2150. DOI: 10.1016/j.combustflame.2014.01.022 (cited on page 165).

Deutz, Sarah et al. "Cleaner production of cleaner fuels: wind-to-wheel–environmental assessment of CO 2-based oxymethylene ether as a drop-in fuel". In: *Energy & Environmental Science* 11.2 (2018), pp. 331–343. DOI: 10.1039/C7EE01657C (cited on page 31).

di Mare, Francesca, Knappstein, Robert, and Baumann, Michael. "Application of LES-quality criteria to internal combustion engine flows". In: *Computers and Fluids* 89 (2014), pp. 200–213. DOI: 10.1016/j.compfluid.2013.11.003 (cited on page 98).

Drost, Simon, Schießl, Robert, Werler, Marc, Sommerer, Jörg, and Maas, Ulrich. "Ignition delay times of polyoxymethylene dimethyl ether fuels (OME2 and OME3) and air: Measurements in a rapid compression machine". In: *Fuel* 258 (2019), p. 116070. DOI: 10.1016/j.fuel.2019.116070 (cited on page 48).

Dworschak, Patrick, Berger, Vinicius, Härtl, Martin, and Wachtmeister, Georg. *Neat oxymethylene ethers: combustion performance and emissions of OME 2, OME 3, OME 4 and OME 5 in a single-cylinder diesel engine.* Tech. rep. SAE Technical Paper, 2020 (cited on page 38).

eFuel Alliance. *https://www.efuel-alliance.eu/*. 2023 (cited on pages 4, 5).

Emissions Gap Report 2023: Broken Record – Temperatures hit new highs, yet world fails to cut emissions (again). Tech. rep. United Nations Environment Programme, Nairobi, 2023 (cited on page 1).

ENERXICO Project. *https://enerxico-project.eu/*. 2022 (cited on pages 7, 128, 158).

Engine combustion network. *https://ecn.sandia.gov/* (cited on pages 7, 158, 159).

Espey, C. and Dec, J.E. "The Effect of TDC Temperature and Density on the Liquid-Phase Fuel Penetration in a D. I. Diesel Engine". In: *SAE International* (1995) (cited on page 21).

F. Payri, J. M. Desantes and Arrègle, J. "Characterization of D.I. Diesel Sprays in High Density Conditions". In: *Journal of Engines, SAE International* (1996) (cited on page 19).

Favre, Alexandre. "Equations statistiques des gaz turbulents". In: *Compte-Rendus de l'Académie des Sciences Paris* 246.18 (1958), pp. 2576–2579 (cited on page 93).

Garcia, Antonio, Monsalve-Serrano, Javier, Villalta, David, and Fogue-Robles, Alvaro. "Evaluating OMEx combustion towards stoichiometric conditions in a compression ignition engine". In: *Fuel* 303 (2021), p. 121273. DOI: 10.1016/j.fuel.2021.121273 (cited on pages 38, 39).

Garcia, Antonio, Monsalve-Serrano, Javier, Villalta, David, and Mendoza, María Guzmán. *OMEx Fuel and RCCI Combustion to Reach Engine-Out Emissions Beyond the Current EURO VI Legislation.* Tech. rep. SAE Technical Paper, 2021 (cited on page 6).

Garcia, Antonio, Monsalve-Serrano, Javier, Villalta, David, and Tripathi, Shashwat. *Electric vehicles vs e-fuelled ICE vehicles: comparison of potentials for life cycle CO2 emission reduction.* Tech. rep. SAE Technical Paper, 2022 (cited on page 6).

García, Antonio, Gil, Antonio, Monsalve-Serrano, Javier, and Sari, Rafael Lago. "OMEx-diesel blends as high reactivity fuel for ultra-low NOx and soot emissions in the dual-mode dual-fuel combustion strategy". In: *Fuel* 275 (2020). DOI: 10.1016/j.fuel.2020.117898 (cited on page 4).

Garcia-Carrero, Alba. "Experimental study of the fuel effect on diffusion combustion and soot formation under diesel engine-like conditions". PhD thesis. Universitat Politecnica de Valencia, 2021 (cited on pages 7, 45, 49, 162, 189, 192, 204, 239).

García-Oliver, J. M., Novella, R., Pastor, J. M., and Pachano, L. "Computational study of ECN Spray A and Spray D combustion at different ambient temperature conditions". In: *Transportation Engineering* 2.July (2020). DOI: 10.1016/j.treng.2020.100027 (cited on page 84).

García-Oliver, J. M., Novella, R., Pastor, J. M., and Winklinger, J. F. "Evaluation of combustion models based on tabulated chemistry and presumed probability density function approach for diesel spray simulation". In: *International Journal of Computer Mathematics* 91.1 (2014), pp. 14–23. DOI: 10.1080/00207160.2013.770844 (cited on page 102).

García-Oliver, J.M. "Aportaciones al Estudio Del Proceso de Combustión Turbulenta de Chorros En Motores Diesel Del Inyección Directa". PhD thesis. Universitat Politècnica de València, 2005 (cited on page 20).

García-Oliver, José M, Novella, Ricardo, Micó, Carlos, and Leon-Ceriani, Daiana De. "Numerical analysis of the combustion process of oxymethylene ethers as low-carbon fuels for compression ignition engines". In: *International Journal of Engine Research* 24.5 (2023), pp. 2175–2186. DOI: 10.1177/14680874221113749 (cited on page 43).

García-Oliver, José M., Malbec, Louis-Marie, Toda, Hubert Baya, and Bruneaux, Gilles. "A study on the interaction between local flow and flame structure for mixing-controlled Diesel sprays". In: *Combustion and Flame* 179 (2017), pp. 157–171. DOI: 10.1016/j.combustflame.2017.01.023 (cited on page 185).

García-Oliver, José M., Novella, Ricardo, Micó, Carlos, and Bin-Khalid, Usama. "A numerical investigation of the performance of oxymethylene ethers blended with fossil diesel to reduce soot emissions in compression ignition engines". In: *Fuel* 324 (2022), p. 124768. DOI: 10.1016/j.fuel.2022.124768 (cited on page 43).

Gaydon, A. G. (Alfred Gordon). *The spectroscopy of flames.* eng. Second edition. London: Chapman and Hall, 1974 (cited on page 72).

Geurts, Bernard J and Fröhlich, Jochen. "A framework for predicting accuracy limitations in large-eddy simulation". In: *Physics of fluids* 14.6 (2002), pp. L41–L44. DOI: 10.1063/1.1480830 (cited on page 98).

Ghirelli, Federico and Leckner, Bo. "Transport equation for the local residence time of a fluid". In: *Chemical Engineering Science* 59.3 (2004), pp. 513–523. DOI: 10.1016/j.ces.2003.10.013 (cited on page 109).

Gierlich, Christian Henning, Beydoun, Kassem, Klankermayer, Jürgen, and Palkovits, Regina. "Challenges and Opportunities in the Production of Oxymethylene Dimethylether". In: *Chemie Ingenieur Technik* 92.1-2 (2020), pp. 116–124. DOI: 10.1002/cite.201900187 (cited on page 30).

Gierth, Sandro. "Advanced flamelet tabulation strategies for Large Eddy Simulations of single- and multi-phase turbulent jet flames". en. PhD thesis. Darmstadt: Technische Universität, 2022. DOI: 10.26083/tuprints-00021122 (cited on page 17).

Giesen, Coen van der, Kleijn, René, and Kramer, Gert Jan. "Energy and climate impacts of producing synthetic hydrocarbon fuels from CO2". In: *Environmental science & technology* 48.12 (2014), pp. 7111–7121. DOI: 10.1021/es500191g (cited on page 29).

Global Alliance Powerfuels. "Powerfuels: Missing link to a successful energy transition". In: *Global Alliance Powerfuels: Berlin, Germany* (2019) (cited on page 4).

Global energy-related CO2 emissions by sector. Tech. rep. IEA, Paris, 2020 (cited on page 2).

GmbH, AVL List. *AVL List GmbH. FIRE General Gas Phase Reactions Module v2018; Manual; AVL List GmbH: Graz, Austria, 2018.* 2018 (cited on page 47).

Goeb, Dominik et al. "Oxymethylene ether n-dodecane blend spray combustion: Experimental study and large-eddy simulations". In: *Proceedings of the Combustion Institute* 000 (2020). DOI: 10.1016/j.proci.2020.08.017 (cited on page 46).

Goldsborough, S Scott et al. “Advances in rapid compression machine studies of low-and intermediate-temperature autoignition phenomena”. In: *Progress in Energy and Combustion Science* 63 (2017), pp. 1–78. DOI: 10.1016/j.pecs.2017.05.002 (cited on page 25).

Google scholar. *https://scholar.google.es/*. 16 october 2023 (cited on page 141).

Gordon, Robert L., Masri, Assaad R., and Mastorakos, Epaminondas. “Heat release rate as represented by [OH] × [CH2O] and its role in autoignition”. In: *Combustion Theory and Modelling* 13.4 (2009), pp. 645–670. DOI: 10.1080/13647830902957200 (cited on page 25).

Guzmán, María Gabriela. “Impact of different e-fuels type on light-duty compression ignition engine performance, emissions and CO2 Life cycle analysis”. PhD thesis. Universitat Politecnica de Valencia, 2023 (cited on pages 6, 41).

Haber, L. C. and Vandsburger, U. “A global reaction model for oh* chemiluminescence applied to a laminar flat-flame burner”. In: *Combustion Science and Technology* 175.10 (2003), pp. 1859–1891. DOI: 10.1080/713713115 (cited on page 73).

Hall, Joel Meador and Petersen, Eric L. “An optimized kinetics model for OH chemiluminescence at high temperatures and atmospheric pressures”. In: *International Journal of Chemical Kinetics* 38 (2006), pp. 714–724. DOI: 10.1002/kin.20196 (cited on pages 72, 138).

Hank, Christoph et al. “Comparative well-to-wheel life cycle assessment of OME 3–5 synfuel production via the power-to-liquid pathway”. In: *Sustainable Energy & Fuels* 3.11 (2019), pp. 3219–3233. DOI: 10.1039/C9SE00658C (cited on page 6).

Härtl, M., Gaukel, Kai, Pélerin, Dominik, and Wachtmeister, Georg. “Oxymethylene Ether as Potentially CO2-neutral Fuel for Clean Diesel Engines Part 1: Engine Testing”. In: *MTZ worldwide* 78 (2017), pp. 52–59. DOI: 10.1007/s38313-016-0163-6 (cited on page 39).

Härtl, Martin, Seidenspinner, Philipp, Jacob, Eberhard, and Wachtmeister, Georg. “Oxygenate screening on a heavy-duty diesel engine and emission characteristics of highly oxygenated oxymethylene ether fuel OME1”. In: *Fuel* 153 (2015), pp. 328–335. DOI: 10.1016/j.fuel.2015.03.012 (cited on pages 4, 37).

Haspel, Philip et al. “Large eddy simulation of OME3 and OME4 spray combustion under heavy-duty conditions”. In: *Fuel* 353 (2023), p. 129097. DOI: 10.1016/j.fuel.2023.129097 (cited on pages 47–49, 142).

He, Tanjin et al. “Development of surrogate model for oxygenated wide-distillation fuel with polyoxymethylene dimethyl ether”. In: *SAE International Journal of Fuels and Lubricants* 10.3 (2017), pp. 803–814. DOI: 10.4271/2017-01-2336 (cited on page 71).

He, Tanjin et al. “A chemical kinetic mechanism for the low- and intermediate-temperature combustion of Polyoxymethylene Dimethyl Ether 3 (PODE3)”. In: *Fuel* 212 (2018), pp. 223–235. DOI: 10.1016/j.fuel.2017.09.080 (cited on page 48).

He, Tanjin et al. “A chemical kinetic mechanism for the low-and intermediate-temperature combustion of Polyoxymethylene Dimethyl Ether 3 (PODE3)”. In: *Fuel* 212 (2018), pp. 223–235. DOI: 10.1016/j.fuel.2017.09.080 (cited on page 71).

Hermann Schlichtin, Klaus Gersten. *Boundary-Layer Theory*. Springer Berlin, Heidelberg, 2000. DOI: 10.1007/978-3-662-52919-5 (cited on pages 112, 163).

Higgins, Brian S., Mueller, Charles J., and Siebers, Dennis L. “Measurements of Fuel Effects on Liquid-Phase Penetration in Dl Sprays”. In: *SAE Transactions* 108 (1999), pp. 630–643 (cited on page 21).

Hiroyasu, Hiroyuki, Kadota, Toshikazu, and Arai, Masataka. “Development and Use of a Spray Combustion Modeling to Predict Diesel Engine Efficiency and Pollutant Emissions : Part 1 Combustion Modeling”. In: *Bulletin of JSME* 26.214 (1983), pp. 569–575. DOI: 10.1299/jsme1958.26.569 (cited on page 50).

Hossam A., El-Asrag and Yiguang, Ju. “Direct numerical simulations of NOx effect on multistage autoignition of DME/air mixture in the negative temperature coefficient regime for stratified HCCI engine conditions”. In: *Combustion and flame* 161.1 (2014), pp. 256–269. DOI: 10.1016/j.combustflame.2013.07.012 (cited on page 221).

Huang, Haozhong et al. “Construction of a reduced PODE3/nature gas dual-fuel mechanism under enginelike conditions”. In: *Energy & Fuels* 33.4 (2019), pp. 3504–3517. DOI: 10.1021/acs.energyfuels.8b03926 (cited on page 71).

Iannuzzi, Stefano Emanuele, Barro, Christophe, Boulouchos, Konstantinos, and Burger, Jakob. “Combustion behavior and soot formation/oxidation of oxygenated fuels in a cylindrical constant volume chamber”. In: *Fuel* 167 (2016), pp. 49–59. DOI: 10.1016/j.fuel.2015.11.060 (cited on page 45).

Iannuzzi, Stefano Emanuele, Barro, Christophe, Boulouchos, Konstantinos, and Burger, Jakob. "POMDME-diesel blends: Evaluation of performance and exhaust emissions in a single cylinder heavy-duty diesel engine". In: *Fuel* 203 (2017), pp. 57–67. DOI: 10.1016/j.fuel.2017.04.089 (cited on page 43).

Iyer V. A., Abraham J. "Penetration and Dispersion of Transient Gas Jets and Sprays". In: *Combust. Sci. Technol., 130, pp. 315–334* (1997). DOI: 10.1080/00102209708935747 (cited on page 87).

J., Abraham. "What is Adequate Resolution in the Numerical Computations of Transient Jets?" In: *Transactions of the SAE, 106 (3), pp. 141–155* (1997). DOI: 10.4271/970051 (cited on page 87).

Jacobs, Sascha et al. "Detailed kinetic modeling of dimethoxymethane. Part II: Experimental and theoretical study of the kinetics and reaction mechanism". In: *Combustion and Flame* 205 (2019), pp. 522–533. DOI: 10.1016/J.COMBUSTFLAME.2018.12.026 (cited on pages 47, 48, 71–73, 113, 129, 138, 140, 159).

Kass, Michael, Wissink, Martin, Janke, Chris, Connatser, Raynella, and Curran, Scott. "Compatibility of Elastomers with Polyoxymethylene Dimethyl Ethers and Blends with Diesel". In: *SAE International Journal of Advances and Current Practices in Mobility-V129-99EJ* (2020) (cited on page 41).

Kathrotia, Trupti. "Reaction Kinetics Modeling of OH*, CH*, and C2* Chemiluminescence". PhD thesis. 2011 (cited on pages 72, 74, 75, 138).

Khan, Q, Baek, Seung, and Ghassemi, Hojat. "On the autoignition and combustion characteristics of kerosene droplets at elevated pressure and temperature". In: *Combustion Science and Technology - Combustion Sci Technol* 179 (2007), pp. 2437–2451. DOI: 10.1080/00102200701484605 (cited on page 24).

Kitamura, T, Ito, T, Senda, J, and Fujimoto, H. "Mechanism of smokeless diesel combustion with oxygenated fuels based on the dependence of the equivalence ration and temperature on soot particle formation". In: *International Journal of Engine Research* 3.4 (2002), pp. 223–248. DOI: 10.1243/146808702762230923 (cited on page 221).

Klimenko, A.Y. and Bilger, R.W. "Conditional moment closure for turbulent combustion". In: *Progress in Energy and Combustion Science* 25.6 (1999), pp. 595–687. DOI: 10.1016/S0360-1285(99)00006-4 (cited on page 99).

Kook, Sanghoon and Pickett, Lyle M. "Liquid length and vapor penetration of conventional, Fischer–Tropsch, coal-derived, and surrogate fuel sprays at high-temperature and high-pressure ambient conditions". In: *Fuel* 93 (2012), pp. 539–548. DOI: 10.1016/j.fuel.2011.10.004 (cited on page 162).

Kopp, M., Brower, M., Mathieu, Olivier, Petersen, Eric, and Güthe, Felix. "CO2* chemiluminescence study at low and elevated pressures". In: *Applied Physics B* 107 (2012). DOI: 10.1007/s00340-012-5051-4 (cited on page 74).

Kopp, Wassja A. et al. "Detailed kinetic modeling of dimethoxymethane. Part I: Ab initio thermochemistry and kinetics predictions for key reactions". In: *Combustion and flame* 189 (2018), pp. 433–442. DOI: 10.1016/j.combustflame.2017.07.037 (cited on page 48).

Krisman, Alex, Hawkes, Evatt R., Talei, Mohsen, Bhagatwala, Ankit, and Chen, Jacqueline H. "Characterisation of two-stage ignition in diesel engine-relevant thermochemical conditions using direct numerical simulation". In: 172 (2016), pp. 326–341. DOI: 10.1016/j.combustflame.2016.06.010 (cited on pages 25, 26).

Kukkadapu, Goutham, Kumar, Kamal, Sung, Chih-Jen, Mehl, Marco, and Pitz, William J. "Autoignition of gasoline surrogates at low temperature combustion conditions". In: *Combustion and Flame* 162.5 (2015), pp. 2272–2285. DOI: 10.1016/j.combustflame.2015.01.025 (cited on page 221).

Kulkarni, Aditya et al. "A Force Field for Poly(oxymethylene) Dimethyl Ethers (OMEn)". In: *Journal of Chemical Theory and Computation* (2020). DOI: 10.1021/acs.jctc.9b01106 (cited on pages 67, 68).

L., Pickett, J., Manin, C., Genzale, and al., Siebers D. et. "Relationship Between Diesel Fuel Spray Vapor Penetration/Dispersion and Local Fuel Mixture Fraction". In: *SAE Int. J. Engines 4(1):764-799, 2011* (2011). DOI: 10.4271/2011-01-0686 (cited on page 185).

Larson, Eric D and Yang, Huiyan. "Dimethyl ether (DME) from coal as a household cooking fuel in China". In: *Energy for sustainable development* 8.3 (2004), pp. 115–126. DOI: 0.1016/S0973-0826(08)60473-1 (cited on page 32).

Launder, B.E. and Spalding, D.B. "The numerical computation of turbulent flows". In: *Computer Methods in Applied Mechanics and Engineering* 3.2 (1974), pp. 269–289. DOI: 10.1016/0045-7825(74)90029-2 (cited on page 89).

Lautenschütz, Ludger et al. “Physico-chemical properties and fuel characteristics of oxymethylene dialkyl ethers”. In: *Fuel* 173 (2016), pp. 129–137. DOI: 10.1016/j.fuel.2016.01.060 (cited on page 31).

Law, C. K. and Chung, S. H. “An Ignition Criterion for Droplets in Sprays”. In: *Combustion Science and Technology* 22.1-2 (1980), pp. 17–26. DOI: 10.1080/00102208008952370 (cited on page 24).

Lee, H. and (eds.), J. Romero. *IPCC, 2023: Climate Change 2023: Synthesis Report. Contribution of Working Groups I, II and III to the Sixth Assessment Report of the Intergovernmental Panel on Climate Change*. Tech. rep. IPCC, Geneva, Switzerland, 2023. DOI: 10.59327/IPCC/AR6-9789291691647 (cited on page 1).

Leung, K.M., Lindstedt, R.P., and Jones, W.P. “A simplified reaction mechanism for soot formation in nonpremixed flames”. In: *Combustion and Flame* 87.3 (1991), pp. 289–305. DOI: 10.1016/0010-2180(91)90114-Q (cited on page 50).

Li, Bowen et al. “Combustion and emission characteristics of diesel engine fueled with biodiesel/PODE blends”. In: *Applied Energy* 206 (2017), pp. 425–431. DOI: 10.1016/j.apenergy.2017.08.206 (cited on pages 33, 34).

Lin, Qinjie, Tay, Kun Lin, Zhou, Dezhi, and Yang, Wenming. “Development of a compact and robust Polyoxymethylene Dimethyl Ether 3 reaction mechanism for internal combustion engines”. In: *Energy Conversion and Management* 185 (2019), pp. 35–43. DOI: 10.1016/j.enconman.2019.02.007 (cited on page 71).

Liu, Jialin et al. “Effects of diesel/PODE (polyoxymethylene dimethyl ethers) blends on combustion and emission characteristics in a heavy duty diesel engine”. In: 177 (2016), pp. 206–216. DOI: 10.1016/j.fuel.2016.03.019 (cited on page 38).

Liu, Junheng et al. “An overview of polyoxymethylene dimethyl ethers as alternative fuel for compression ignition engines”. In: *Fuel* 318 (2022), p. 123582. DOI: 10.1016/j.fuel.2022.123582 (cited on pages 32, 36).

Liu, Yao, Tan, Jianguo, Wan, Minggang, Zhang, Lang, and Yao, Xiao. “Quantitative Measurement of OH^* and CH^* Chemiluminescence in Jet Diffusion Flames”. In: *ACS Omega* 5 (26 2020), pp. 15922–15930. DOI: 10.1021/acsomega.0c01093 (cited on page 206).

Lv, Delin et al. “Development of a reduced diesel/PODEn mechanism for diesel engine application”. In: *Energy Conversion and Management* 199 (2019), p. 112070. DOI: 10.1016/j.enconman.2019.112070 (cited on page 71).

Ma, Xiao et al. “PLII-LEM and OH* Chemiluminescence Study on Soot Formation in Spray Combustion of PODEn-Diesel Blend Fuels in a Constant Volume Vessel”. In: *International Powertrains, Fuels and Lubricants Meeting*. SAE International, 2017. DOI: 10.4271/2017-01-2329 (cited on page 45).

Ma, Yue, Cui, Longxi, Ma, Xiao, and Wang, Jianxin. “Optical study on spray combustion characteristics of PODE/diesel blends in different ambient conditions”. In: *Fuel* 272 (2020), p. 117691. DOI: 10.1016/j.fuel.2020.117691 (cited on page 45).

Maes, Noud et al. “Characterization of Spray A flame structure for parametric variations in ECN constant-volume vessels using chemiluminescence and laser-induced fluorescence”. In: *Combustion and Flame* 174 (2016), pp. 138–151. DOI: 10.1016/j.combustflame.2016.09.005 (cited on page 140).

Maes, Noud et al. “Characterization of Spray A flame structure for parametric variations in ECN constant-volume vessels using chemiluminescence and laser-induced fluorescence”. In: *Combustion and Flame* 174 (2016), pp. 138–151. DOI: 10.1016/j.combustflame.2016.09.005 (cited on page 205).

Martin Rieth and Jackie Chen. *Spray A double injection DNS and OME flamelet analysis*. 2022. URL: https://ecn.sandia.gov/workshop/ECN8/ECN7.14.mp4 (cited on page 145).

Martinez, María. “Computational study of the Injection Process in Gasoline Direct Injection (GDI) Engines”. PhD thesis. 2022 (cited on page 98).

Masri, A.R. “Challenges for turbulent combustion”. In: *Proceedings of the Combustion Institute* 38.1 (2021), pp. 121–155. DOI: 10.1016/j.proci.2020.07.144 (cited on page 30).

Masri, A.R. *Turbulent Combustion Modeling*. Springer, Netherlands, 2011, pp. 355–380. (Cited on page 219).

Mastorakos, E., Baritaud, T.A., and Poinsot, T.J. “Numerical simulations of autoignition in turbulent mixing flows”. In: *Combustion and Flame* 109.1 (1997), pp. 198–223. DOI: 10.1016/S0010-2180(96)00149-6 (cited on page 25).

Mastorakos, Epaminondas. “Ignition of turbulent non-premixed flames”. In: *Progress in Energy and Combustion Science* 35 (2009). DOI: 10.1016/j.pecs.2008.07.002 (cited on page 131).

Mastorakos, Epaminondas. “Ignition of turbulent non-premixed flames”. In: *Progress in Energy and Combustion Science* 35.1 (2009), pp. 57–97. DOI: 10.1016/j.pecs.2008.07.002 (cited on page 220).

Mastorakos, Epaminondas. “Ignition of turbulent non-premixed flames”. In: *Progress in Energy and Combustion Science* 35.1 (2009), pp. 57–97. DOI: 10.1016/j.pecs.2008.07.002 (cited on page 25).

Matsukawa, Yoshiya et al. “Reaction pathway for nascent soot in ethylene pyrolysis”. In: *Combustion and Flame* 167 (2016), pp. 248–258. DOI: 10.1016/j.combustflame.2016.02.008 (cited on page 33).

Matzen, Michael and Demirel, Yaşar. “Methanol and dimethyl ether from renewable hydrogen and carbon dioxide: Alternative fuels production and life-cycle assessment”. In: *Journal of cleaner production* 139 (2016), pp. 1068–1077. DOI: 10.1016/j.jclepro.2016.08.163 (cited on page 29).

Maus, Dipl-Ing Wolfgang and Jacob, E. “Synthetische Kraftstoffe-OME1: Ein potenziell nachhaltig hergestellter Dieselkraftstoff Synthetic Fuels-OME1: A Potentially Sustainable Diesel Fuel”. In: *https://www. emitec. com/* 12.21 (2014), p. 2018 (cited on page 37).

Mico, C. “Development of measurement and visualization techniques for characterization of mixing and combustion processes with surrogate fuels.” PhD thesis. niversitat Politècnica de València, 2015. DOI: 10.4995/Thesis/10251/58991 (cited on page 20).

Minamoto, Yuki and Chen, Jacqueline H. “DNS of a turbulent lifted DME jet flame”. In: *Combustion and flame* (2016). DOI: 10.1016/j.combustflame.2016.04.007 (cited on page 26).

Mompó, Juan Manuel. “Engineering Large Eddy Simulation of Diesel Sprays”. In: *Riunet* (2014). DOI: 10.4995/Thesis/10251/37345 (cited on pages 96, 182).

Moriue, O. et al. “Effects of dilution by aromatic hydrocarbons on staged ignition behavior of n-decane droplets”. In: 28.1 (2000), pp. 969–975. DOI: 10.1016/S0082-0784(00)80303-3 (cited on page 24).

Moriue, Osamu, Mikami, Masato, Kojima, Naoya, and Eigenbrod, C. “Numerical simulations of the ignition of n-heptane droplets in the transition diameter range from heterogeneous to homogeneous ignition”. In: *Proceedings of the Combustion Institute* 30 (2005), pp. 1973–1980. DOI: 10.1016/j.proci.2004.08.248 (cited on page 24).

Mukhopadhyay, Saumyadip and Abraham, John. “Influence of compositional stratification on autoignition in n-heptane/air mixtures”. In: *Combustion and Flame* 158.6 (2011), pp. 1064–1075. DOI: 10.1016/j.combustflame.2010.10.007 (cited on page 25).

N., Maes. “The Life of a Spray”. PhD thesis. Technische Universiteit Eindhoven, 2019 (cited on page 27).

Naber, J. and Siebers, D. “Effects of Gas Density and Vaporization on Penetration and Dispersion of Diesel Sprays”. In: *SAE International* (1996) (cited on page 22).

Naud, Bertrand, Novella, Ricardo, Pastor, José Manuel, and Winklinger, Johannes F. “RANS modelling of a lifted H2/N2 flame using an unsteady flamelet progress variable approach with presumed PDF”. In: *Combustion and Flame* 162.4 (2015), pp. 893–906. DOI: 10.1016/j.combustflame.2014.09.014 (cited on pages 82, 113, 127, 159).

Nguyen, Tuan M., Dahms, Rainer N., Pickett, Lyle M., and Tagliante, Fabien. “The Corrected Distortion model for Lagrangian spray simulation of transcritical fuel injection”. In: *International Journal of Multiphase Flow* 148 (2022). DOI: 10.1016/j.ijmultiphaseflow.2021.103927 (cited on pages 83, 84).

Niemeyer, Kyle E, Daly, Shane R, Cannella, William J, and Hagen, Christopher L. “Investigation of the LTC fuel performance index for oxygenated reference fuel blends”. In: *Fuel* 155 (2015), pp. 14–24. DOI: 10.1016/j.fuel.2015.04.010 (cited on page 221).

Niu, Bo et al. “Construction of reduced oxidation mechanisms of polyoxymethylene dimethyl ethers (PODE1–6) with consistent structure using decoupling methodology and reaction rate rule”. In: *Combustion and Flame* 232 (2021), p. 111534. DOI: 10.1016/j.combustflame.2021.111534 (cited on pages 47, 71, 129, 140).

Nour, Mohamed, Attia, Ali MA, and Nada, Sameh A. “Improvement of CI engine combustion and performance running on ternary blends of higher alcohol (Pentanol and Octanol)/hydrous ethanol/diesel”. In: *Fuel* 251 (2019), pp. 10–22. DOI: 10.1016/j.fuel.2019.04.026 (cited on page 33).

Novella, R., García, A., Pastor, J.M., and Domenech, V. “The role of detailed chemical kinetics on CFD diesel spray ignition and combustion modelling”. In: *Mathematical and Computer Modelling* 54.7 (2011), pp. 1706–1719. DOI: 10.1016/j.mcm.2010.12.048 (cited on page 93).

Novella, Ricardo, Bracho, Gabriela, Gomez-Soriano, Josep, Fernandes, Cássio S., and Lucchini, Tommaso. “Combustion system optimization for the integration of e-fuels (Oxymethylene Ether) in compression ignition engines”. In: *Fuel* 305 (2021), p. 121580. DOI: 10.1016/j.fuel.2021.121580 (cited on page 43).

O'Rourke, P J. "Collective drop effects on vaporizing liquid sprays". In: (1981) (cited on page 88).

Omari, Ahmad, Heuser, Benedikt, and Pischinger, Stefan. "Potential of oxymethylenether-diesel blends for ultra-low emission engines". In: *Fuel* 209.July (2017), pp. 232–237. DOI: 10.1016/j.fuel.2017.07.107 (cited on pages 38, 39, 47).

OpenFOAM. *https://www.openfoam.com/*. The Open Source CFD Toolbox. User Gide Version 1.6, 2009. (Cited on pages 8, 44).

Organización Meteorológica Mundial. "Estado del clima mundial en 2011–2015". In: (2016) (cited on page 1).

Pachano, Leonardo. "CFD Modeling of combustion and soot production in diesel spray". PhD thesis. Universitat Politecnica de Valencia, 2020 (cited on pages 8, 83, 87, 93, 94, 100, 111, 161, 162, 184, 207).

Pachano, Leonardo et al. "A two-equation soot-in-flamelet modeling approach applied under Spray A conditions". In: *Combustion and Flame* 231 (2021), p. 111488. DOI: 10.1016/j.combustflame.2021.111488 (cited on page 50).

Pachauri, R.K and Reisinger, A. (eds.) *Climate Change 2007: Synthesis Report. Contribution of Working Groups I, II and III to the Fourth Assessment Report of the Intergovernmental Panel on Climate Change*. Tech. rep. IPCC, Geneva, Switzerland, 2007 (cited on page 1).

Pachiannan, Tamilselvan et al. "A literature review of fuel effects on performance and emission characteristics of low-temperature combustion strategies". In: *Applied Energy* 251 (2019), p. 113380. DOI: 10.1016/j.apenergy.2019.113380 (cited on page 221).

Pajares, Miguel. *Refugiados climáticos: Un gran reto del siglo XXI*. Rayo Verde, 2020 (cited on page 1).

Pandal, Adrian et al. "Computational and Experimental Investigation of Interfacial Area in Near-Field Diesel Spray Simulation". In: *SAE International Journal of Fuels and Lubricants* 10 (2017). DOI: 10.4271/2017-01-0859 (cited on page 32).

Pandal Blanco, Adrian. "Implementation and Development of an Eulerian Spray Model for CFD simulations of diesel Sprays". PhD thesis. Universitat Politècnica de València, 2016 (cited on page 100).

Paola, G. De, Mastorakos, E., Wright, Y. M., and Boulouchos, K. "Diesel Engine Simulations with Multi-Dimensional Conditional Moment Closure". In: *Combustion Science and Technology* 180.5 (2008), pp. 883–899. DOI: 10.1080/00102200801894273 (cited on page 99).

Pastor, J., Garcia-Oliver, Jose, Pastor, Jose, and Vera-Tudela, W. "One-Dimensional Diesel spray modeling of multicomponent fuels". In: *Atomization and Sprays* 25 (2015), pp. 485–517. DOI: 10.1615/AtomizSpr.2014010370 (cited on page 67).

Pastor, J., Payri, Raul, Garcia-Oliver, Jose, and Briceno, Francisco. "Analysis of transient liquid and vapor phase penetration for diesel sprays under variable injection conditions". In: *Atomization and Sprays* 21 (2011), pp. 503–520. DOI: 10.1615/AtomizSpr.2011003721 (cited on page 22).

Pastor, J. V., Garcia-Oliver, J. M., Bermudez, V., and Micó., C. "Spray Characterization for Pure Fuel and Binary Blends under Non-Reacting Conditions". In: *SAE International* (2014). DOI: 10.4271/2014-01-1407 (cited on page 21).

Pastor, Jose, Garcia-Oliver, Jose, Antonio, Garcia, and López, Andrés. "An Experimental Investigation on Spray Mixing and Combustion Characteristics for Spray C/D Nozzles in a Constant Pressure Vessel". In: *SAE, International Powertrains, Fuels & Lubricants Meeting* (2018). DOI: 10.4271/2018-01-1783 (cited on page 185).

Pastor, José, Antonio, Garcia, Micó, Carlos, and Lewiski, Felipe. "An optical investigation of Fischer-Tropsch diesel and Oxymethylene dimethyl ether impact on combustion process for CI engines". In: *Applied Energy* 260 (2020), p. 114238. DOI: 10.1016/j.apenergy.2019.114238 (cited on page 41).

Pastor, Jose V, Payri, Raul, Garcia-Oliver, Jose M, and Nerva, Jean-Guillaume. "Schlieren Measurements of the ECN-Spray A Penetration under Inert and Reacting Conditions". In: *SAE 2012 World Congress & Exhibition*. SAE International, 2012 (cited on page 22).

Pastor, José V, García-Oliver, José M, Micó, Carlos, and García-Carrero, Alba A. "An experimental study with renewable fuels using ECN Spray A and D nozzles". In: *International Journal of Engine Research* 23.10 (2022), pp. 1748–1759. DOI: 10.1177/14680874211031200 (cited on pages 204, 223).

Pastor, José V, López, J Javier, García, José M, and Pastor, José M. "A 1D model for the description of mixing-controlled inert diesel sprays". In: *Fuel* 87.13-14 (2008), pp. 2871–2885. DOI: doi.org/10.1016/j.fuel.2008.04.017 (cited on page 46).

Pastor, Jose V., Garcia-Oliver, Jose M, Micó, Carlos, and Tejada, Francisco J. "Combustion Behaviour of Blends of Synthetic Fuels in an Optical Single Cylinder Engine". In: *15th International Conference on Engines and Vehicles*. SAE International, 2021. DOI: 10.4271/2021-24-0038 (cited on page 42).

Pastor, Jose V., Garcia-Oliver, Jose M., Micó, Carlos, and Tejada, Francisco J. "Comparison of the Diffusive Flame Structure for Dodecane and OMEXFuels for Conditions of Spray A of the ECN". In: *SAE Technical Papers* 2020 (2020), pp. 1–10. DOI: 10.4271/2020-01-2120 (cited on page 174).

Pastor, Jose V., García-Oliver, Jose M., Micó, Carlos, and Tejada, Francisco J. "Characterization of the oxymethylene ether fuels flame structure for ECN Spray A and Spray D nozzles". In: *Applied Energy* 332 (2023). DOI: 10.1016/j.apenergy.2022.120475 (cited on pages 41, 141, 192, 195, 197, 199, 201, 203, 204).

Pastor, José V., García, Antonio, Micó, Carlos, and Lewiski, Felipe. "An optical investigation of Fischer-Tropsch diesel and Oxymethylene dimethyl ether impact on combustion process for CI engines". In: *Applied Energy* 260 (2020). DOI: 10.1016/j.apenergy.2019.114238 (cited on page 4).

Pastor, José V., García, Antonio, Micó, Carlos, and Lewiski, Felipe. "Simultaneous high-speed spectroscopy and 2-color pyrometry analysis in an optical compression ignition engine fueled with OMEX-diesel blends". In: *Combustion and Flame* 230 (2021), p. 111437. DOI: 10.1016/j.combustflame.2021.111437 (cited on page 41).

Pastor, José V., García-Oliver, José M., Micó, Carlos, García-Carrero, Alba A., and Gómez, Arantzazu. "Experimental Study of the Effect of Hydrotreated Vegetable Oil and Oxymethylene Ethers on Main Spray and Combustion Characteristics under Engine Combustion Network Spray A Conditions". In: *Applied Sciences* 10.16 (2020), p. 5460. DOI: 10.3390/app10165460 (cited on pages 32, 141, 158, 164, 168, 192, 204).

Payri, F., Novella, R., Pastor, J.M., and Pérez-Sánchez, E.J. "Evaluation of the approximated diffusion flamelet concept using fuels with different chemical complexity". In: *Applied Mathematical Modelling* 49 (2017), pp. 354–374. DOI: 10.1016/j.apm.2017.04.024 (cited on page 102).

Payri, Francisco, García-Oliver, Jose M., Novella, Ricardo, and Pérez-Sánchez, Eduardo J. "Influence of the n-dodecane chemical mechanism on the CFD modelling of the diesel-like ECN Spray A flame structure at different ambient conditions". In: *Combustion and Flame* 208 (2019), pp. 198–218. DOI: 10.1016/j.combustflame.2019.06.032 (cited on page 131).

Payri, R., García, J.M., Salvador, F.J., and Gimeno, J. "Using spray momentum flux measurements to understand the influence of diesel nozzle geometry on spray characteristics". In: *Fuel* 84.5 (2005), pp. 551–561. DOI: https://doi.org/10.1016/j.fuel.2004.10.009 (cited on page 160).

Payri, R., Gimeno, J., Bardi, M., and Plazas., A. H. "Study Liquid Length Penetration Results Obtained with a Direct Acting Piezo Electric Injector". In: *Applied Energy* (2013). DOI: 10.1016/j.apenergy.2013.01.027 (cited on page 21).

Payri, R., Gimeno, J., Bracho, G., and Vaquerizo, D. "Study of Liquid and Vapor Phase Behavior on Diesel Sprays for Heavy Duty Engine Nozzles". In: *Applied Energy* (2016). DOI: 10.1016/j.applthermaleng.2016.06.159 (cited on page 21).

Payri, Raul, García-Oliver, Jose M., Xuan, Tiemin, and Bardi, Michele. "A study on diesel spray tip penetration and radial expansion under reacting conditions". In: *Applied Thermal Engineering* 90 (2015), pp. 619–629. DOI: 10.1016/j.applthermaleng.2015.07.042 (cited on page 165).

Payri, Raul, García-Oliver, Jose M., Xuan, Tiemin, and Bardi, Michele. "A study on diesel spray tip penetration and radial expansion under reacting conditions". In: *Applied Thermal Engineering* 90 (2015), pp. 619–629. DOI: 10.1016/j.applthermaleng.2015.07.042 (cited on pages 185, 189).

Pei, Yuanjiang et al. "Large eddy simulation of a reacting spray flame with multiple realizations under compression ignition engine conditions". In: *Combustion and Flame* 162.12 (2015), pp. 4442–4455. DOI: 10.1016/j.combustflame.2015.08.010 (cited on page 86).

Pei Y. Hawkes E., Kook S. "A Comprehensive Study of Effects of Mixing and Chemical Kinetic Models on Predictions of n-heptane Jet Ignitions with the PDF Method". In: *Proc. Combust. Inst. 34* (2013). DOI: 10.1007/s10494-013-9454-z (cited on page 100).

Pélerin, Dominik, Gaukel, Kai, Härtl, Martin, Jacob, Eberhard, and Wachtmeister, Georg. "Potentials to simplify the engine system using the alternative diesel fuels oxymethylene ether OME1 and OME36 on a heavy-duty engine". In: *Fuel* 259 (2020), p. 116231. DOI: 10.1016/j.fuel.2019.116231 (cited on pages 37, 39).

Pellegrini, Leonardo, Patrini, Renata, and Marchionna, Mario. "Effect of POMDME Blend on PAH Emissions and Particulate Size Distribution from an In-Use Light-Duty Diesel Engine". In: *SAE 2014 World Congress and Exhibition*. SAE International, 2014. DOI: 10.4271/2014-01-1951 (cited on page 37).

Pellegrini, Leonardo et al. *Combustion behaviour and emission performance of neat and blended polyoxymethylene dimethyl ethers in a light-duty diesel engine*. Tech. rep. SAE Technical Paper, 2012 (cited on pages 37, 42).

Pera, C., Colin, O., and Jay, S. "Development of a FPI Detailed Chemistry Tabulation Methodology for Internal Combustion Engines". In: *Oil and Gas Science and Technology - Revue de l'IFP* 64 (3 2009), pp. 243–258. DOI: 10.2516/ogst/2009002 (cited on page 102).

Pérez-Sánchez, E.J. "Application of a flamelet-based combustion model to diesel-like reacting sprays". PhD thesis. Universitat Politecnica de Valencia, 2019 (cited on pages 8, 96, 100, 103, 185, 186).

Pérez-Sánchez, Eduardo J, Garcia-Oliver, Jose M, Novella, Ricardo, and Pastor, Jose M. "Understanding the diesel-like spray characteristics applying a flamelet-based combustion model and detailed large eddy simulations". In: *International Journal of Engine Research* (2019). DOI: 10.1177/1468087419864469 (cited on page 186).

Peter, Andreas et al. "Mixture formation analysis of polyoxymethylenether injection". In: *Atomization and Sprays* 30.11 (2020), pp. 843–859. DOI: 10.1615/AtomizSpr.2020035250 (cited on pages 45, 79).

Peters, N. "Laminar diffusion flamelet models in non-premixed turbulent combustion". In: *Progress in Energy and Combustion Science* 10.3 (1984), pp. 319–339. DOI: 10.1016/0360-1285(84)90114-X (cited on pages 78, 80).

Peters, N., Hocks, W., and Mohiuddin, G. "Turbulent mean reaction rates in the limit of large activation energies". In: *Journal of Fluid Mechanics* 110 (1981), pp. 411–432. DOI: 10.1017/S0022112081000815 (cited on page 78).

Peters, Norbert. "Turbulent combustion: The state of the art". In: *Turbulent Combustion*. Cambridge Monographs on Mechanics. Cambridge University Press, 2000, pp. 1–65. DOI: 10.1017/CBO9780511612701.002 (cited on pages 69, 72, 78).

Pickett, Lyle M. et al. "Relationship Between Diesel Fuel Spray Vapor Penetration/Dispersion and Local Fuel Mixture Fraction". In: *SAE Int. J. Engines* (2011) (cited on page 22).

Pierce, Charles D. and Moin, Parviz. "Progress-variable approach for large-eddy simulation of non-premixed turbulent combustion". In: *Journal of Fluid Mechanics* 504 (2004), pp. 73–97. DOI: 10.1017/S0022112004008213 (cited on page 72).

Pitsch, Heinz. "Large-Eddy simulation of turbulent combustion". In: *Annual Review of Fluid Mechanics* 38.1 (2006), pp. 453–482. DOI: 10.1146/annurev.fluid.38.050304.092133 (cited on page 182).

Pitsch, Heinz and Ihme, Matthias. "An unsteady/flamelet progress variable method for LES of nonpremixed turbulent combustion". In: *43rd AIAA Aerospace Sciences Meeting and Exhibit*. 2005, p. 557 (cited on pages 48, 79).

Pitsch, Heinz Günter. "Modellierung der Zündung und Schadstoffbildung bei der dieselmotorischen Verbrennung mit Hilfe eines interaktiven Flamelet-Modells; 1. Aufl." Zugl.: Aachen, Techn. Hochsch., Diss., 1997. PhD thesis. Göttingen, 1998, VI, 148 S. : Ill., graph. Darst. (Cited on page 80).

Pöllmann, Simon, Härtl, Martin, and Wachtmeister, Georg. "Injection Process of the Synthetic Fuel Oxymethylene Ether: Optical Analysis in a Heavy-Duty Engine". In: *SAE Powertrains, Fuels & Lubricants Meeting*. SAE International, 2020 (cited on page 42).

Pomraning, Eric. "Development of Large Eddy Simulation Turbulence Models". PhD thesis. University of Wisconsin-Madison, 2000. DOI: 10.13140/2.1.2035.7929 (cited on page 96).

Pomraning, Eric and Rutland, Christopher J. "Dynamic one-equation nonviscosity large-eddy simulation model". In: *AIAA journal* 40.4 (2002), pp. 689–701. DOI: 10.2514/2.1701 (cited on page 182).

Pope, S. B. "An explanation of the turbulent round-jet/plane-jet anomaly". In: *AIAA Journal* 16.3 (1978), pp. 279–281. DOI: 10.2514/3.7521 (cited on page 93).

Pope, Stephen B. "Ten questions concerning the large-eddy simulation of turbulent flows". In: *New Journal of Physics* 6.1 (2004), p. 35. DOI: 10.1088/1367-2630/6/1/035 (cited on page 182).

Pope, Stephen B. *Turbulent Flows*. Cambridge University Press, 2000. DOI: 10.1017/CBO9781316179475 (cited on pages 90, 98).

Preuß, Josefine, Munch, Karin, and Denbratt, Ingemar. "Performance and emissions of renewable blends with OME3-5 and HVO in heavy duty and light duty compression ignition engines". In: *Fuel* 303 (2021). DOI: 10.1016/j.fuel.2021.121275 (cited on page 141).

Reitz, R. and Bracco, F. "Mechanisms of Breakup ofRound Liquid Jets, The Encyclopedia of Fluid Mechanics". In: *The Encyclopedia of Fluid Mechanics* Vol. 3 (1986), pp. 223–249 (cited on page 18).

Reitz, Rolf and Bracco, F. "Mechanisms of breakup of round liquid jets". In: *Encyclopedia of Fluid Mechanics* 3 (1986) (cited on page 87).

Rodriguez, Sal. *LES and DNS Turbulence Modeling*. Springer International Publishing, 2019, pp. 197–223. DOI: 10.1007/978-3-030-28691-0_5 (cited on pages 90, 95).

Rutland, Christopher J. and Bharadwaj, Nidheesh. "A Large Eddy simulation study of sub-grid two-phase interaction in particle-laden flows and diesel engine sprays". In: *Atomization and Sprays* 20.8 (2010), pp. 673–695. DOI: 10.1615/AtomizSpr.v20.i8.20 (cited on page 96).

S., Deng, P., Zhao, M., Mueller, and C., Law. "Stabilization of laminar non-premixed DME/air coflow flames at elevated temperatures and pressures". In: *Combustion and Flame* 162.12 (2015), pp. 4471–4478. DOI: 10.1016/j.combustflame.2015.08.019 (cited on page 25).

Sagaut, P. *Large eddy simulation for incompressible flows: an introduction*. Springer Science and Business Media, 2006 (cited on page 95).

Sanchis, Enrique. "Desarrollo y aplicacion de una metodologia para la tabulacion de la cinética química detallada asociada a la oxidación de hidrocarburos". In: *Universitat Politecnica de Valencia* (2012) (cited on page 103).

Sandberg, Mats. "What is ventilation efficiency?" In: *Building and Environment* 16.2 (1981), pp. 123–135. DOI: 10.1016/0360-1323(81)90028-7 (cited on page 109).

Sarathy, S Mani et al. "Three-stage heat release in n-heptane auto-ignition". In: *Proceedings of the Combustion Institute* 37.1 (2019), pp. 485–492. DOI: 10.1016/j.proci.2018.07.075 (cited on page 25).

Schemme, Steffen, Samsun, Remzi Can, Peters, Ralf, and Stolten, Detlef. "Power-to-fuel as a key to sustainable transport systems – An analysis of diesel fuels produced from CO2 and renewable electricity". In: *Fuel* 205 (2017), pp. 198–221. DOI: 10.1016/j.fuel.2017.05.061 (cited on page 39).

Schmidt, David P. and Rutland, C.J. "A New Droplet Collision Algorithm". In: *Journal of Computational Physics* 164.1 (2000), pp. 62–80. DOI: 10.1006/jcph.2000.6568 (cited on page 88).

Schroll, Peter, Wandel, Andrew P, Cant, R Stewart, and Mastorakos, E. "Direct numerical simulations of autoignition in turbulent two-phase flows". In: *Proceedings of the Combustion Institute* 32.2 (2009), pp. 2275–2282. DOI: 10.1016/j.proci.2008.06.057 (cited on page 25).

Senecal, P. K., Pomraning, E., Richards, K. J., and Som, S. "Grid-convergent spray models for internal combustion engine CFD simulations". In: 2012, pp. 697–710. DOI: 10.1115/ICEF2012-92043 (cited on page 83).

Senecal, P. K., Pomraning, E., Richards, K. J., and Som, S. "An investigation of grid convergence for spray simulations using an les turbulence model". In: vol. 2. SAE International, 2013. DOI: 10.4271/2013-01-1083 (cited on pages 83, 84).

Senecal, P. K. et al. "Large Eddy Simulation of Vaporizing Sprays Considering Multi-Injection Averaging and Grid-Convergent Mesh Resolution". In: *Journal of Engineering for Gas Turbines and Power* 136.11 (2014), p. 111504. DOI: 10.1115/1.4027449 (cited on page 84).

Shin, Dong-hyuk, Sandberg, RD, and Richardson, ES. "Self-similarity of fluid residence time statistics in a turbulent round jet". In: *Journal of Fluid Mechanics* 823 (2017), pp. 1–25. DOI: 10.1017/jfm.2017.304 (cited on pages 110, 111).

Shin, Donghoon, Ryu, Changkook, and Choi, Sangmin. "Computational Fluid Dynamics Evaluation of Good Combustion Performance in Waste Incinerators". In: *Journal of The Air and Waste Management Association* 48 (1998), pp. 345–351. DOI: 10.1080/10473289.1998.10464046 (cited on page 109).

Shukla, P.R and J. Skea, (eds.) *Climate Change 2022: Mitigation of Climate Change. Contribution of Working Group III to the Sixth Assessment Report of the Intergovernmental Panel on Climate Change*. Tech. rep. Cambridge University Press, 2022 (cited on pages 1, 2).

Siebers and L., Dennis. "Liquid-Phase Fuel Penetration in Diesel Sprays". In: *International Congress & Exposition*. SAE International, 1998 (cited on page 22).

Singh, Srijna, Ailaboina, Akhil, Battistoni, Michele, Danish, Mohammad, and Saha, Kaushik. "Numerical Investigation of Cavitation Behavior for Dodecane and OME3 Fuel in ECN Spray C Injector Nozzle". In: *Proceedings of the 1st International Conference on Fluid, Thermal and Energy Systems*. Ed. by Sudev Das, Narasimha Mangadoddy, and Jaap Hoffmann. Singapore: Springer Nature Singapore, 2024, pp. 59–69 (cited on page 45).

Smith, Gregory P., Park, Chung, and Luque, Jorge. "A note on chemiluminescence in low-pressure hydrogen and methane–nitrous oxide flames". In: *Combustion and Flame* 140.4 (2005), pp. 385–389. DOI: 10.1016/j.combustflame.2004.11.011 (cited on pages 72, 138).

Sreedhara, S. and Lakshmisha, K.N. "Autoignition in a non-premixed medium: DNS studies on the effects of three-dimensional turbulence". In: *Proceedings of the Combustion Institute* 29.2 (2002), pp. 2051–2059. DOI: 10.1016/S1540-7489(02)80250-4 (cited on page 25).

Stanković, I and Merci, Bart. "Analysis of auto-ignition of heated hydrogen–air mixtures with different detailed reaction mechanisms". In: *Combustion Theory and Modelling* 15.3 (2011), pp. 409–436. DOI: 10.1080/13647830.2010.542830 (cited on page 25).

Stauch, Rainer, Lipp, S., and Maas, U. "Detailed numerical simulation of the autoignition of single n-heptane droplets in air". In: *Combustion and Flame* 145 (2006), pp. 533–542. DOI: 10.1016/j.combustflame.2005.12.013 (cited on page 24).

Stauch, Rainer and Maas, U. "The ignition of single n-heptane/iso-octane droplets". In: *International Journal of Heat and Mass Transfer* 50 (2007), pp. 3047–3053. DOI: 10.1016/j.ijheatmasstransfer.2006.12.005 (cited on page 24).

Stauch, Rainer and Maas, U. "The ignition of methanol droplets in a laminar convective environment". In: *Combustion and Flame* 153 (2008), pp. 45–57. DOI: 10.1016/j.combustflame.2007.12.001 (cited on page 24).

Strauß, Lukas, Rieß, Sebastian, and Wensing, Michael. "Mixture formation of OME35 and 1-Octanol in comparison with diesel-like Dodecane under ECN Spray A conditions". In: *Frontiers in Mechanical Engineering* 9 (2023). DOI: 10.3389/fmech.2023.1083658 (cited on page 44).

Sun, Wenyu et al. "Speciation and the laminar burning velocities of poly (oxymethylene) dimethyl ether 3 (POMDME3) flames: An experimental and modeling study". In: *Proceedings of the Combustion Institute* 36.1 (2017), pp. 1269–1278. DOI: 10.1016/j.proci.2016.05.058 (cited on pages 33, 48, 71).

Sun, Wenyu et al. "Exploration of the oxidation chemistry of dimethoxymethane: Jet-stirred reactor experiments and kinetic modeling". In: *Combustion and Flame* 193 (2018), pp. 491–501. DOI: 10.1016/j.combustflame.2018.04.008 (cited on page 71).

Sun, Zhongcheng et al. “Combustion characteristics of oxymethylene dimethyl ether-diesel blends: An experimental investigation using a constant-volume combustion chamber”. In: *Fuel* 360 (2024), p. 130587. DOI: 10.1016/j.fuel.2023.130587 (cited on page 45).

Tagliante, Fabien et al. “A conceptual model of the flame stabilization mechanisms for a lifted Diesel-type flame based on direct numerical simulation and experiments”. In: *Combustion and Flame* 201 (2019), pp. 65–77. DOI: 10.1016/j.combustflame.2018.12.007 (cited on pages 27, 215).

Tamura, Masayuki et al. “Collisional Quenching of CH(A), OH(A), and NO(A) in Low Pressure Hydrocarbon Flames”. In: *Combustion and Flame* 114.3 (1998), pp. 502–514. DOI: 10.1016/S0010-2180(97)00324-6 (cited on pages 72, 138).

Tan, Yong Ren et al. “Sooting characteristics of polyoxymethylene dimethyl ether blends with diesel in a diffusion flame”. In: *Fuel* 224 (2018), pp. 499–506. DOI: 10.1016/j.fuel.2018.03.051 (cited on pages 33, 35).

Tanabe, M et al. “Spontaneous ignition of liquid droplets from a view of non-homogeneous mixture formation and transient chemical reactions”. In: *Symposium (International) on Combustion*. Vol. 26. 1. Elsevier. 1996, pp. 1637–1643 (cited on page 24).

Tejada, Francisco Jose. “Analysis of fuel effects on the diffusive flame structure using advanced optical techniques in a single cylinder optical engine”. PhD thesis. Universitat Politecnica de Valencia, 2023 (cited on pages 7, 46, 49).

The overall CO2 impact for drive technologies in individual transport today and in the future. Tech. rep. Frontier economics, 2019 (cited on page 5).

The Role of E-fuels in Decarbonising Transport. Tech. rep. IEA, Paris, 2024 (cited on page 4).

Theinnoi, Kampanart, Suksompong, Porjade, and Temwutthikun, Warirat. “Engine performance of dual fuel operation with in-cylinder injected diesel fuels and in-port injected DME”. In: *Energy Procedia* 142 (2017), pp. 461–467. DOI: 10.1016/j.egypro.2017.12.072 (cited on page 33).

Tripathi, Shashwat. “Life Cycle Analysis of Different Powertrain Technologies for Decarbonising Road Transportation”. PhD thesis. Universitat Politecnica de Valencia, 2023 (cited on page 6).

Tuan Nguyen, Fabien Tagliante, Julien Manin, Lyle Pickett, Hyung-Sub Sim, Kevin Wan and Angela Wu. *Investigation of Formaldehyde and PAH Behavior Using LES of N-dodecane and OME*. 2022. URL: https://ecn.sandia.gov/workshop/ECN9/ECN8.1.mp4 (cited on page 221).

Uchida, Tadashi, Kurita, Yukio, and Kubo, Masaji. "The dipole moments and the structure of polyoxymethylene dimethyl ethers". In: *Journal of Polymer Science* 19.92 (1956), pp. 365–372. DOI: 10.1002/pol.1956.120199215 (cited on page 39).

United Nations Climate Change Conference COP28. Tech. rep. United Nations, 2023 (cited on page 1).

United Nations climate change: the Paris Agreement. Tech. rep. United Nations, 2020 (cited on page 1).

Van Oijen, JA and De Goey, LPH. "Modelling of premixed laminar flames using flamelet-generated manifolds". In: *Combustion science and technology* 161.1 (2000), pp. 113–137. DOI: 10.1080/00102200008935814 (cited on page 102).

Wei, Jiangjun et al. "Morphology analysis of soot particles from a modern diesel engine fueled with different types of oxygenated fuels". In: *Fuel* 267 (2020), p. 117248. DOI: 10.1016/j.fuel.2020.117248 (cited on page 33).

Westbrook, Charles K. "Chemical kinetics of hydrocarbon ignition in practical combustion systems". In: *Proceedings of the combustion institute* 28.2 (2000), pp. 1563–1577. DOI: 10.1016/S0082-0784(00)80554-8 (cited on page 25).

Wierzba, A. "Deformation and breakup of liquid drops in a gas stream at nearly critical Weber numbers". In: (2006). DOI: 10.1007/BF00575336 (cited on page 20).

Wiesmann, Frederik, Bauer, Esra, Kaiser, Sebastian A., and Lauer, Thomas. "Ignition and Combustion Characteristics of OME and N-Dodecane: A Comparison Based on CFD Engine Simulations and Optical Experiments". In: (2023). DOI: 10.4271/2023-01-0305 (cited on page 141).

Wiesmann, Frederik et al. "Numerical and Experimental Investigations on the Ignition Behavior of OME". In: *Energies* 15 (18 2022). DOI: 10.3390/en15186855 (cited on pages 141, 185).

Wiesmann, Frederik et al. "Numerical and Experimental Investigations on the Ignition Behavior of OME". In: *Energies* 15.18 (2022). DOI: 10.3390/en15186855 (cited on pages 47, 49).

Wiesmann, Frederik et al. "Numerical study of novel OME16 combustion mechanism and spray combustion at changed ambient environments". In: *Frontiers in Energy* (2024). DOI: 10.1007/s11708-024-0926-8 (cited on pages 47, 49).

Williams, Forman A. “Recent Advances in Theoretical Descriptions of Turbulent Diffusion Flames”. In: 1975. DOI: 10.1007/978-1-4615-8738-5_5 (cited on page 78).

Winklinger, Johannes Franz. “Implementation of a Combustion Model based on the Flamelet Concept and its Application to turbulent reactive Sprays”. PhD thesis. Universitat Politecnica de Valencia, 2014 (cited on pages 8, 100, 103).

Wu, Yixuan, Ays, Isabelle, and Geimer, Marcus. “Analysis and Preliminary Design of Oxymethylene ether (OME) Driven Mobile Machines”. In: *Preprint.* (2019) (cited on page 142).

Xuan, Tiemin et al. “A conceptual model of polyoxymethylene dimethyl ether 3 (PODE3) spray combustion under compression ignition engine-like conditions”. In: *Combustion and Flame* 261 (2024), p. 113296. DOI: 10.1016/j.combustflame.2024.113296 (cited on page 46).

Xue, Qingluan, Som, Sibendu, Senecal, Peter K., and Pomraning, E. “Large Eddy simulation of fuel-spray under non-reacting IC engine conditions”. In: *Atomization and Sprays* 23.10 (2013), pp. 925–955. DOI: 10.1615/AtomizSpr.2013008320 (cited on pages 185, 186).

Yang, Yi, Boehman, André L., and Simmie, John M. “Effects of molecular structure on oxidation reactivity of cyclic hydrocarbons: Experimental observations and conformational analysis”. In: *Combustion and Flame* 157.12 (2010), pp. 2369–2379. DOI: 10.1016/j.combustflame.2010.04.015 (cited on page 69).

Yao, Tong et al. “A compact skeletal mechanism for n-dodecane with optimized semi-global low-temperature chemistry for diesel engine simulations”. In: *Fuel* 191 (2017), pp. 339–349. DOI: 10.1016/j.fuel.2016.11.083 (cited on pages 73, 130, 138).

Yi, T et al. “Autoignition-controlled flame initiation and flame stabilization in a reacting jet in crossflow”. In: *Proceedings of the Combustion Institute* 37.2 (2019), pp. 2109–2116. DOI: 10.1016/j.proci.2018.06.057 (cited on page 25).

Zacherl, Florian, Wopper, Christoph, Schwanzer, Peter, and Rabl, Hans-Peter. “Potential of the Synthetic Fuel Oxymethylene Ether (OME) for the Usage in a Single-Cylinder Non-Road Diesel Engine: Thermodynamics and Emissions”. In: *Energies* 15.21 (2022), p. 7932. DOI: 10.3390/en15217932 (cited on page 38).

Zádor, Judit, Taatjes, Craig A, and Fernandes, Ravi X. "Kinetics of elementary reactions in low-temperature autoignition chemistry". In: *Progress in energy and combustion science* 37.4 (2011), pp. 371–421. DOI: 10.1016/j.pecs.2010.06.006 (cited on page 25).

Zeng, Wei, Xu, Min, Zhang, Gaoming, Zhang, Yuyin, and Cleary, David J. "Atomization and vaporization for flash-boiling multi-hole sprays with alcohol fuels". In: *Fuel* 95 (2012), pp. 287–297. DOI: 10.1016/j.fuel.2011.08.048 (cited on page 21).

Zhang, Min, Ong, Jiun Cai, Pang, Kar Mun, Bai, Xue-Song, and Walther, Jens H. "Large eddy simulation of transient combustion and soot recession in the ECN Spray A and D flames". In: *Fuel* 329 (2022), p. 125384. DOI: 10.1016/j.fuel.2022.125384 (cited on page 223).

Zheng, Zunqing et al. "Experimental study on the combustion and emissions fueling biodiesel/n-butanol, biodiesel/ethanol and biodiesel/2, 5-dimethylfuran on a diesel engine". In: *Energy* 115 (2016), pp. 539–549. DOI: 10.1016/j.energy.2016.09.054 (cited on page 33).